THE VARIATION OF OPTICAL AND ELECTRICAL PROPERTIES DUE TO ANNEALING OF THIN, VAPOUR-QUENCHED ALUMINIUM FILMS

****
******
****
**
*

A Thesis Submitted for the Degree of

Doctor of Philosophy

in The University of Aston in Birmingham

Kevin Richard O'Shea, M.Sc.
M. Inst. P.

Physics Department
September 1971

To my wife

ABSTRACT

This thesis contains the results of simultaneous observations of the changes of optical and electrical properties of thin aluminium films deposited in ultra-high vacuum on to various substrates at 77°K, and subsequently raised to room temperature and then annealed to about 550°K.

The optical constants n and k were measured using an ellipsometer of simple construction and the defect concentration was estimated from electrical resistivity.

Oxidation of an aluminium surface was found to be significant even at a total pressure of 1.5×10^{-9} torr but observations on several films enabled a correction to be applied.

Films below 15 nm thickness, deposited at 77°K on glass substrates showed an irreversible fall of resistance of up to 40% when warmed to room temperature. The techniques used in radiation damage recovery were employed and the observations were found to be consistent with the migration of 'Dumbell' ⟨100⟩ interstitials to vacancies.

During the fall of resistance, a simultaneous rise of the product nk, which is proportional to optical absorption, was observed for all films at a wavelength of 0.549μ . This was not consistent with the Drude-Zener formulae and was attributed to an increase of the inter-band absorption peak centred at 0.8μ for aluminium.

Optical measurements over an extended wavelength range (0.49μ to 1.94μ) for films on both glass and single crystal potassium bromide substrates also showed that the anneal from 77°K to room temperature always produced development of the inter-band absorption peak and a shift of the maximum towards higher energy. This occurred over and above the known effect of temperature.

The movement of the peak is interpreted as an ordering effect producing development of the (200) component of the pseudo-

potential and hence an increase of the inter-band absorption in the region of the symmetry point W on the (200) Bragg reflection plane of the Brillouin zone.

During annealing to 550^{o}K of totally oxidised films, it was found that on glass substrates the free electron value of nk increased, while on the crystal substrates the value decreased. This was interpreted as a difference in thermal expansion between the film and substrate. On the glass substratesthe films were compressed beyond the elastic limit and the defect concentration was increased, whereas on the crystal substrates the films were extended and true annealing occurred. On both substrates the inter-band contribution was increased by the anneal.

I N D E X

CHAPTER 1

INTRODUCTION

The variation of the optical properties of metals due to annealing, which is the subject of the present work, has been associated with several areas of research which have traditionally been pursued independently. Material is drawn from these different fields in the interpretation and discussion of the new results and it therefore seems appropriate to divide the review of the relevant subject matter into the following sections:

1. Optical theory and optical constants of metals.
2. Thin film conductivity.
3. Defects and annealing of defects in metals.
4. Ellipsometry

1.1 Optical properties of metals

Following the discovery of the electron by J. J. Thomson in 1897, it was realised almost at once that the remarkable electrical conductivity of metals could be explained by assuming the presence in these materials of a "free electron" gas. The link between electrical conductivity and the response of a metal to light i.e. a high frequency electric field, was first suggested by Drude in 1902.[1] According to Drude, collisions of the electrons with the metal ions resulted in a loss of energy which caused the optical electric field to be attenuated exponentially with penetration into the metal. Under these conditions it has been found necessary to introduce the concept of a complex refractive index, as first proposed by Cauchy.[2] According to this treatment, the electric field inside the metal is represented by

$$E = E_0 \, e^{-\frac{k\omega x}{c}} \cos \omega \left(\frac{nx}{c} - t \right)$$

where n is the refractive index and k is called the extinction coefficient. In the complex form this becomes

$$E = E_0 \, e^{-i\omega \left(\mathcal{N} \frac{x}{c} - t \right)}$$

where $\mathcal{N} = n - ik$ and is called the complex refractive index.*

* Sometimes in the literature $\mathcal{N}$ is written $\mathcal{N} = n + ik$, in which case the exponent is also positive.

The distance into the metal in which the field intensity is attenuated by $\frac{1}{e}$, called the penetration depth δ, is given by

$$\delta = \frac{c}{k\omega} = \frac{\lambda_{vac}}{2\pi k}$$

If in the long wavelength region of the infra red the Hagen-Rubens relation[3]

$$n = k = \frac{\sigma_0}{\nu}$$

is assumed to hold, then it can be shown that

$$\delta = \frac{c}{(2\pi\omega\sigma_0)^{1/2}}$$

where σ_0 is the D. C. conductivity and ν is the frequency.

For most metals δ is of the order of 20 n.m. so that it is only possible to measure the optical properties of this very thin surface layer. Any variation in structure which makes this layer non-representative of the bulk metal will lead to serious error in the determination of bulk optical constants.

During the years 1900 to 1920, a number of investigators attempted to produce measurements of optical constants and compare them with those predicted by the Drude theory, and its extension by Zener[4] and others. For example, the work of Hagen and Rubens[5] and Fosterling and Freedericksz[6] in the infra red, met with some success especially for the alkali metals which closely follow a one-free-electron model, and for the noble metals for which cleaner surfaces can be produced. Also, the concept of an 'ideal' metal containing a cloud of completely free electrons, explained the results of Wood[7] who found that the alkali metals became transparent in the ultra violet. Zener[4] showed that for the condition

$$\frac{4\pi Ne^2}{m\omega^2} > 1$$

where N = free electron density

m = free electron mass

an ideal metal would be totally reflecting, whereas when

$$\frac{4\pi Ne^2}{m\omega^2} < 1$$

it would be transparent. The values of ω predicted for the sudden change-over were in reasonable agreement with those measured by Wood.[7]

Even at that time it was realised that these early results were probably unreliable owing to the various methods of surface polishing, which were thought to result in a hardened surface layer of small crystallites.[8] The well-known failure of the classical theory to explain the magnitudes of electron specific heats and mean free paths between ion collisions led to Sommerfeld's[9] application of 'quantised free electron' theory in which it emerged that only those free electrons near the Fermi energy were responsible for conduction. The resulting equations were identical in form to those of Drude but the interpretation was different. For example, the direct current conductivity σ_0 was given by

$$\sigma_0 = \frac{Ne^2\lambda}{mv}$$

where λ = mean free path AT THE FERMI ENERGY

v = mean velocity AT THE FERMI ENERGY

However, the actual magnitudes of mean free paths and their variation with temperature as predicted by the above equation, disagreed with experimental results by as much as two orders of magnitude in some cases. Further progress was made possible by the abandonment of the ideas of scattering by ion cores and the representation of electrons by Bloch[10] wave functions which enabled them to travel throughout the metal lattice without attenuation so long as the potential due to the ion cores was perfectly periodic. According to this theory, scattering of electron waves was produced only by departures from perfect periodicity due to lattice vibrations and crystal defects. The subsequent development of the band theory of conduction by Kronig[11], Frolich[12] and Wilson[13] among others, was able to explain the broad features of electrical conduction and optical properties of metals. In particular, the band theory showed that for most metals absorption in the infra red was mainly due to acceleration of free electrons, for which the Drude-Zener theory was applicable, while in the visible and ultra-violet regions quantum transitions predominate (i.e. inter-band or internal photo-

electric transitions). Mott and Jones[8] in 1936 derived theoretical values of wavelength at which quantum absorption should begin.

For aluminium in the infra-red, the quantised free electron model is a good approximation because this metal behaves very nearly as if there were three free electrons per atom. Independent evidence for this comes from measurements of free carrier density from the Hall effect.[14]

The infra-red optical properties of metals at low temperatures conflicted with the Drude-Zener theory, however. The theory predicted that at low temperatures the optical absorption would become very small whereas experimentally the absorption remained large. The conflict was largely resolved and agreement with experiment improved in all cases when Dingle[15] and Ginsburg[16] applied the theory of the anomalous skin effect, discovered by Pippard,[17] to absorption in the microwave region. In this way, account was taken of the fact that at low temperatures the electron mean free path increases until it exceeds the penetration depth δ of the electromagnetic field. This leads to increased absorption in the surface layer.[18]

Although, as we have seen, the early experimental results are open to doubt, Drude and the other early workers were able to contribute much to the development of highly sophisticated measuring techniques involving polarised light which still form the basis of present day methods. See Section 2.

The data available at the end of 1957 was reviewed by Schulz[19] who concluded that for some elements, including aluminium in the infra-red, the Drude theory agrees reasonably well with experimental results, but in other cases there is poor agreement or wide discrepancy. Attempts have been made to improve this situation by allowing the Drude parameters to be frequency dependent.[20] Gurzhi[21] proposed that the relaxation time, τ should follow the

form

$$\frac{1}{\tau} = A + B\omega^2$$

which was applied to gold by Abelès and Theye.[22] Roberts[23] proposed that the Drude theory should be modified to include more than one class of free electron having different parameters; although this has received little support.

Schulz also concluded that most of the variation in results could be traced to sample defects. This situation was improved by the development of the techniques of vacuum evaporation of metals and of electro-polishing. These methods eliminated the hard polishing layer referred to previously.[24]

In 1960, Mendelowitz[25] examined the validity of the Drude-Zener formulae for aluminium over the entire range 0.25μ to 5μ wavelength, using the results of Hass,[26] Schulz and Tangherlini[27] and Beattie and Conn.[28] He concluded that the theory gave a good qualitative description, except in the region of 0.9μ , where the presence of an inter-band absorption peak was then only suspected. The parameters he deduced were 2.4 free electrons per atom and a relaxation time, τ of 1.2×10^{-15} sec.

After 1960, when as a result of great advances in vacuum technique, metal layers could be produced at pressures below 10^{-8} torr, so that the effects of occluded gas and surface oxidation were reduced, significant differences in measured optical constants were found for aluminium, compared with specimens produced at higher pressures. It was observed by Bennet[29] et al., in the visible and by Madden[30] et al. in the ultra-violet, that the measured values of n, k and normal reflectance R were all larger than previous measurements, made under poorer vacuum. This was shown in recent results by Fane and Neal[31] and by O'Shea and Fane[32], to be consistent with the absence of a surface film of oxide. The normal reflectance data of Bennet[29] et al. and of Madden[30] et al. was analysed in 1963 by Ehrenreich[33] et al. using the Kramers-Kronig relations[34][35][36] to deduce the real and imaginary parts of the

dielectric constant, ϵ , in the range 0 to 22 eV. (See Fig.1) They analysed the results, as they had previously done for copper[36] by separating ϵ into a free electron term, $\epsilon^{(f)}$, which was assumed to follow formulae similar to those of Drude, and a bound electron term $\epsilon^{(b)}$. Then, observing that interband transitions did not begin until o.7eV the parameters of $\epsilon^{(f)}$ were obtained from measurements below this value. They obtained a plasma frequency corresponding to $\hbar\omega_p$ = 12.7eV and a relaxation time, τ of 5.12 x 10^{-15} sec. These parameters were then used to calculate the contribution $\epsilon^{(f)}$ in the visible and ultra-violet regions which were then subtracted from the experimental measurements. The difference then gave the contribution of bound electrons $\epsilon^{(b)}$. The absorption due to $\epsilon^{(b)}$ was then shown to be a narrow peak centred on 1.5 eV which was compared with band structure calculations made by Segall[37] and shown to be in reasonable agreement. (See Fig.2A)

There were differences in the effective optical electron mass (1.5 against 1.2 from band theory) and also estimates of the direct current conductivity were too low by a factor of 2.

An extensive analysis of the results available for aluminium was made in 1970 by Powell[38]. The reflectance data of Bennett[29] and of Madden[30] were still considered to be the best available although recent evidence suggests that surface oxidation was probably present.[32]

Powell concluded that there was no more satisfactory model for ϵ than the one which used

$$\epsilon_\omega = \epsilon_\omega^{(f)} + \epsilon_\omega^{(b)}$$

The analysis was carried out by a method different from that employed by Ehrenreich et al., and the inter band absorption peak around 1.5 eV was shown to approach more closely to that predicted by recent band structure calculations of Hughes[39] et al.

A greater understanding of the inter band contribution to optical properties had come with the development of more advanced Solid State theory in the years 1960 to 1965, when greater use was

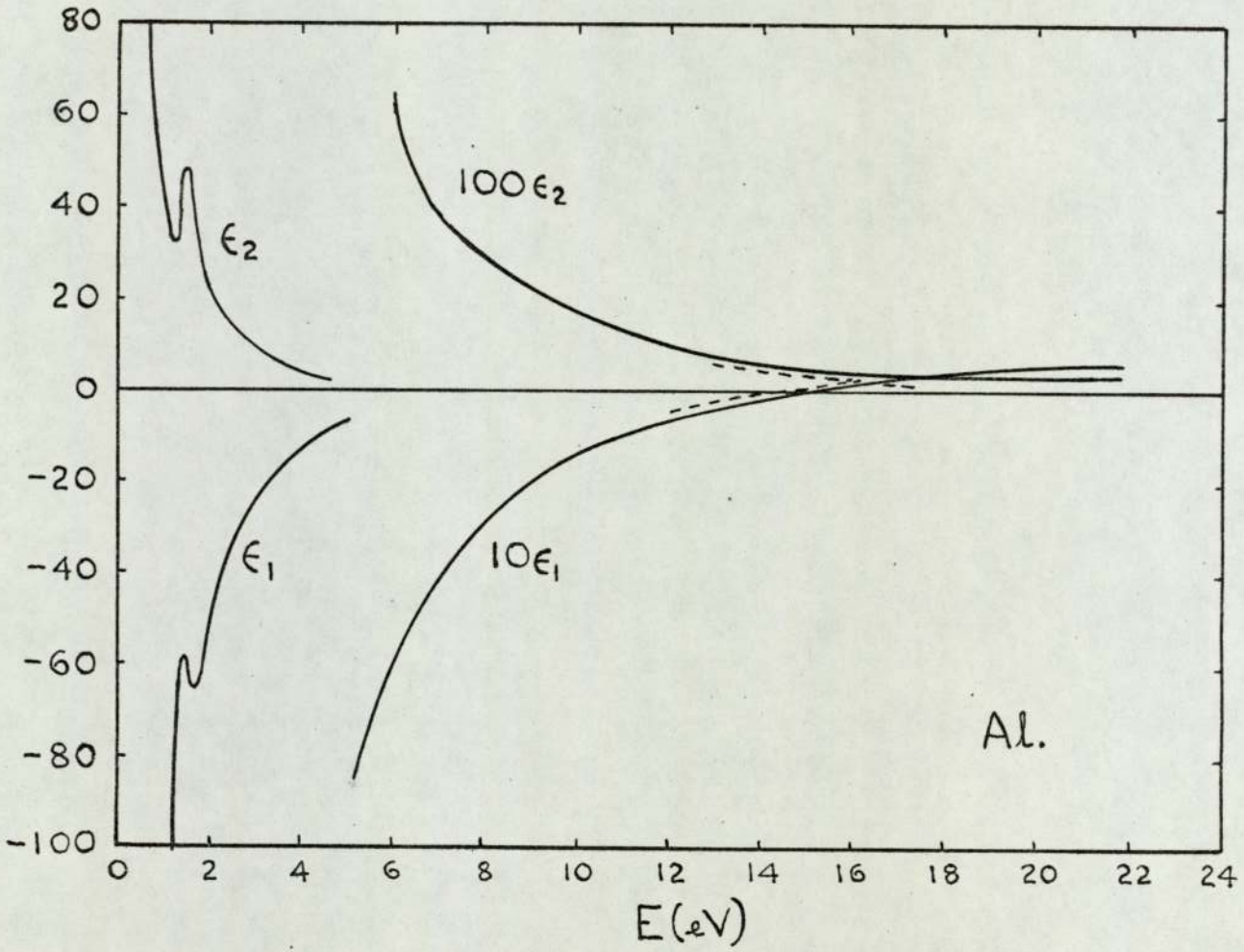

FIG. 1. DIELECTRIC CONSTANT OF Al. $\epsilon = \epsilon_1 - i\epsilon_2$

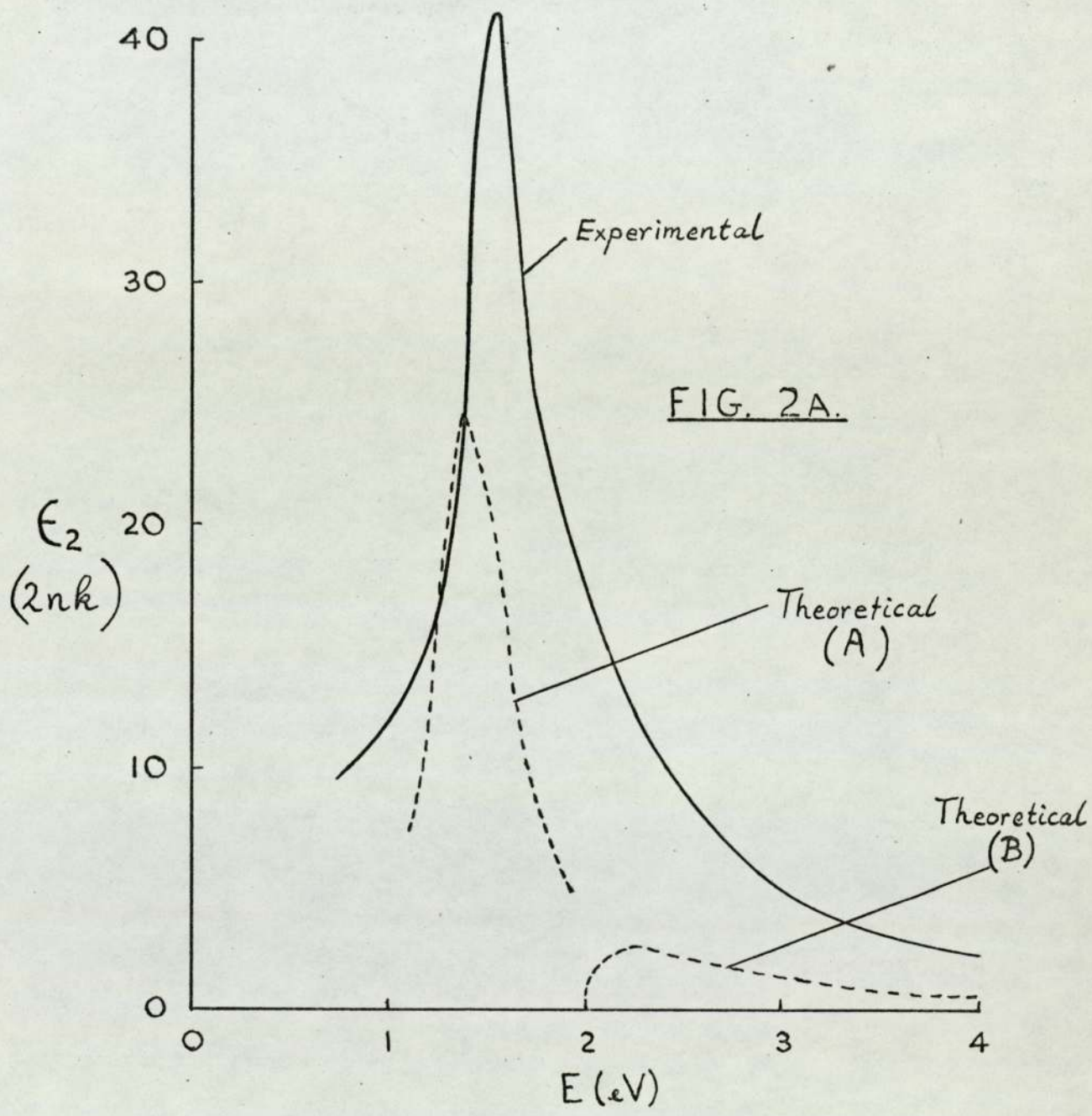
40
30
20
10
0
ϵ_2 (2nk)
Experimental
Theoretical (A)
Theoretical (B)
0
1
2
3
4
E (eV)

FIG. 2A.

FIG. 2A

made of the concept of pseudo-potential developed by Harrison,[40] Heine[41][42] and Ziman[43] and others. By assuming that the valence electrons experience only the weak potential of the screened ions one is able to use a pseudo-potential V(r), expanded as a Fourier series over all reciprocal lattice vectors g:

$$V(r) = \sum V_g \, e^{2\pi i g.r}$$

with the one electron Schrödinger equation. Solving this equation enabled Fourier components, Vg, to be calculated and a whole range of metal properties to be theoretically investigated. The Fourier components of the pseudo-potential determine the band structure of the metal and also any other property that depends on the electron interaction with the ion lattice; for example, the de-Haas van-Alphen effect, cyclotron resonance, phonon spectra and the absorption of ultra-sound, and also the temperature of the transition to the super-conducting state.[24]

The de Haas van-Alphen effect is observable as a change of magnetic susceptibility with applied magnetic field and comes about because the Fermi energy oscillates as a function of magnetic field. This in turn comes about because of discontinuities in the density of states.[44] In 1963 Ashcroft[45] proposed a pseudo-potential model to fit the de Haas van-Alphen data in aluminium and was able to calculate Vg for several important crystal directions. These components, Vg, were used by Hughes[39] et al. to predict the shape of the interband absorption peak in aluminium around 1.5 eV which gave good agreement with experiment. (See Fig.2B)

Ashcroft[46] has recently refined the theoretical relation between inter-band absorption and the Fourier components of the pseudo-potential, deriving an expression for optical mass.

The experimental determination of Vg, along with its temperature variation, is clearly of great interest. The latter can only be done by measuring the optical constants in the inter-band region at various temperatures.[24] As discussed previously, most

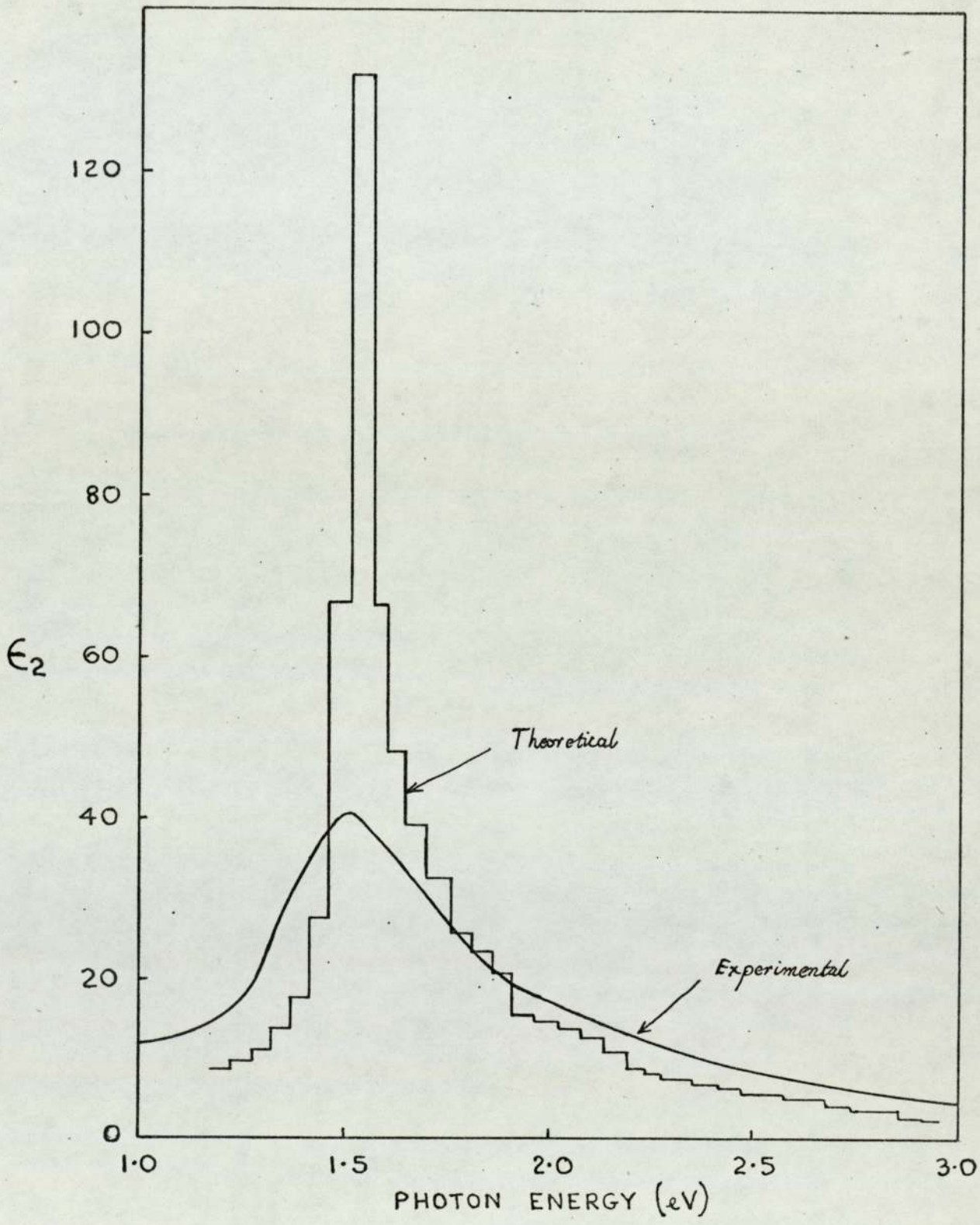

FIG. 2B. OPTICAL INTERBAND ABSORPTION OF ALUMINIUM.

measurements of n and k are unacceptable for comparison with theory, and hence for the determination of fundamental properties of metals, because of uncertain structure and cleanliness of the surface layer. The value of future work in this field will depend on the extent to which experimentalists can produce specimens that match the assumptions of the theory. Namely,

i) Ultra-pure single crystal metal films, perhaps produced expitaxially, which would have
ii) negligable or known defect structure,
iii) atomically smooth surfaces, and
iv) total absence of surface contamination or surface oxide film.

So far, no-one claims to have done this. The oxidation problem with aluminium may prove insoluble except by the method suggested by Madden[30] et al., and used in this laboratory,[32] of measuring the effects of oxidation with time and then extrapolating back to the original clean surface.

As Mayer[47] has pointed out, the optical properties of thin metal films, since they depend closely on electrical conductivity, must also depend on film thickness. There is as yet no complete theoretical treatment of mean free path effects on optical properties, although these "size-effects" are well understood for electrical conductivity.

Drumheller[48] in 1964 considered a polycrystalline film in terms of a film impedance, a resistive part and a reactive part which could be related to inter-grain capacity. He found that the reflectivity of Bismuth so calculated, agreed well with experimental values.

1.2 Thin Film Conductivity

Several authors have followed the original suggestion of Thomson[49] that the electrical resistivity of a thin film will increase when the electron mean free path is restricted by the

surfaces of the film. The work of Fuchs[50] and Sondheimer[51] resulted in an accepted theory which could predict quantitatively the variation of resistivity with thickness. From their studies it followed that if the electron scattering at the film boundaries is mainly diffuse (a now generally accepted assumption) then the conductivity for thickness d is given by

$$\sigma_d = \frac{3}{4}\sigma \frac{d}{\ell}\left(\frac{1+p}{1-p}\right) \log_e \frac{\ell}{d}$$

If $d < \ell$

and by

$$\sigma_d = \sigma\left[1 + \frac{3}{8}(1-p)\frac{\ell}{d}\right]^{-1}$$

If $d > \ell$

where σ = bulk conductivity

p = coeff. of specular reflection

ℓ = electron m.f.p. in bulk crystal, at the same temperature.

It can be seen that if $p=0$ (totally diffuse reflection) the ratio $\frac{\sigma}{\sigma_d}$ departs from unity, but if $p=1$ then the thickness effect disappears.

The extensive and elaborate work of Mayer[47] in 1958 on alkali metal films has shown that when precautions are taken to ensure that the assumptions of the theory are valid, then the agreement with experiment is extremely close. (See Fig.3).

Anomalous results are invariably associated with faults in film preparation, poor vacuum or impure materials, leading to different defect structures of films or to irreversible changes in resistivity due to changes in defect concentrations. Much useful information can come from a study of the defect structure itself, and its influence on film resistivity. A number of workers have taken quenched metal foils and compared the resistivity changes with observed defect structures seen in electron microscopy. For example, Cotterill[52] arranged for very pure aluminium foils (7μ thick) to be heated electrically to 650°C and quenched in distilled water. Resistivity increases produced by the quenching

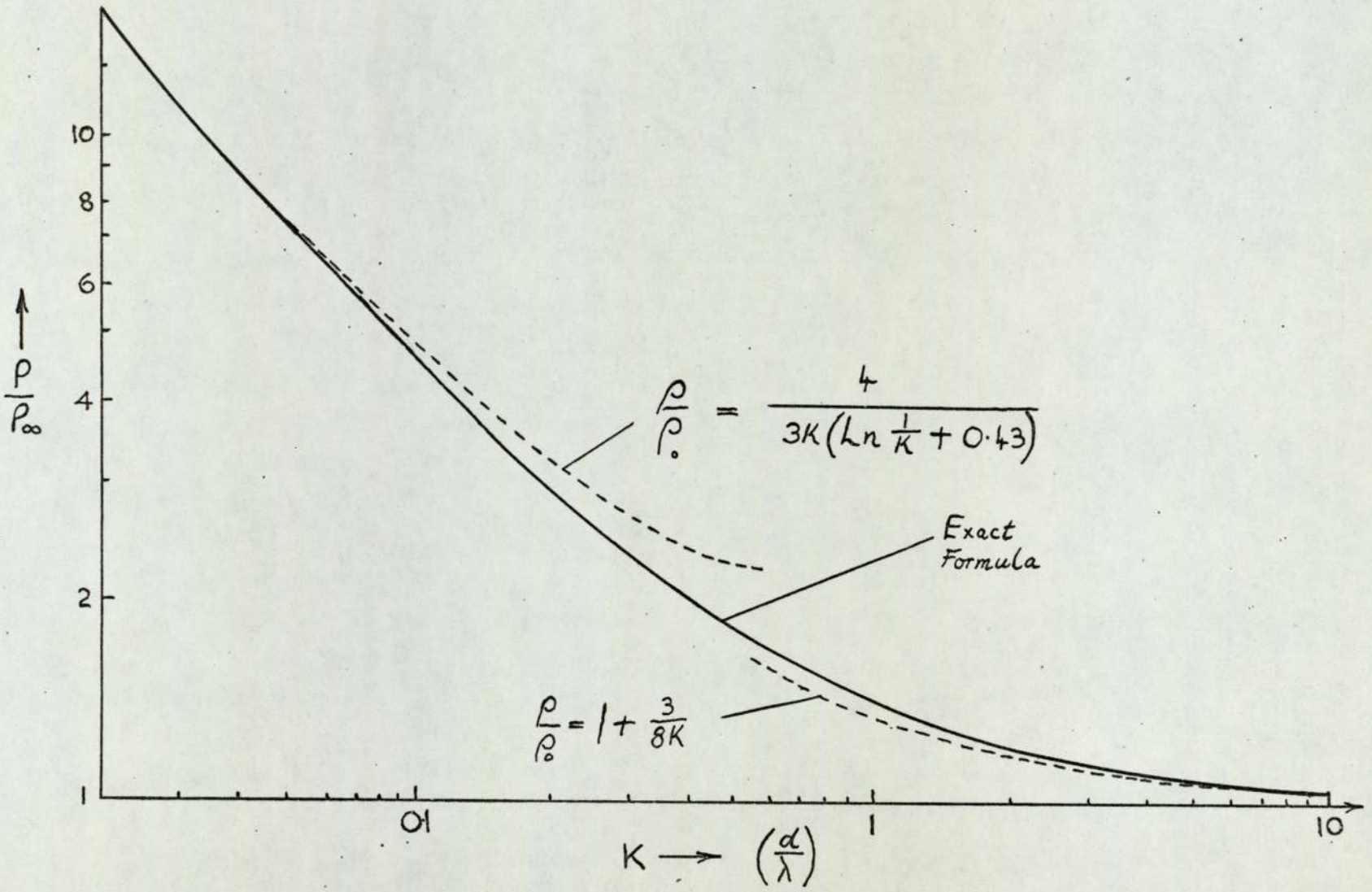

FIG. 3. RESISTIVITY OF METAL FILMS AGAINST REDUCED THICKNESS

were measured at -196°C. After annealing at 70°C for some time part of the resistivity increase, attributed to vacancies, annealed out. The same specimen, after electrolytic thinning, was examined on an electron microscope and found to contain a high concentration of dislocation loops, which was measured directly. Hence the resistivities introduced by known concentrations of both vacancies and dislocations were estimated. Cotterill found that

$$\rho_{disloc.} = (7 \pm 2) \times 10^{-19} \beta. \quad \Omega\,cm^3$$

β = concentration of dislocations per cm^2

and

$$\rho_{vacancy} = (1.4 \pm 0.3) \times 10^{-6}\ \Omega.cm \text{ per atomic \% vacancy}$$

The measurements of $\rho_{disloc.}$ although larger, were probably more reliable than previous measurements done by deformation and quenching of foils performed by Yoshida[53], $10^{-19} \beta.\ \Omega\,cm^3$; Clareborough[54], $3.3 \times 10^{-19} \beta.\ \Omega\,cm^3$; and Silcox and Wheelan[55], $3 \times 10^{-19} \beta.\ \Omega\,cm^3$; who had not used the same specimen for resistivity and dislocation density measurements.

The measurements of $\rho_{vacancy}$, which were produced with the aid of the results of Panseri and Fedherigi[56] were lower than those made by Simmons and Ballufi[57], ($3 \times 10^{-6}\ \Omega\ cm$ per % vac.)

More recent determinations of $\rho_{disloc.}$ by Rider and Foxon[58] in 1966, who used two identically treated specimens, indicate a value of $(2.9 \pm 0.4) \times 10^{-19} \beta.\ \Omega\,cm^3$ at liquid nitrogen temperature. They claimed that the thinning procedure of Cotterill removed some of the dislocations, thereby indicating a high value of $\rho_{disloc.}$. An extension of the work of Yoshida[59] in 1965 showed that the resistivity of voids, i.e. aggregates of vacancies, in aluminium could be given by $2.5 \times 10^{-12} d^2.\ \Omega\,cm^3$ where d was a measure of the void size. This formula, produced for voids larger than 5 n.m. was found to give results comparable with other methods even

for single vacancies.

Scattering of electrons by the grain boundaries of crystallites in polycrystalline films must also contribute to the increased resistivity in thinner films, for which the grain size is usually smaller. Komnik and Palatnik[60] in 1964 drew attention to some systematic differences in polycrystalline bismuth films which had been deposited at 70°C and at 120°C. The variations were explained in a consistent way by considering the different mean crystallite size of the specimens. Neuman and Wen[61], 1966, have shown the considerable improvement in understanding of the size effect in bismuth that can be achieved by plotting conductivity against grain size and not against film thickness. (See Figs. 4A and 4B.) This agrees well with the theory of Ivanov and Papov[62] that (in Bismuth) the mean free path is determined solely by the crystallite size. A similar work by Mayadas[63], in 1969, on polycrystalline aluminium films concluded that the Fuchs-Sondheimer theory alone was not sufficient to explain the thickness dependence of resistivity. Assuming a surface scattering coefficient of $p = 0$ as is usual[64], the results indicated an increase of intrinsic mean free path with increasing film thickness. (See Fig.5) Measurements of grain size by transmission electron microscopy showed that grain size increased with film thickness, and was in fact about equal to film thickness[63]. This conclusion was also reached by Kooy[65] who observed columnar growth of selected crystallite orientations as shown in Fig.6. The study concluded that the thickness dependence of resistivity (over and above that of the Fuchs-Sondheimer theory) was a grain boundary effect.

Electrical noise studies of such films at low frequencies have confirmed that grain boundary scattering plays an important part in resistivity.[66]

A theoretical model for the prediction of resistivity increase for thinner films, taking into account the reduced grain size, was

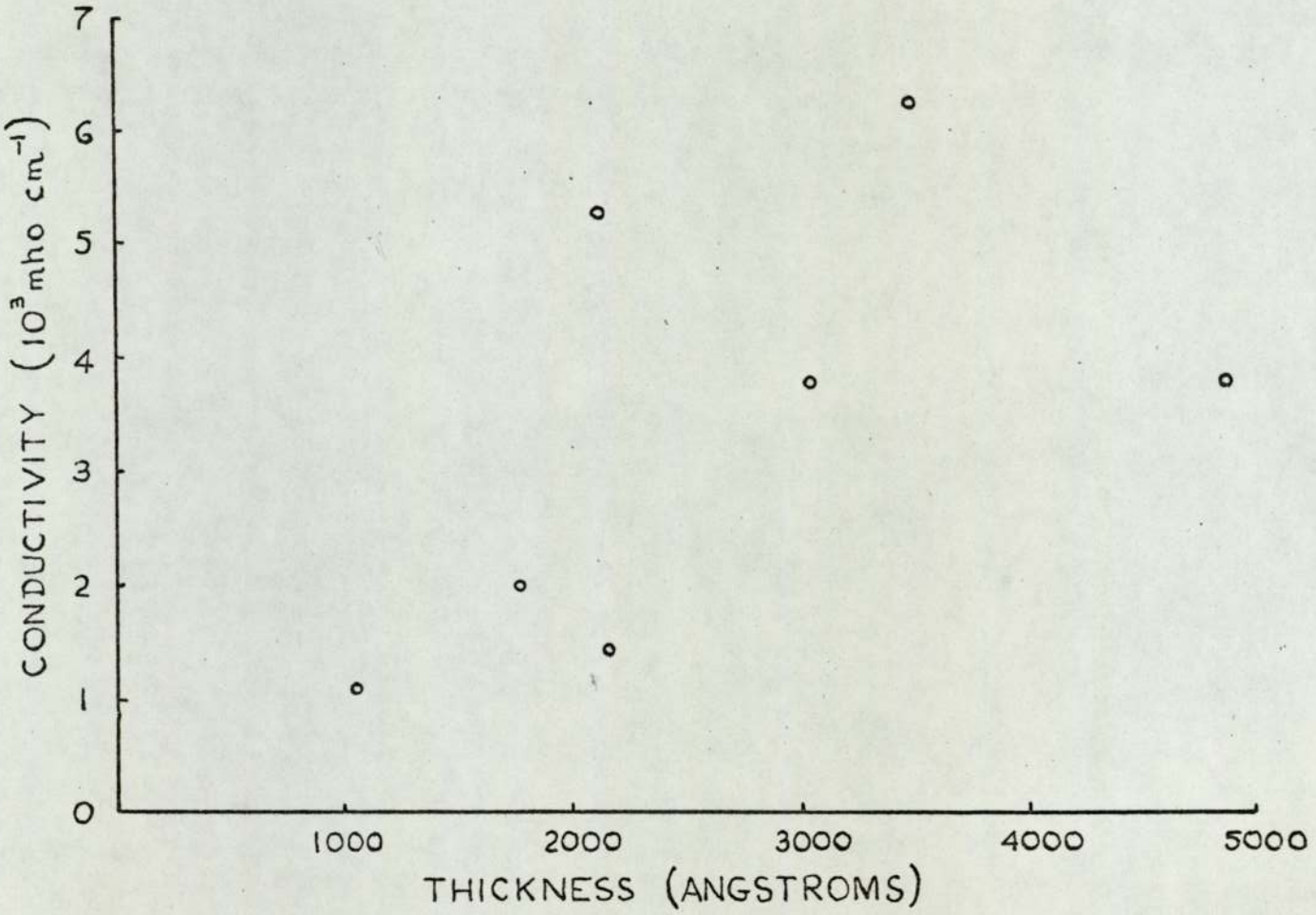

FIG. 4A. CONDUCTIVITY OF BISMUTH THIN FILMS AS A FUNCTION OF THEIR THICKNESS.

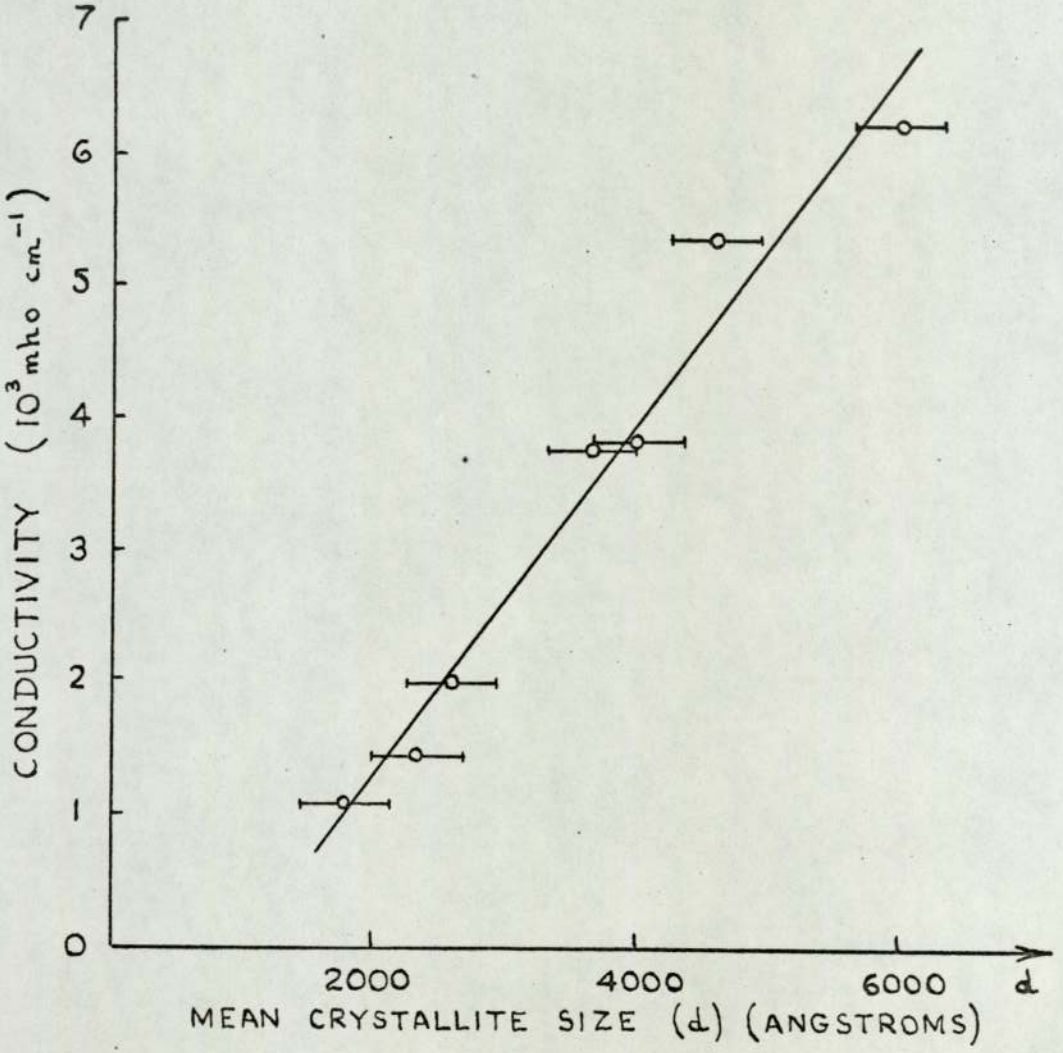

FIG. 4B. CONDUCTIVITY OF BISMUTH THIN FILMS AS A FUNCTION OF MEAN CRYSTALLITE SIZE.

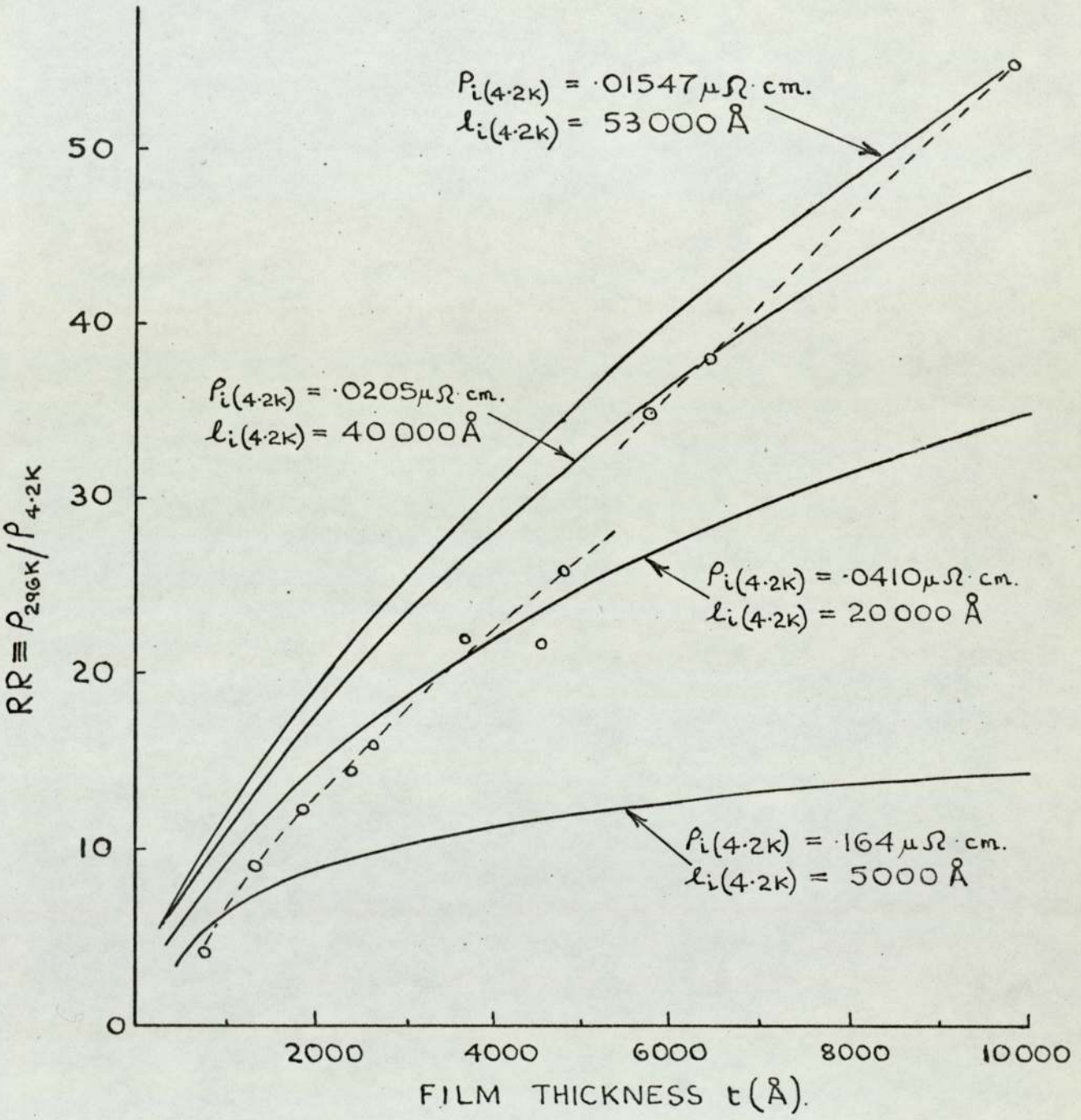

FIG. 5. EXPERIMENTAL RESULTS OF MAYADAS FITTED TO THEORETICAL CURVES (FULL LINES)

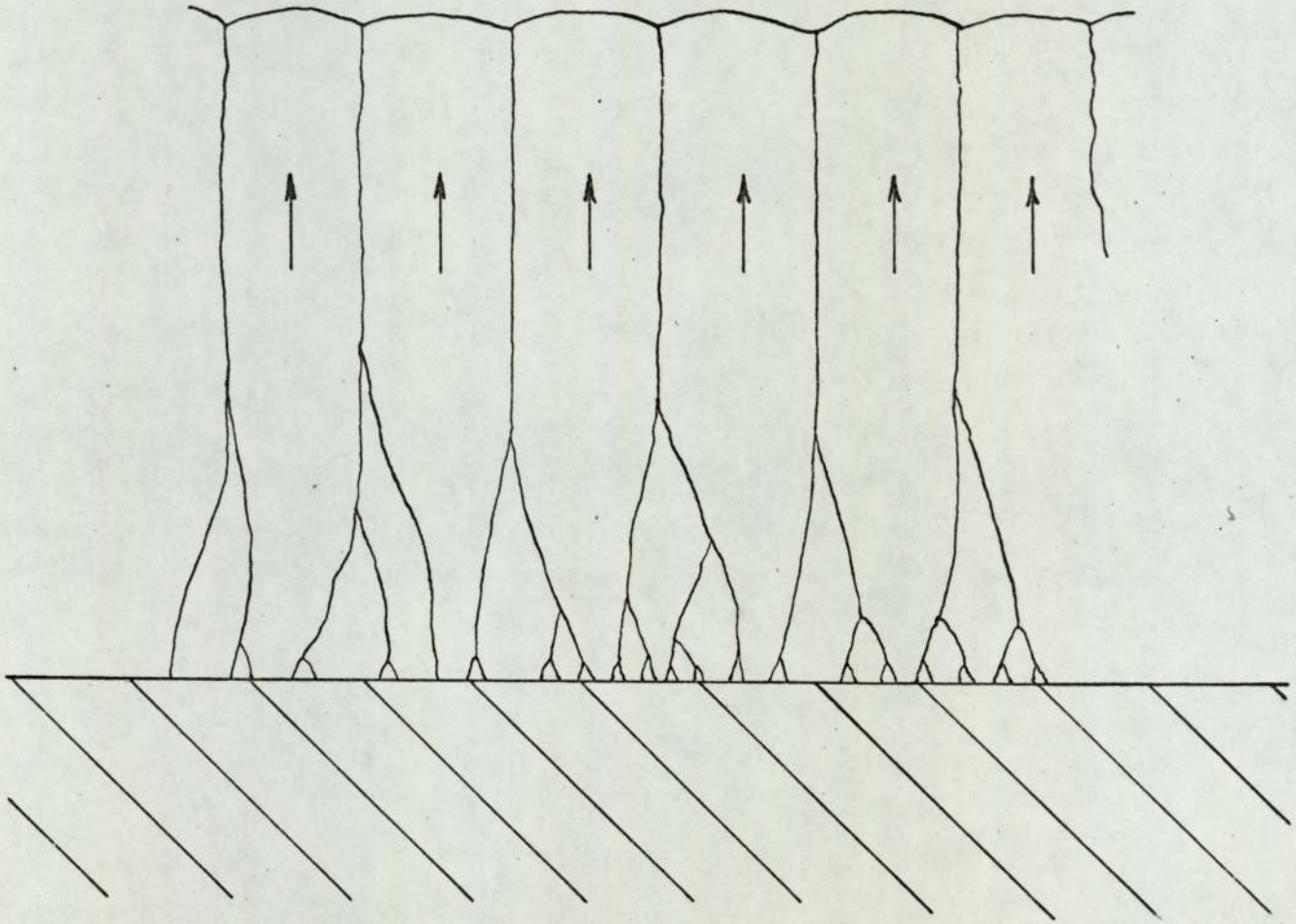

FIG. 6. COLUMNAR GROWTH.

explored by Mayadas[67] et al. and was shown to predict similar behaviour to the Fuch s-Sondheimer theory. In fact, this similarity is to be expected since the constraints are of similar mathematical form, whether the size effects are internal (i.e. grain boundary) or external (i.e. surface). It seems clear that any work involving a correlation of various thin film properties should ideally include a measurement of grain size.

The concentrations and types of defects in the metal crystalline structure, then, are of great importance, and produce variations in conductivity, in mechanical properties, and in optical behaviour. Some of the large amount of experimental information available on the annealing of defects in metals will now be discussed.

1.3 Defects and defect annealing in metals

It was first observed by Buckel and Hilsch[68] that thin films of pure metals, deposited on to substrates held at low temperatures, showed an extremely high resistivity on deposition. When warmed to room temperature, the resistivity decreased dramatically, sometimes by as much as 40% The reduction in resistivity was found to be irreversible and was attributed to structural changes in the films. Buckel[69] found evidence of phase changes occurring on warming films of bismuth, zinc and gallium. More recent work by Bosnell[70] on films of Yttrium, Scandium and iron and also by Bosnell and Voisey[71] on molybdenum found that all these materials showed evidence of phase transformations as a result of warming. The last example of molybdenum films is particularly striking as shown in Fig.7. The structure changed from almost amorphous (grain size less than 2 n.m.) through face-centred cubic, to body-centred cubic as for normal molybdenum. Many workers have shown that the presence of impurities may profoundly modify these phase changes and much work on the recovery of resistivity of dilute alloys has been reported, for example the work of Mader and Norwick.[72] On

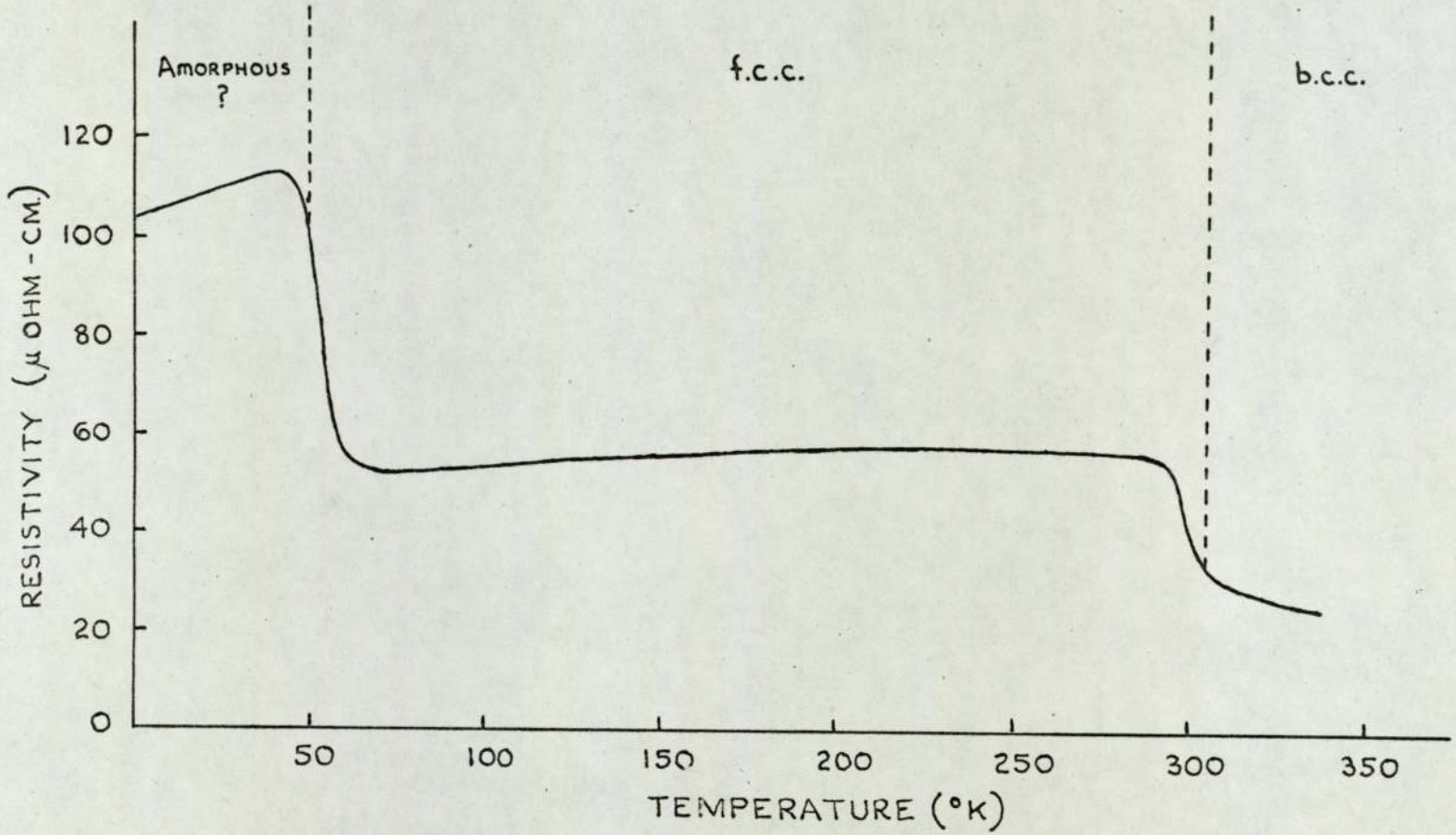

FIG 7. RESISTIVITY vs. TEMPERATURE FOR A MOLYBDENUM FILM DEPOSITED ONTO A LIQUID-HELIUM-COOLED SUBSTRATE.

the other hand, there is a great deal of evidence to show that very pure metals, with low Debye temperatures, θ_D evaporated in ultra-high vacuum, do not show phase transformations. These materials, of which aluminium is one, condense from the vapour to form a crystalline film even when the substrate is held at liquid helium temperature. The grain size, however, is very small. Buckel and Hilsch (among others) have clearly shown this to be the case by means of electron diffraction patterns for the materials aluminium, lead and mercury. Chopra, in a recent review[73] of the effects of evaporation conditions on the structure of metal films, and the phase changes that ensue as a result of heat treatment, also agrees that very pure films of metals of low θ_D produced in good vacuum are crystalline when deposited and do not therefore show phase changes on warming. What, then, is the mechanism for resistivity reduction in these materials? The deposited films, though crystalline, contain large numbers of defects of all kinds, frozen into the film as the vapour condenses. On warming, the thermal energy available exceeds the activation energy of migration of many of the defects, which then become mobile and anneal out. It is of interest to compare the fall of resistivity on warming a vapour-quenched film with the recovery of a bulk specimen in which crystal defects have been introduced at low temperature, and subsequently allowed to warm up. Fortunately, there are two well-established methods of doing this, both of which provide numerous experimental results for comparison purposes.

i) The first method is to heat the bulk specimen to a high temperature, whereupon the equilibrium concentration of defects, following an expression of the form $e^{-\frac{u_f}{kT}}$, where u_f is the energy of formation, is increased. The hot sample is then 'quenched' at rates of temperature fall greater than 10^4 deg. C./sec. so that the defects are 'frozen in.'(74) Calculations

show that the concentration of defects produced is usually low and in the case of vacancies is of the order of 10^{-3}%.

ii) The second method is the well-established technique of nuclear radiation damage in solids. From 1950 onwards, the needs of the nuclear power programme made essential the study of the effects of α, β and γ radiations on solids. These energetic radiations may displace atoms from their lattice positions and hence lead to the formation of many types of defect; dislocations, vacancies, interstitials, etc. These often profoundly affect the strength and elasticity, or even the dimensions, of the materials. Typical defect concentrations are of the order of 10^{-2} (i.e. 1%).[75]

Neither quenching a bulk sample, or subjecting it to intense doses of radiation are likely, then, to produce such large defect concentrations as vapour quenching (estimated by several workers to be as high as 10 atomic %).[72][32] However, the similarities between the recoveries do provide worthwhile comparison, and will be attempted in this work.

The recovery of resistivity when a damaged sample is warmed occurs in several distinct stages, the broad features of which are common to all metals and are shown in Fig.8. Each stage is characterised by a different activation energy and occurs between fixed temperatures. For Stage I, approximately below 100°K, the thermal energy available is very small (0.1 eV or less) and the recovery in this stage is unanimously attributed to the migration of interstitials or Frenkel-pairs (i.e. interstitials falling into nearby vacancies).[76] Above 100°K the recovery is attributed to the migration of vacancy clusters, and other interstitials. Stage III, generally around 300°K, is characterised by activation energies of about 0.6 eV to 0.7 eV and is generally attributed to

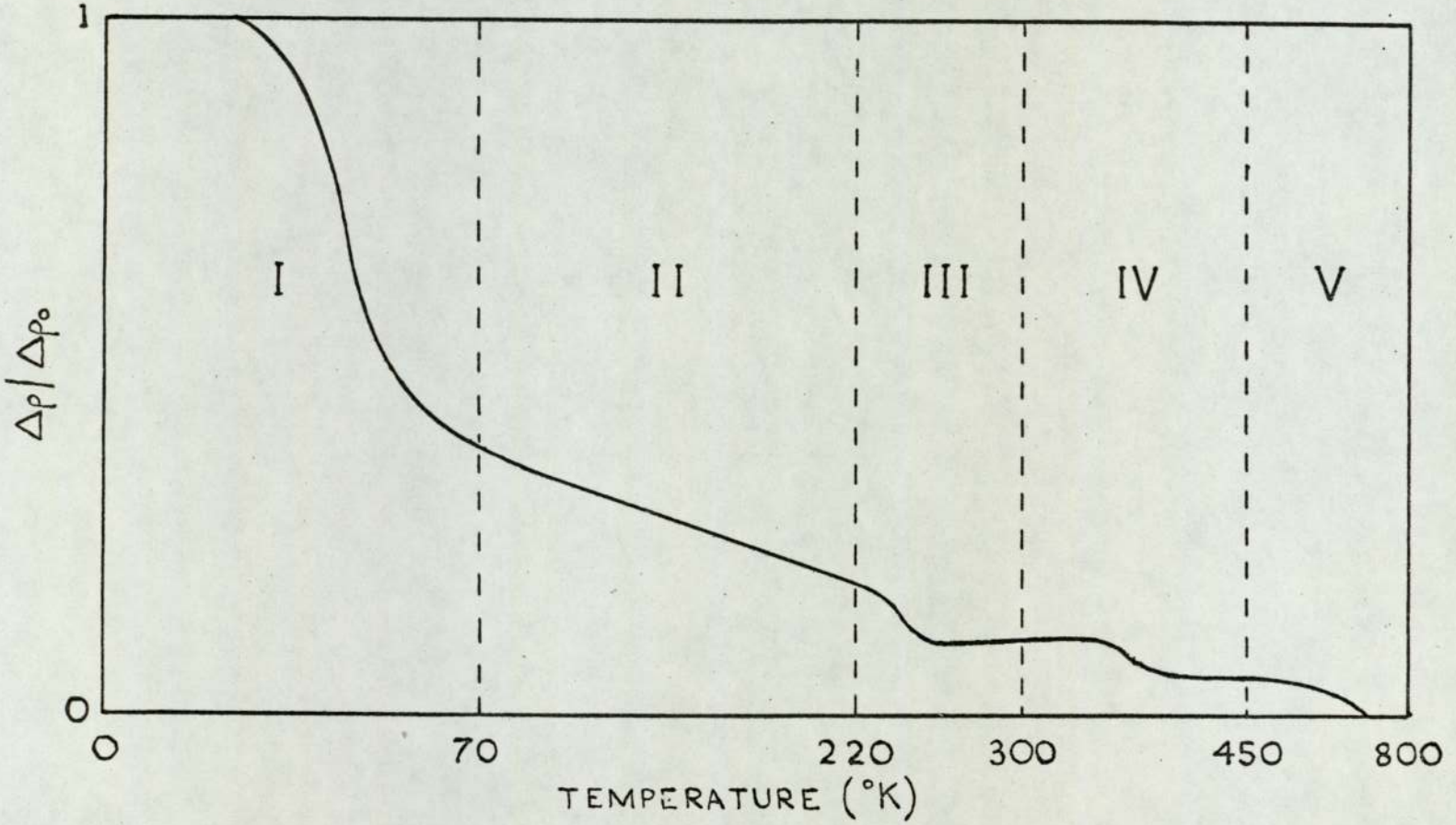

FIG. 8. RECOVERY OF RESISTIVITY IN COPPER ON ISOCHRONAL ANNEALING.

single vacancy migration.[75][77][78] In many cases, recovery is complicated by over-lapping of processes and other effects such as the annealing of dislocations. Grain growth also affects the resistivity.[79]

An important proposition of Seeger[80] in 1958, which was later extended by Meechan et al.[81] and Bauer et al.[82] is that there are two stable forms of interstitial configuration with different activation energies. This has now gained general acceptance (see the 1968 review of Lidiard[83]). One form of interstitial configuration has a migration energy U_m of around 0.1 eV and migrates freely in Stage I. The other has U_m around 0.6 eV and migrates in Stage III. These configurations are tentatively identified as ⟨110⟩ Crowdion and ⟨100⟩ dumbell respectively. See Figs.9A and 9B.

It is possible, then, that the Stage III recovery (100°K to 300°K) which is the subject of much of this work, could be attributed to 'dumbell' interstitial migration to vacancies, which are anihilated in the process. Such a process would show second order kinetics. (See Section 5.) Vacancies which remain would be expected to anneal later in Stage IV. Theoretical calculations of migration energies in copper by Johnson and Brown[84] predict $U_m = 0.05$ eV for the 'dumbell' and $U_m = 0.25$ eV for the 'Crowdion.' Experimental work on aluminium subjected to electron bombardment by Sosin and Rachal[85] in 1963 showed that Stage II (around 140°K) had an activation energy of 0.22 eV and first order kinetics, while Stage III (from 140°K to 270°K) had an activation energy of 0.45 eV and second order kinetics. Since the latter energy does not correspond to U_m for vacancies as found from quenching experiments, it does seem likely that the postulate of two forms of interstitial configuration applies to aluminium as for copper and gold.

This introduction began with a discussion of the optical properties of metals. Some of the experimental techniques used in

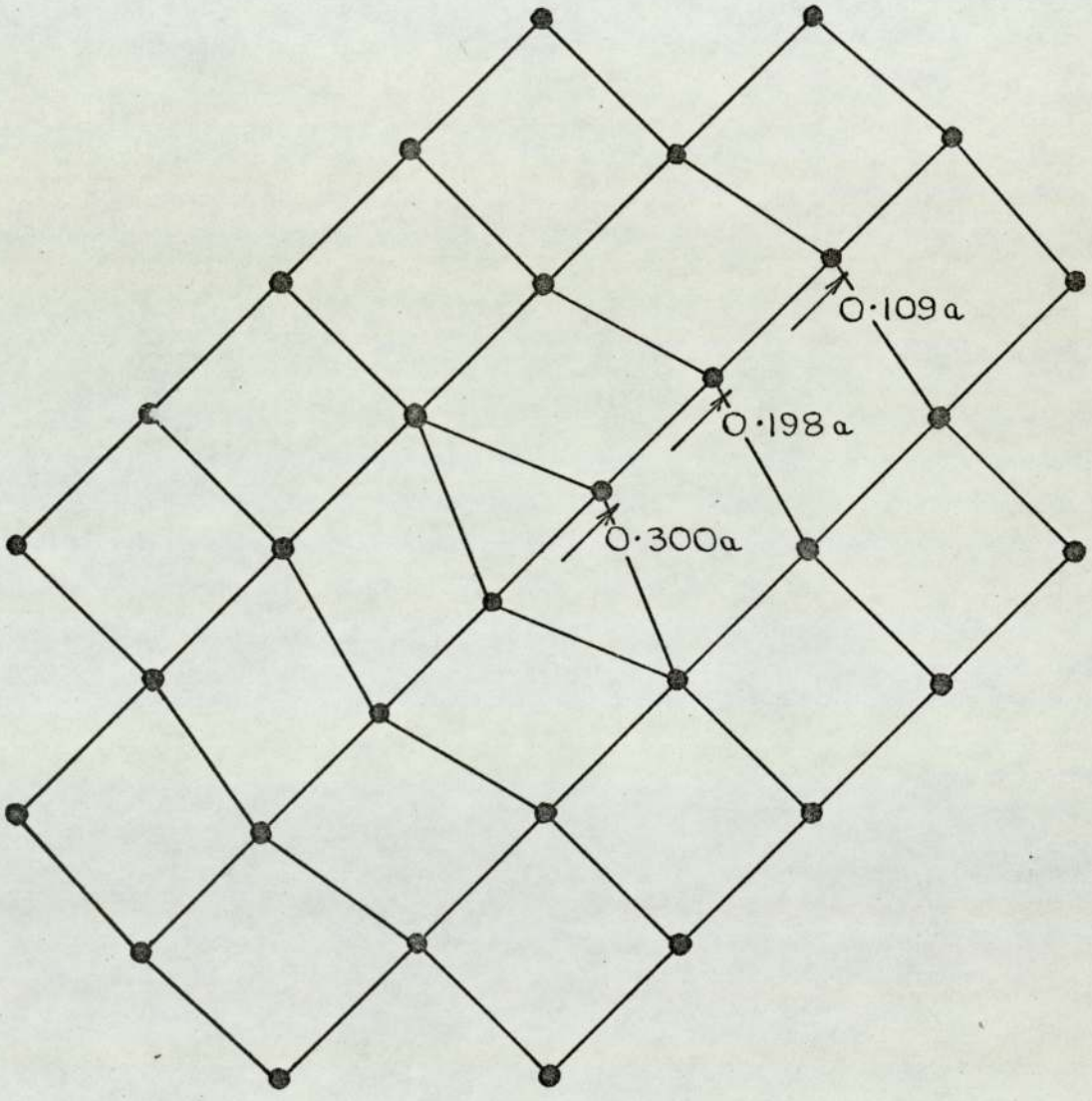

FIG. 9A. THE ⟨110⟩ CROWDION INTERSTITIAL CONFIGURATION.

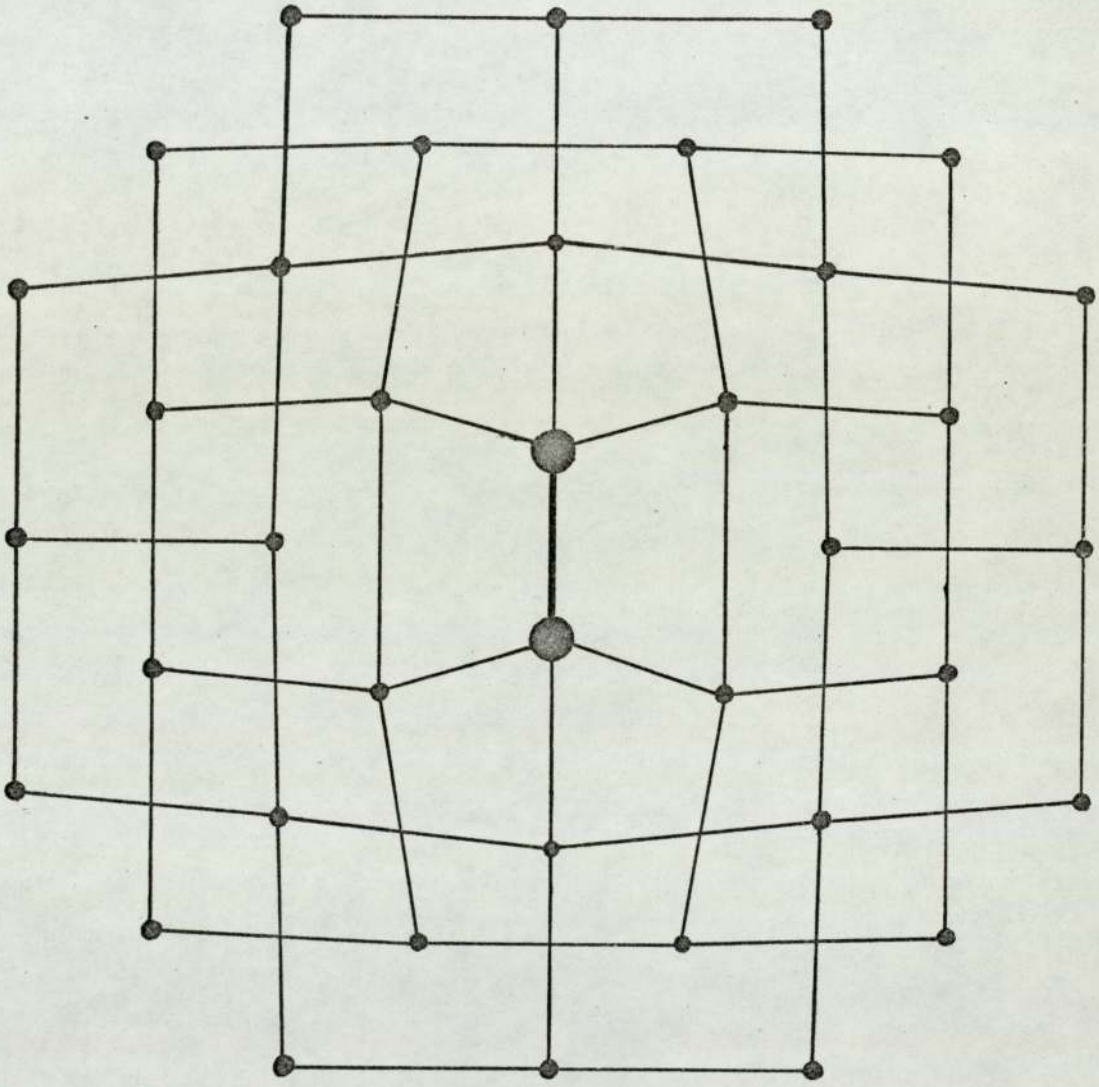

FIG. 9B.

THE ⟨100⟩ DUMB-BELL INTERSTITIAL CONFIGURATION.

measuring them, particularly the method of Ellipsometry as used in this work, will now be considered in detail.

1.4 Ellipsometry

There are various optical techniques available for the measurement of thickness, t and optical constants, n and k of metal films. The use of multiple beam interferometry developed by Tolanski[86] enables film thickness to be determined with great accuracy. See Section 4.2.3.

The optical constants may be determined by measuring the intensities of the light transmitted and reflected from both sides of the film, as proposed by Murmann;[87] although this requires a separate determination of thickness. Malé[88] has shown that the film thickness may be obtained from the same experiment if sets of curves of reflectance and transmittance against thickness are drawn up for a range of values of n and k. It is preferable to measure n, k and t simultaneously because thin films are known to vary in density so that a separate measurement of geometric thickness may not correspond to the thickness t in the optical equations.

Schopper[89] devised a method of doing this which involved measuring the reflected and transmitted intensities and also the associated phases; a difficult experimental problem. However, the laborious preparation of standard curves, as in Malé's method, was avoided. These and other methods are summarised and discussed by Heavens.[90]

However , the most versatile technique and the one chosen for the present work involves the measurement of the change in the state of polarisation of a beam of light after reflection and is now known as 'Ellipsometry.'

When plane polarised light falls on a surface the incident light can be resolved into components parallel and perpendicular to the plane of incidence, for which the reflection coefficients are different; and are usually denoted by r_p and r_s respectively.

(See Section 2.1) For a single clean surface, these coefficients can be derived from basic electro-magnetic theory in terms of refractive index and angle of incidence. For a clean dielectric surface, the plane of polarisation is merely rotated due to the different amplitude ratio in the reflected light, but if the dielectric surface is covered with a thin film there will be a phase difference between light coming from the upper and lower surfaces. In this case, and also in the case of a single absorbing surface, the process of reflection introduces a phase difference Δ between the (p) and (s) components as well as changing the ratio of their amplitudes by a factor, conveniently expressed as $\tan \Psi$. This factor is thus a measure of the relative absorption. Expressed in its simplest form, the fundamental equation of ellipsometry gives the ratio of the reflection coefficients, ρ of the (p) and (s) components as

$$\rho = \frac{r_p}{r_s} = \tan \Psi \, e^{i\Delta}$$

where Ψ and Δ are functions of the optical constants of the media bounding the surfaces, the wavelength of the light used and the angle of incidence. (See Section 2.1) In general the reflected light is elliptically polarised. The ellipticity and azimuth are related to Ψ and Δ and can be measured by introducing a phase difference equal and opposite to that produced by the reflection so that plane polarised light is re-established. This process is known as 'compensation.' (For details see Section 2.2.)

Any change in the surface film produces changes in the parameters Ψ and Δ which are in turn related to the optical constants n and k, and to the thickness t of the film. The calculations are generally extremely laborious, especially for absorbing films, so that electronic computation is essential.

The foundations of ellipsometry were laid at the end of the last century by Rayleigh[91] and particularly by Drude[92] who, in

1891, derived the fundamental equation of ellipsometry from Maxwell's equations with suitable boundary conditions. A bibliography of the theoretical work of Drude and of other early contributors is given by Winterbottom[93]. Drude was unable to solve the equation explicitly for n, k and t, but obtained approximate solutions for films of thickness small compared to the wavelength of light used. The extreme sensitivity of polarimetric methods was realised by Rayleigh in 1892 when he found that light reflected from water at the Brewster angle had, contrary to the Fresnel equations, a small negative ellipticity. He concluded that the effect was due to a contaminating film of grease on the water surface which he estimated to be less than 1 n.m. in thickness.

Although the optical properties of metals were studied by means of reflectivity measurements, as already described [3][6], few specific references to the use of ellipsometry were made in succeeding years, probably because of the development of other methods of determination of film thickness, such as multiple beam interferometry. It was used, however, in the study of metal surfaces by Tool[94] in 1910 and by Hauschild[95] in 1920. A concise exposition of the subject by Fry[96] in 1927 lead Ives[97] to make use of the technique in the measurement of the thickness of rubidium films deposited in vacuo on glass and platinum surfaces. Summers[98] also used the method in a brief study of molybdenum surfaces.

The first detailed experimental work using the Drude technique was by Tronstad[99] who investigated the chemically-produced passivity of iron and steel mirrors. Tronstad also investigated the optical constants of a mercury surface[100] which he used as a standard surface for the calibration and adjustment of the ellipsometer, since it was found to give more reproducible results than any surface produced by mechanical polishing. Tronstad also investigated the corrosive effect of ozone and water on various metallic surfaces[101] and showed that the corrosion rate depended

markedly on the water content of the ozone.

In order to test certain features of the free electron theory, Lowery et al. made several measurements of the optical constants of copper, for polished surfaces[102] and for surfaces produced by evaporation of the metal in high vacuum.[103] Extensive measurements were also made of copper-nickel[104] and copper-zinc[105] alloys.

Lebernight and Lustman[106] investigated the oxidation of iron and nickel and verified Drude's equations for thinner films (i.e. less than 10 n.m.)

Until about 1940, the instruments used were often normal spectrometers, modified to carry polarising and analysing prisms and a quarter wave plate. Detection was by eye using half-shade devices, either Nakamura plates or later Tronstad[107] half-shade devices. The introduction of photomultiplier detection around 1940 made possible great improvements in sensitivity and accuracy, and also enabled measurements to be made over a wider range of wavelengths. For example, McPherson[108] was able to measure the optical constants of copper-aluminium alloys over the wavelength range 380 to 1000 n.m.

A revival of interest came around 1945 with the work of Rothen[109], who was responsible for the term "ellipsometry", and later by Rothen and Hanson.[110] They developed the technique of calibration of an ellipsometer using a surface coated with a known number of barium stearate monolayers.

In 1955, in the extensive review by Winterbottom[93] results of optical constants for bulk metals (mainly iron, aluminium and copper) were presented for the visible region of the spectrum. The development of polarising devices for the infra-red, for example the selenium plates used by Elliott et al.,[111] made possible the development by Beattie[112] of an ellipsometric technique for metals extending to 12 microns wavelength. (See Section 2.3) Previously, the most generally accepted results at these wavelengths were the reflectance measurements of Fosterling and Freedericksz,[6] although

there were serious theoretical limitations on the accuracy of such measurements, as shown by Beattie and Conn.[28] As already discussed, infra-red measurements on metals are extremely important in order to assess the validity of the Drude-Zener theory.

Around this time, it became clear that two different approaches to ellipsometry were developing. In the work on metals, the variations in surface smoothness, sample structure and also the uncertainty in the extent of surface oxidation or contamination meant that an instrument of simple construction gave sufficient accuracy, whereas in the measurement of the less reactive transparent materials such as glass, etc., more sophisticated instruments were thought to be required. The first view, initiated by Beattie and Conn was adopted by Hayfield and White[113] in a study of corrosion and oxidation in metals; by Neal et al.[114] in an investigation of the annealing of aluminium films, and by Miller[115] in the investigation of the optical properties of liquid metals. It is also the view adopted in this work where, for visible wavelengths, the compensator method of McCrackin[116] is used and where for infra-red wavelengths the method of Beattie[112] is used. In both cases the instrument is comparatively simple, inexpensive and demountable in order that it may be used in conjunction with an ultra-high vacuum system.

Work on the general technique of ellipsometry was continued by McCrackin et al.[116] who reviewed the procedure for alignment and calculation of results; and by Archer[117] who made extensive studies of silicon surfaces using the exact theoretical equations. Double beam devices used in transmission polarimetry, in connection with the sugar industry, were introduced into ellipsometers by Archard et al.[118] and in 1963 Bor and Pryzbylski[119], using their double beam instrument, claimed an accuracy for the setting of the polaroids of one minute of angle. The basis of this form of instrument is that one beam is used as a reference, and the difference in output of the two photocell detectors is measured. A great practical

disadvantage is the need for two identical specimens, one for each beam.

More recent developments have lead to some highly sophisticated instruments employing the Faraday effect. This idea was developed by Gilham.[120]

The 'magneto-optic' or 'Faraday' effect is observable as a rotation of the plane of polarisation when light passes through a dielectric in the presence of a magnetic field. Gilham employed lead-zinc borate glass in the form of cylindrical rods 10 cm in length overwound with a copper coil carrying an alternating current of 1 amp at 50 Hz . With this arrangement, the plane of polarisation was found to oscillate at 50 Hz through 6 degrees. When this light passed through the analyser prism on to the photomultiplier, an alternating intensity of light was received, resulting in a convenient output signal.

Further developments by Gilham and King[121] lead to the development of a commercial instrument produced by Bendix Electronics. Independent development of an equally accurate instrument took place in the United States by Williamson et al.[122]

Several instruments have been developed on the basic design of King[114], for example that of Seward[124] which as well as accurate mechanical parts and Glan-Foucault prism polarisers,[125] employed a detection system using two Faraday cells, M and C, as shown in Fig.10. The first cell is fed with a constant alternating current signal of frequency f, which causes the plane of polarisation to oscillate at the same frequency f. The light then passes through the second cell C and an analysing prism A on to a photomultiplier PM. The photomultiplier produces an assymetrical Cos^2 signal which has a basic 2f component with an f component superimposed. An electronic analysis unit detects the f component and feeds into the compensator cell C a suitable current to reduce the f component to zero. The value of this current is proportional to the angular difference

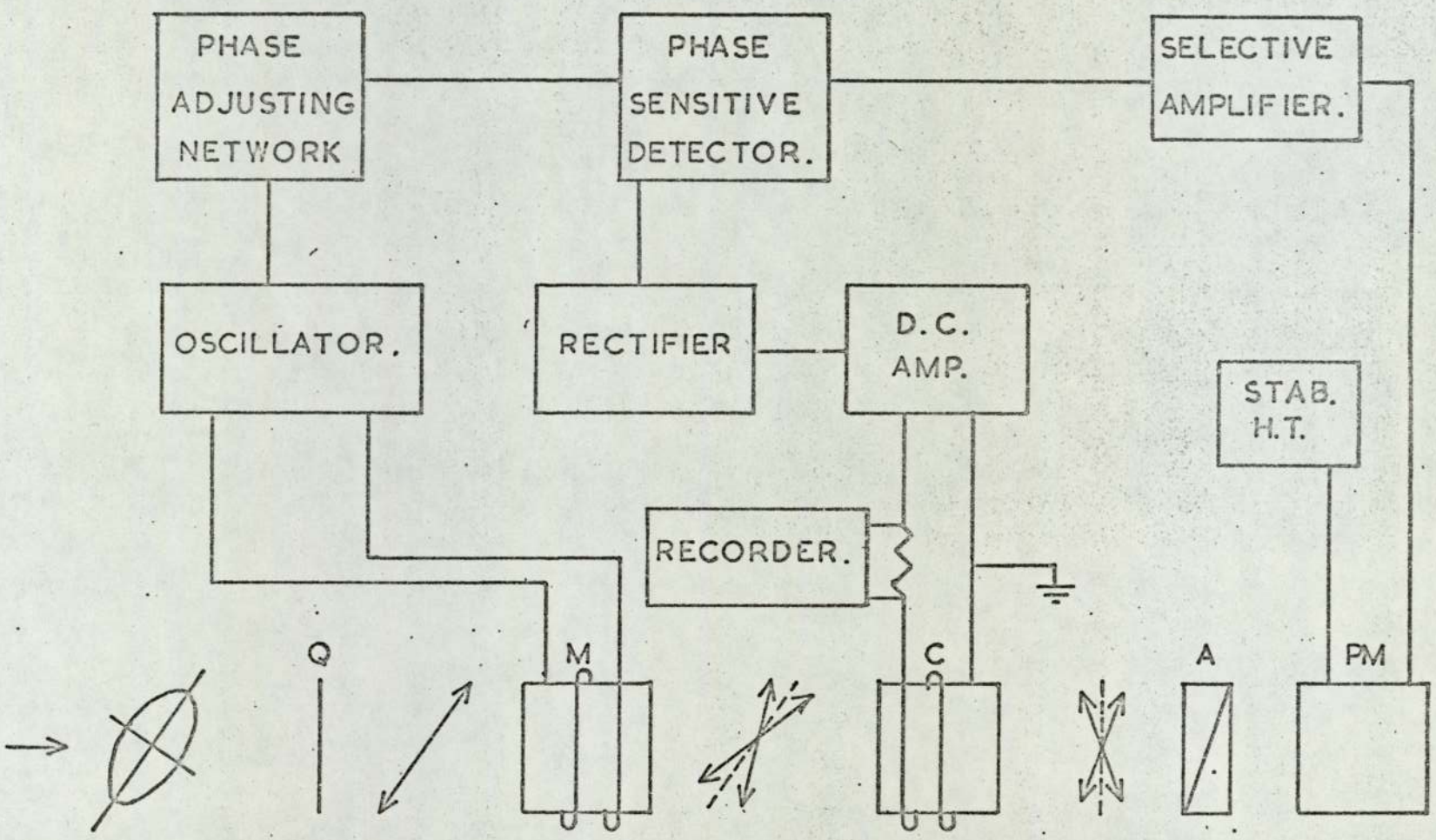

FIG. 10 ANALYSIS SYSTEM (after SEWARD)

between the actual analyser azimuth and the azimuth at which it would be "crossed" with respect to the incoming polarised light. In this way, the analyser can be set accurately to $\pm$ 5 seconds of angle.

CHAPTER 2

ESSENTIAL THEORY

2.1 Optical inter-band absorption in aluminium

The crystal lattice of aluminium is face-centred cubic. The reciprocal lattice is therefore body-centred cubic and has a centred primitive cell, or Brillouin zone, as shown in Fig. 11. The symbols on the symmetry points or axes are a conventional notation that provide identification of corresponding wave functions. Calculations of the energy bands for the principal symmetry axes, made by Ehrenreich et al.[36] are shown in Fig. 12. This shows that the only inter-band transitions below 8 eV at symmetry points are those between the two occupied states W_2^1 and W_3 and the unoccupied state at W_1. The calculated transition energies are 1.4 and 2.0 eV respectively. Since the experimental peak value of optical absorption, which is proportional to $\epsilon_2 = 2nk$, occurs in the region of 1.55 eV, it is clear that the region around W contributes significantly to this absorption. Ehrenreich also pointed out that the inter-band transitions in the vicinity of the [110] axis (i.e. the Σ axis) also commence at 1.4 eV and will make a contribution to the observed absorption about 50% larger than that from the W region. This comes about because the second and third band states below and above the Fermi energy respectively, are parallel, See Fig. 12.

Detailed calculations of the magnitudes and shapes of the theoretical optical absorption curves due to transitions at W and Σ were also made by calculating the energies in a three-dimensional mesh (10^6 points per zone) making use of the appropriate pseudopotential model for aluminium. A histogram of the joint densities of states was plotted by counting the points that satisfied the proper occupancy conditions. The results have been shown already in Fig. 2A, in which the peak (A) represents the

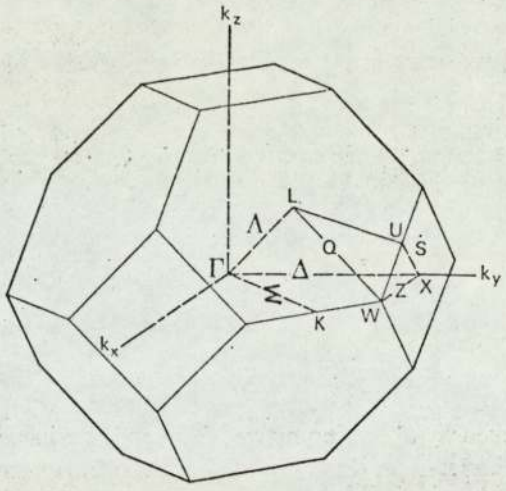

Fig. 11. The Brillouin Zone for Aluminium (f.c.c.)

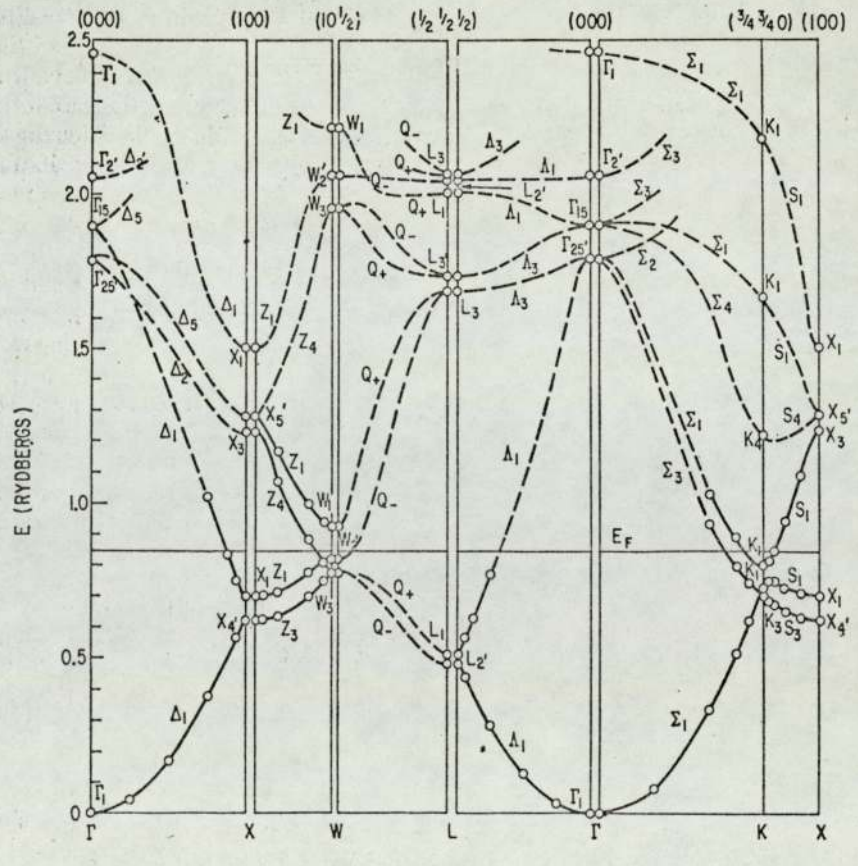

Fig. 12. The calculated energy bands along the symmetry axes for aluminium (after Ehrenreich et al.)

sum of the contributions from transitions between the W_2^1 and W_1 bands and between the Σ_3 and the Σ_1 bands. Curve (B) is associated with the transition from the W_3 to the W_1 bands. For comparison, the experimentally determined inter-band absorption is also shown.

An experimental investigation of the inter-band transitions enables the values of the Fourier components of the pseudo-potential to be determined. According to Harrison[40A], the pseudo-potential may be written

$$V_g = F_g f_g \qquad (\text{A})$$

where F_g is the geometrical structure factor as encountered in X-ray diffraction theory, and f_g is a factor depending on the individual ion potentials. It is clear that the only V_g that differ from zero are those for which the structure factor is not equal to zero. There is also the additional limitation that the only important V_g are those for which the corresponding Bragg planes intersect the sphere of free electrons. It follows that for aluminium the only important pseudo-potential components are V_{111} and V_{200}.[24] (i.e. those components of the pseudo-potential for the (111) and (200) Bragg planes.)

It is shown by Motulevitch[24], using an approximation based on a linear combination of two plane waves, and also by Ehrenreich et al.,[36] that the difference in band energy along the Σ axis is almost constant for aluminium and has the value $2.V_{200}$. Hence the value of V_{200} is given by half the energy of the absorbed light quanta at the maximum of the interband peak.

$$V_{200} = \frac{1.55}{2} = 0.77 \text{ eV}$$

This value is in good agreement with the estimate made from the de Haas - van Alphen effect by Ashcroft, namely 0.764 eV.[45]

At first sight, it might be expected that the main electronic characteristics of N*, the effective conduction electron

density, S_F, the total area of the Fermi surface and v_F, the average electron velocity on the Fermi surface, would not depend on temperature since the energy of the conduction electron E_F, is of the order of 10eV and is much larger than the thermal energy, kT. However, the dependence of the electron characteristics on temperature is connected not with the thermal motion of the electrons, but with the thermal motions of the ions. The lattice vibrations disturb the periodicity and cause the geometric structure factor to decrease according to the well-known Debye-Waller factor in X-ray diffraction theory. Since the value of V_g depends directly on the structure factor according to equation ( ), it may be seen that the Fourier components of the pseudo-potential should decrease at higher temperatures. As a result, N^*, S_F and v_F all increase at higher temperatures[24] and it is to be expected that the maximum of the inter-band absorption peak will be shifted to lower energy (i.e. longer wavelength).

During the course of the present work, this was shown to be the case by Hodgson[147] in 1970 and was confirmed more recently by Liljenvall et al.,[125A] whose results are shown in Fig. 12A. The ellipsometric technique of Beattie was employed to provide measurements of the optical absorption of opaque aluminium films deposited and maintained in ultra-high vacuum. The peak value of absorption was seen to occur at lower energies (i.e. longer wavelengths) for increased temperatures. This was interpreted as a reduction in the value of the V_{200} component of the pseudo-potential in good agreement with the effects of the Debye-Waller factor. Several films on different substrates produced identical results. They concluded, therefore, that the variations shown in Fig. 12A were true temperature effects and were not due to other factors such as contamination, annealing or strain.

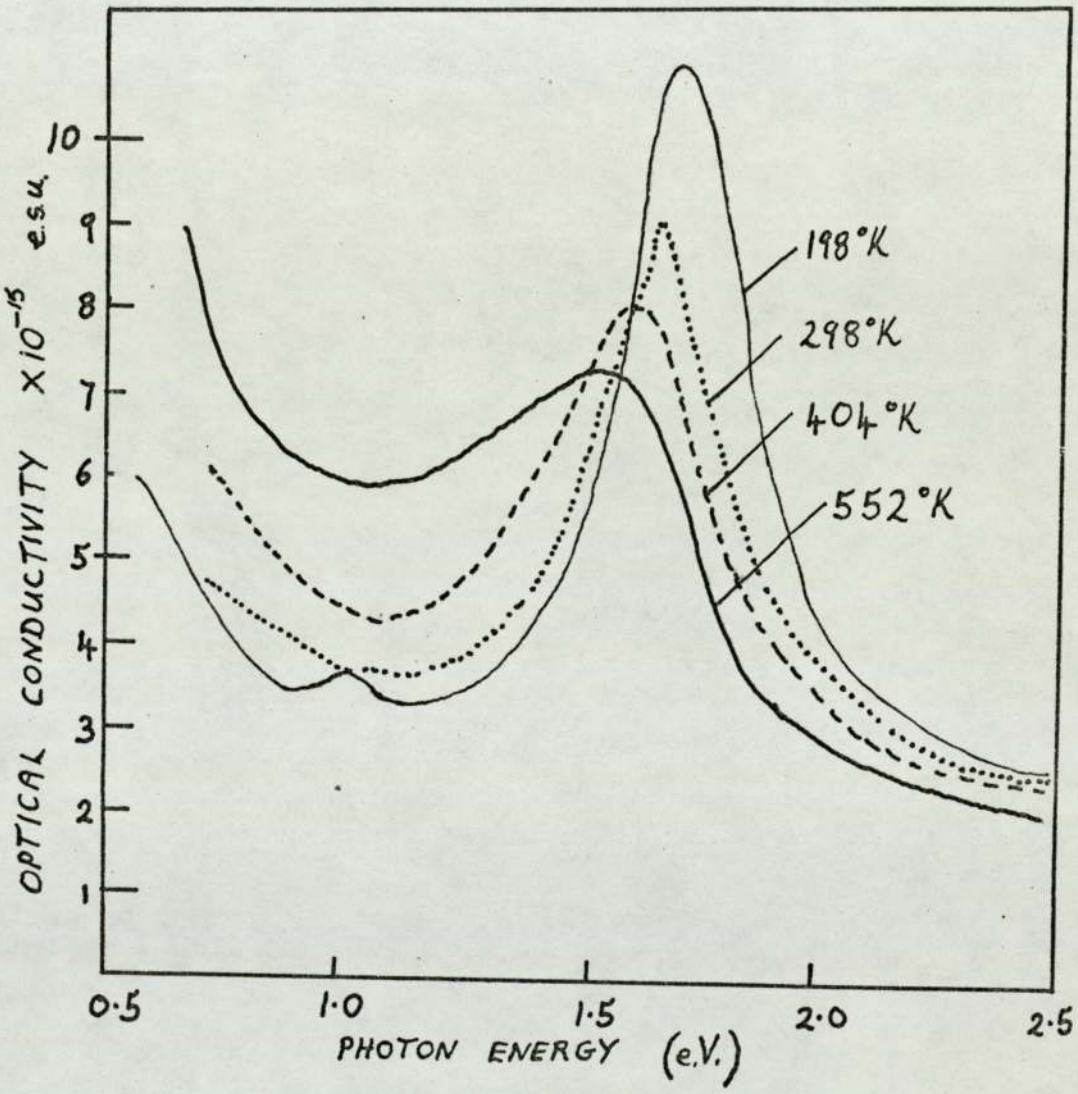

OPTICAL ABSORPTION OF ALUMINIUM WITH TEMPERATURE (after Liljenvall)

FIG. 12A.

The effect of structural changes on the pseudo-potential components and hence on the band structures, have so far been neglected although Moĭulevitch[24] has pointed out (p.93) that different structures in the sample under investigation can lead to appreciable changes in the properties of the conduction electrons and their interaction with the lattice because of changes in the band structure and the additional scattering due to crystal defects and crystallite boundaries. The results of the present work on the optical and electrical changes produced by annealing are discussed in Section 6.2 in the light of these considerations.

2.2 General Basis of Ellipsometry

In principle, the amplitude and phase of a beam of light reflected or transmitted by a thin film, or combination of films, may be determined by solving Maxwell's equations with the appropriate boundary conditions. The problem is considerably simplified by the use of Fresnel coefficients r and t, where r is the ratio of reflected to incident amplitudes, and t is the ratio of transmitted to incident amplitudes. For different boundaries between media the notation used here is adapted from that of Abelès,[126] and used by Heavens.[90] A superscript + or - indicates the direction of propagation with respect to the normal to the film. The direction of the plane of polarisation of any orientation is specified with respect to the plane of incidence. The wave vectors are resolved into components parallel and perpendicular to the plane of incidence, and are denoted by a subscript (p) or (s) respectively. The media are numbered and the material identified by this number. As mentioned previously, if a medium is absorbing, the refractive index is a complex quantity $\mathcal{N} = n - ik$, in which the imaginary part is related to the absorption of energy by the medium. For non-normal incidence, the angles of refraction become complex quantities.

The physical interpretation of this lies in the fact that the planes of equal phase are no longer parallel to the planes of equal amplitude.[127] It may be shown that the Fresnel coefficients are given by:

$$r_{12(p)} = \frac{E_{1p}^-}{E_{1p}^+} = \frac{\mathcal{N}_1 \cos\phi_2 - \mathcal{N}_2 \cos\phi_1}{\mathcal{N}_1 \cos\phi_2 + \mathcal{N}_2 \cos\phi_1}$$

$$r_{12(s)} = \frac{E_{1s}^-}{E_{1s}^+} = \frac{\mathcal{N}_1 \cos\phi_1 - \mathcal{N}_2 \cos\phi_2}{\mathcal{N}_1 \cos\phi_1 + \mathcal{N}_2 \cos\phi_2}$$

for light travelling from medium 1 to medium 2 having an angle of incidence ϕ_1, and angle of refraction ϕ_2. Similar expressions exist for the transmitted (p) and (s) components.

The above equations may be applied to a single film, which is assumed to be homogeneous and isotropic and to have parallel plane boundaries as indicated in Fig. 13. This represents a parallel beam of plane polarised light of unit amplitude and wavelength λ falling on an absorbing film of thickness d and complex refractive index $\mathcal{N}_2$, supported on an absorbing substrate of index $\mathcal{N}_3$. The complex amplitudes of the successive beams reflected and transmitted by the film are shown in Fig. 13, in which β_2 represents the amplitude and phase change in traversing the film once,

$$\beta_2 = \frac{2\pi}{\lambda} \mathcal{N}_2 d \cos\phi_2$$

The reflected amplitude from the whole system is thus given by the infinite series;

$$r_{13} = r_{12} + t_{12}t'_{12}r_{23}\, e^{-2i\beta_2} - t_{12}t'_{12}r_{12}\left[r_{23}\right]^2 e^{-4i\beta_2} + \cdots\cdots$$

which may be summed to give:

$$r_{13} = r_{12} + \frac{t_{12}t'_{12}r_{23}\, e^{-2i\beta_2}}{1 + r_{12}r_{23}\, e^{-2i\beta_2}}$$

It follows from the conservation of energy[90] that $t_{12}t'_{12} = 1 - \left[r_{12}\right]^2$

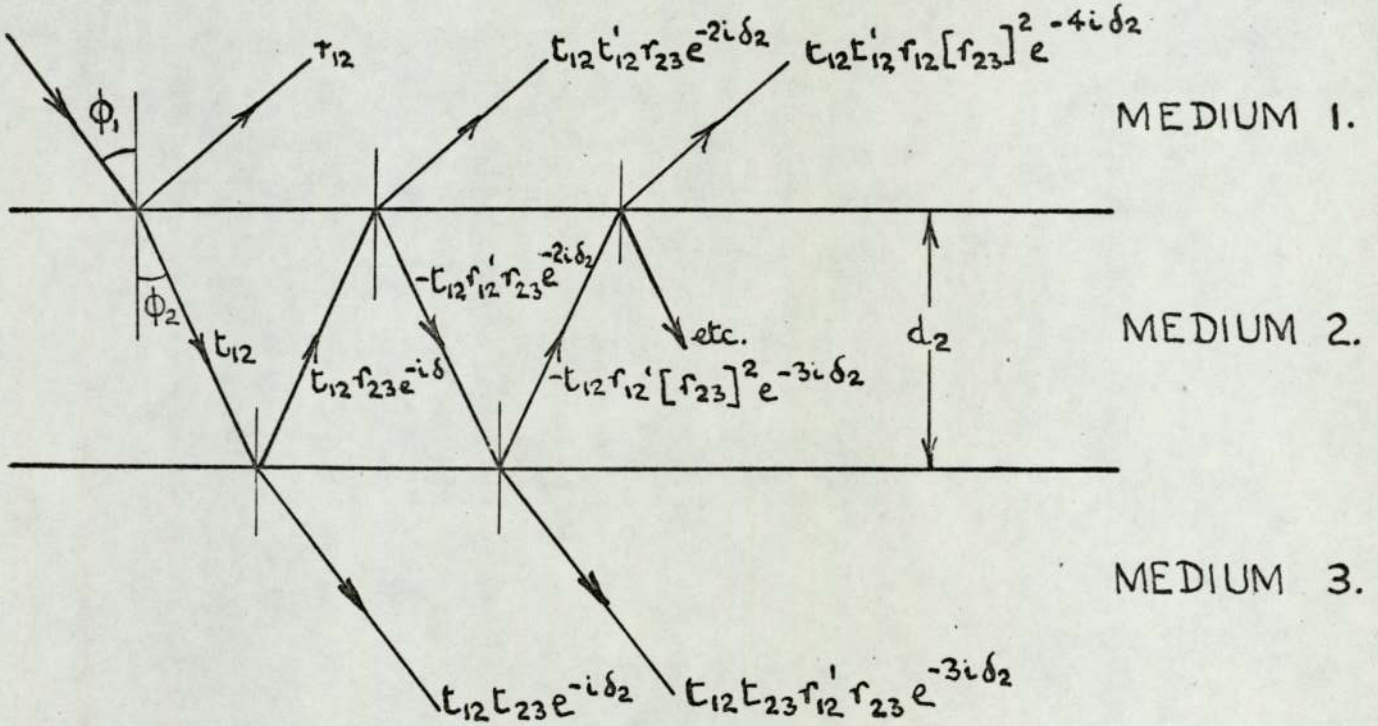
r_{12}
$t_{12}t'_{12}r_{23}e^{-2i\delta_2}$
$t_{12}t'_{12}r_{12}[r_{23}]^2e^{-4i\delta_2}$
ϕ_1
MEDIUM 1.
$-t_{12}r'_{12}r_{23}e^{-2i\delta_2}$
ϕ_2
t_{12}
$t_{12}r_{23}e^{-i\delta}$
etc.
$-t_{12}r'_{12}[r_{23}]^2e^{-3i\delta_2}$
d_2
MEDIUM 2.
MEDIUM 3.
$t_{12}t_{23}e^{-i\delta_2}$
$t_{12}t_{23}r'_{12}r_{23}e^{-3i\delta_2}$

FIG. 13.

and substituting this into the previous expressions, the reflected amplitude becomes

$$r_{13} = \frac{r_{12} + r_{23}\, e^{-2i\delta_2}}{1 + r_{12} r_{23}\, e^{-2i\delta_2}} = \rho e^{i\Delta} \qquad \text{(say)}$$

where ρ is the amplitude ratio and Δ is the difference in phase of the reflected light compared to the incident light. Two identical expressions exist for the (p) and (s) components although the numerical values are different, because the Fresnel coefficients are themselves different. The ratio of amplitude changes for the (p) and (s) components is given by

$$\frac{r_{13(p)}}{r_{13(s)}} = \frac{\rho_{(p)}\, e^{i\Delta_p}}{\rho_{(s)}\, e^{i\Delta_s}} = \frac{\rho_{(p)}}{\rho_{(s)}}\, e^{i(\Delta_p - \Delta_s)}$$

For convenience, this ratio is usually expressed in the form

$$\frac{r_{13(p)}}{r_{13(s)}} = \mathrm{Tan}\,\Psi\, e^{i\Delta}$$

As we shall now show, the ellipsometer measures Tan Ψ , the relative amplitude reduction and Δ , the difference in phase change for the (p) and (s) components. The parameters Ψ and Δ are thus related, through the Fresnel coefficients, to the refractive index and thickness of the film, and the angle of incidence. The derivation of n and k for the film from the measured values of Ψ and Δ is extremely laborious, so that an electronic computer is essential. An Algol programme, fully described in Appendix 2, is used to predict values of Ψ and Δ for a range of values of n and k for the film, whose thickness is measured in a subsidiary experiment. The true values of n and k are then found by inspection by finding consistency between values of n, k, d, Ψ and Δ on standard graphs as explained in Appendix 2.

The extension of the calculations to several layers is possible since a single film, bounded by two surfaces, has an

effective reflection coefficient and phase change. Such a film may be replaced by a single surface having the same properties, as indicated in Fig.14. In this way, it is possible to start at the supporting substrate and work upwards through each layer to the surface, as performed by Rouard,[128] or to start at the surface and work downwards towards the substrate, as proposed by Vašiček.[129] For use in the section on oxidation of aluminium films, the author has developed a programme to compute the parameters for a system of three layers, i.e. the system oxide - metal - substrate, using the method of Vašiček. This program is also included in Appendix 2.

2.3 Theory of Compensator method of Ellipsometry

The basis of the compensator method, as used in this work is illustrated in Fig.15. Plane polarised light, produced by the polariser P, is incident on the specimen with azimuth ψ i.e. its plane of polarisation inclined at an angle ψ to the plane of incidence. Conventionally, inclinations are considered positive if anticlockwise from the plane of incidence, looking towards the on-coming light. On reflection from the specimen the difference in amplitude reduction and the difference in phase change between the (p) and (s) components ensures that the reflected light is, in general, elliptically polarised, i.e. the tip of the electric vector moves in an ellipse with azimuth of the major axis χ , and ellipticity (ratio of minor to major axes) δ . This elliptically polarised light then passes through the compensator, which consists of a bi-refringent sheet of mica. As described more fully in section 4.1.3, the compensator used here is of an exact thickness to produce a 90 degree phase difference between the ordinary and extraordinary ray (i.e. it is a quarter wave plate) for the particular wavelength of light used (549 nm). If, then, the fast axis of the compensator is arranged to be

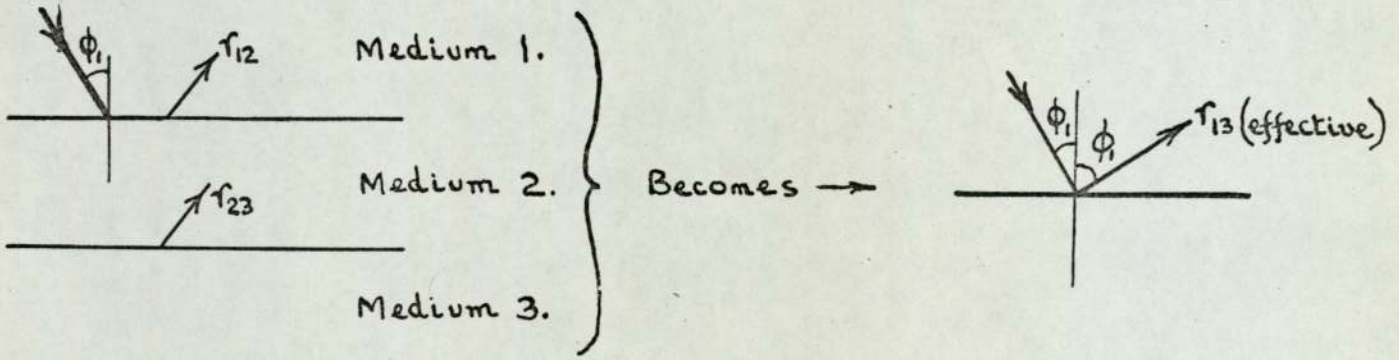
ϕ_1
r_{12}
Medium 1.
r_{23}
Medium 2.
Medium 3.
Becomes
ϕ_1
ϕ_1
r_{13} (effective)

FIG. 14.

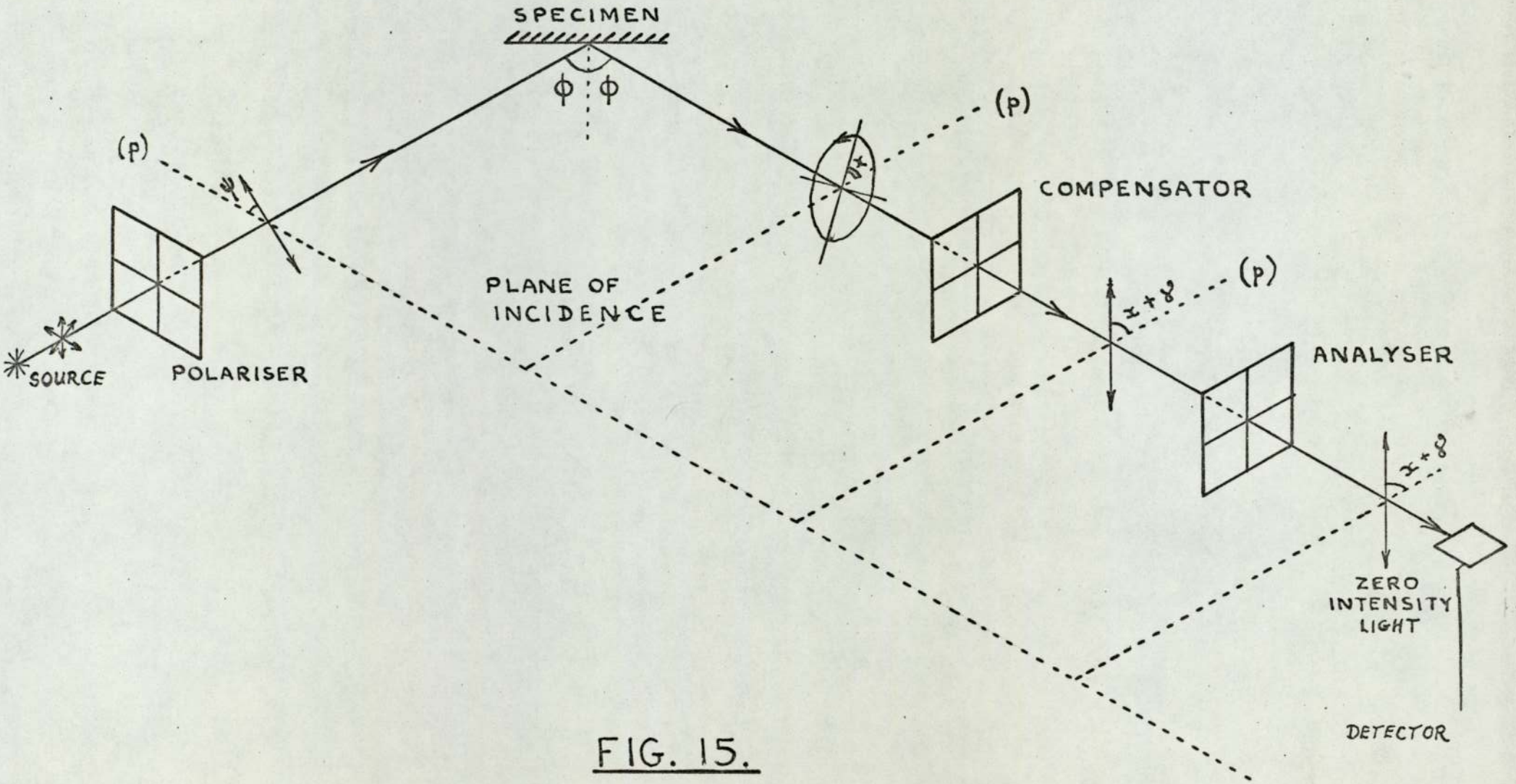
SPECIMEN
Φ
Φ
(p)
(p)
COMPENSATOR
PLANE OF
INCIDENCE
(p)
ANALYSER
SOURCE
POLARISER
ZERO
INTENSITY
LIGHT
DETECTOR

FIG. 15.

parallel to the major axis of the reflected ellipse, the vibrations along the major and minor axes of the ellipse (for which a phase difference of 90 degrees exists) are again brought into phase, and plane polarised light results. The azimuth of this 'compensated' plane polarised light will be at an angle δ' to the major axis of the ellipse. See Fig. 16.

Finally, the light passes through the analysing polaroid A, which may be rotated until its transmission axis is perpendicular to the plane of polarisation. In this condition and only in this condition, the light intensity received by the photo-multiplier detector is zero.

The experimental procedure is considerably simplified if the compensator is first locked with its fast axis at exactly 45 degrees to the plane of incidence. The polariser and analyser are then adjusted for minimum light intensity received by the photomultiplier. The situation then corresponds to that shown in Fig. 16. The azimuth of the reflected ellipse is always 45 degrees, or in other words, the amplitudes of the reflected (p) and (s) components are equal, i.e. E_p^- and E_s^- are equal.

The azimuth ψ of the polariser is then equal to the parameter Ψ mentioned previously for, from Fig. 16;

$$\tan \psi = \frac{E_s^+}{E_p^+} \qquad (1)$$

But,

$$\operatorname{Tan} \Psi = \frac{\rho_{(p)}}{\rho_{(s)}} = \frac{\left(\frac{E_p^-}{E_p^+}\right)}{\left(\frac{E_s^-}{E_s^+}\right)} = \frac{\left(\frac{E_p^-}{E_s^-}\right)}{\left(\frac{E_p^+}{E_s^+}\right)}$$

Since from above, $\frac{E_p^-}{E_s^-} = 1.0$

then $\operatorname{Tan} \Psi = \frac{1}{\left(\frac{E_p^+}{E_s^+}\right)} = \frac{E_s^+}{E_p^+}$

Hence, from (1) $\tan \psi = \tan \Psi$

$$\psi = \Psi$$

The ellipticity δ' is related to the phase difference Δ

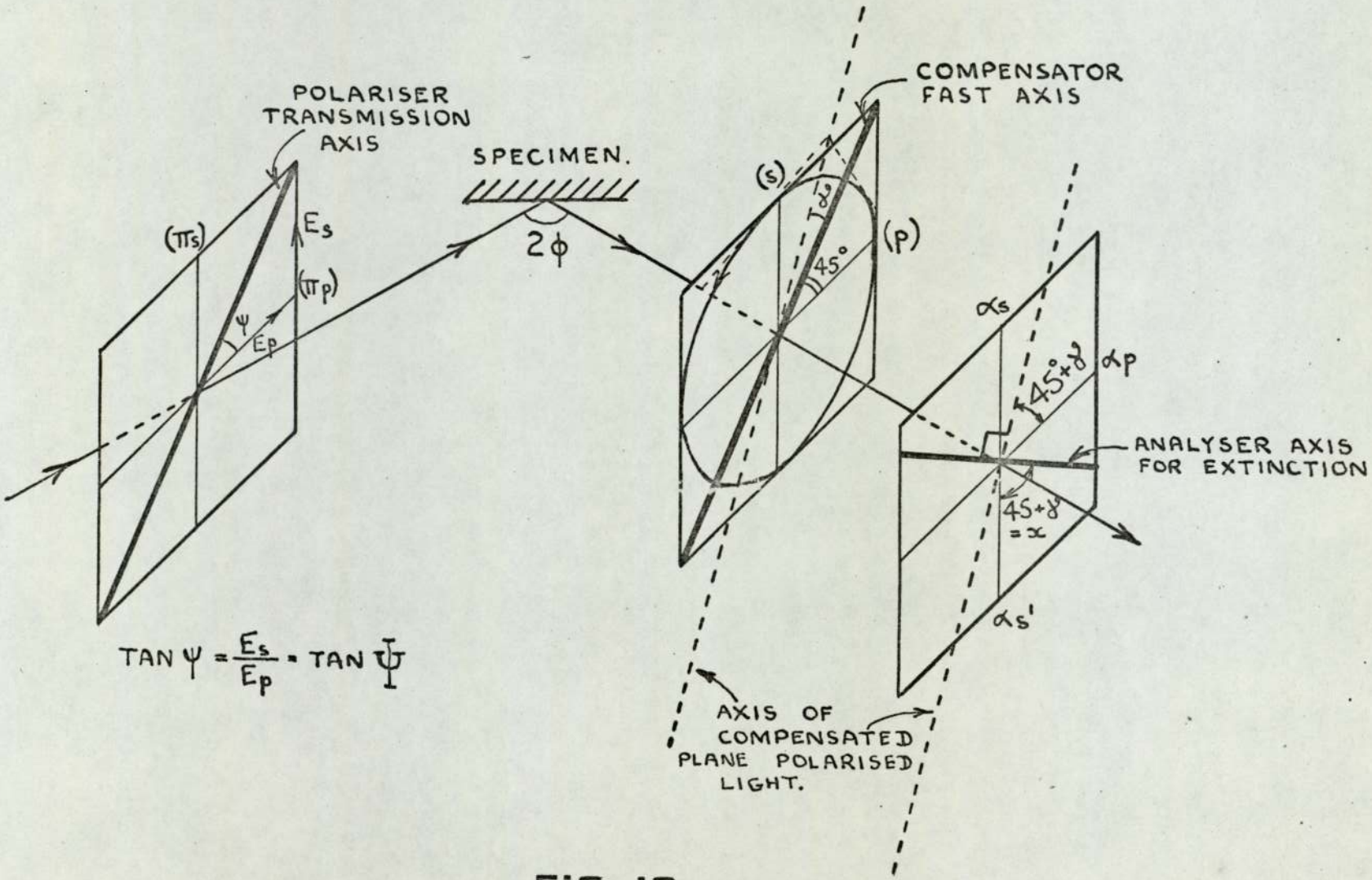
POLARISER
TRANSMISSION
AXIS
SPECIMEN.
COMPENSATOR
FAST AXIS
(πs)
Es
(πp)
Ψ
Ep
2φ
(s)
(p)
45°
αs
45+δ
αp
ANALYSER AXIS
FOR EXTINCTION
45+δ
=x
αs'
AXIS OF
COMPENSATED
PLANE POLARISED
LIGHT.
TAN Ψ = Es/Ep = TAN Ψ

FIG. 16.

between the (p) and (s) components. In general, it may be shown that

$$\tan \Delta = \frac{\tan 2\gamma}{\sin 2\chi}$$

Since, from above $\chi = 45^{\circ}$, $\sin 2\chi = 1.0$

and $\tan \Delta = \tan 2\gamma$

$$\Delta = 2\gamma$$

The ellipticity γ and hence the phase difference Δ is determined from the analyser azimuth, as shown in Fig.16. The azimuth of the compensated light is $45 + \gamma$, so that the azimuth of the analyser in its extinction position will be $45 + \gamma$ with respect to α_s', the perpendicular to the plane of incidence. It is this quantity, marked x on Fig.16, which is measured experimentally.

Since $x = 45 + \gamma = 45 + \frac{\Delta}{2}$

then $\Delta = 2x - 90$

In general, pairs of polariser and analyser azimuths for extinction occur which fall into four zones. McCrackin[116] gives a detailed explanation of the effect, although it should be noted that in his paper, the names 'polariser' and 'analyser' are interchanged with those in this work, because his experimental arrangement has the compensator placed before the reflection.

The total of 32 pairs of polariser and analyser positions for extinction can be understood in a methodical fashion by representing the state of polarisation of light by means of the Poincaré sphere.[130] For the general representation of ellipticallypolarised light, three parameters are required:

a) the ratio of minor to major axes, or ellipticity which $= \frac{b}{a} = \tan \gamma$ (say)

b) the azimuth of the major axis, χ

c) the rotation direction, conventionally positive

if anti-clockwise looking towards the on-coming light.

On the Poincaré sphere, Fig.17, the longitude represents twice the azimuth, and the latitude represents twice the ellipticity. The factor 2 arises because rotation of a polaroid through 180^{o} (i.e. 360^{o} on the Poincaré sphere) results in an optically identical situation. The northern hemisphere represents clockwise rotations and the southern hemisphere anti-clockwise rotations. The equator, χ = zero, represents plane polarised light of variable azimuth. The poles, $\chi = 45^{o}$, represent circularly polarised light. Thus any state of polarisation may be represented by a single point on the surface of the Poincaré sphere (PS).

The readings on the polariser and analyser scales where the planes of transmission are parallel or perpendicular to the plane of incidence are known as the reference azimuths of the polaroids. The nomenclature devised by the author serves to name each reference azimuth unambiguously as shown in Fig.18. The polariser and analyser scales are represented by π and α respectively. As is usual (p) and (s) indicate the directions parallel and perpendicular to the plane of incidence. The dash notation represents the optically equivalent scale reading at 180^{o}.

Consider a plan of the Poincaré Sphere, Fig.19. P_1 represents the plane polarised light falling on the specimen, having azimuth ψ (shown as longitude 2ψ on PS). Since from Fig.16, $\tan\psi = \frac{E_s}{E_p}$, then $\pi_p P_1$ represents E_s and $\pi_s P_1$ represents E_p, the components perpendicular and parallel to the plane of incidence respectively. The relative amplitude reduction on reflection alters the ratio of these components $\frac{\pi_p P_1}{\pi_s P_1}$. The azimuth of P_1 (i.e. the setting of the polariser) is adjusted until the components are equal after reflection and can be represented by the point P' on Fig.19. P_1 is therefore the

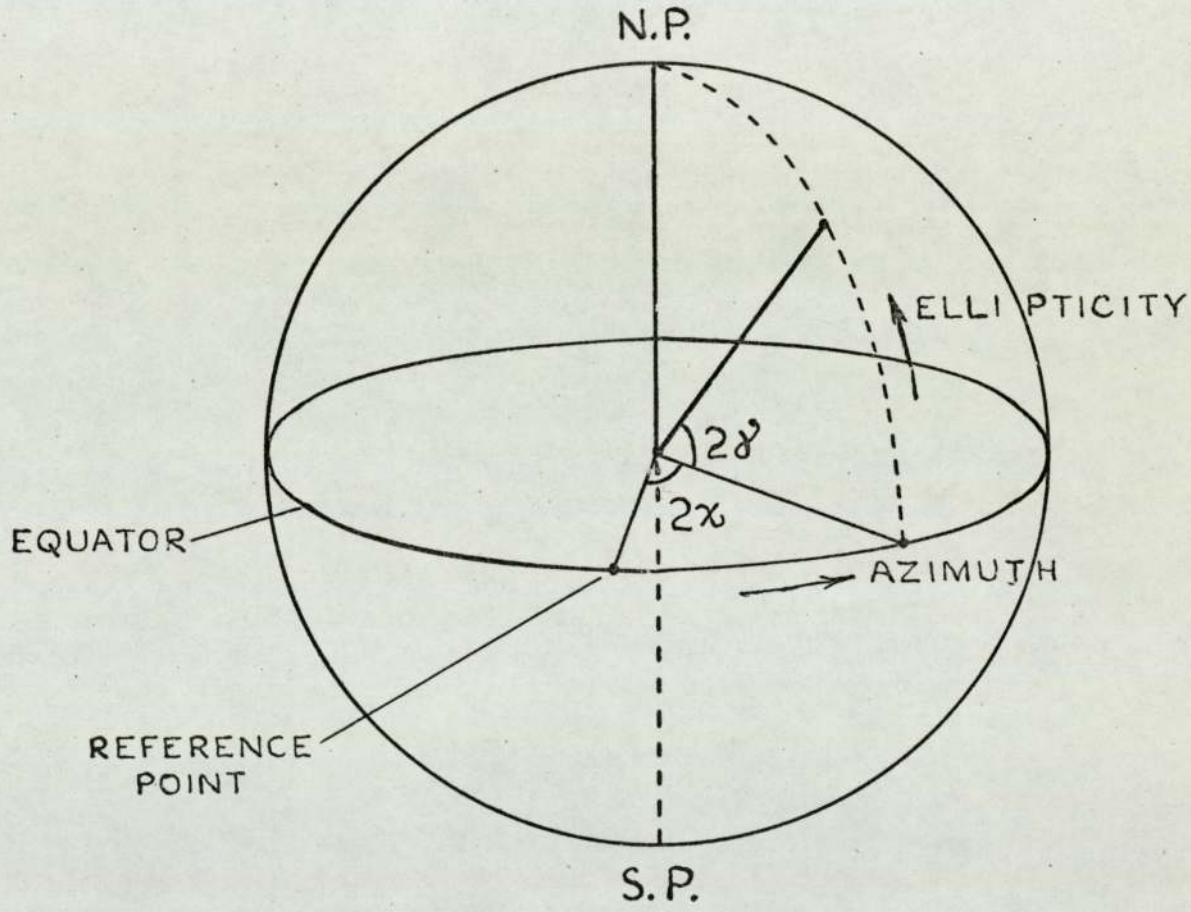

POINCARÉ SPHERE

FIG. 17.

π_p Polariser reference position that transmitts parallel to the plane of incidence.

π_p' Position at 180 degrees to the above.

π_s Polariser reference position that transmitts perpendicular to the plane of incidence.

π_s' Position at 180 degrees to the above.

α_p Analyser reference position that transmitts parallel to the plane of incidence.

α_p' Position at 180 degrees to the above.

α_s Analyser reference position that transmitts perpendicular to the plane of incidence.

α_s' Position at 180 degrees to the above.

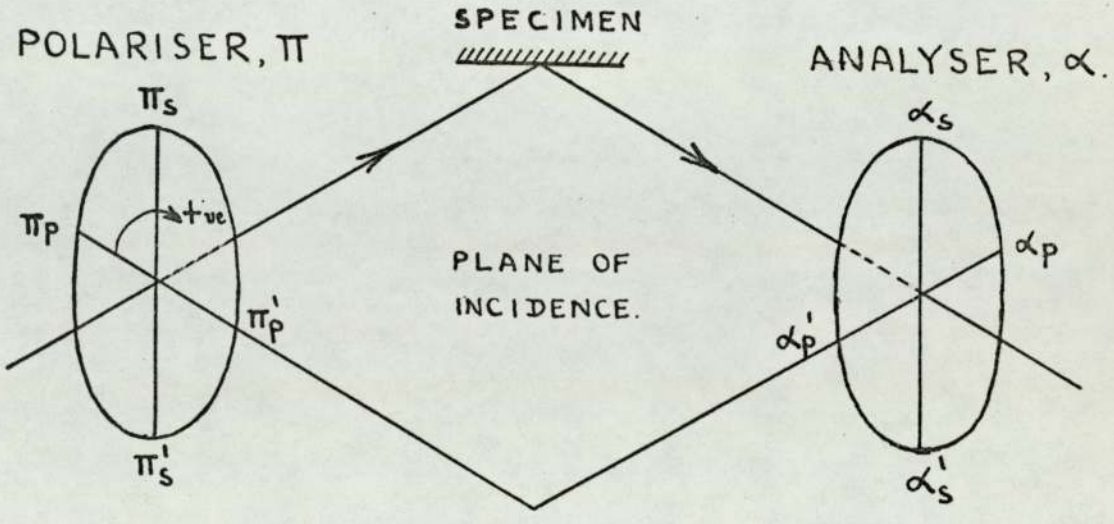

FIG 18

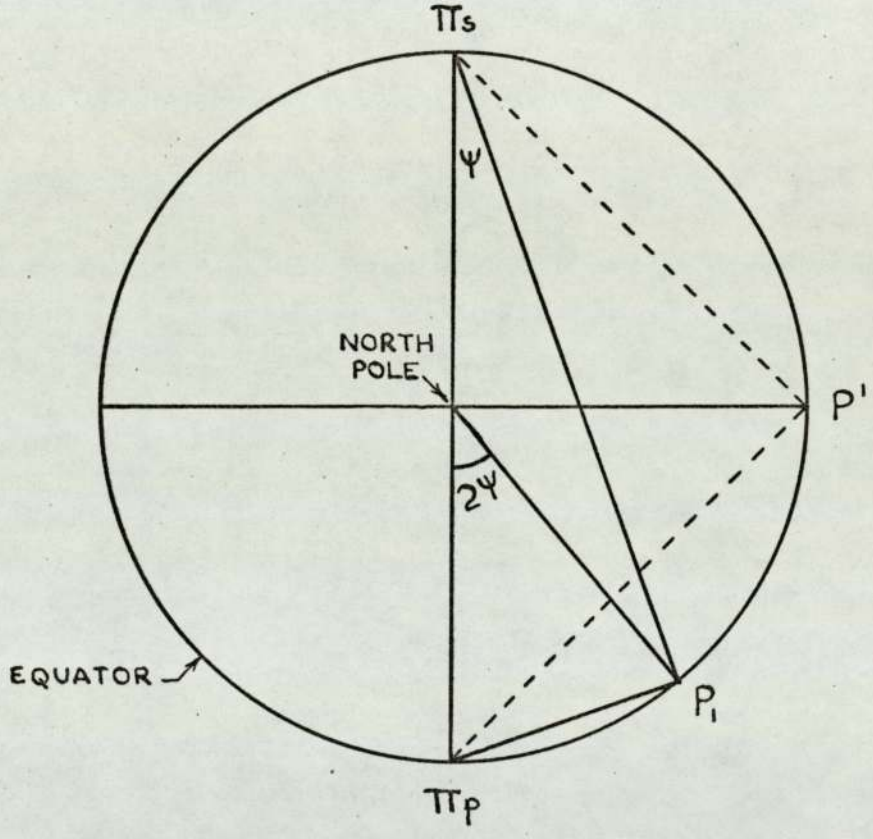

PLAN OF POINCARÉ SPHERE

FIG. 19.

polariser setting for extinction between π_p and π_s which are 90^o apart, but shown as 180^o on P.S.

Consider the relative phase retardation Δ between the (p) and (s) components. The effect of the reflection from the specimen as regards phase is to convert the linear vibration P' to an elliptical vibration Z by rotation about the axis $\pi_p \pi_s$ by an amount Δ. See Fig.20. (Clockwise rotation as seen from the fast axis, say π_s.)

The effect of the compensator will now be considered. The compensator fast axis is locked at azimuth Q at 45 degrees to the plane of incidence as shown in Fig.21. Note that Q coincides with P'. The compensator introduces a relative retardation of 90^o (i.e. one quarter wavelength) so that any elliptical vibration on the great circle $Q'OP'$ is converted into plane polarised light, represented by a point on the equator. Therefore, the elliptically polarised light Z is converted to plane polarised light P'' on the equator. Note that the angle Δ remains constant during this rotation. Finally, the plane polarised light P'' passes to the analyser adjusted into the 'crossed' position, A_1 (A1 is at 90^o to P'' but is shown as 180^o on P.S.).

The relative phase retardation Δ may be calculated from reference to Fig.21. If the analyser azimuth for extinction A_1 is at a measured angle x to α_s (shown as $2x$ on P.S.), then

$$2x = 90 + \Delta$$

$$\Delta = 2x - 90$$

For convenience Δ has been shown less than 90^o but the method is still applicable if Δ is greater than 90^o.

As well as the polariser position for extinction P_1, there is also a position P_2 which is symmetrically placed about π_p. See Fig.22. There are also two non-significant positions at 180^o to each. Fig.22 also shows the corresponding analyser extinction positions A_1 and A_2 which are seen to be perpendicular

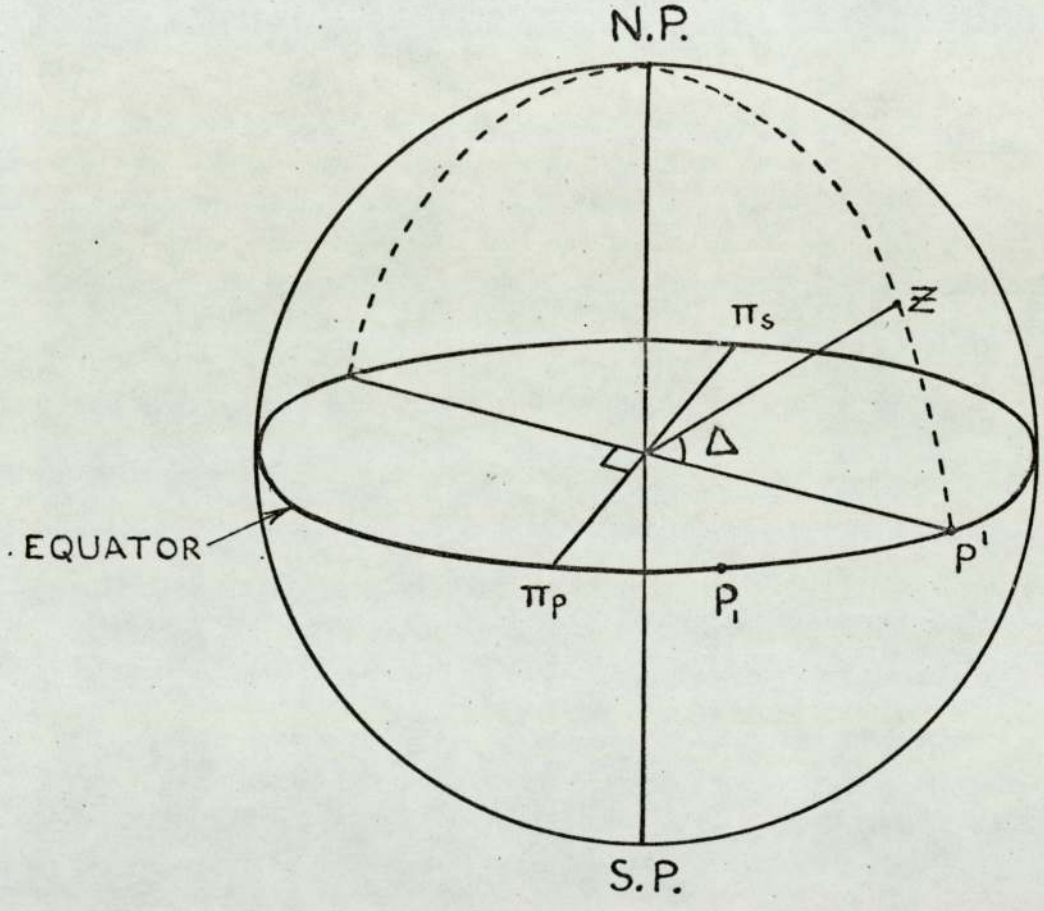

REFLECTED LIGHT IS ELLIPTICALLY POLARISED AND IS REPRESENTED BY POINT Z.

FIG. 20.

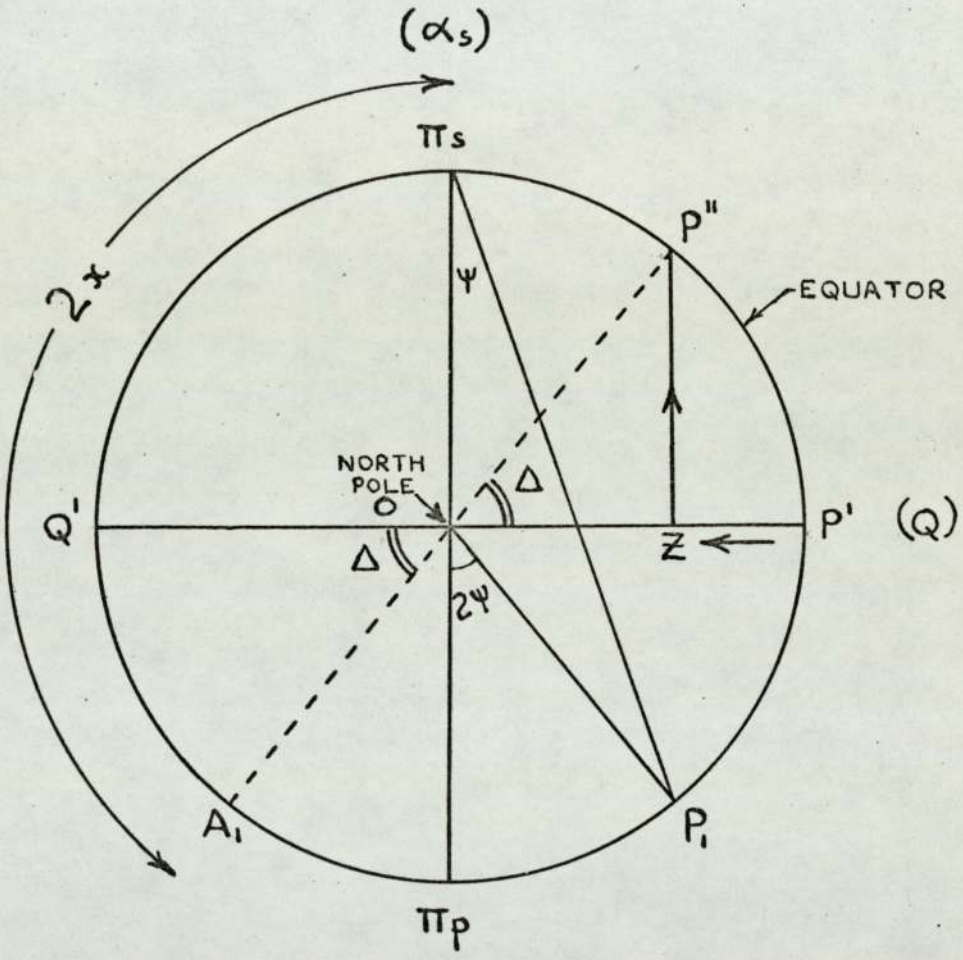

FIG.21.

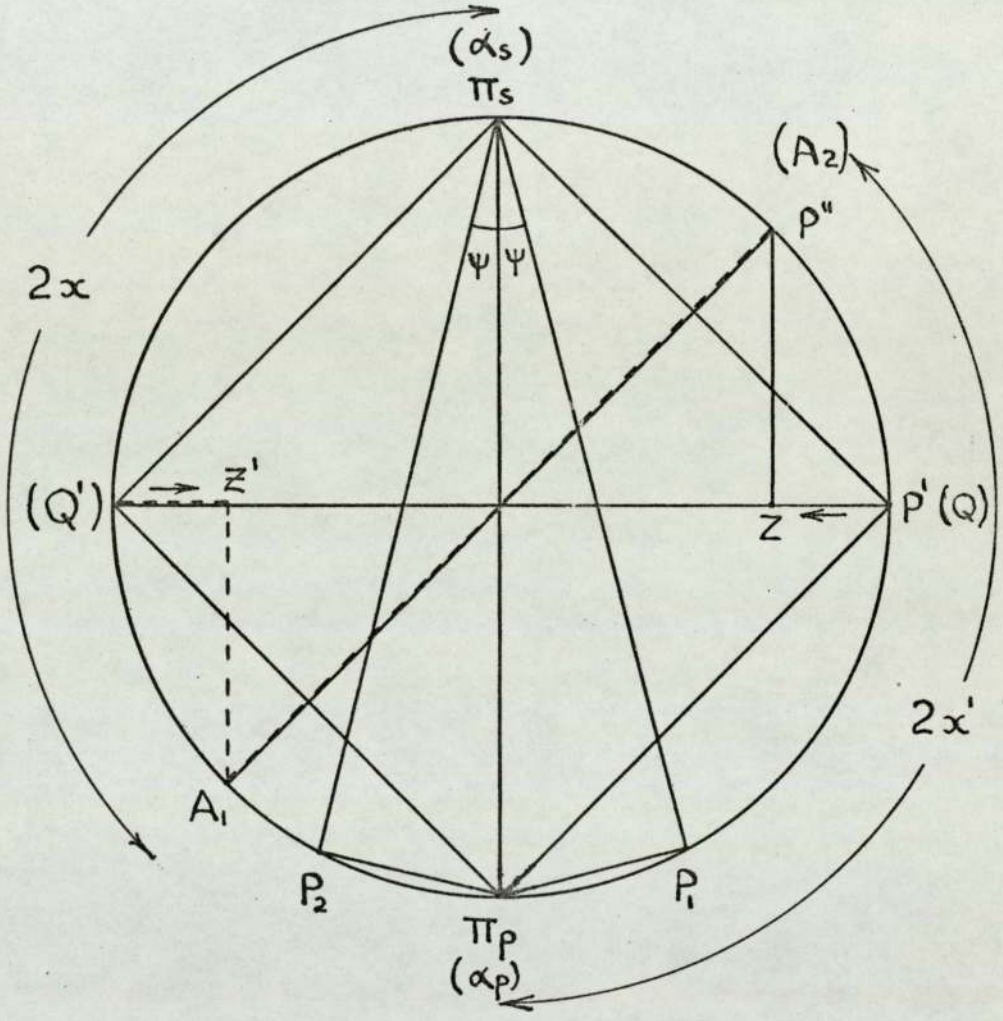

FIG. 22.

to each other (180^{o} apart on P.S.). The dotted lines represent the southern hemisphere. The scheme that develops, then, is as follows: the two polariser positions for extinction, P_1 and P_2 are symmetrical about π_p (the plane of incidence). The two corresponding analyser positions A_1 and A_2 are at right angles to each other, and are at an angle x from α_s and α_p respectively. Two more pairs of extinction positions, designated 3 and 4, exist at 180^{o} to all the above positions. Further, compensation of the reflected light is also possible with the fast axis at an azimuth of -45^{o}, i.e. with the compensator locked at 90^{o} from its first position. In this case the compensation is effected by an anticlockwise rotation of the point Z about the axis $Q'P'$ in Fig.21, instead of a clockwise rotation. The polariser extinction positions are unaffected but the analyser extinction positions occur at the same angle x on the other sides of α_s and α_p. Four more pairs of extinction positions are thus produced, making a total of eight pairs, as shown in the table of results in Appendix 3. Any single measurement in the table has an equivalent position at 180^{o} so that 16 pairs of measurements are possible. Finally, rotation of the compensator through 180^{o} in both cases doubles the possible number of results, making 32 pairs in all. It is not necessary to measure all 32 pairs of positions. Clearly, in the experiments undertaken here, time would not allow this. However, great care must be taken in the choice of measurements to be taken. Several workers have reported an obscure effect which tends to make some pairs of results consistently larger than average and some smaller. The effect is discussed by McCrackin.[116] Measurements to be undertaken must be chosen in such a way that the same number of "high" and "low" pairs are selected. The averaged result will then be acceptably close to the average if all possible measurements had been made. As can be seen from the specimen results in Appendix 3, suitable pairs were found to be those

designated 1 and 2, for the compensator azimuths + 45° and -45°. This makes four pairs of measurements taken.

2.4 Theory of Beatties' method for ellipsometry in the infra red.

In 1954, Beattie and Conn[28] showed theoretically that the determination of optical constants in the infra-red was most accurately performed by measuring the parameters Ψ and Δ. Reflectivity measurements suffered from inherent insensitivity. On the basis of the initial theory by Conn and Eaton,[131] Beattie[112] devised the following method for the determination of the ellipsometric parameters which does not require a compensator, and is therefore useful when measurements are required over a range of wavelengths.

The method involves the measurement of the absolute intensity of light transmitted by the system, polariser-specimen surface-analyser, for four different azimuths of the polaroids.

Consider the system shown in Fig.23. A beam of monochromatic, plane polarised light of azimuth ψ_p is produced by the polariser and falls on the specimen. If the electric amplitude is E, then the components of the electric vector (at any time t) incident on the specimen are given by:

$$E_{(p)} = E \cos\psi_p \cos\omega t$$
$$E_{(s)} = E \sin\psi_p \cos\omega t$$

If r_p and r_s are the Fresnel reflection coefficients from the surface in the (p) and (s) directions then the reflected electric vectors will be:

$$E_p^- = E r_p \cos\psi_p \cos(\omega t + \delta_p)$$
$$E_s^- = E r_s \sin\psi_p \cos(\omega t + \delta_s)$$

where δ_p and δ_s are the phase retardations for the (p) and (s) components. The instantaneous electric vector transmitted through the analyser is given by the sum of the components of each vibration parallel to the transmission axis. Let the azimuth of

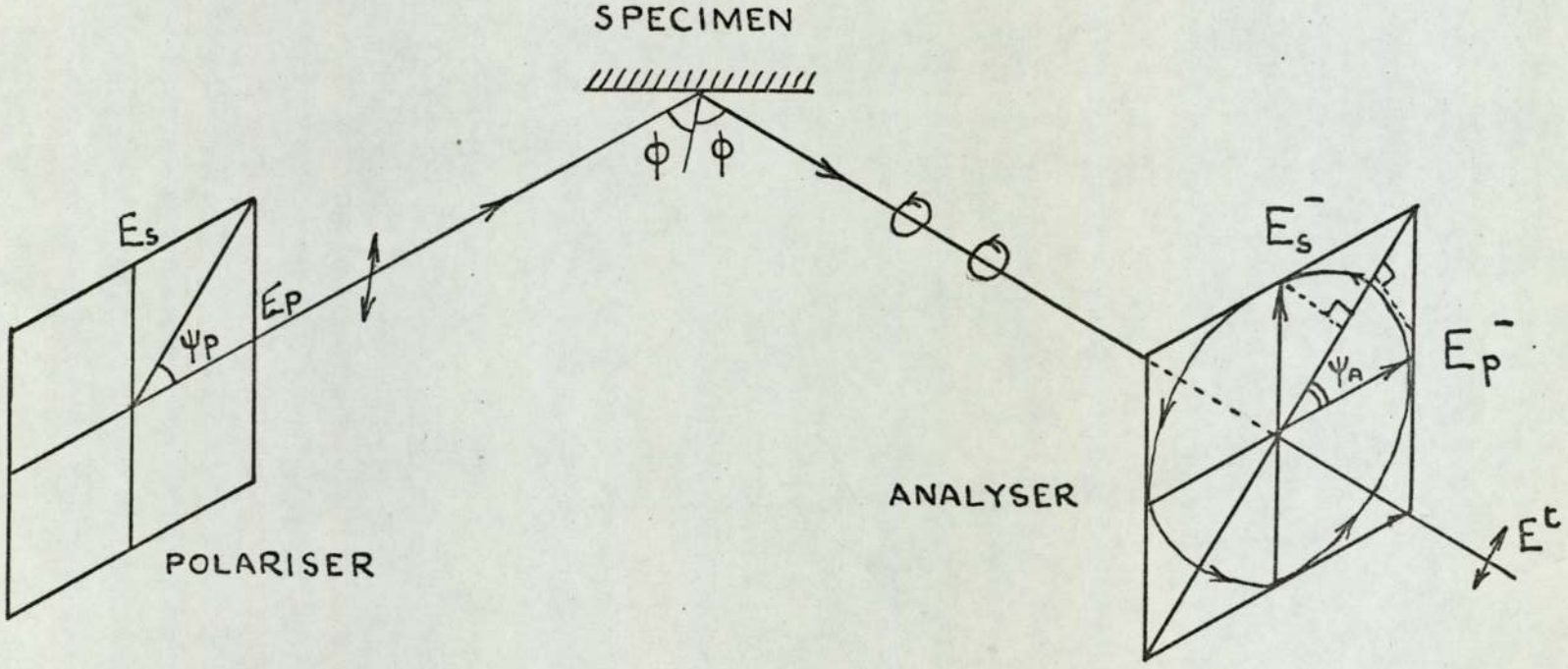

BASIS OF BEATTIES METHOD

FIG. 23.

the transmission axis be ψ_A , as shown in Fig.23.

Hence, the transmitted electric vector is:

$$E^t = Er_p \cos\psi_p \cos\psi_A \cos(\omega t + \delta_p) + Er_s \sin\psi_p \sin\psi_A \cos(\omega t + \delta_s)$$

The transmitted intensity, I^t at any instant, is given by the square of the above expression which, after some trigonometrical manipulation gives:

$$I^t = E^2 r_p^2 \cos^2\psi_p \cos^2\psi_A \cos^2(\omega t + \delta_p) + E^2 r_s^2 \sin^2\psi_p \sin^2\psi_A \cos^2(\omega t + \delta_s)$$

$$+ \tfrac{1}{4} E^2 r_p r_s \sin 2\psi_p \sin 2\psi_A \cos(2\omega t + \delta_p + \delta_s) + \tfrac{1}{4} E^2 r_p r_s \sin 2\psi_p \sin 2\psi_s \cos(\delta_p - \delta_s)$$

When the time-averaged intensity (that which is measured experimentally) is calculated from the above expression, using the standard results;

Time averaged $\cos^2(\omega t + \delta_p) = \frac{1}{2}$

Time averaged $\cos(2\omega t + \delta_p + \delta_s) = 0$

the measured intensity, expressed as a function of ψ_p and ψ_A , becomes:

$$I(\psi_p, \psi_A) = E^2 \left\{ \tfrac{1}{2} r_p^2 \cos^2\psi_p \cos^2\psi_A + \tfrac{1}{2} r_s^2 \sin^2\psi_p \sin^2\psi_A + \tfrac{1}{4} r_p r_s \sin 2\psi_p \sin 2\psi_A \cos\Delta \right\}$$

where $\Delta = \delta_p - \delta_s$

Writing $\rho = \frac{r_p}{r_s} = \tan\Psi$

then,

$$I(\psi_p, \psi_A) = \tfrac{1}{2} E^2 r_s^2 \left\{ \rho^2 \cos^2\psi_p \cos^2\psi_A + \sin^2\psi_p \sin^2\psi_A + \tfrac{1}{2} \rho \sin 2\psi_p \sin 2\psi_A \cos\Delta \right\}$$

For metals of high conductivity, r_s^2 differs little from unity so that it can be incorporated into an intensity I_o , such that $I_o = \frac{1}{2} E^2 r_s^2$.

The intensity then measured may be expressed as:

$$I(\psi_p, \psi_A) = I_o \left\{ \sin^2\psi_p \sin^2\psi_A + \rho^2 \cos^2\psi_p \cos^2\psi_A + \tfrac{1}{2} \rho \sin 2\psi_p \sin 2\psi_A \cos\Delta \right\} \quad (2)$$

Beattie's method involves the measurement of four intensities for which the polariser azimuth, ψ_p is set at $+45^\circ$ and the

analyser azimuth has the values $+90^{\circ}$, 0, $+45^{\circ}$, -45°. From equation (2) above, these are

$$I_1\left(+\tfrac{\pi}{4}, +\tfrac{\pi}{2}\right) = \tfrac{1}{2} I_o$$
$$I_2\left(+\tfrac{\pi}{4}, 0\right) = \tfrac{1}{2} I_o \rho^2$$
$$I_3\left(+\tfrac{\pi}{4}, +\tfrac{\pi}{4}\right) = \tfrac{1}{4} I_o (1 + \rho^2 + 2\rho \cos\Delta)$$
$$I_4\left(+\tfrac{\pi}{4}, -\tfrac{\pi}{4}\right) = \tfrac{1}{4} I_o (1 + \rho^2 - 2\rho \cos\Delta)$$

It may be shown[112] that

$$\rho = \sqrt{\frac{I_2}{I_1}} = \tan\Psi \qquad (3)$$

and

$$\cos\Delta = \tfrac{1}{2}\left(\frac{1}{\rho} + \rho\right)\left\{\frac{I_3 - I_4}{I_3 + I_4}\right\} \qquad (4)$$

Equation (4) provides a measurement of Δ, largely independent of ρ, since the quantity $\frac{1}{2}\left(\frac{1}{\rho} + \rho\right)$ differs very little from unity. The method provides a useful check in that $I_1 + I_2$ should be equal to $I_3 + I_4$. In practice, this is found to be true to 1 or 2%. Errors due to incorrect reference azimuths are minimised by measuring the four corresponding intensities on the opposite sides of the reference azimuths and averaging.

i.e. $$I(\psi_p, \psi_a) = I(-\psi_p, -\psi_a)$$

The experiments carried out have thus involved the measurement of eight different intensities at each wavelength.

Some specimen results are given in Appendix 4.

CHAPTER 3

INTRODUCTION TO THE EXPERIMENTAL WORK

The purpose of the present investigations was to continue and extend the study of the relationship between optical constants and structure already initiated in this laboratory.[114][31] Changes of optical constants with annealing had been observed and although it was thought that the growth of an oxide layer could be a contributing factor, no detailed study of this aspect had been made.[31] The analysis of anncaling effects was limited to a narrow range of wavelengths, 546 to 549 nm, and no emphasis had been placed on interband transitions.

By performing simultaneous measurements of the optical constants and electrical resistivity during annealing, it was hoped that the variations in optical constants could be correlated with structural changes brought about by the annealing of defects in the specimen. For such correlations to be successful, the growth of surface layers of aluminium oxide would have to be entirely eliminated or, if this were not possible with the apparatus available, some way of applying a correction to the experimental results in order to obtain values relating to the clean metal surface would have to be found.

It was decided that two possible methods of eliminating the oxidation problem would be attempted. Firstly, the method used by Madden et al.[30] of studying the oxidation rate for a number of similar specimens and then making appropriate corrections to all experimental measurements; and secondly, the technique of allowing the aluminium specimen to become totally oxidised by exposure to the atmosphere (i.e. to permit the formation of the equilibrium layer of oxide, known to be approximately 3.5 nm in thickness) and then to observe the variations in properties as a result of annealing. The latter method would only be useful if

it could be shown that the oxide layer itself did not increase in thickness, or change significantly in its optical constants, as a result of annealing.

It was considered that the correlation of optical and electrical changes would be most readily observed on specimens which show comparatively large variations. Accordingly, it was decided that aluminium films of thickness less than 20 nm would be the subject of the experiments because:

i) the disordering influence of the substrate leads to a greater concentration of defects in thinner films, and tends to be less important for thicker ones.

ii) the formation of aluminium oxide causes a reduction in thickness of the metal and leads to a higher resistance; an effect which is proportionately greater for a thinner film.

iii) due to the penetration depth of electro-magnetic waves in a highly absorbing metal (approx. 10 nm in Aℓ) the optical measurements give information on the entire thickness of the film.

Measurements of the optical constants of metals, particularly over a wide range of wavelengths and at different temperatures, are important for a variety of reasons. In the first place, a better understanding of the structural dependence of these constants should ultimately lead to a more accurate interpretation of the real and imaginary parts of the refractive index. Apart from the elucidation of the interaction between photons and electrons, optical measurements can be of value when considered in relation to various phenomena in metal physics. As discussed in section 2.1, the determination of the optical constants in the region of inter band transitions enables the principle Fourier components of the pseudo potential model to be estimated. These

components determine not only the optical properties of the metal but also the de Haas - van Alphen effect, cyclotron resonance, the absorption of ultra sound in a magnetic field and the temperature of transition to the superconducting state. Hence it is possible to use optically determined data in the interpretation of other experimental data. The great advantage of the optical method of determining the Fourier components of the pseudo-potential, Vg, is that this is the only method by which the temperature dependence of these components may be determined. In general, the values of Vg become smaller for higher temperatures, and it is possible to estimate the resulting changes of effective free electron density, Fermi surface area and mean electron velocity at the Fermi level.[24] The optical effective mass and the band gaps related to zone structure may also be estimated.

The other methods mentioned above for obtaining detailed information about the Fermi surface require comparatively large electron mean-free-paths and are therefore limited to applications which involve very low temperatures and high purity metals.

Aluminium is a particularly good subject for fundamental investigation since it follows closely the nearly-free electron approximation, having three free electrons per atom. The zone structure and Fermi surface are well understood and band energies have been calculated in detail, notably by Ehrenreich et al.[33] thus facilitating the interpretation of variations in optical results due to annealing. Furthermore, the very high stacking fault energy means that other types of defect may be studied during annealing experiments. It is also available in very pure form and is readily evaporated to form thin metallic films.

In addition to the above fundamental physical considerations, aluminium also finds considerable use in the technology of thin film devices and is frequently used for contacts and connections

in integrated circuits. Difficulties have been encountered as a result of oxidation and also of electro-migration[162] so that an investigation of the properties of the metal may be of practical importance.

CHAPTER 4

EXPERIMENTAL DETAILS

4.1 Apparatus

4.1.1 The Vacuum System

The vacuum system was a conventional one as used by Fane and Neal[31] and is shown in Fig.24. The stainless steel experimental chamber was pumped by a four-stage diffusion pump charged with D C. 705 oil. This pump was backed through a liquid nitrogen trap by a 42 $l.min^{-1}$ rotary pump. A water-cooled baffle and two liquid nitrogen traps separated the chamber from the pumps, the upper one being positioned so that it could be baked with the chamber to 400°C. Aluminium wire seals (0.625 mm diam.) were used between the chamber and the cold traps and indium wire seals between the traps and the diffusion pump where the system is not subject to baking. A plan view of the experimental chamber is shown in Fig.25, along with the optical arrangement. All flanges used copper gasket seals.

In order to maintain the substrate at any desired temperature, as required in some of the experiments, the author designed the arrangement shown in Fig.26. The substrate, either Corning 0211 glass or polished single crystal of potassium bromide, was supported on a stainless steel block, welded to a stainless steel tube which formed the central finger. Inside this finger was a second narrower tube with a heater block welded to the end. When bolted in position, this heater block made good contact with the substrate block as indicated in Fig.26. To ensure good thermal contact, a disc of copper foil 0.025 inches thick was softened by heating and quenching in water, and placed between the heater and substrate blocks. The heater was constructed of 200 turns of 38 SWG cotton-covered eureka wire, further insulated by brushed-on layers of "Eco-coat" 672 compound. (Emerson and Cuming Inc., U.S.A.) When operated on mains voltage through a variac trans-

FIG. 24. VACUUM SYSTEM

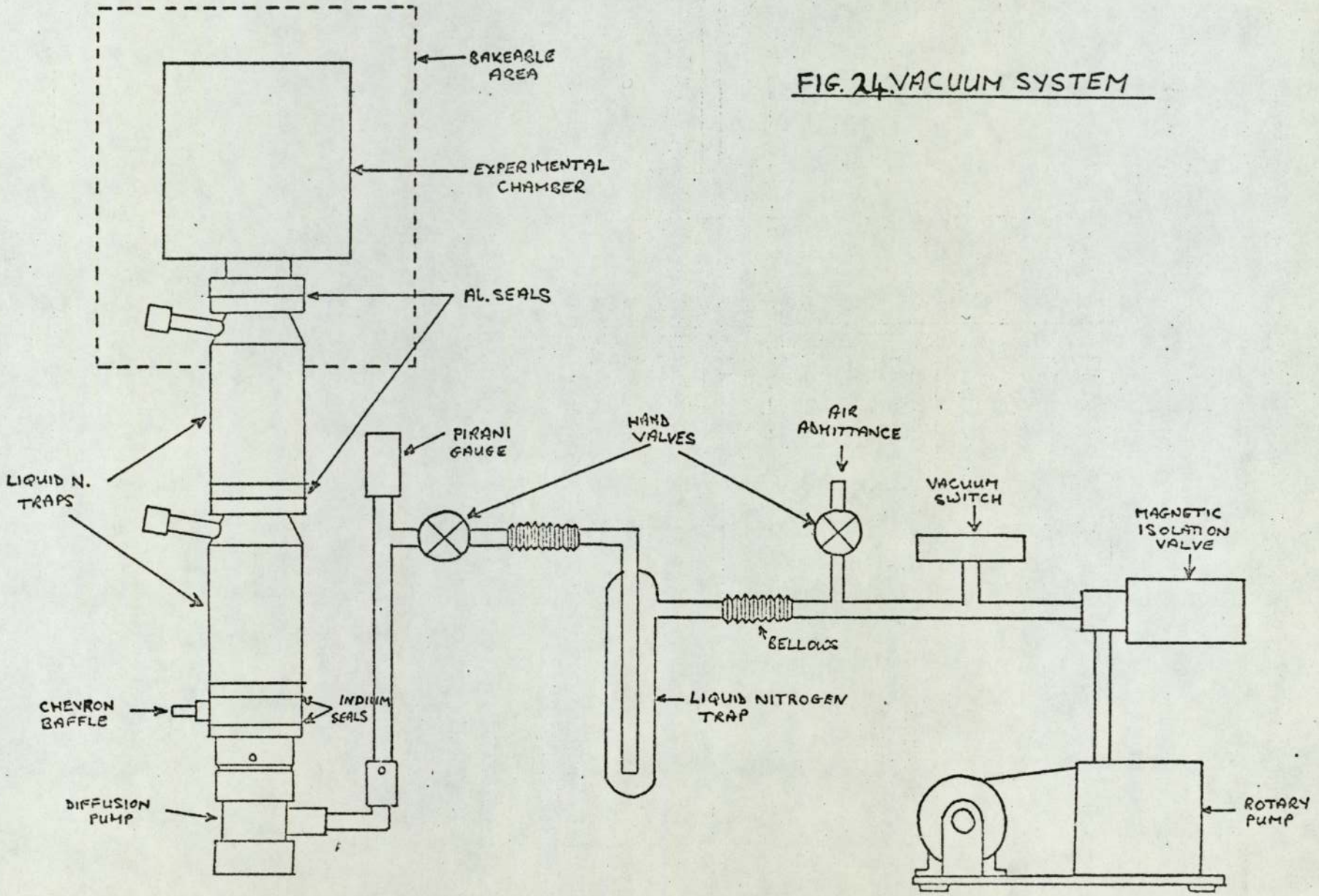

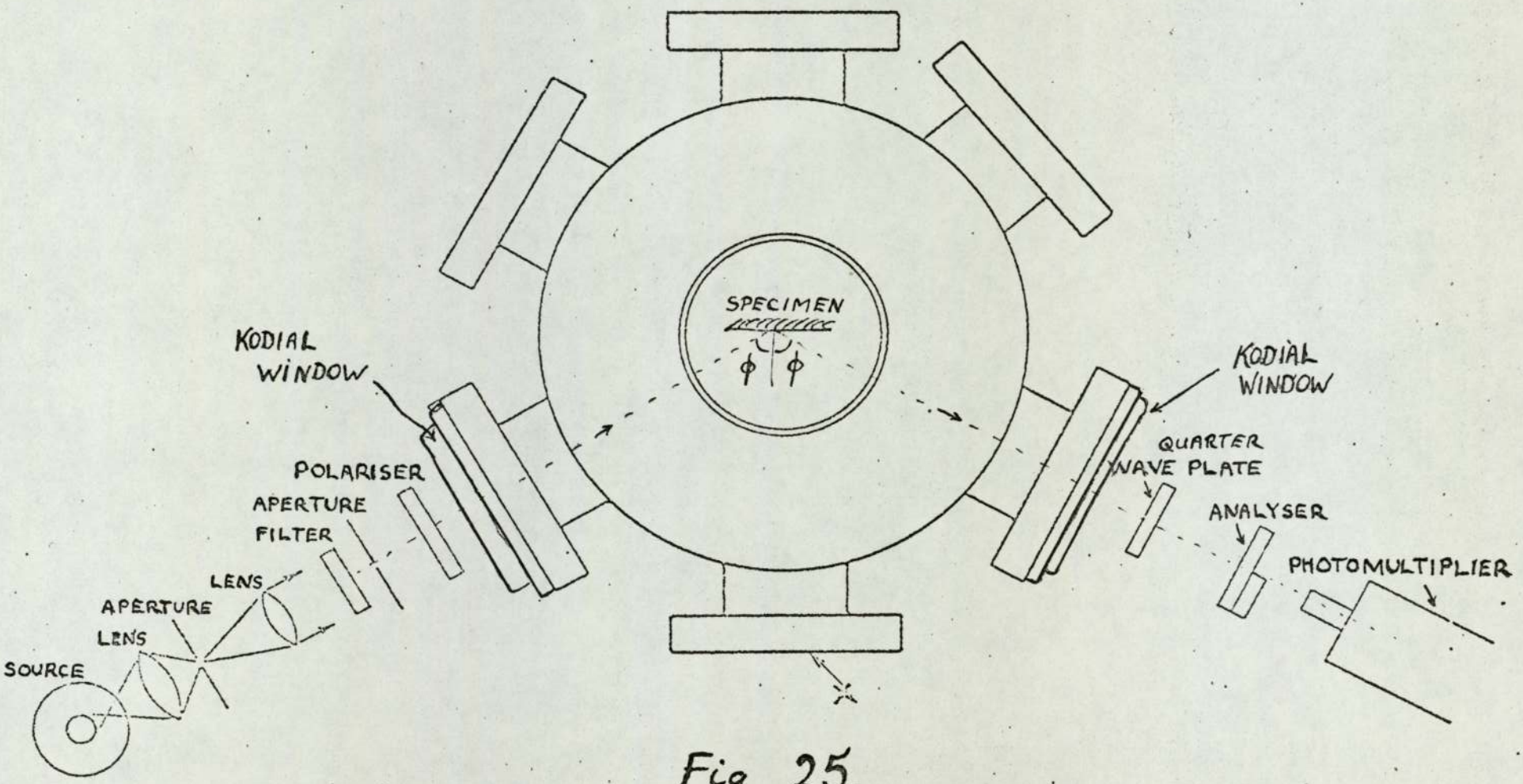
SPECIMEN
KODIAL WINDOW
KODIAL WINDOW
POLARISER
APERTURE FILTER
QUARTER WAVE PLATE
ANALYSER
PHOTOMULTIPLIER
LENS
APERTURE
LENS
SOURCE

Fig. 25.

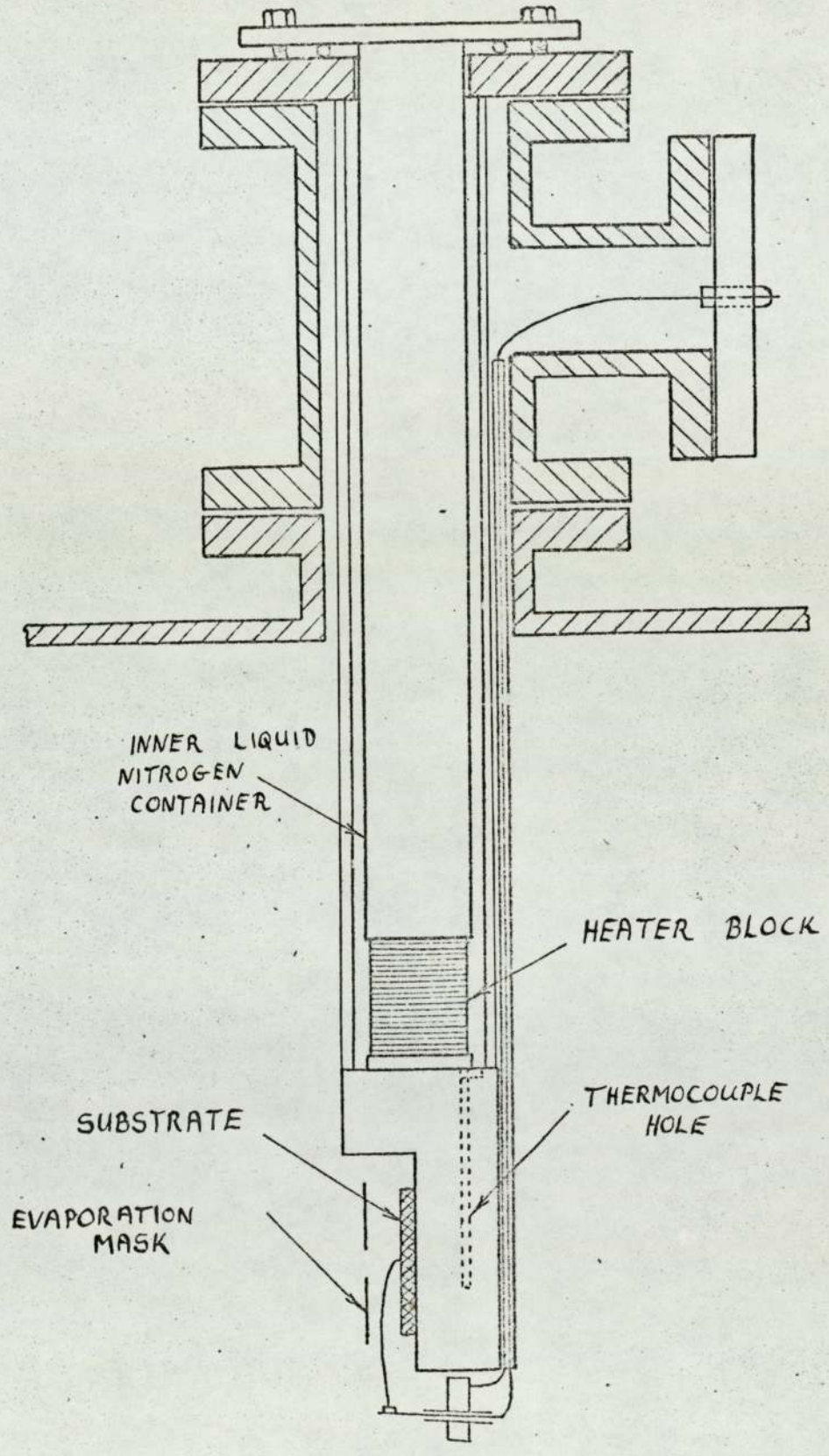
INNER LIQUID
NITROGEN
CONTAINER
HEATER BLOCK
THERMOCOUPLE
HOLE
SUBSTRATE
EVAPORATION
MASK

FIG. 26.

former, the heater carried a maximum current of 400 mA and gave a power of approximately 100 watts. This was sufficient to raise the temperature of the substrate block to 280°C, as measured on a copper-constantan thermocouple inserted into the block, or, with the inner finger filled with liquid nitrogen, to maintain an equilibrium temperature of any value between -196°C and room temperature. The lead-through connections for the heater and thermocouple were raised above the upper flange by means of copper tubes 12 cm long in order to avoid condensation of moisture on the connections. See Fig.27. A general view of the apparatus assembled is shown in Fig.28

The experimental chamber also incorporated a 'Mini-Mass' mass spectrometer for residual gas analysis and a quartz crystal thickness monitor, mounted in a side arm so that the crystal was the same distance from the evaporation filament as the specimen substrate. This is shown in Fig.29, which also shows the magnetically operated shutter made of nickel foil which was used to protect the substrate during out-gassing. A bakeable leak valve, type MD6 supplied by Vacuum Generators Ltd., allowed the total pressure to be varied and accurately controlled during the experiments involving oxidation of the specimens.

Electrical connections to the specimens were made via an eight-way ultra high vacuum lead-out and nickel wires insulated with ceramic beads and pyrex glass tubes. The final connections to the specimens were made with gold wires (0.005" diam.) thermally bonded on to special contact areas. See section 4.2.1. The size of the specimen film was defined by evaporation masks as indicated on Fig.30. This same figure also shows the mask for the evaporation of a duplicate film on to the junction of an evaporated thin-film thermocouple of copper-nickel. This second film was used in some of the experiments to determine the true specimen temperature relative to the substrate block. See section 5.1

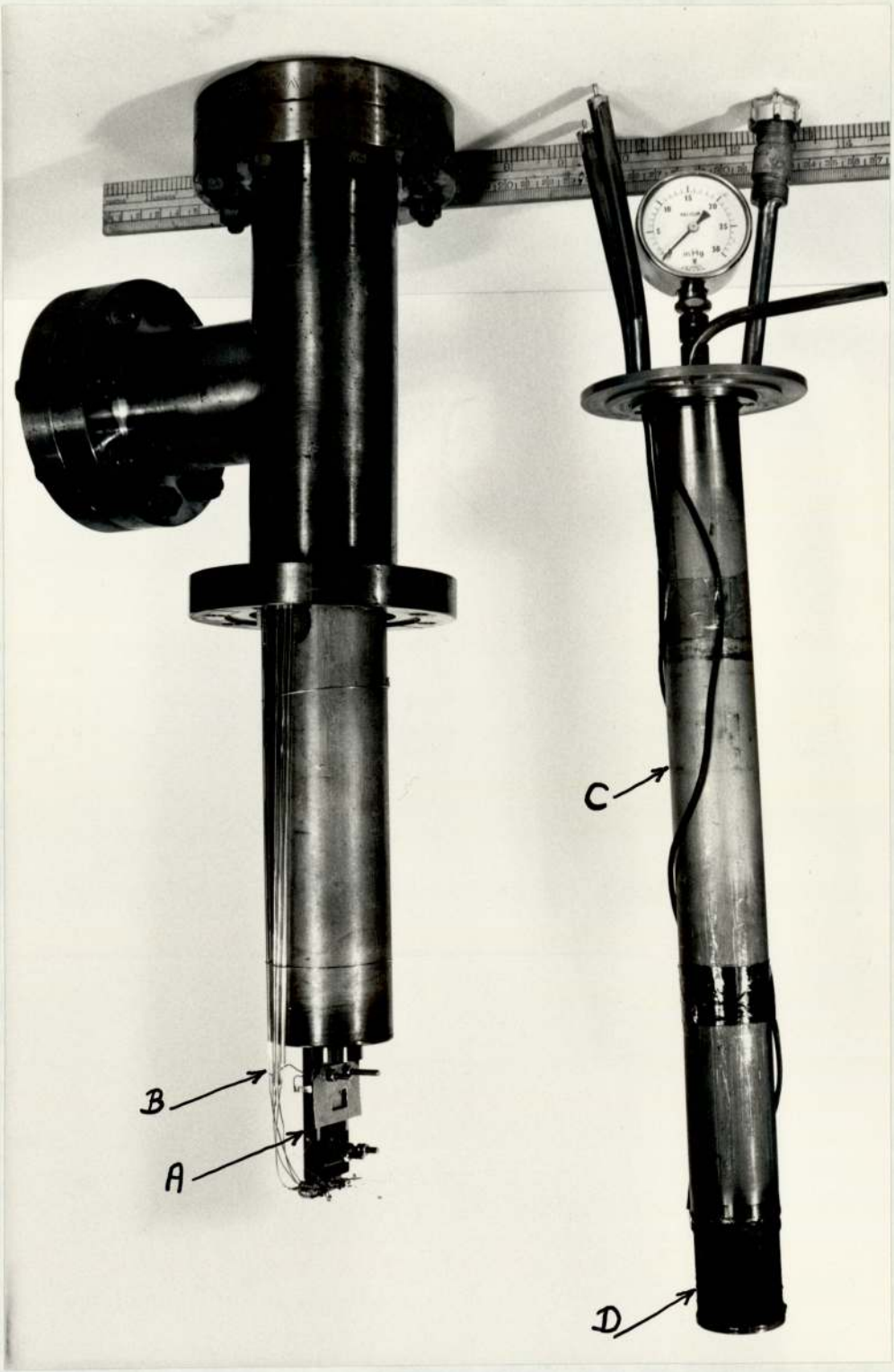

FIG. 27

A. Substrate mounting block
B. Insulated electrical connections to specimen film
C. Inner container for liquid nitrogen
D. Heater coil on stainless steel block

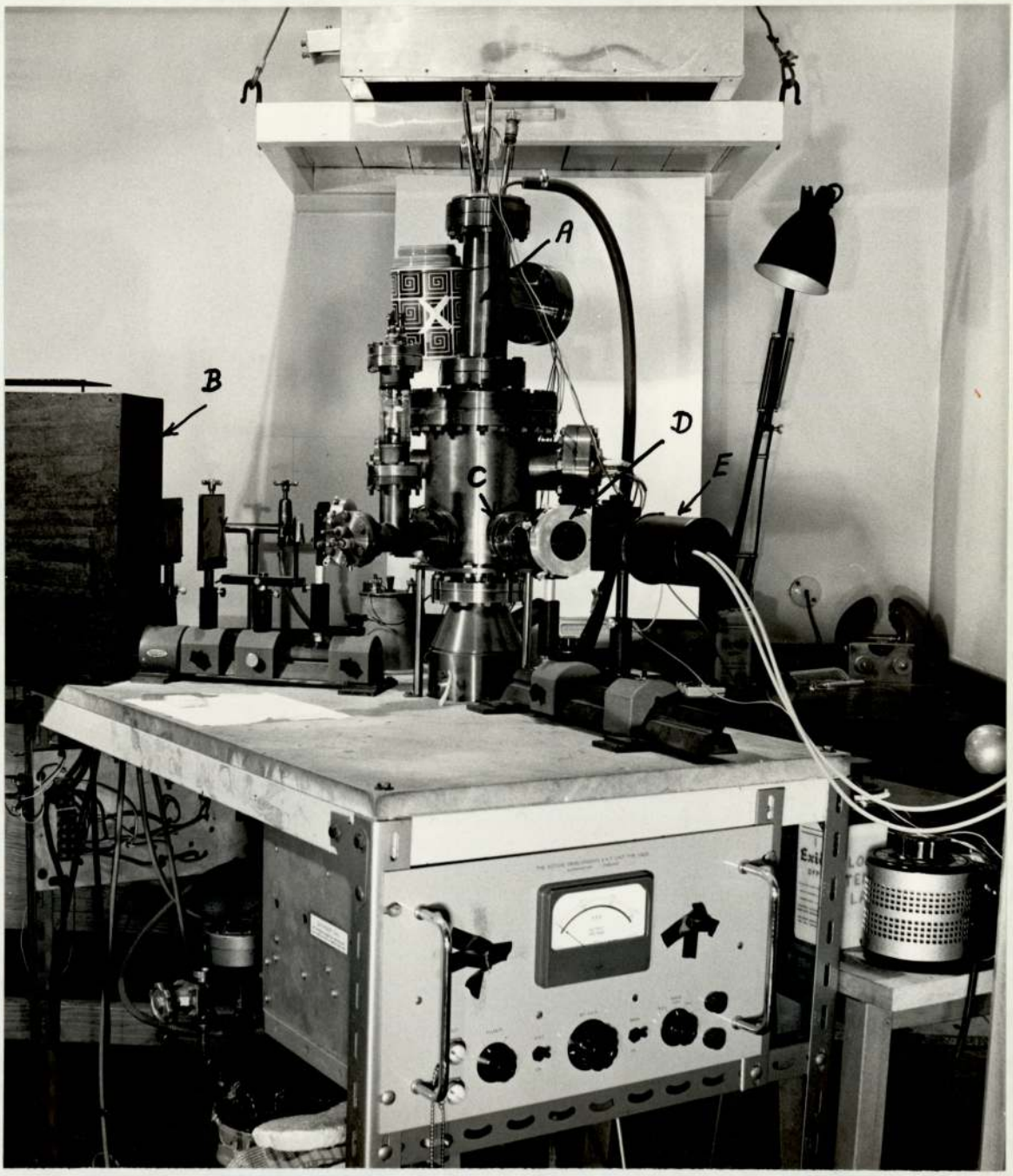

FIG. 28

A. Liquid nitrogen cold finger
B. Ellipsometer lamp
C. Kodial glass window on specimen chamber
D. Analyser polaroid in divided circle
E. Photomultiplier detector

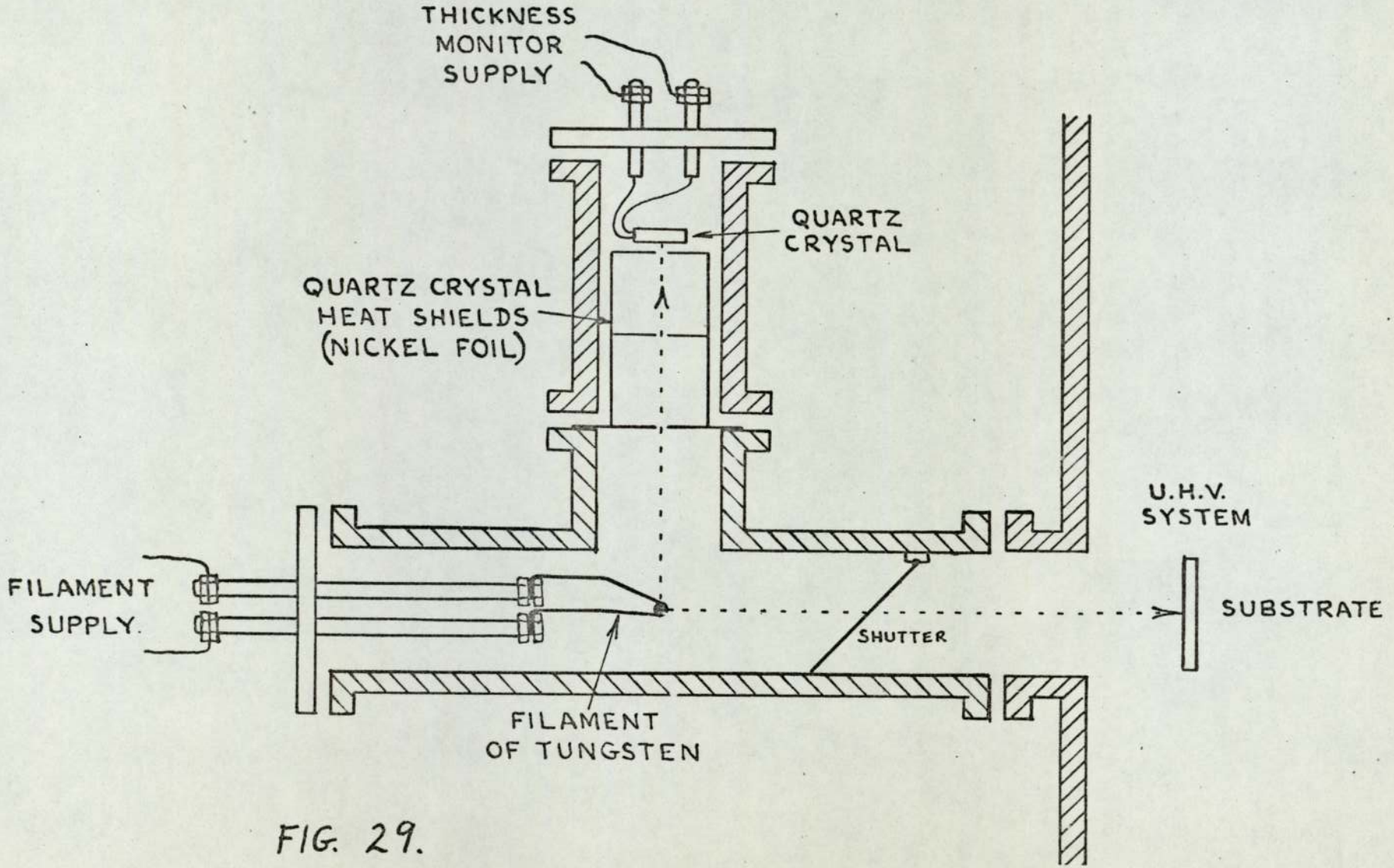
THICKNESS
MONITOR
SUPPLY
QUARTZ
CRYSTAL
QUARTZ CRYSTAL
HEAT SHIELDS
(NICKEL FOIL)
U.H.V.
SYSTEM
FILAMENT
SUPPLY
SUBSTRATE
SHUTTER
FILAMENT
OF TUNGSTEN

FIG. 29.

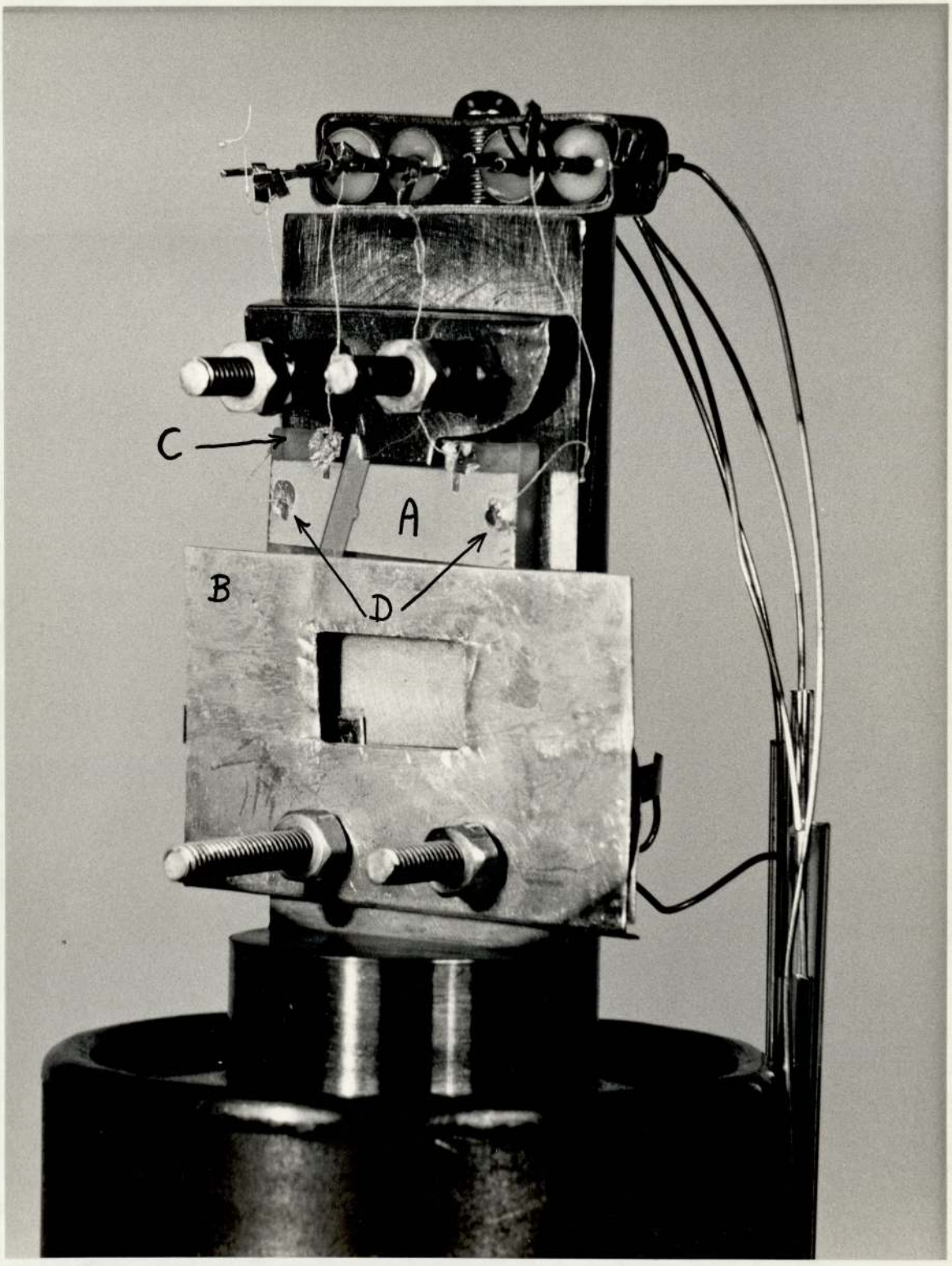

FIG. 30

A. Specimen film
B. Evaporation mask
C. Potassium bromide substrate
D. Gold wire bonded connections

4.1.2 The Ellipsometer

The ellipsometer itself consisted of two triangular section optical benches bolted to fixed plates on the vacuum bench. These benches, together with their components on sliding saddles, were easily removed during baking of the vacuum system. The light source was a 24 volt, 150 watt tungsten filament projector lamp, operated from a 13 volt transformer. This lamp provided adequate intensity in the visible and near infra-red regions. A condenser lens L1, in Fig.25, focuses the light on a pin-hole which is arranged to be at the focus of the lens L2. The wavelength of the parallel beam of light thus formed is chosen by means of a Balzer interference filter F, having a pass-band of about 2 nm. The aperture A_2 restricted the beam so that the divergence was less than 0.005 radian. The beam was arranged to pass through the polariser and to enter the vacuum space through optically flat Kodial glass windows. These were found to be sufficiently transparent out to 2μ wavelength. After falling on the specimen film at an angle of approximately 64 degrees, the light was reflected out of the chamber, through the compensator and analyser polaroids to the photomultiplier detector. The finger which supports the specimen film is mounted on a rotatable flange to facilitate optical alignment. The saddles that support the optical components have lateral adjustment for the same purpose. The angle of incidence was measured by the method described in section 4.2.6 after every alignment.

Two different combinations of polarising filters and detectors were used for the experiments at the fixed wavelength of 549 nm, and for the measurements over a range of wavelengths in the visible and near infra-red. These will now be described.

4.1.3 Form of Ellipsometer used at 549 nm. - The Quarter Wave Plate

The method of compensation used is that due to

Winterbottom[93] and is fully described in section 2.3. The polariser and analyser consist of HN22 polaroid in graduated circular vernier scales. These were supplied by the Precision Tool and Instrument Company, and are accurate to within $\pm$ 2 minutes of angle. The quarter wave plate is part of a Senarmont compensator and is made of mica sheet, also mounted in a circular scale. Essentially, quarter wave plates can be constructed of any birefringent material for which the refractive indices for the ordinary and extraordinary rays differ. Representing these indices by n_o and n_e respectively, the phase difference between these two rays after passing through the plate will be given by

$$\delta = \frac{2\pi}{\lambda}(n_e - n_o)h$$

where h is the thickness of the plate. For an exact quarter wave plate δ equals $\frac{\pi}{2}$ and is determined solely by h. The actual thickness of mica required is only 0.00135 inches so that absolutely exact quarter wave plates are difficult to achieve. It is therefore necessary to calibrate them to ensure that the actual phase difference falls within the required limits. In the present work, calibration was carried out using the method of Jarrard.[132] Briefly, this method requires elliptically polarised light to be passed through the compensator, C and the analyser A. Extinction of the light is achieved for compensator and analyser positions represented by C_1 and A_1 respectively. Compensator and analyser are then moved, first together, and then independently to a new extinction position represented by C_2 and A_2 respectively. As shown by Jarrard, the phase difference introduced by the compensator is then given by

$$\cos\delta = \frac{\tan(A_1 - A_2)}{\tan(C_1 - C_2)}$$

The results obtained for various wavelengths are shown in Fig.31

The error imparted to the analyser setting if a non-exact quarter wave plate is used is discussed by Seward[124] who shows

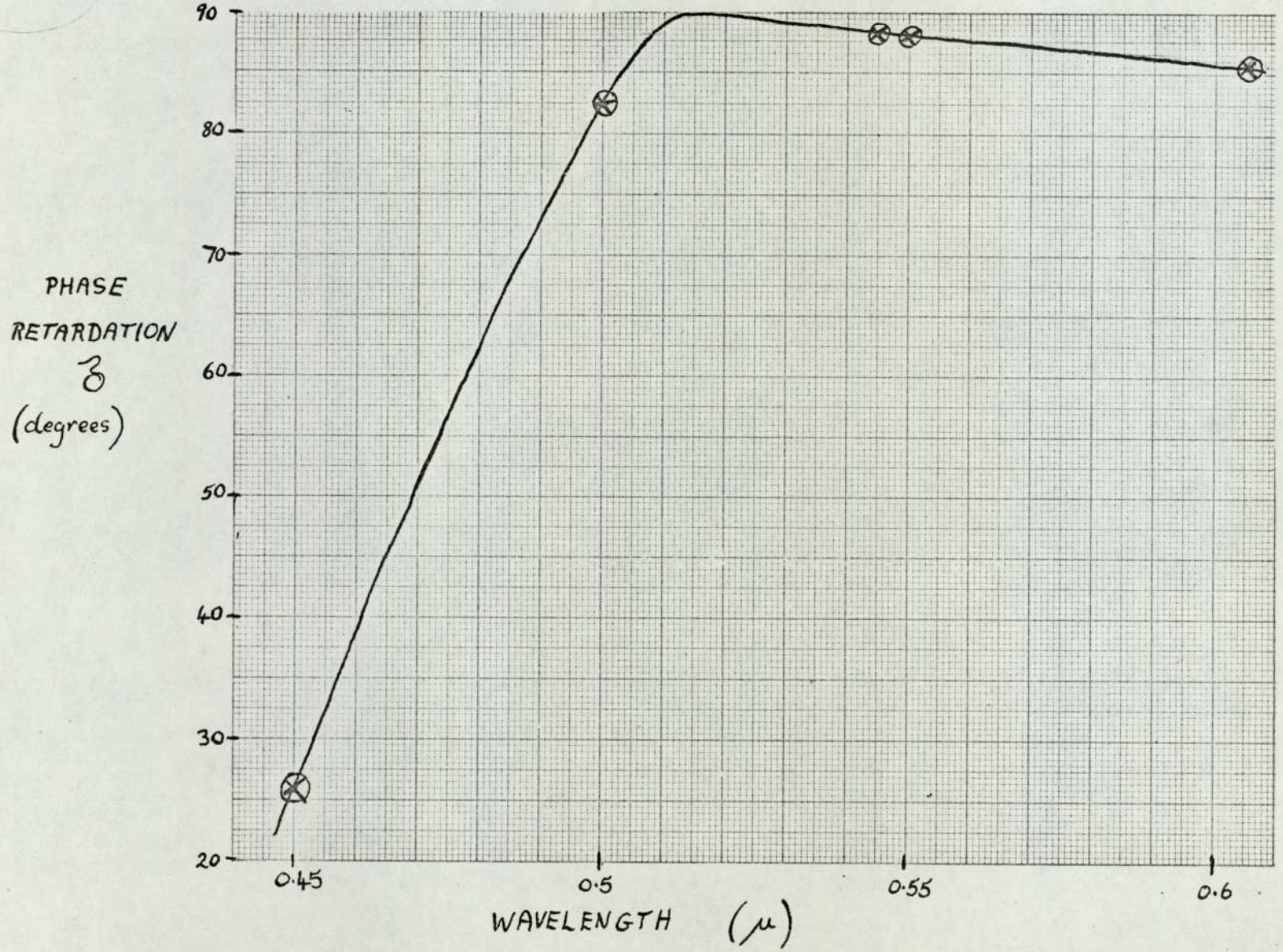
PHASE
RETARDATION
δ
(degrees)
90
80
70
60
50
40
30
20
0·45
0·5
0·55
0·6
WAVELENGTH (μ)

FIG. 31.

that if the quarter wave plate is in error by an amount ϵ (i.e. $\delta = \frac{\pi}{2} \pm \epsilon$), and if it is used to compensate an ellipticity γ, then the error in analyser setting, $d\alpha$ is given by

$$\text{Tan}\, 2d\alpha = \frac{\epsilon^2 \sin^2\gamma \cos 2\gamma}{2 - \epsilon^2 \sin^2 2\gamma}$$

For the values of ellipticity that occur in the present experiments (typically 70°) calculations show that an error of 2 degrees in the quarter wave plate would lead to an analyser error of less than 1 minute of angle. It may be concluded from Fig.31, therefore, that the quarter wave plate is acceptable over the wavelength range 505 nm to 565 nm. Accordingly, a wavelength of 549 nm was chosen for the experiments.

The detector used was a photomultiplier type 6094B, supplied by E.M.I. Electronics Ltd., and was used in conjunction with a stabilised power supply type 532/D from 'Isotope Developments' Ltd. Since the compensator method depends on the measurement of minimum light intensities, the detector does not have to be completely screened from the room lights.

4.1.4 Form of Ellipsometer used for Measurements in the near Infra-red Region

The method used is due to Beattie[112] and is fully described in section 2.4. The polaroids consisted of HR grade, oriented linear polymer material which were useful out to 2μ wavelength, as can be seen from Fig.32. The detector used was a photomultiplier by Mullard, type 150CVP which incorporated a special cathode of cesium iodide on oxidised silver. The spectral response of this cathode is shown in Fig.33, and it may be seen that there is sufficient sensitivity over the range of wavelengths covering the inter-band absorption peak in aluminium (0.7 to 1.0μ) Since the method depends on absolute intensity measurements, the detector was housed in a light-tight box with a shutter. The same stabilised power supply was used, along with the control circuit

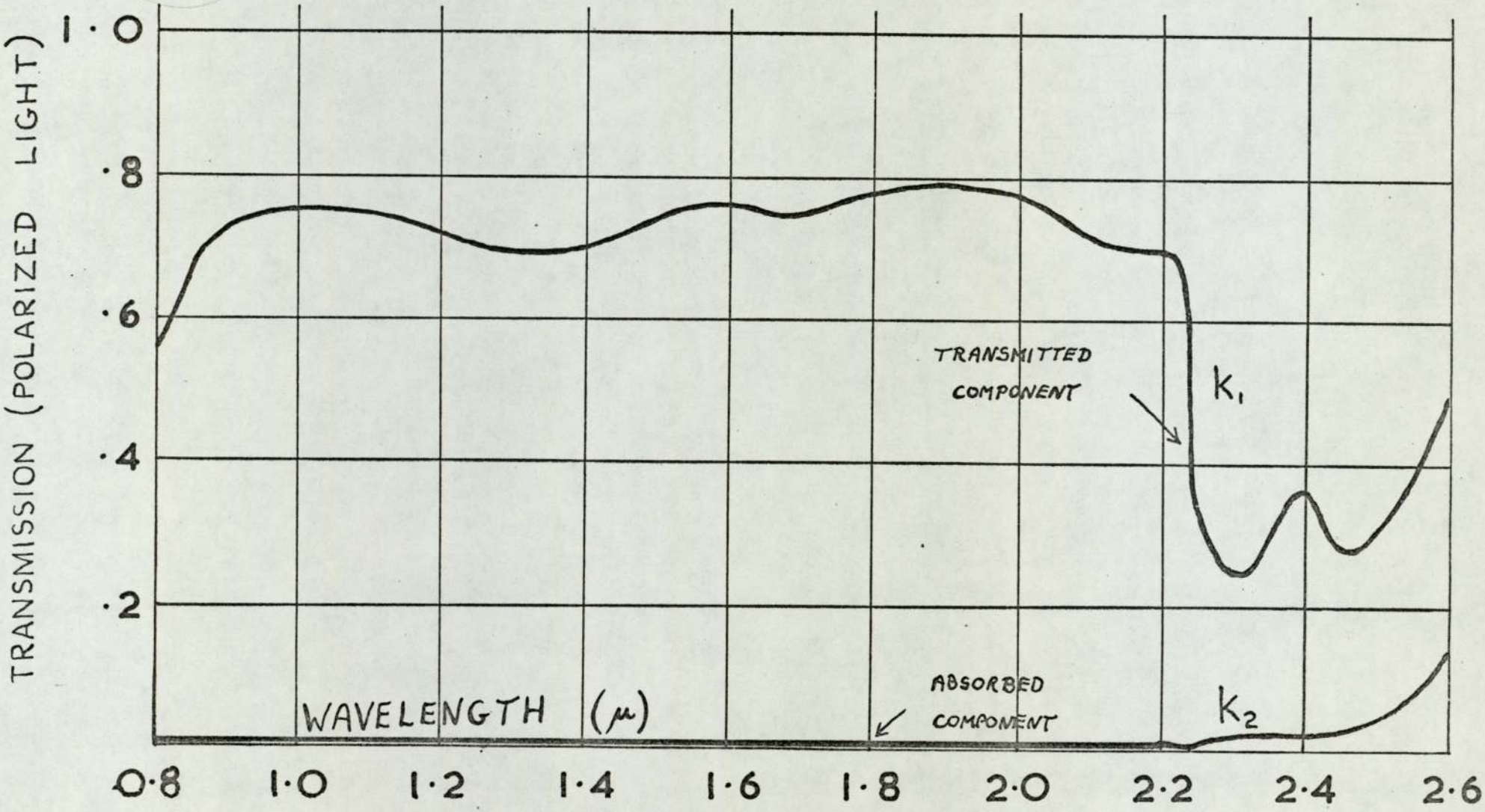

FIG. 32. SPECTRAL PROPERTIES OF HR POLAROID.

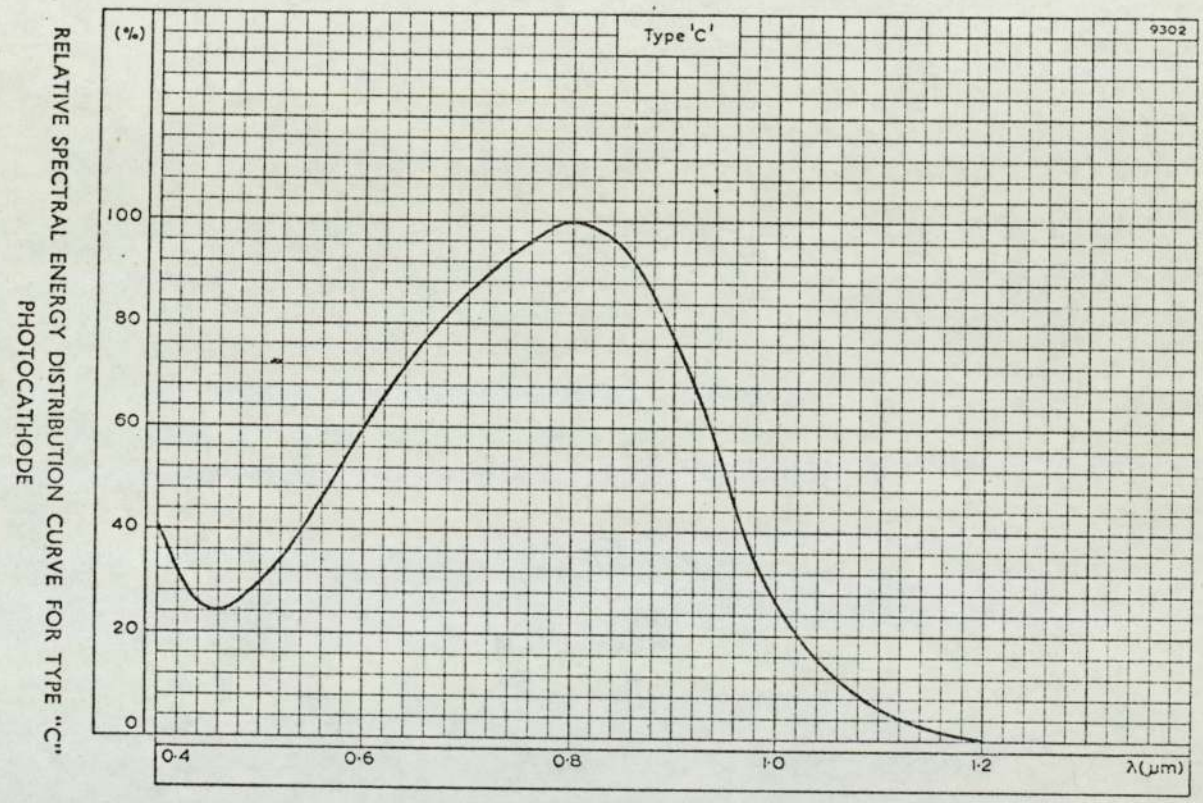

FIG. 33. SPECTRAL RESPONSE OF 150 CVP PHOTOMULTIPLIER

shown in Fig.34. According to Beattie,[112] the efficiency of the polarisers must be high. It was found that the HR polaroid used here gave acceptable efficiency (> 99%) over the spectral range 0.65μ to 2.0μ , although the intensity transmitted by a single polaroid became very small at the shorter wavelength.

4.2 Experimental Procedure

4.2.1 Substrate Preparation

All substrates were ground on the reverse side with grade 200 carborundum, in order to prevent stray reflections from the back of the substrate which had not been included in the theory. Substrate cleaning is important in this work, as the state of the substrate surface is known to affect the initial growth of the specimen. For the 0211 glass substrates the process involved standing overnight and then boiling for ten minutes in detergent solution, five successive rinses in distilled water, followed by boiling in iso-propyl alcohol. After five minutes ultrasonic cleaning, the glass was finally de-greased by withdrawal from boiling iso-propyl alcohol vapour. Contact areas for the gold wire connections were then deposited on the glass by means of an evaporation mask. It was found that a thin film of nichrome (~ 20 nm) followed by a layer of aluminium (~ 100 nm) provided a secure contact area which remained adhered to the glass throughout subsequent temperature cycling. Gold wires (0.005" diameter) were then thermally bonded on to these areas with the apparatus shown in Fig.35.

The single crystal substrates were cleaved from slabs of potassium bromide with the 100 planes parallel to the surface. This was verified using an X-ray diffractometer. The planes were visibly "stepped" and required polishing. This was carried out in successive stages by grinding first with grade 100 carborundum on a glass plate, then with grade H rouge and finally with grade O rouge on selvyt cloth. In all cases paraffin was used as a

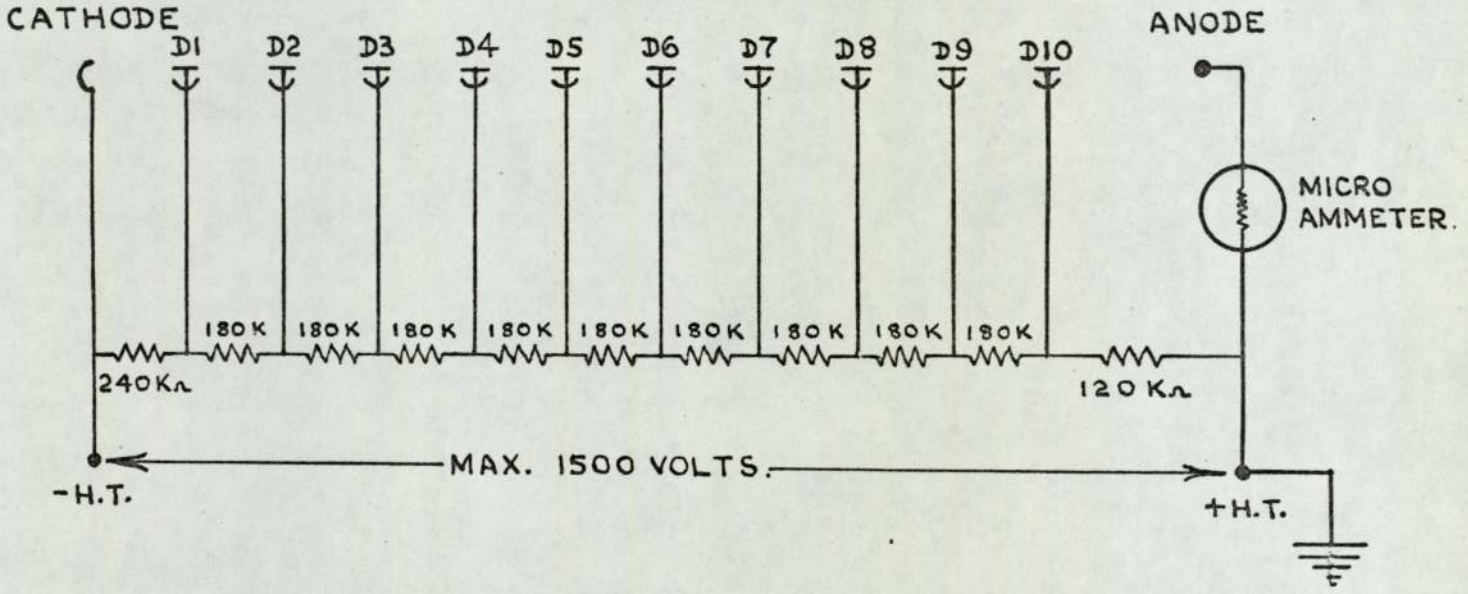

CONTROL CIRCUIT OF PHOTOMULTIPLIER (150CVP).

FIG. 34.

FIG. 35

A. Heated probe.

B. Contact areas on substrate.

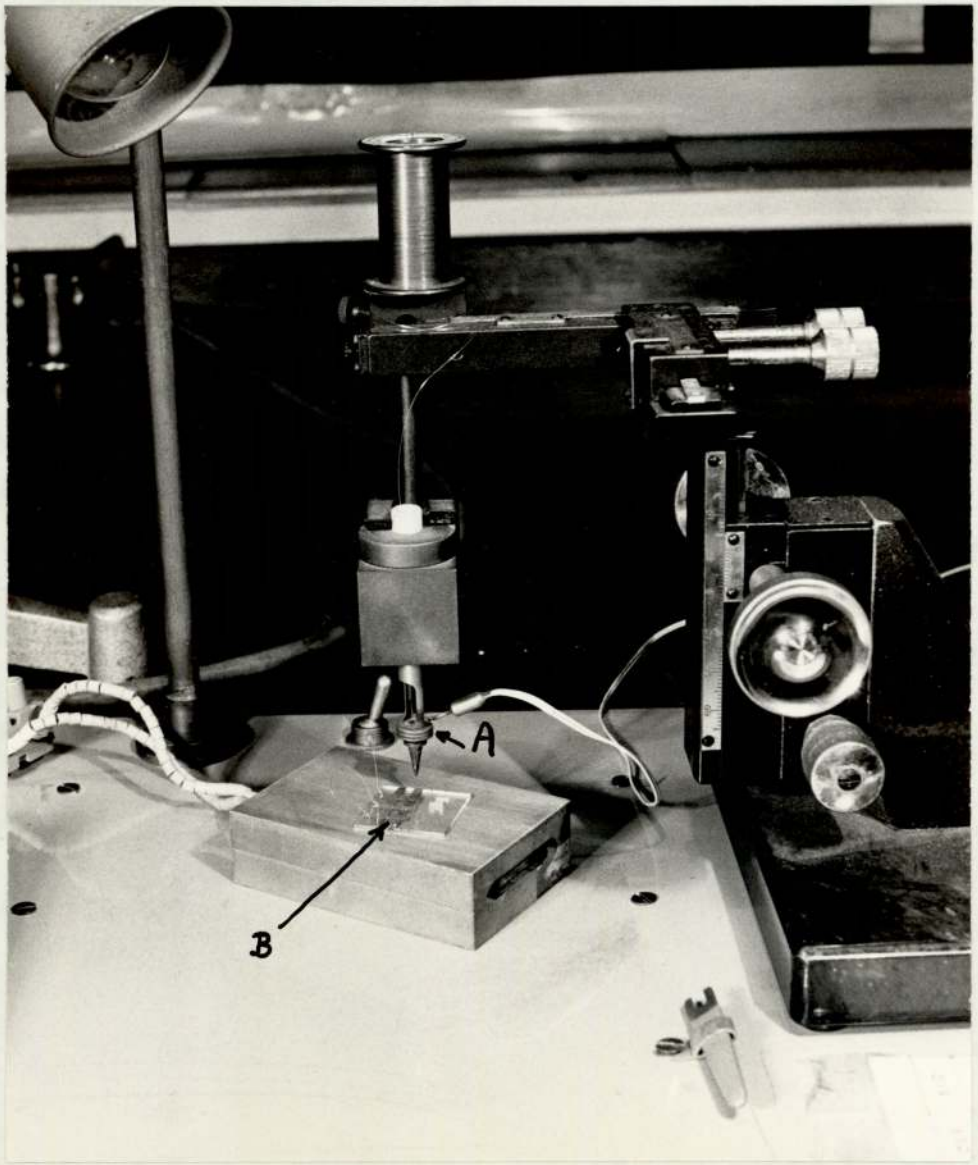

suspension agent, as suggested by Landry and Mitchell.[133] The crystal was finally washed in warm paraffin, the remaining traces of which would be removed during baking of the vacuum system. The same diameter gold wires were thermally bonded on to aluminium contact areas as before, but using only light pressure. It was found that if too great a pressure were used, the point of the probe would sink into the soft crystal and fracture the contact area.

4.2.2 Preparation of Specimen Films

The bake-out of the vacuum system consisted of at least 12 hours at 400°C, during which time the evaporation filament was kept dull red and the ionisation gauge filament on. When cooled, and with all the cold traps filled, the ultimate pressure was consistently below 2×10^{-10} torr.

The specimen of 99.999% pure aluminium was evaporated from a tungsten filament at a rate of approximately 5 nm/min in all cases. The maximum pressure during evaporation was held below 2×10^{-8} torr. The resistance of the specimen film was measured manually on a potentiometer, using the circuit shown in Fig.36. Normal precautions were taken in reversing the film current of 100 μA to avoid thermal effects.

4.2.3. Measurement of Specimen Film Thickness

Since the film thickness is an important parameter in the calculation of optical constants, each film thickness was estimated by several methods. The principal technique used was that of multiple beam interferometry, as described by Scott.[134] After removal from the ultra-high vacuum system, the specimen films were overlaid with an opaque layer of aluminium and placed under the partially silvered flat on the turntable of an interference microscope, type N.130, as supplied by Hilger and Watts. On illumination of the assembly with white light the reflected beam was seen to be deficient in a series of lines within an

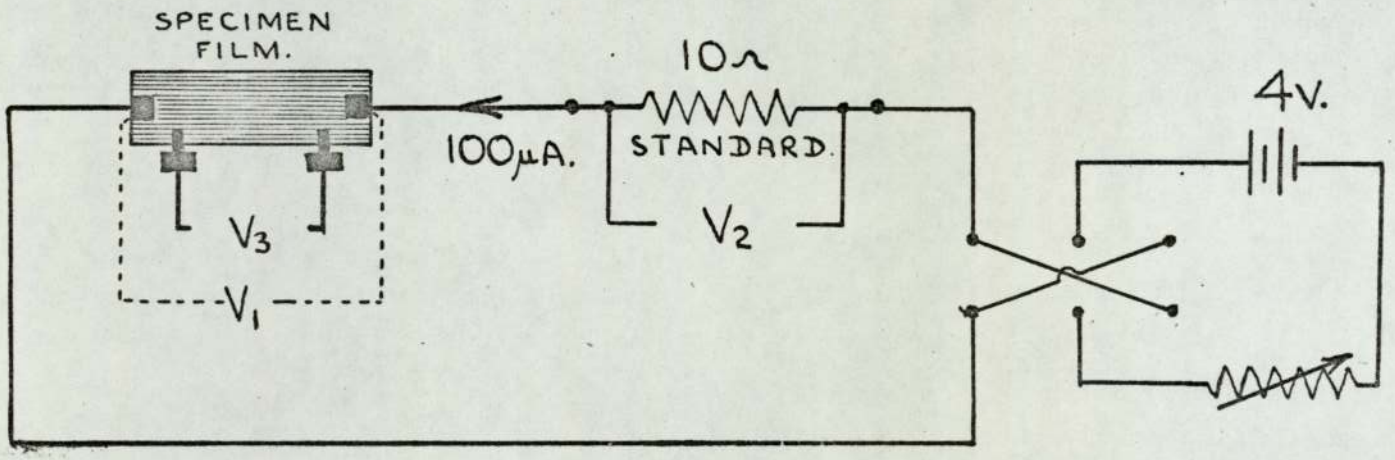

CIRCUIT FOR FILM RESISTANCE MEASUREMENT.

FIG. 36.

otherwise continuous spectrum. The fringes are now generally known as "Fringes of equal chromatic order."

Consider the overlaid specimen film under the half-silvered optical flat such that a small parallel air gap exists, as indicated in Fig.37. A frequency exists in the incident light such that m wavelengths are contained within the path length $2y_1$. Hence

$$2y_1 = m\lambda - \frac{\delta}{\pi}\lambda \tag{10}$$

where m = order of the fringe (not necessarily integral)

δ = phase change on reflection.

A shorter wavelength λ' also exists such that $(m + 1)$ wavelengths are contained in the same path length. Hence

$$2y_1 = (m+1)\lambda' - \frac{\delta}{\pi}\lambda' \tag{11}$$

The phase parameter $\frac{\delta}{\pi}$ in (10) will in general be a function of wavelength but it has been shown by Koehler[134A] for silver and by Shultz[134B] for aluminium, that the function is almost constant at 0.97 in the visible spectrum. If, therefore, $\frac{\delta}{\pi}$ is assumed to be independent of wavelength, then an integral number of wavelengths within the gap results in destructive interference and the production of a fringe. Thus

$$\left(m - \frac{\delta}{\pi}\right) = \frac{\lambda'}{\lambda - \lambda'} \tag{12}$$

In the region y_2, of slightly different path length to y_1, there exists a different wavelength, λ_1 such that a fringe of the same order m is produced. Hence

$$2y_2 = m\lambda_1 - \frac{\delta}{\pi}\lambda_1 \tag{13}$$

The thickness of the specimen film, t, is then given from (13) and (10)

$$t = y_2 - y_1 = \tfrac{1}{2}\left(m - \tfrac{\delta}{\pi}\right)(\lambda_1 - \lambda)$$

$$t = \left(m - \tfrac{\delta}{\pi}\right)\frac{\Delta\lambda}{2} \tag{14}$$

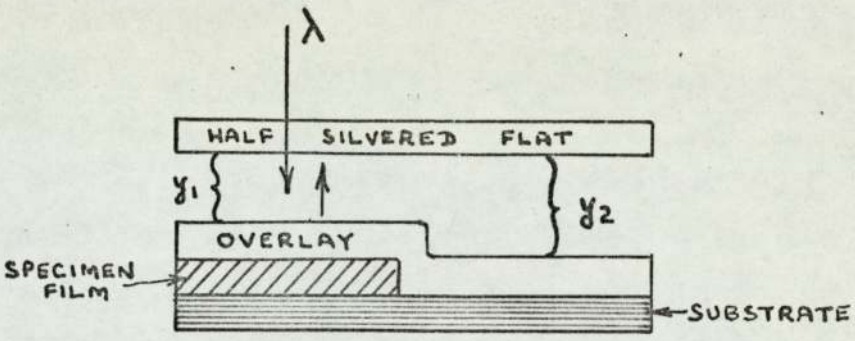

FIG. 37.

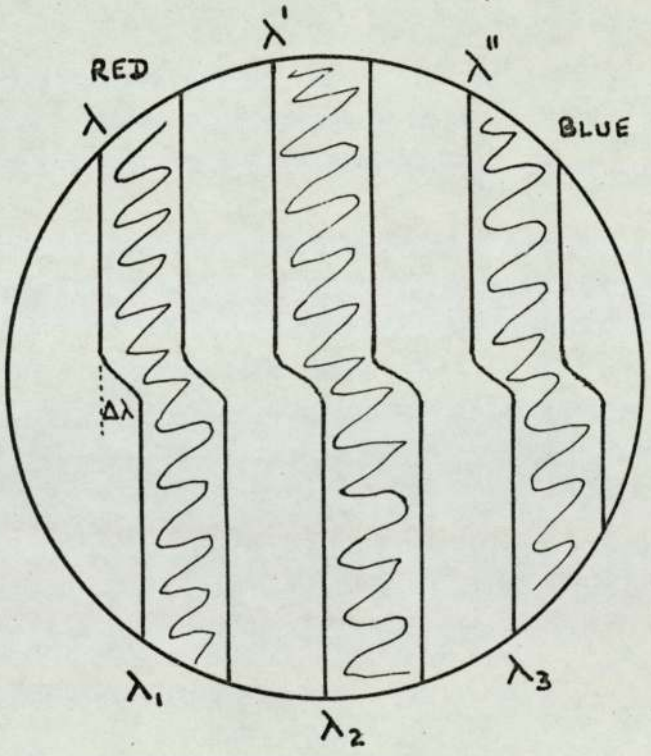

FRINGES OF EQUAL CHROMATIC ORDER

FIG. 38.

The field of view in the spectrometer is therefore a continuous spectrum with a series of stepped fringes superimposed as shown in Fig.38.

From measurements of the wavelengths λ^{i}, the order for a number of fringes was obtained, which should increase as consecutive intergers towards the violet end of the spectrum. Measurements of λ_i were also made which yielded $\Delta\lambda$ and hence the film thickness.

The less exact theory in which the phase change on reflection is neglected is adequate for thick specimens where large orders can be used, but for thinner films where smaller orders must be employed, the error introduced becomes greater. For example, at $m = 8$ the error is only 0.5%, whereas at $m = 1$ the error would become 3%.[134A][134B]

In addition to thickness measurement by the above technique, several independent estimates of thickness were made both during and after deposition by the following methods:

i) Quartz crystal thickness monitor.

ii) Photographic densitometer to measure the amount of light transmitted by the films according to the method of Murr.[135]

iii) Electrical resistivity.

iv) Changes of ellipsometer parameters Ψ and Δ on total final oxidation of the films.

v) Mechanical measurements using a 'talystep' instrument.

Where appropriate, a correction was applied for the thickness of the oxide layer present. When all these methods gave consistent results, the film thickness was finalised and computations for n and k performed on an ICL 1905 computer. The programs used are based on the exact ellipsometer theory and are described fully in Appendix 2.

4.2.4 Determination of reference azimuths

The readings on the divided circles of the polariser and analyser that correspond to the transmission axes of the polaroids being parallel and perpendicular to the plane of incidence are known as the reference azimuths. In the two methods of ellipsometry undertaken, both the compensator method used at 549 nm and the method of Beattie used in the near infra-red, the experimental azimuths are expressed relative to the plane of incidence. It is therefore necessary to determine the reference azimuths very accurately. Assuming that the ellipsometer is aligned, approximate values are quickly obtained by removing each polaroid in turn from the ellipsometer and arranging for light from a lamp to be reflected at approximately 56 degrees from a glass plate, placed flat on a bench, and to pass through the polaroid. Each polaroid in turn is rotated until minimum light is visible through the polaroid. As shown in Fig.39, the transmission axis is then approximately vertical. On returning the polaroids to the ellipsometer, on which the plane of incidence is approximately horizontal, the transmission axes are therefore set roughly perpendicular to the plane of incidence. The settings need not be accurate, as more precise settings are found later. The process so far merely serves to distinguish between horizontal and vertical polarisation directions.

The compensator is next removed from the ellipsometer, and with the light being reflected from a metal surface, the following procedure is adopted for both N22 and HR polaroids.

The polariser is rotated through 90 degrees so that the transmission axis is horizontal (i.e. parallel to the plane of incidence). The analyser is allowed to remain with its transmission axis perpendicular to the plane of incidence. With a small voltage applied to the photomultiplier, a slight adjustment of polariser and then analyser serves to reduce the signal to a minimum. The process is repeated, with the voltage steadily increasing, until with the full

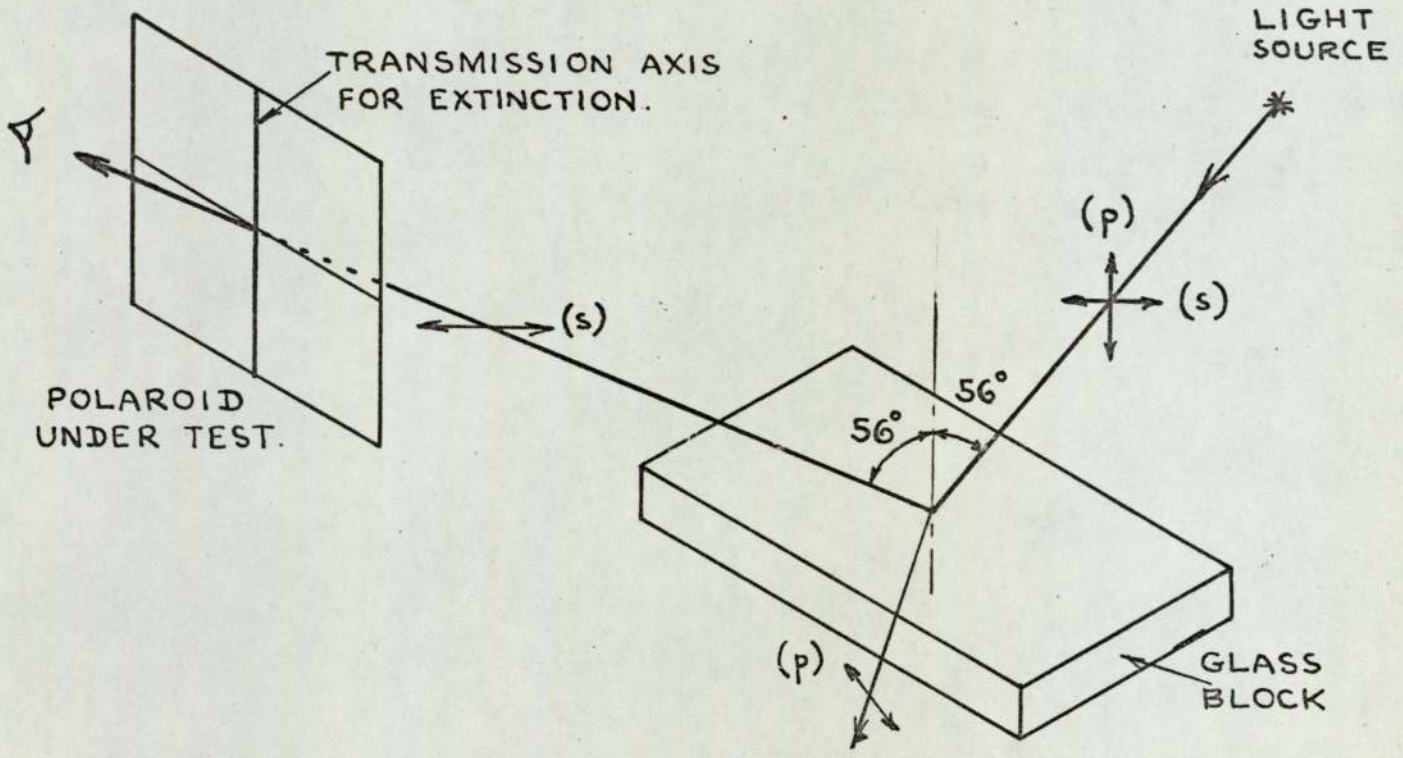

DETERMINATION OF REFERENCE AZIMUTHS (APPROXIMATE)

FIG. 39.

allowed value of 1500 volts, minimum light is detected.

The exact polarizer azimuth for extinction is obtained by measuring the azimuths at equal intensities on each side of the minimum. The extinction position is the average of the two values. With the polariser set at its extinction position the analyser extinction position is obtained by the same method of measuring the analyser azimuths giving equal intensities on either side of the minimum.

It can be shown that the intensity of light received by the photomultiplier, as a function of the polariser azimuth, is symmetrical about its extinction position for any analyser setting; and also if the polariser is set to its extinction position, the intensity as a function of analyser setting is symmetrical about the analyser extinction position. These conditions are necessary and sufficient to establish the procedure. The direct method of setting the polariser and analyser to give minimum transmission is less precise. Rotation of 5 to 10 degrees is sufficient to attain the greatest accuracy.

Polariser and analyser azimuths now correspond to π_p and α_s respectively in the author's notation. Both polariser and analyser are then rotated through 90^o in a positive sense (i.e. anti-clockwise looking towards the on-coming light) and the entire procedure repeated. These alternative positions correspond to azimuths π_s and α_p and would be 90^o exactly from the first positions for correctly aligned apparatus.

The theoretical basis of the above method is that only in these two select positions, when the light incident on the metal is plane polarised in either the (p) or (s) directions, is the reflected light plane polarised and capable of being extinguished by the analyser. For other polariser positions, the reflected light is elliptically polarised and cannot be extinguished by the analyser. There are, of course, non-significant positions at 180 degrees to each scale reading and these are represented by the dash ($'$) in the author's notation in Fig. 18.

To obtain a reference position for the compensator (when used) the polariser and analyser are set to a pair of related reference positions and the compensator returned to the ellipsometer in the position shown in Fig.25. By rotation of the compensator, a position of minimum transmitted light is obtained. The exact compensator reference position is then obtained by measuring compensator azimuths giving equal intensities on either side of the minimum. This position corresponds to either the fast or slow axis of the compensator being parallel to the plane of incidence, because, once again, it is only when the light incident on the compensator is plane polarised in a direction parallel to either the fast or slow axis that plane polarised light emerges through the compensator, enabling the analyser to produce extinction. The procedure is repeated for the alternative compensator position which is 90 degrees from the first position for correctly aligned apparatus. Once again, there are non-significant positions at 180 degrees to both the above positions.

4.2.5 Procedure for determination of Ψ and Δ for a specimen at 549 nm using the Compensator Method

The essential basis of the method, as explained in section 2.2, is that the azimuth of the plane polarised light incident on the specimen is arranged so that the reflected light has equal components in the (p) and (s) directions. (i.e. The reflected amplitude ratio $\frac{E_p}{E_s} = 1.0$.) Because of the phase difference, Δ between these components, the reflected light will always be elliptically polarised with its major axis at 45 degrees to the plane of incidence, and have an ellipticity that depends on Δ. If the compensator is set with its axes at 45 degrees to a reference position, this ensures that the axes of the compensator coincide with the axes of the reflected ellipse. Light of any ellipticity is then compensated i.e. converted to plane polarised light having an azimuth that depends on the ellipticity, and hence on Δ. This is shown in

Fig.16. The procedure, then, is as follows:

The compensator is locked at 45 degrees to a reference position. As before, the polariser and analyser are successively turned to give minimum light intensity, while gradually increasing the photomultiplier voltage. The polariser extinction position, say P_1, is then found by "bracketing" the minimum position. With the polariser then set at its extinction position, the analyser extinction position, say A_1, is likewise found by "bracketing". The setting procedure is repeated for a polariser azimuth in another quadrant, but not 180 degrees away, giving readings P_2 and A_2 on polariser and analyser respectively. Two other polariser positions, P_3 and P_4, together with their corresponding analyser positions A_3 and A_4, are also measured. It is found that P_3 and P_4 are at approximately 180 degrees to P_1 and P_2 respectively. A_3 and A_4 are also at 180 degrees to A_1 and A_2 respectively.

The compensator is then turned through 90 degrees so that the fast axis azimuth is -45 degrees, with respect to the plane of incidence, and four different pairs of polariser and analyser settings obtained in the same way. As explained in section 2.2, time did not allow for measurements to be made in all four zones during some of the experiments. In this case, only those pairs of results designated 1 and 2, were recorded for each compensator setting.

Consider the polariser readings:

It has been shown in section 2.3 that P_1 and P_2 are symmetrically placed about π_p. In general, the polariser settings are symmetrically placed about the plane of incidence. $P_1 - \pi_p$ should equal $\pi_p - P_2$. In general, the average is taken

$$\frac{(P_1 - \pi_p) + (\pi_p - P_2)}{2} = \Psi$$

As shown in section 2.3, using the Poincaré sphere, $\tan\Psi$ equals the relative amplitude reduction between the (p) and (s) components produced by reflection from the specimen.

Consider the analyser readings:

As shown in section 2.3, using the Poincaré sphere, A_1 and A_2 are always separated by approximately 90 degrees. $\alpha_s - A_1$ should equal $\alpha_p - A_2$. In general the average is taken

$$\frac{(\alpha_s - A_1) + (\alpha_p - A_2)}{2} = x$$

where the angle 2x - 90 degrees gives the relative phase retardation, Δ between the (p) and (s) components.

4.2.6 Procedure for determination of Ψ and Δ for a specimen in the near infra-red region, using Beattie's Method.

As explained in section 2.4, the absolute intensity of the light beam transmitted by the system of polariser - specimen - analyser is measured for eight pairs of settings of polariser and analyser. These correspond to the intensity I for polariser azimuth ψ_p and analyser azimuth ψ_A , written as $I(\psi_p, \psi_A)$, for the following values

$$I_1 = I\left(+\tfrac{\pi}{4}, +\tfrac{\pi}{2}\right) \quad ; \quad I_2 = I\left(+\tfrac{\pi}{4}, 0\right)$$

$$I_3 = I\left(+\tfrac{\pi}{4}, +\tfrac{\pi}{4}\right) \quad ; \quad I_4 = I\left(+\tfrac{\pi}{4}, -\tfrac{\pi}{4}\right)$$

Four equivalent values are also measured for which the polaroid azimuths are all made negative. In general, $I(+\psi_p, +\psi_A) = I(-\psi_p, -\psi_A)$ and this serves as a check on the setting of the azimuths. The circular scale readings for all these azimuths are first calculated from the reference azimuths and tabulated. Rapid changes from one setting to the next are then possible during the experiments so that the eight measurements can normally be made in approximately 3 minutes. Since absolute intensity measurements areinvolved, the output of the lamp must not vary significantly in this time. The lamp is therefore switched on and allowed to reach an equilibrium (usually ten minutes) before measurements were commenced.

Possible errors due to background illumination were avoided

by covering the ellipsometer pin-hole with a metal foil and setting the zero of the photomultiplier detector with its shutter open. The foil was then quickly removed and the intensity reading taken.

After averaging the values of I(+) and I(-), the parameters Ψ and Δ are then calculated, as explained in section 2.4, from the formulae:

$$\text{Tan}\,\Psi = \sqrt{\frac{I_2}{I_1}} = \rho$$

$$\text{Cos}\,\Delta = \tfrac{1}{2}\left(\frac{1}{\rho} + \rho\right)\left(\frac{I_3 - I_4}{I_3 + I_4}\right)$$

Once the parameters Ψ and Δ have been determined, either by the above method or by that described in the previous section, the experimental values are compared with theoretical values calculated for the approximately known values of optical constants. The computer programs used for this purpose are described fully in Appendix 2. The procedure for the determination of the final values of n and k, which the author has found most convenient, is indicated in Figs.39A and 39B. Graphs of Ψ and Δ are plotted against n for various values of k. The measured values of Ψ and Δ for the specimen are then drawn as horizontal lines on these graphs. For example, the experimental value of Ψ on Fig.39A is 33.65 degrees and of Δ on Fig.39B is 134 degrees. By placing two straight-edges on the graphs for the same value of k, e.g. 4.75, the corresponding values of n, given by the intercept with the horizontal line, are seen to differ, being 1.035 on Fig.39A and 0.82 on Fig.39B. By reducing the value of k and moving both straight-edges together, the values of n at the intercept become closer, until they coincide when n becomes 0.90. The k value at this point is 4.65 on both graphs. Thus the optical constants for the specimen in this example are n = 0.90 and k = 4.65.

4.2.7 Determination of Angle of Incidence

The angle of incidence is determined after each alignment of

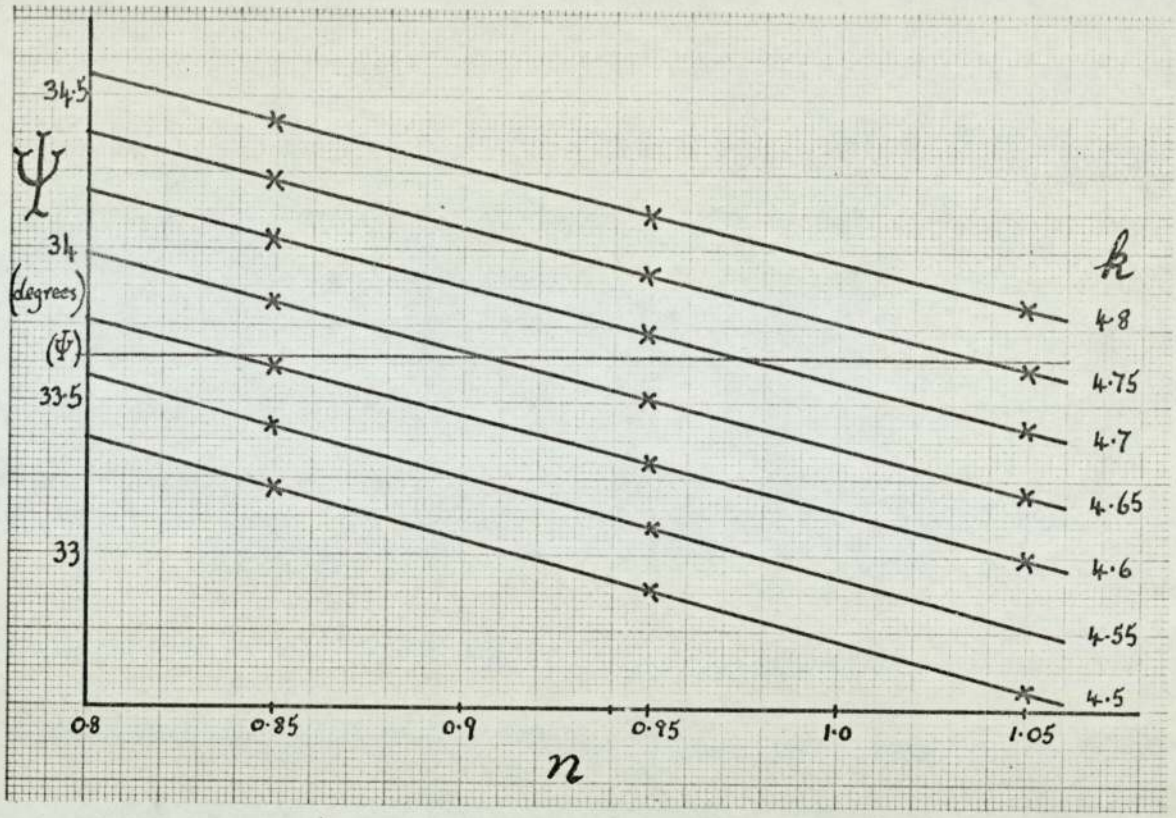

FIG 39A

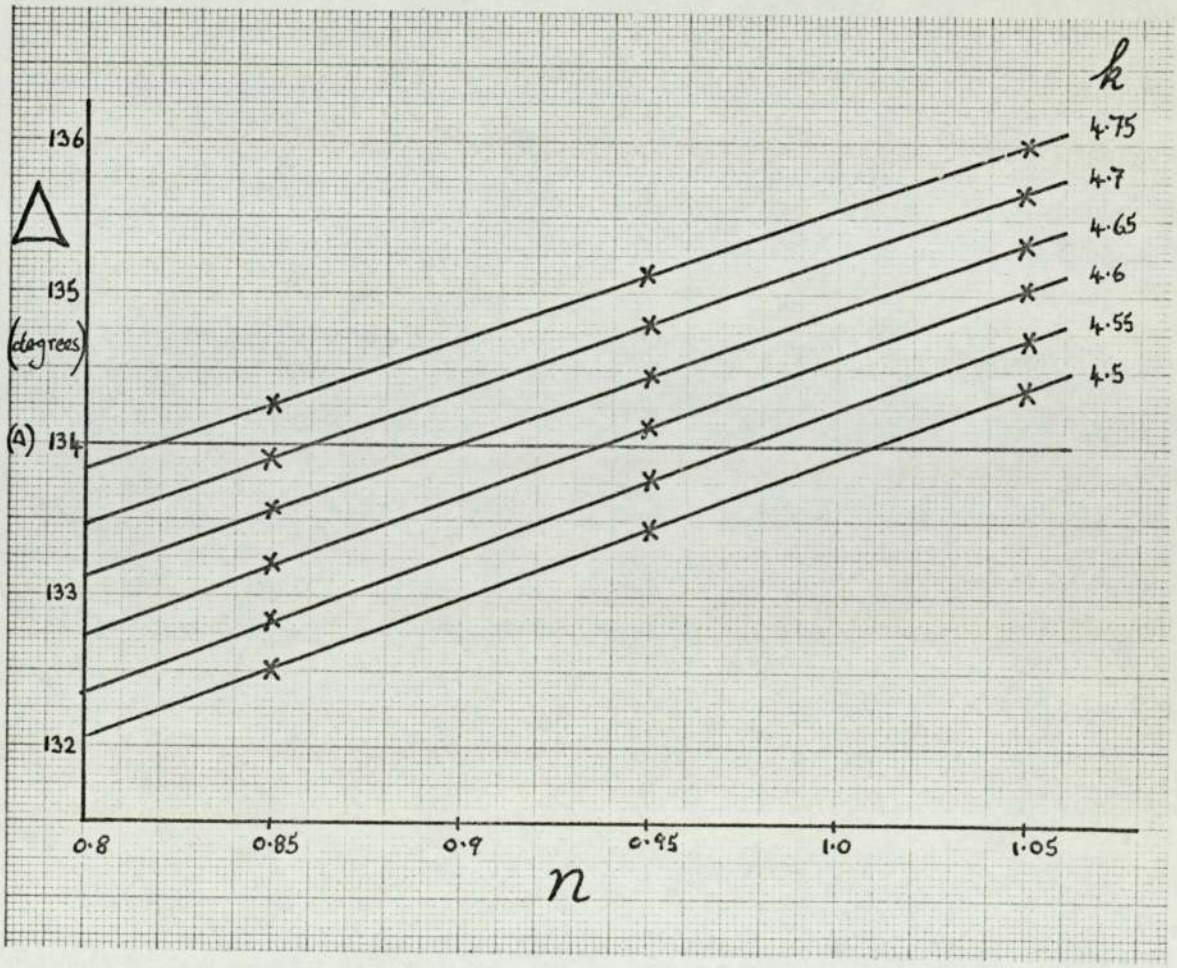

FIG 39B

CALCULATED PARAMETERS FOR 12·5 nm FILM THICKNESS

the ellipsometer by removing the detector and replacing it with a small telescope. Four saddles, each holding a sharp pointed spike were positioned on the ellipsometer benches, as shown in Fig.40. The saddles were adjusted so that their points were all in line with the illuminated pin hole as seen through the telescope.

The distances between the points were measured as accurately as possible and the angle of incidence, ϕ , calculated by simple trigonometry. The possible error in ϕ , thus determined, is estimated as $\pm$ 20 minutes of angle.

4.2.8 Sources of error

Errors due to mis-alignment can be largely eliminated by careful adjustment of the apparatus before measurement commences. Further possible errors due to incorrect reference azimuths or incorrect setting of the polaroids may be minimised by taking the mean values of measurements in different quadrants.

The kodial glass windows, through which the light enters and leaves the vacuum chamber, are strained by the atmospheric pressure on one side of them,and could possibly affect the state of polarisation of the transmitted light. Accordingly, at the end of each experiment, when the chamber has been opened for several days and a stable oxide film formed on the specimen, two sets of measurements were taken. The first set was taken with the undisturbed windows in position and a high vacuum inside the chamber; the second set was taken at atmospheric pressure with both windows removed. Any difference in the observed parameters Ψ and Δ between the two sets is attributed to the effects of the windows, and appropriate adjustments are made to all previous measurements for the same specimen. The correction to Ψ is usually less than 1 degree and for Δ is invariably less than 2 degrees.

Probably the most serious source of error is multiple reflections from the components of the optical system. These produce a number of beams of decreasing intensity and of different

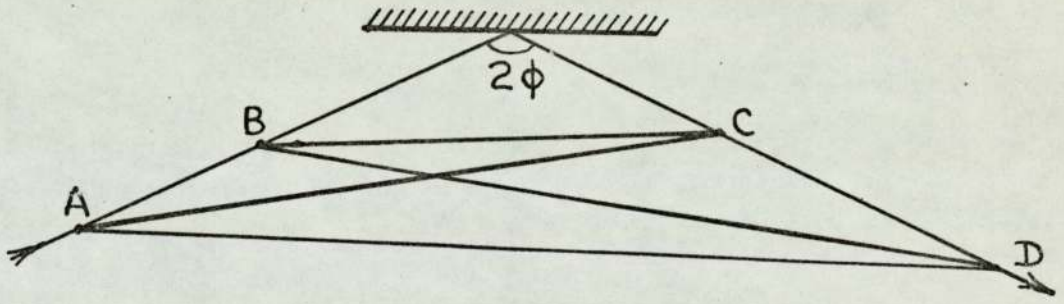

MEASUREMENT OF ANGLE OF INCIDENCE.

FIG. 40.

states of polarisation which influence the settings of both polariser and analyser. Errors introduced by this effect cannot be eliminated by any manipulation of the readings. Winterbottom[93] has shown that errors of as much as 1 degree in Ψ and $\frac{1}{2}$ degree in Δ can arise from this source. Uncertainty in the value of film thickness, especially for thinner films, and also in smoothness of the surfaces, means that the total error in the absolute values of n and k may be as high as 10% in some cases. However, the most important sources of error are likely to remain constant during an experiment so that the changes of n and k, with which the present work is chiefly concerned, are probably of greater reliability, estimated at 1-2%.

CHAPTER 5

RESULTS AND DISCUSSION FOR 549 nm.

5.1 Anneal from 77°K. Electrical Measurements

The variation of resistance of a typical film (film 2) with temperature is shown in Fig.41. During the initial warm-up from the deposition temperature of 77°K to room temperature (Stage III anneal) there is a fall of resistance amounting to about 40% of the initial value. Thicker films (e.g. film 3) show the same effect but the proportional change is less, as can be seen in Fig.42. Around room temperature there is a resistance minimum, followed by an approximately linear rise with temperature as in normal metallic behaviour. Returning the specimen to 77°K shows that irreversible changes have taken place.

At this stage the temperature coefficients of resistivity for film 2 and for the thicker film 3 were 0.0015 per °C and 0.0012 per °C respectively. The values of resistivity at 0°C were 12.1 $\mu\Omega$.cm and 12.7 $\mu\Omega$.cm respectively. These may be compared with bulk aluminium for which the temperature coefficient of resistivity is 0.0045 per °C and the resistivity at 0°C is 2.45 $\mu\Omega$cm.

A detailed examination of the stage III anneal has been made for a number of films. The determination of δR, the resistance attributable to the annealing of defects, was obtained by subtracting the post-anneal value of resistance at each temperature as is illustrated in Fig.43. Semi-logarithmic plots of δR against $\frac{1}{T}$ are shown in Fig.44 and are compared with the published results of Buckel and Hilsch[68] for a 20 nm film. The straight lines obtained indicate an annealing process with a single activation energy, as confirmed by Lidiard.[83]

Further experiments were performed to carry out a "ratio of slopes" analysis to determine this activation energy. As explained fully in Appendix 1, it is required to measure the rate of fall of

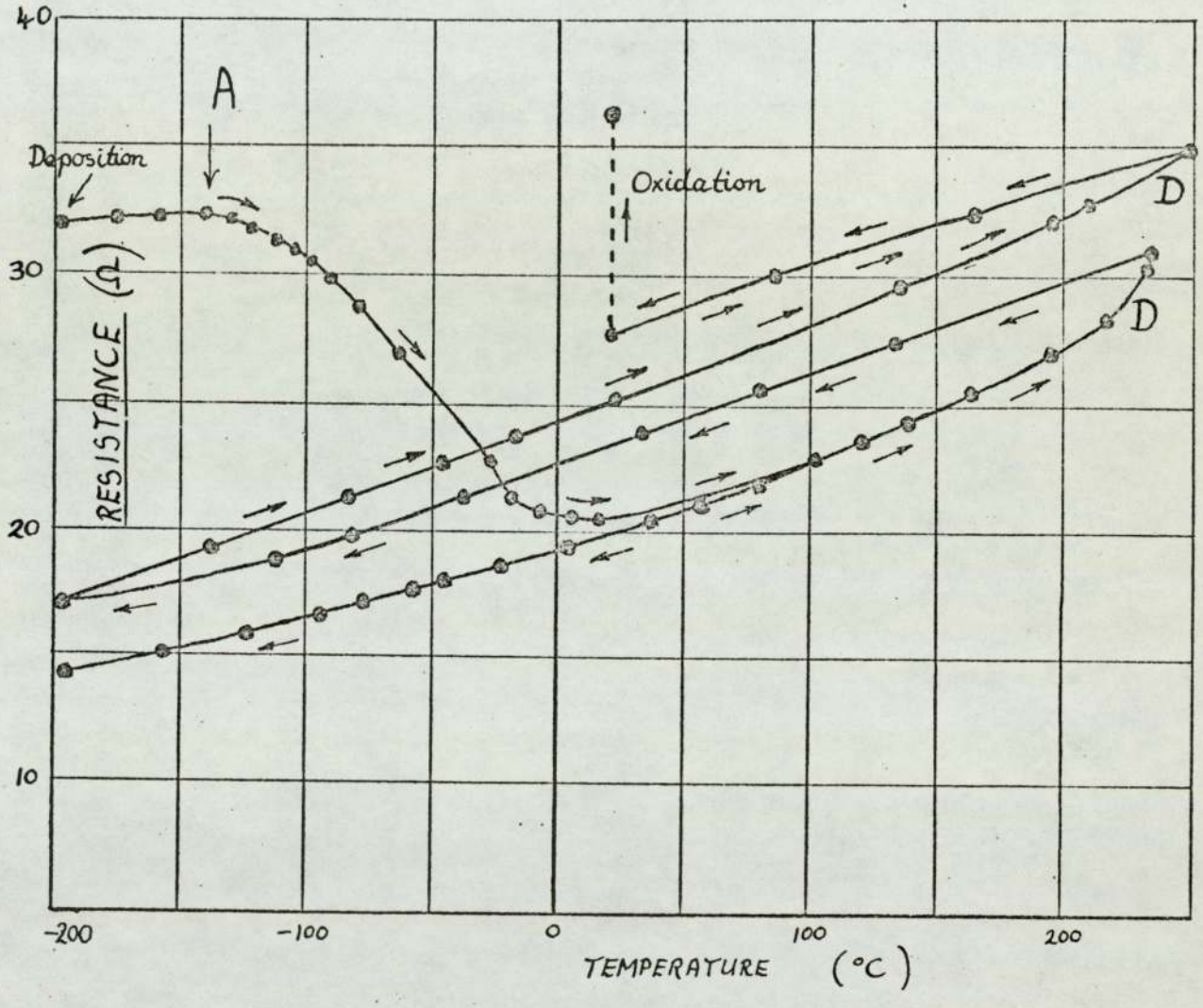
40
30
20
10
A
Deposition
Oxidation
D
D
RESISTANCE (Ω)
-200
-100
0
100
200
TEMPERATURE (°C)

FIG. 41

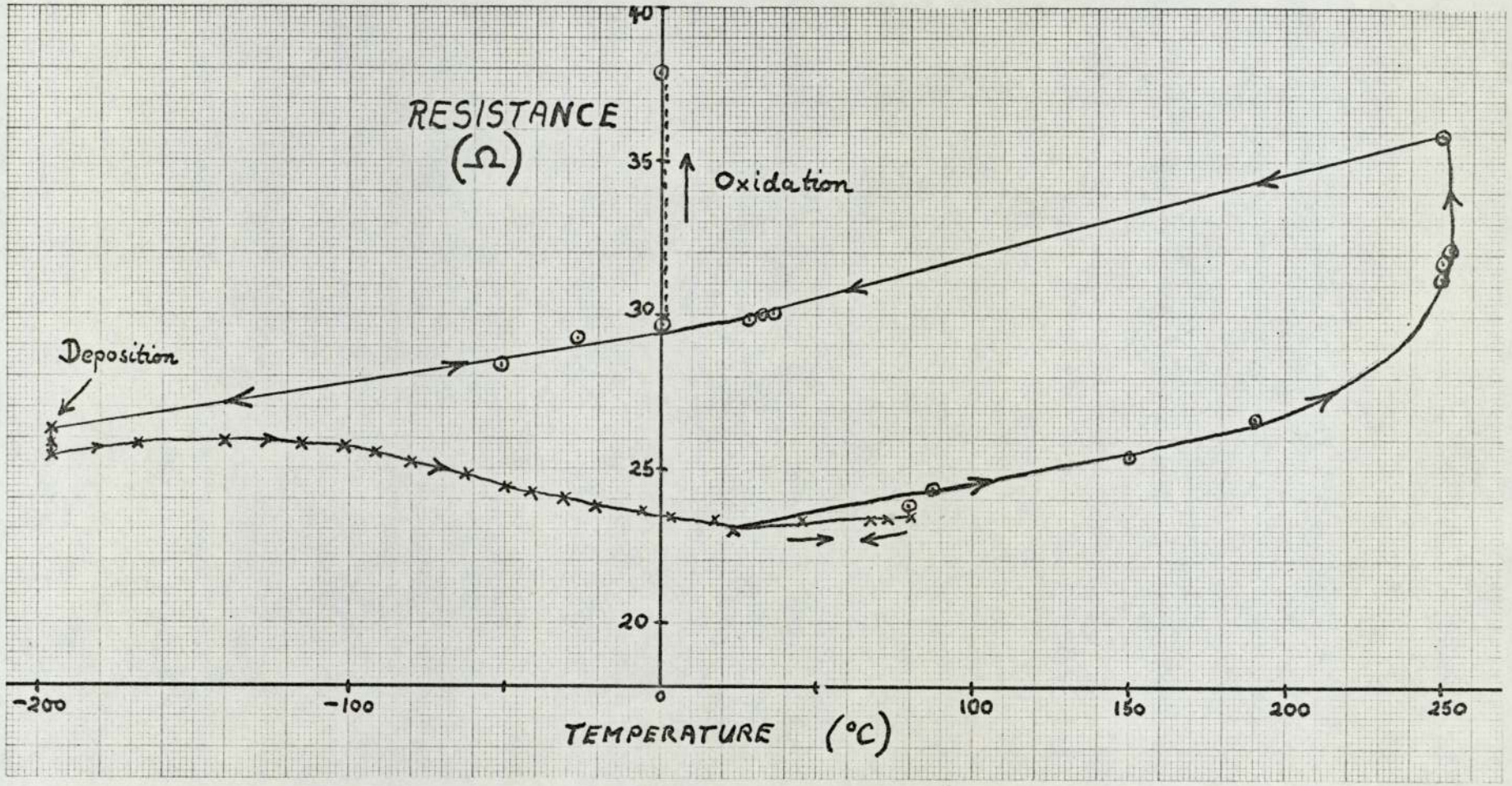

FIG. 42. RESISTANCE VARIATION for Film 3.

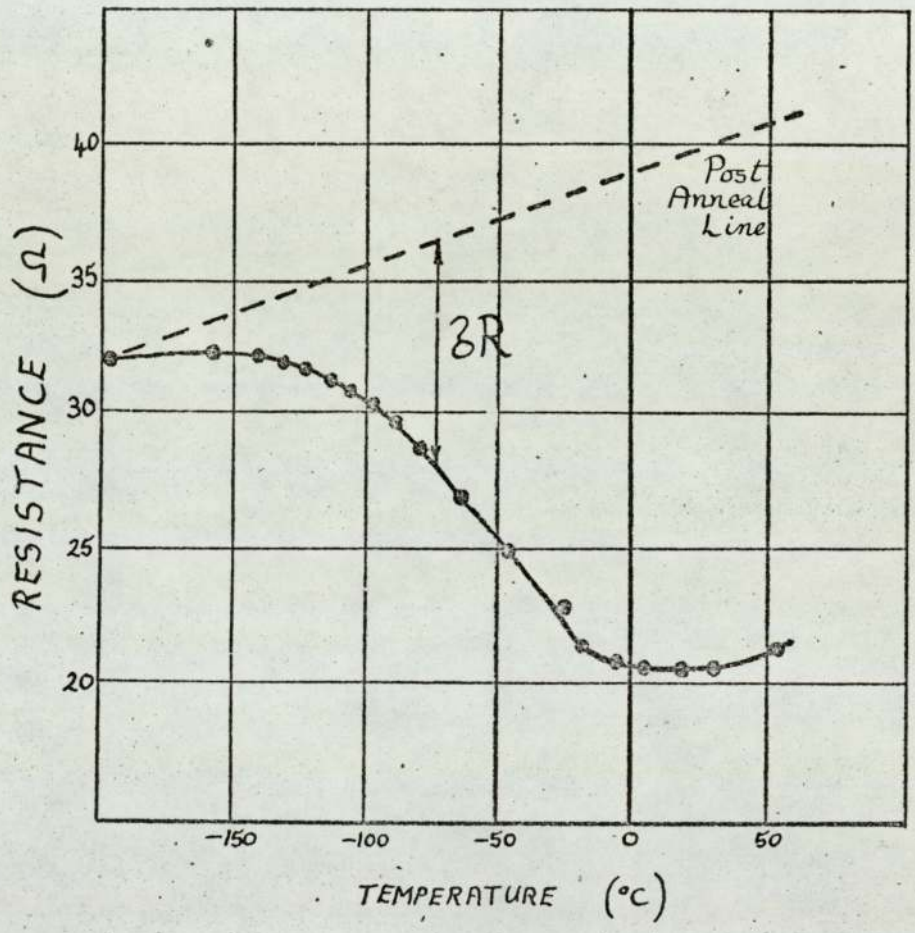
RESISTANCE (Ω)
40
35
30
25
20
Post Anneal Line
δR
−150
−100
−50
0
50
TEMPERATURE (°C)

FIG. 43

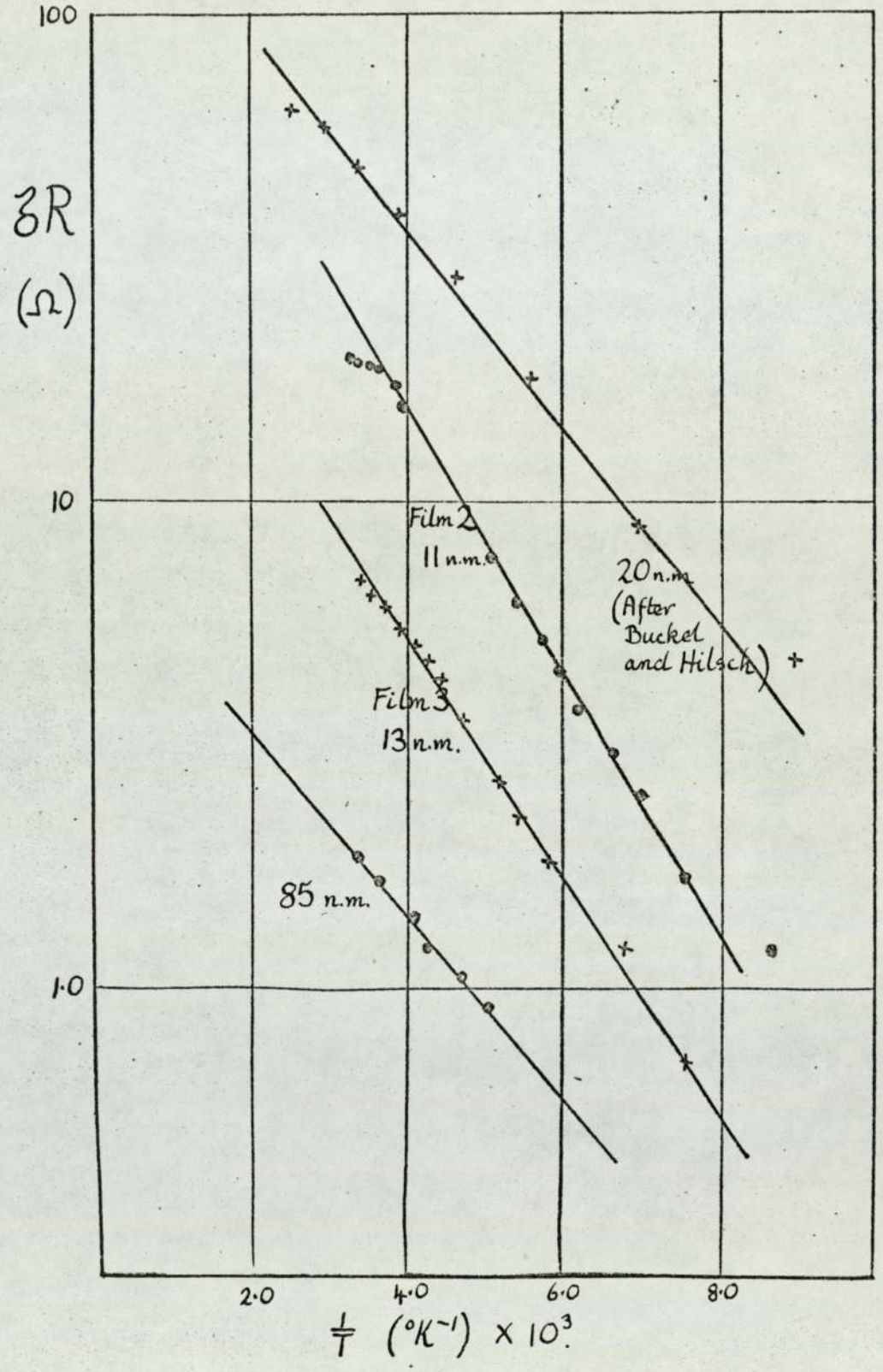

FIG. 44.

VARIATION of ℛR against $\frac{1}{T}$ for VARIOUS FILM THICKNESSES

resistance with time at two fixed temperatures T_1 and T_2 which should be close together. The ratio of these slopes just before and just after the change lead to the activation energy u, defined by the equation:

$$\frac{\left[\frac{d(\Delta R)}{dt}\right]_{At\ T_1}}{\left[\frac{d(\Delta R)}{dt}\right]_{At\ T_2}} = \exp.\left[\frac{u}{k}\left(\frac{1}{T_1}-\frac{1}{T_2}\right)\right]$$

Fig.45 is typical of several films investigated, the mean activation energy of which was found to be 0.20 ± 0.05 eV. This value is rather lower than expected, and will be discussed later.

The results obtained above show marked similarity with those of Ceresawa[136] in which cold working of bulk aluminium at 77°K produced defects which annealed out between -100°C and 0°C with an activation energy of 0.5 eV. These defects he proposed to be single vacancies. On the other hand, Neugebaur[137] shows by means of electron microscopy that the fall of resistance in quenched metal films on warming, is caused by grain growth. Andrews[138] has estimated the specific grain boundary resistivity in pure aluminium as $2.45 \times 10^{-12}\ \Omega\ cm^2$ and on this basis, the magnitudes of resistance fall for the films considered is quite consistent with the reduction of grain boundary area as the crystal grains grow from a deposition value of around 0.4 nm to a size of the order of the film thickness, 11 nm.

It is relevant here to consider the actual mechanism of grain growth as envisaged by Gleiter.[139] The grain boundaries contain large numbers of trapped vacancies and the migration of atoms from a shrinking grain to a growing grain could be equally well thought of as the migration of vacancies in the opposite direction. Hence the migration of single or multiple vacancies, previously trapped on grain boundaries, would appear a reasonable explanation for the fall

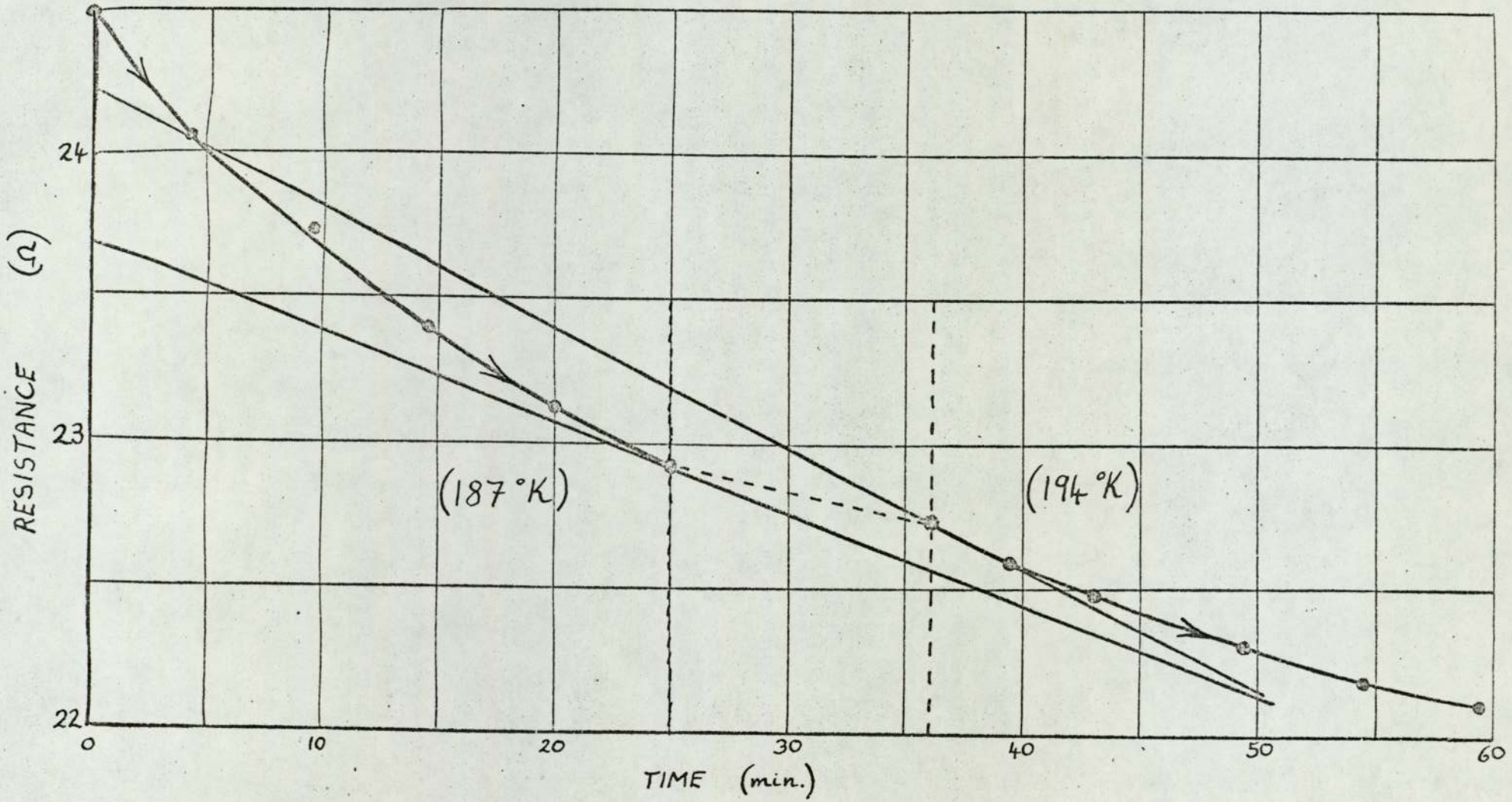

Determination of Activation Energy for Film 12.

FIG. 45.

of resistance on warming a vapour quenched film. However, there are two objections to this. The first is that the observed value of activation energy is too low by a factor of three, compared to accepted values for vacancy migration obtained from radiation damage and from quenching experiments. For example, de Sorbo and Turnbull[140] and also Frederighi[141] agree on a value of 0.63 ± 0.05 eV for vacancy migration in aluminium. The second objection is that vacancy migration alone would lead to first order reaction kinetics (see Appendix 1), whereas, when the recovery of resistivity is analysed according to the technique of Meechan and Brinkman[142] the order of reaction is found to be greater than 2. A simplified version of the same technique, due to Sosin and Rachal[143] is indicated in Fig.46, for a typical film (film 12). If ΔR, the excess resistance above the post-anneal value at each temperature, is taken as a measure of the defect concentration, then for second order kinetics,

$$\frac{d(\Delta R)}{dt} = -K(\Delta R)^2$$

where K is a constant.

On integration this gives

$$\frac{1}{\Delta R} = K't + Z$$

so that a graph of $\frac{1}{\Delta R}$ against time would be a straight line. This is almost true for the results shown in Fig.46, and so it may be concluded that the order of reaction for the recovery of these films is close to second order.

In view of this evidence, it seems unlikely that vacancy migration is the sole cause of resistivity recovery. The migration of interstitial atoms into vacancies would lead to second order kinetics, and this appears to explain the results most satisfactorily. If the existence of two stable forms of interstitial configuration, as described in section 1.3, is accepted, then the interpretation of the recovery is consistent with that of Sosin and Rachal[143] who attributed the stage III recovery to the

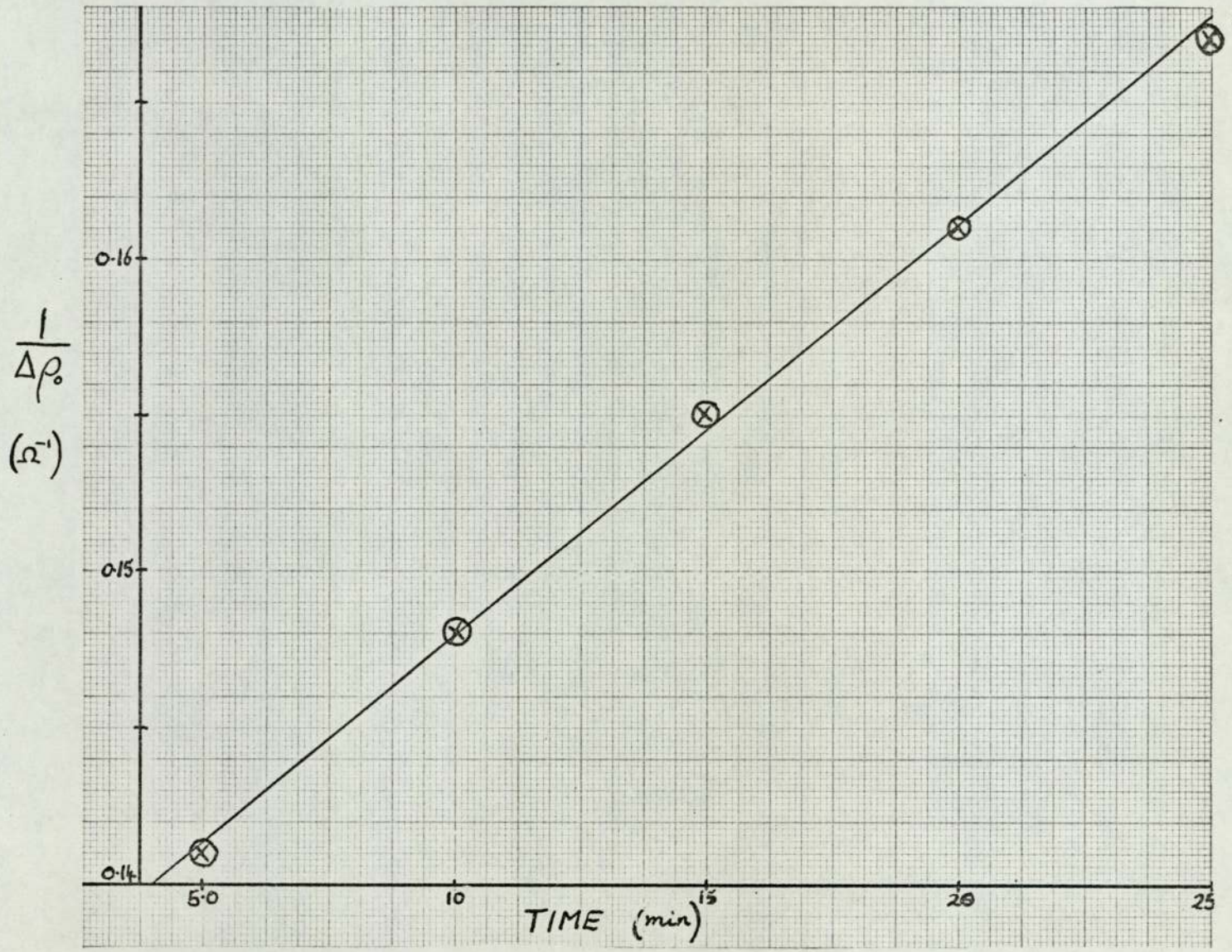

FIG. 46. CHECK FOR SECOND-ORDER REACTION (Film 12)

migration of the second form of interstitial. The problem remains, however, that the measured activation energy of 0.2 eV is lower than that measured by Sosin and Rachal during experiments on the recovery of aluminium after electron irradiation. (0.45 eV). However, Dawson et al.[144] in 1968, drew attention to the possibility that for high defect concentrations, activation energies may be reduced by the attraction between defects. It does appear likely that the defect concentration in films vapour quenched at 77°K would be extremely high; much greater than the 1% typical of radiation damage experiments. Indeed, if we take the resistivity of vacancies alone as that given by Cotterill[52] as 1.4×10^{-6} Ω cm per atomic % vacancy, then the defect contribution to resistivity would indicate about 6.5 atomic % vacancy. It is interesting to note that Mader and Nowick[72] deduce a similar figure of 7 atomic % vacancy in quenched copper and silver films. If the extra resistivity were due entirely to interstitial atoms, for which the resistivity is some four times greater than for vacancies,[72] the defect concentration would still be as high as 2%. In practice, the extra resistivity is probably due to a combination of interstitials and vacancies, having a combined concentration between 2 and 7 per cent.

These very large defect concentrations are in accord with the proposal of Monch[145] that densities of vapour quenched films are much less than those of bulk materials. For substances of high Debye temperature, such as aluminium (380°K) the reduction may be of the order of 10%. Direct measurements of the density of aluminium films made by Hartman[145A] using a quartz crystal microbalance are shown in Fig.47. For films of thickness 11 nm to 13 nm, as used in the experiments reported here, the density may clearly be expected to be considerably lower than that of bulk aluminium.

It seems reasonable, then, to ascribe the fall of resistance

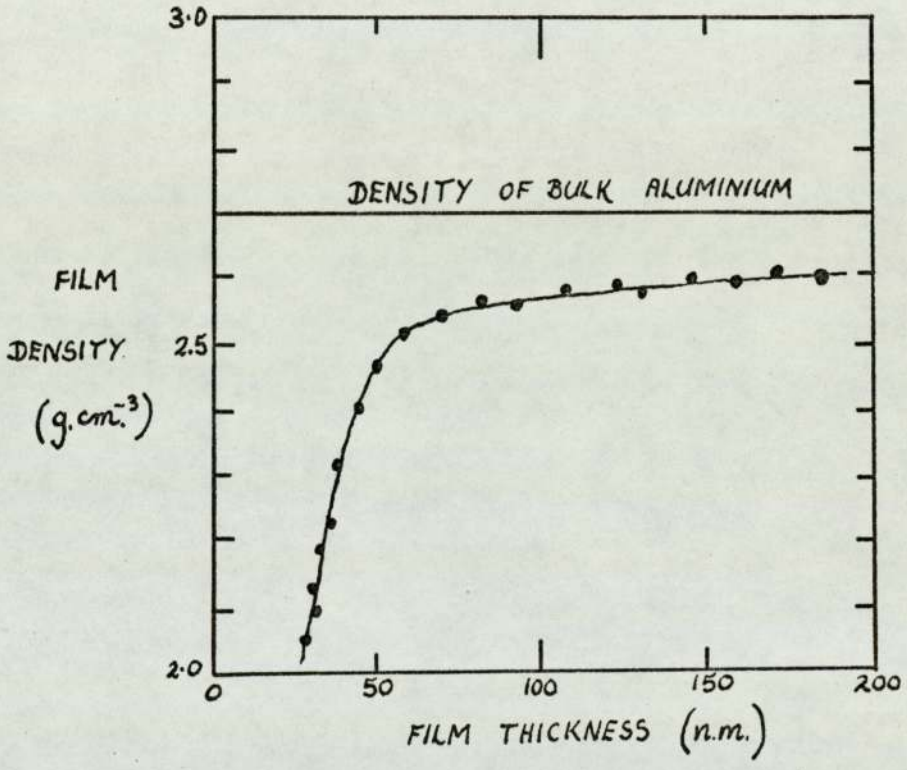

FIG. 47.

DENSITY of ALUMINIUM with Film Thickness

(After Hartman)

on warming quenched films to the migration of interstitials to vacancies trapped at grain boundaries, a process giving rise to second order kinetics. The activation energy measured would then be smaller than the value of 0.45 eV obtained in radiation damage experiments because of the very large concentration of vacancies, surrounding each interstitial. This being so, it may be expected that as the annealing proceeded, the annihilation of vacancies would result in a rise of activation energy. The possibility is examined in Fig.48, in which the measured activation energy is plotted against the mean temperature at which the measurement took place. The uncertainty is quite large, but it may be tentatively concluded that such is the case.

On commencement of the stage III anneal, the resistance of the specimens was always found to increase slightly at first, as can be seen in Fig.41 (point A). This is explained in a consistent way by considering the rise in temperature of the substrate during film deposition. To verify this, a thin-film copper-nickel thermocouple was deposited on the substrate where an aluminium film could be deposited directly over the junction. The thermocouple was annealed and calibrated both before and after formation of the specimen film. A temperature rise of 60°C was recorded as a result of a thermal radiation from the filament and a further rise of 5°C occurred as the specimen film was formed from the vapour.

It has previously been pointed out[68] that halting the warm-up at any temperature θ and cooling again to 77°K results in linear metallic behaviour between θ and 77°K, a further fall of resistance occurring only when the temperature θ is exceeded.

The indication is that the true deposition temperature was some 65°C above liquid nitrogen temperature. This is then seen to correspond to the peak value of resistance during the warm-up. (See point A on Fig.41) The magnitude of the above effect is consistent with other direct measurements of temperature rise during film

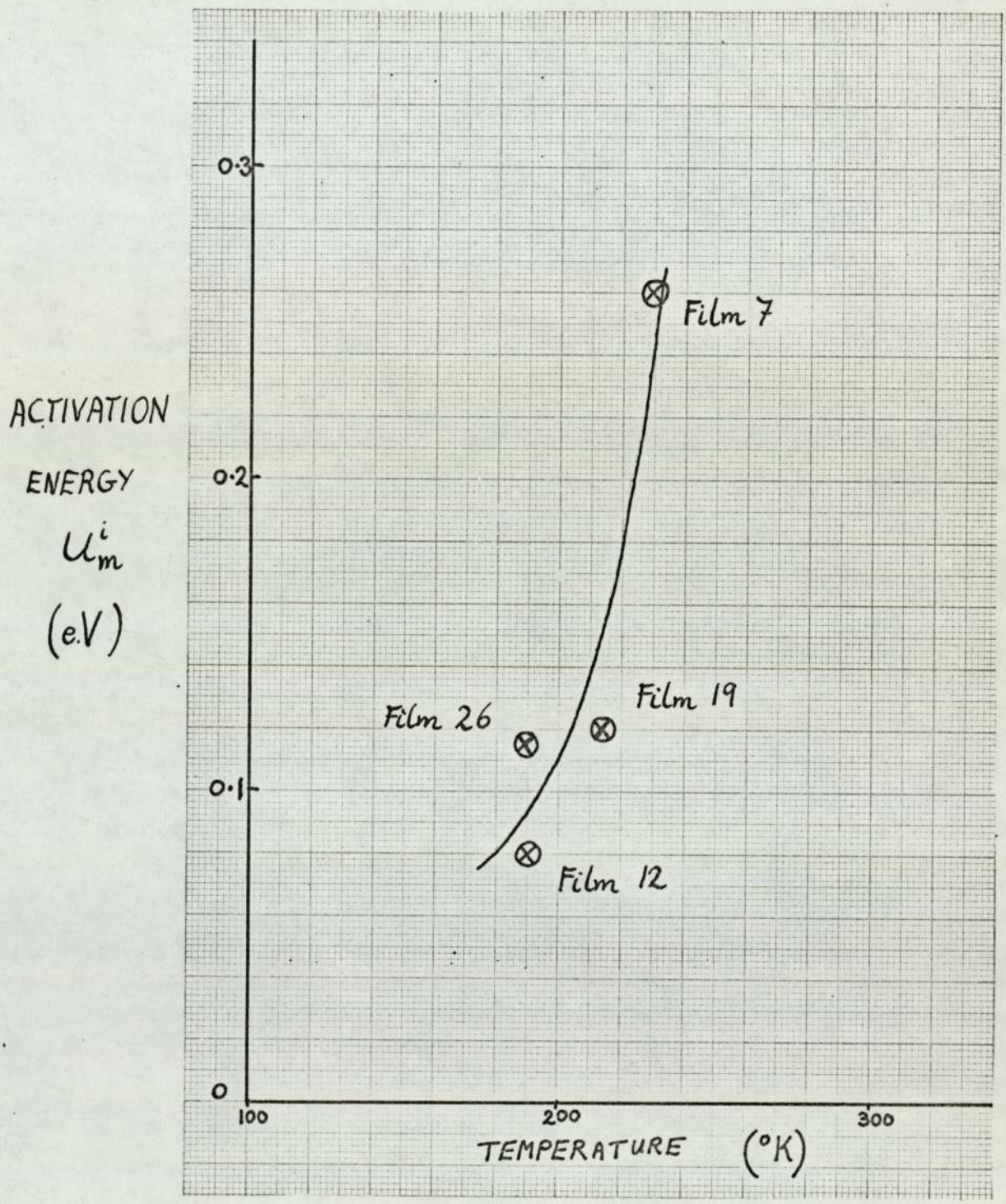

FIG. 48.

VARIATION OF ACTIVATION ENERGY WITH TEMPERATURE

deposition made by Namba[146], who used evaporated thin film thermocouples of gold and nickel to measure the temperature rise during deposition of gold films.

5.2 Anneal from 77°K. Optical Measurements

The variation of optical parameters Ψ and Δ for a typical film (film 2) after correction for strain in the windows, is shown in Fig.49 for the entire duration of an experiment. As for all other films, the value of both Ψ and Δ were observed to rise during the first warm-up (during which time the resistance was falling). In terms of the complex refractive index $\mathcal{N} = n - ik$, these changes can be interpreted as an increase in the value of k and an increase in the value of n, the product nk thus becoming greater. (Compare Table 1 and Table 2 below.)

TABLE 1 Measurements after deposition of films at 77°K

Film Number	Metal Thickness (nm)	Ψ	Δ	n	k	n^2-k^2	nk
2	11.0	36.13	136.58	0.70	5.45	-29.21	3.82
3	13.0	35.55	139.22	1.08	5.15	-25.35	5.55
7	12.5	33.88	134.77	0.92	4.73	-21.52	4.35
12	12.5	33.38	133.87	0.92	4.61	-20.40	4.24
8	12.0	32.53	133.57	0.98	4.55	-19.74	4.48

TABLE 2 Measurements at room temperature after the stage III anneal

Film Number	Metal Thickness (nm)	Ψ	Δ	n	k	n^2-k^2	nk
2	11.0	36.67	138.88	0.79	5.67	-31.53	4.48
3	13.0	36.05	140.55	1.12	5.30	-26.84	5.94
7	12.5	34.20	136.47	1.10	4.88	-22.60	5.37
12	12.5	33.52	135.84	1.05	4.73	-21.27	4.97
8	12.0	33.19	134.47	1.12	4.62	-20.09	5.18

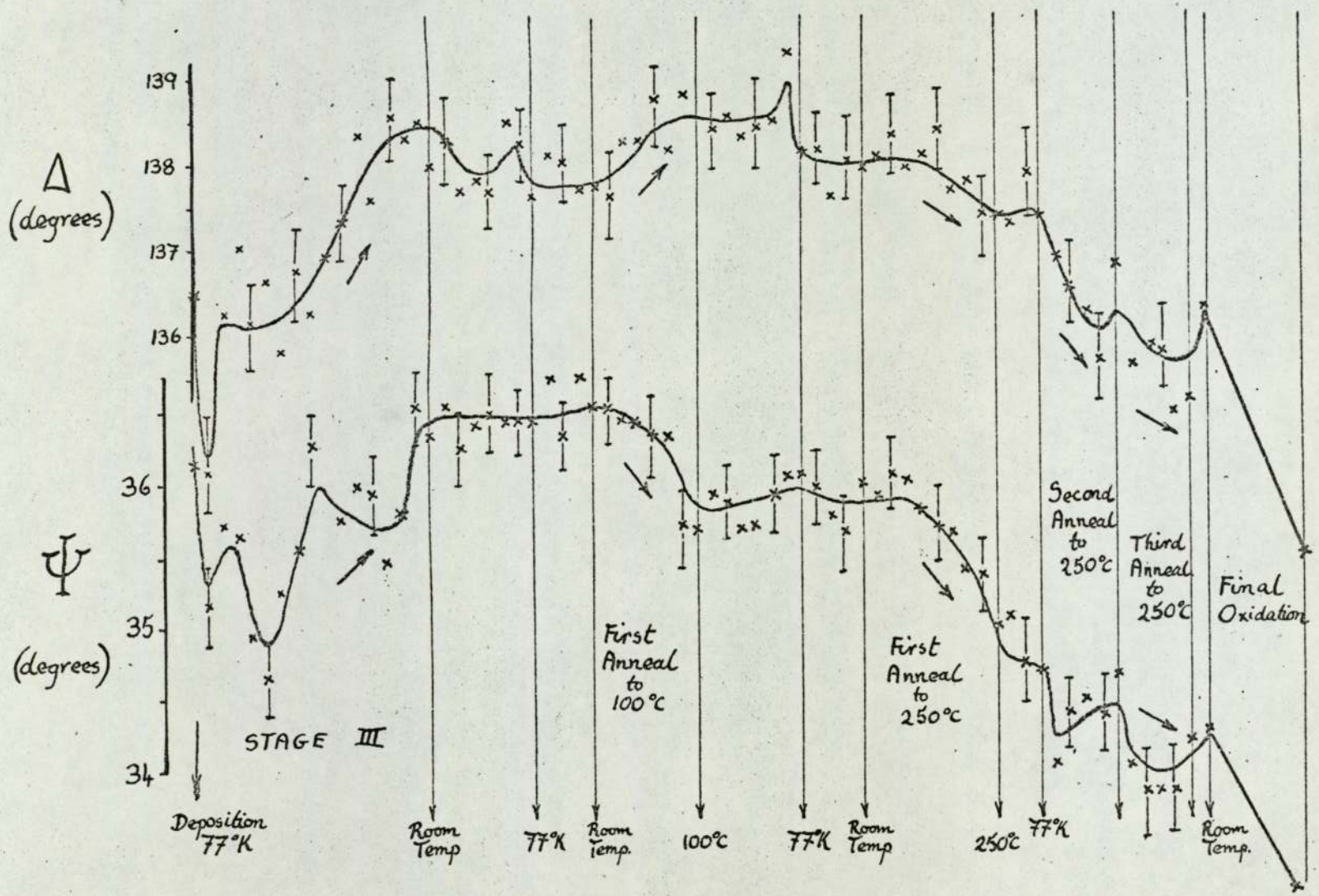

FIG. 49. OPTICAL RESULTS FOR FILM 2

On the whole, the measured values of n, at room temperature, are in reasonable agreement with theoretical values for bulk aluminium given by Ehrenreich et al.[36], namely n = 0.99 and k = 6.6 at a wavelength of 550 nm. Those films which were returned to liquid nitrogen temperature immediately after the stage III anneal showed no observable change in Ψ and Δ (see Fig.49). The changes produced then, by the stage III anneal, are irreversible and cannot be explained as a temperature effect. Measurements at different temperatures of the optical absorption in aluminium, made by Hodgson[147] and of the optical constants of aluminium reported by Motulevitch,[24] confirm that at the wavelength of these experiments (549 nm) any temperature effect would be extremely small. The results of section 6.2 also support this view. The changes produced by the anneal are summarised in Table 3 below:

TABLE 3 Changes produced by stage III anneal

Film Number	Metal Thickness (nm)	Increase of Ψ^0	Increase of Δ^0	% fall of n^2-k^2	% Rise of nk	% Rise in Conductivity
2	11.0	0.54	2.30	7.95	43	37
3	13.0	0.50	1.33	5.90	7	10
7	12.5	0.32	1.70	5.00	23	26
12	12.5	0.14	1.97	4.30	18	28
8	12.0	0.20	0.90	1.80	16	23

To assess the results of Table 3 in the light of the optical theory of metals, the standard Drude-Zener approximations for conduction electrons may be recalled;

$$\epsilon_1 = n^2 - k^2 = 1 - \frac{4\pi N^* e^2}{m\omega^2} \qquad (4)$$

$$\epsilon_2 = 2nk = \frac{4\pi N^* e^2}{m\omega^2\tau} \qquad (5)$$

$$\sigma_o = \frac{N^* e^2 \tau}{m} \qquad (6)$$

where the complex dielectric constant $\epsilon = \epsilon_1 - i\epsilon_2$; N^* is the effective electron density and τ their relaxation time; σ_o is the d.c. conductivity.

These equations were derived for conduction electrons only and do not apply in the region where interband absorption occurs. Fig.50 is a sketch of the general shape of the absorption spectrum of aluminium and shows that the present measurements, made at 2.5 eV, fall in a region of the aluminium absorption spectrum where interband transitions are still significant. However, equation (4) is still valid in this region although equation (5) is not, as shown by Sokolov.(148)

Table 3 shows that the Stage III anneal produces a drop in the value of n^2-k^2, indicating from equation (4) that the value of $\frac{N^*}{m}$ has increased. In a qualitative way it would be expected that the disappearance of vacancies would lead to anincrease of N^*, the effective electron density. In fact, Table 3 indicates a correlation between the fall of n^2-k^2 and the rise of conductivity, some of which is caused by the annihilation of vacancies.

Taking film 2 as an example, Table 3 also shows that the increase of $\frac{N^*}{m}$, $\sim 8\%$ is insufficient to account for the observed increase of conductivity, $\sim 37\%$. Equation (6) shows that to account for the observed increase of conductivity it is therefore necessary that the relaxation time, τ, should increase at the same time, by about 30%.

The combined effect of an increase of $\frac{N^*}{m}$ and an increase of τ would be expected to produce, from equation (5), a reduction of the conduction electron contribution to nk of approximately 23%. However, the effect of the annealing is to increase the interband contribution to the absorption, (see also section 6.2), so that the

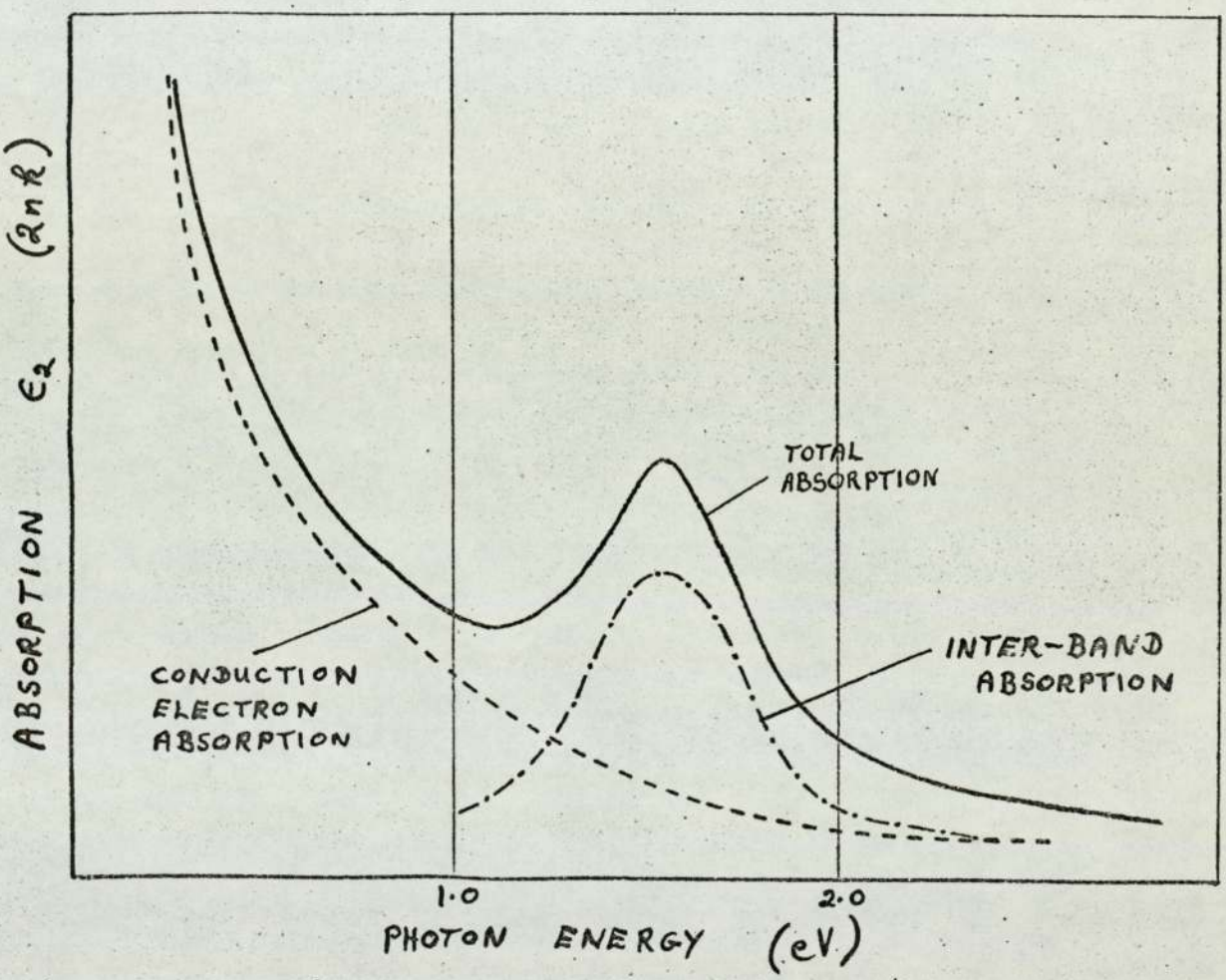

FIG. 50

SKETCH OF OPTICAL ABSORPTION SPECTRUM IN ALUMINIUM

observed value of nk increases by approximately 40%. Abeles and Theye[149], working with gold films, have also observed larger values of nk for films of increased perfection in the region of interband transitions. The proposed increase of $\frac{N^*}{m}$ and the increase in τ as the vacancies are annealed out of the film are also in agreement with the results of Abeles and Theye.[149]

5.3 High temperature anneals. Stage IV

5.3.1 Anneal to 100°C

The changes of Ψ and Δ when a typical film (film 2) is heated to 100°C are shown in Fig.49. The value of Ψ falls while the value of Δ rises. Table 4 shows that this corresponds to a rise of n accompanied by a small reduction in the value of k.

TABLE 4 Anneal to 100°C for film 2 (11.0 nm)

	Ψ	Δ	n	k	n^2-k^2	nk	Resistance (Ω)
Before 100°C Anneal	36.67	138.88	0.79	5.67	-31.53	4.48	20.6
After 100°C Anneal	35.82	139.82	0.98	5.60	-30.40	5.48	20.0

The anneal produced only a small decrease in resistance (Fig.41). The observed changes can be explained by two opposing effects; firstly, annealing, which makes Δ and Ψ increase and the resistance fall, and secondly oxidation, which makes Δ and Ψ fall and the resistance rise.

5.3.2 Anneal to 250°C

During the heating of film 2 to 250°C, it was observed that the resistance increased at higher temperatures at a greater rate than would result from lattice vibrations alone. Similar results were also observed for subsequent heating cycles (see points D on Fig.41). At the same time, (Fig.49), the values of Ψ and Δ both show a decrease. The direction of change of these three variables are the same as during final oxidation of the film (Figs.41 and 49).

The extent of changes on final oxidation also indicate that

some oxidation had already taken place during the life of the film. In fact, Fig.41 and Fig.49 show that, after the first few hours, there is a steady upward drift in resistance and a downward drift of Ψ and Δ, all indicating oxidation.

5.4 Oxidation Experiments

Further experiments were undertaken in which films were deposited under identical conditions and maintained in ultra-high vacuum for varying lifetimes before finally exposing them to the atmosphere. Table 5, together with Fig.51. shows a clear dependence of the extent of these final changes on the lifetimes of the films. We may conclude that oxidation was occurring throughout the life of the films.

TABLE 5 Effect of film lifetime

Film Number	Thickness (nm)	Total Lifetime (hrs)	Final Fall of Ψ^o	Final Fall of Δ^o	Final Reduction of Conductivity (%)
8	12.0	3	8.56	13.83	162
7	12.5	$7\frac{1}{2}$	6.36	11.80	120
12	12.5	43	5.73	10.40	88
3	13.0	219	1.65	6.80	24

Calculations indicate a rate of oxide formation of 0.05 nm per hour on a completely fresh surface. For the measured partial pressure of oxygen of 2×10^{-11} torr during the experiment, this oxidation rate is consistent with times of monolayer formation, assuming a "sticking coefficient" of unity. Table 5 may also be used to extrapolate to a hypothetical 'zero' lifetime and thus to make a correction for oxidation effects. This has been done for the values in Table 2 so that the changes produced by the stage III anneal shown in Table 3 should relate to a clean, un-oxidised surface.

Further experiments were undertaken to observe the effect

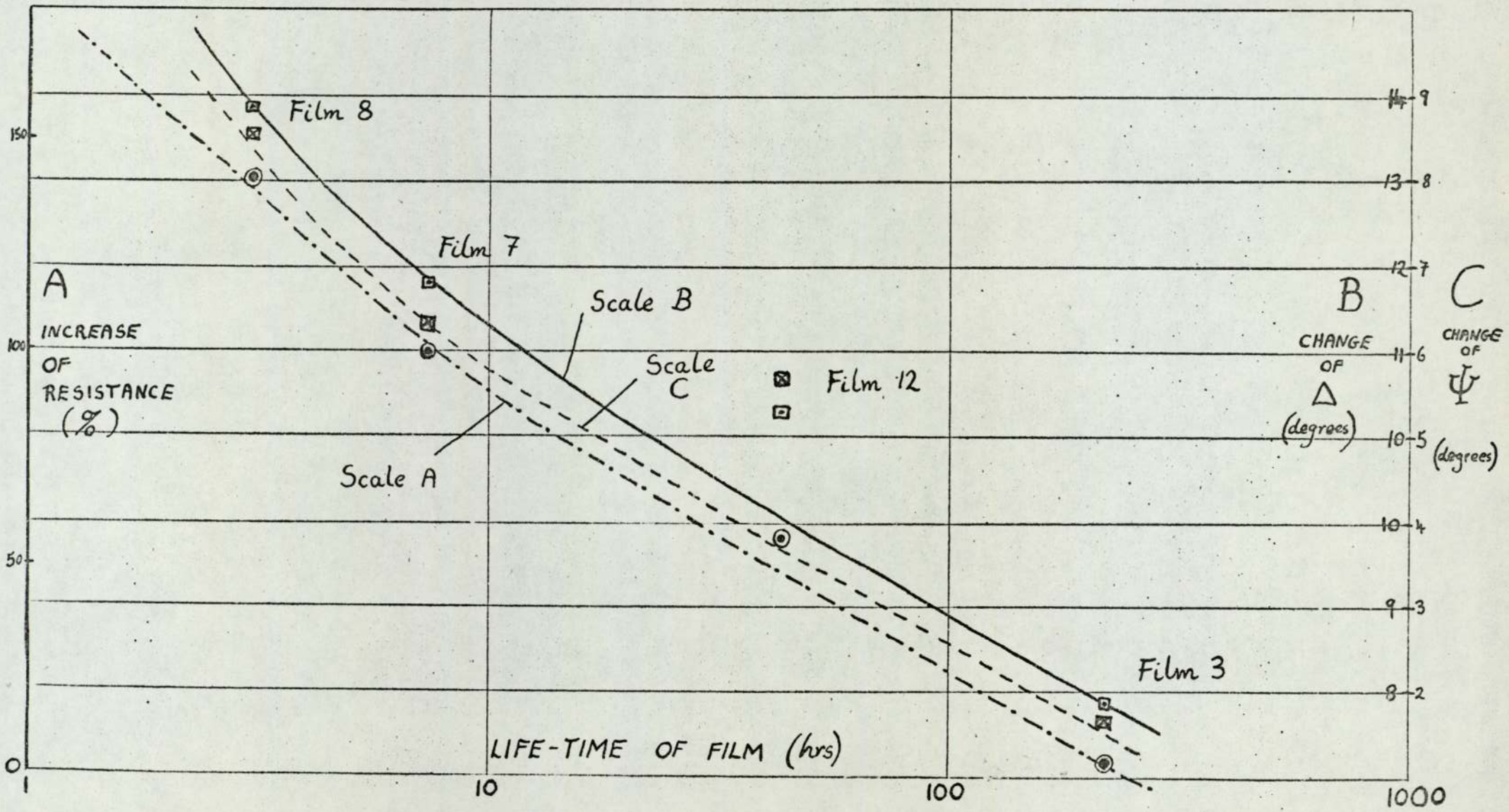

FIG. 51. CHANGES ON FINAL OXIDATION against FILM LIFETIME

of an increase of total pressure on the properties of a film maintained at a constant temperature (46°C) in ultra-high vacuum. Normal air was admitted through the variable leak valve into the experimental chamber until the pressure stabilised at the required value. Fig.52 shows the corresponding variation of Ψ , Δ and resistance which all proceed in the direction of oxidation, even at the total pressure of 1.5×10^{-9} torr, again equivalent to a rate of 0.05 nm per hour on a clean surface. The rate is seen to increase to 0.4 nm per hour at a higher pressure of 1.5×10^{-8} torr, and to return to the original rate when the pressure is reduced again. The linear dependence of oxide layer thickness on log (time) agrees with the previous findings of Fane and Neal.[31]

The above results are important in view of the large number of optical measurements on aluminium published, in which base pressures are quoted of the order of 10^{-6} torr or higher. Measurements made at these pressures are almost certainly performed on oxidised surfaces. It is of interest to note that if an oxidised surface were interpreted as a clean surface, the calculated values of n and k would both be smaller than the true values. This reaffirms the conclusions of Fane and Neal[31] for thicker films. It does mean, however, that the changes of n and k produced during annealing of thinner films (Neal et al.[114]) must be partly explained by oxide formation.

One possible way of avoiding the problem and obtaining annealing data for high temperature anneals would be completely to oxidise a film by exposing it to the atmosphere for several days and, when the equilibrium layer of approximately 3.5 nm of oxide was reached, then to anneal the film in vacuo.

5.5 Annealing of totally oxidised films to 260°C

The results of such experiments are shown in Figs.53 and 54 for films deposited at 77°K and 296°K respectively. The changes produced are similar for both films, namely a rise of resistance,

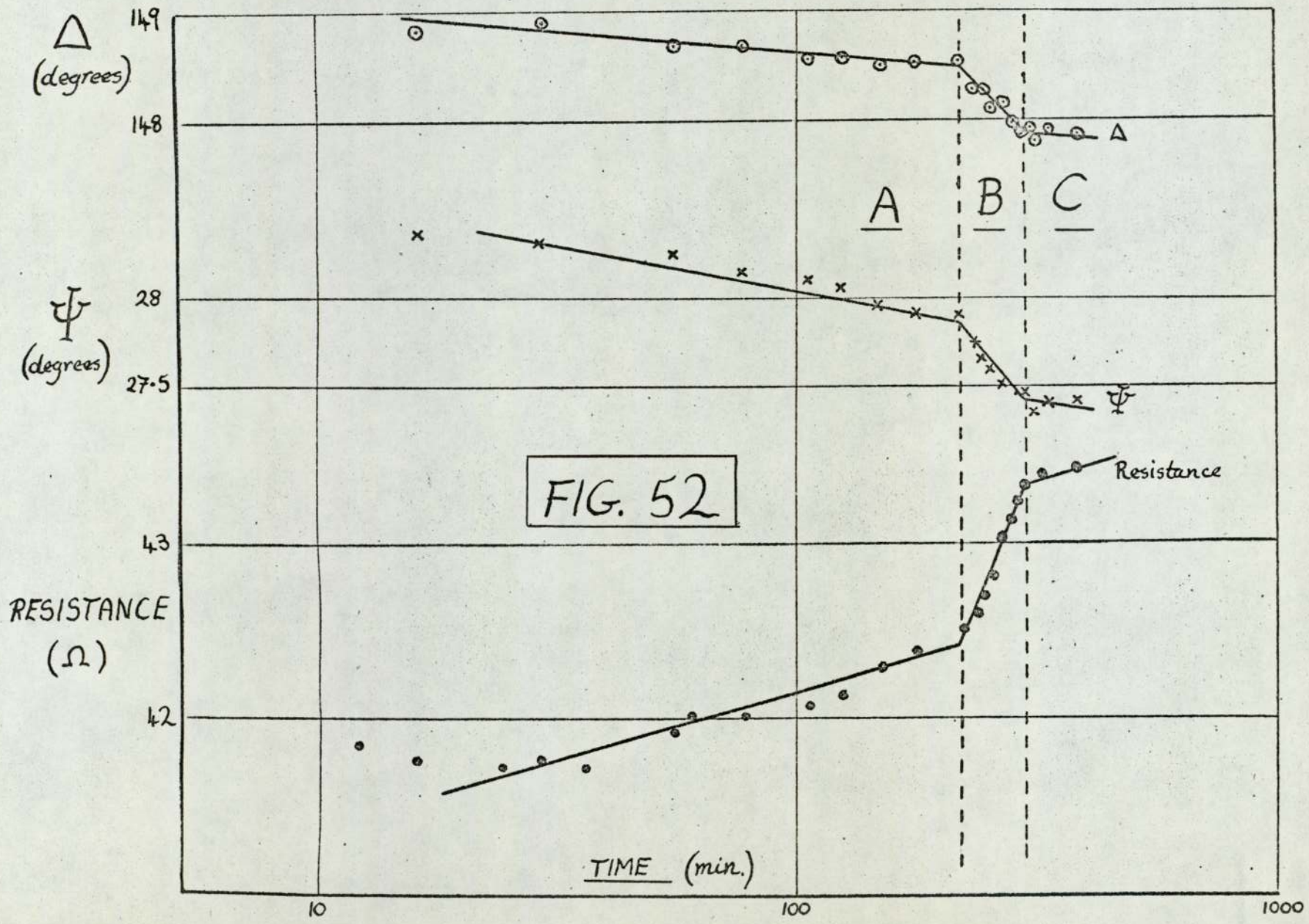
Δ (degrees)
149
148
Ψ (degrees)
28
27·5
RESISTANCE (Ω)
43
42
A
B
C
Δ
Ψ
Resistance
TIME (min.)
10
100
1000

FIG. 52

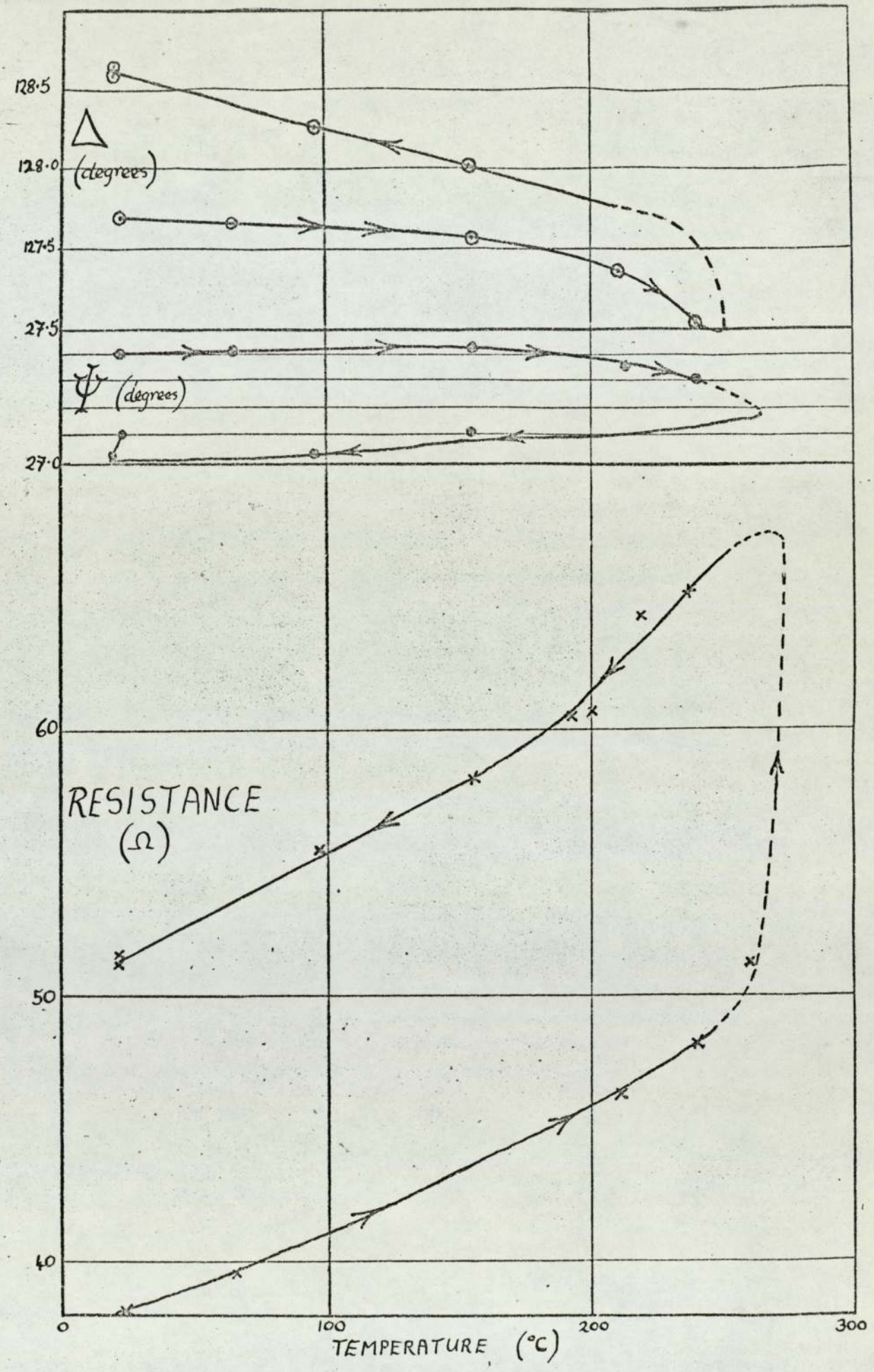

FIG. 53 ANNEAL OF OXIDISED FILM

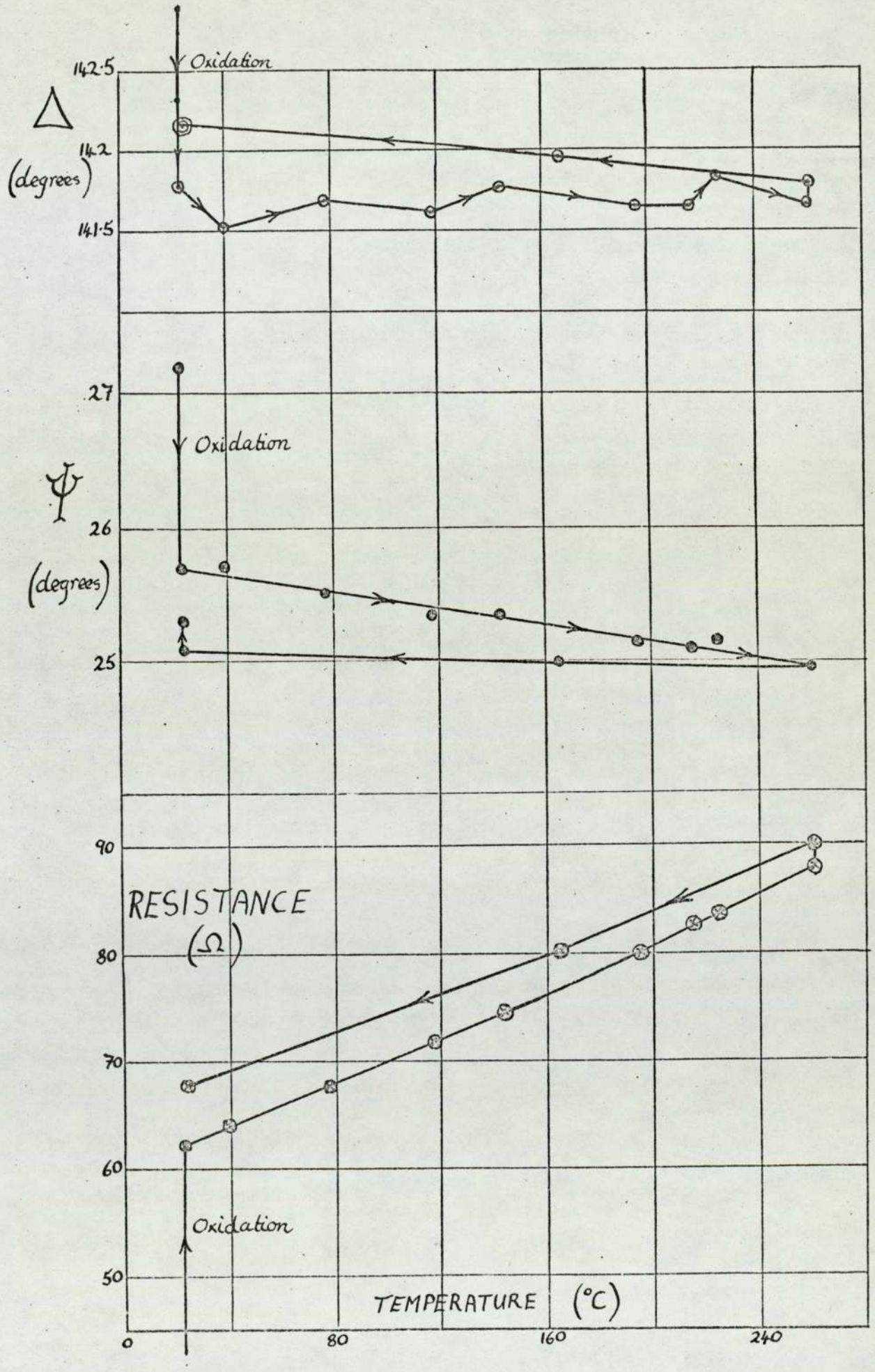

FIG 54. ANNEAL OF FULLY OXIDISED FILM

a fall of Ψ and a rise of Δ. Program 3, described in Appendix 2, has been applied to the results assuming that the refractive index of the oxide was 1.635 as measured by Vasiček.[150] For the thickness of films involved, the interpretation is a rise in the value of n and a small reduction in k. The changes produced in the high temperature anneal of film 12 (which was deposited at 77°K) are shown in Table 6, in which all measurements were made at room temperature.

TABLE 6 Effect of Anneal to 260°C

Film Number		Ψ	Δ	n	k	n^2-k^2	nk	Resistance(Ω)
12	Before 250°C Anneal	33.52	135.84	1.05	4.73	-21.27	4.97	38.2
	After 250°C Anneal	33.12	136.84	1.16	4.72	-20.93	5.48	51.3

The experiments of Klei[151] confirm that the oxide layer in aluminium only grows significantly above the equilibrium value of 3.5 nm for temperatures in excess of 350°C and so may be assumed to remain of constant thickness during these annealing experiments. Calculations using program 3 show that any probable variation in refractive index due to annealing in the oxide layer itself is negligible. A reduction of 10% in the oxide refractive index leads to increases of Ψ and Δ of 0.02 and 0.15 degrees respectively; with the possible error introduced for estimates of n and k of less than 1%.

This being the case, the increase of resistance and also the larger value of n are attributed to a higher defect concentration, possibly brought about by the differential thermal expansion between the glass substrate and the film producing an increase of dislocation density, as suggested by Grimes et al.[152]

CHAPTER 6

RESULTS OVER AN EXTENDED WAVELENGTH RANGE

Using the Balzer interference filters to provide monochromatic light, and the ellipsometric method of Beattie, previously described, measurements of Ψ and Δ were made on aluminium films of various thicknesses on substrates of Corning 0211 glass and later on single crystal potassium bromide. The range of wavelengths used was sufficiently wide for the region of interband transitions to be included.

6.1 Specimens on glass substrates

6.1.1 Anneal from 77°K to room temperature. Stage III

Some results for a film (film 19) of 11 nm thickness, deposited at liquid nitrogen temperature on a glass substrate and subsequently annealed are presented in Figs. 55 and 56, which show the variations throughout the spectrum of Ψ and Δ respectively. The curves show that over the wavelength range investigated (0.499μ to 1.15μ) the initial warming from deposition (curve A) to room temperature (curve B) produces an increase of both Ψ and Δ. The resulting changes of n and k are tabulated in Table 7. The changes in the product nk, which is related to the optical absorption, are plotted in Fig.57. It can be seen that the inter-band absorption peak is almost absent on deposition and appears to be moved to lower energy (1.24 eV) compared to the accepted value for bulk aluminium (1.55 eV). As a result of the Stage III anneal, the value of nk rises. This indicates increased optical absorption for all wavelengths. At the same time the maximum value of inter-band absorption is moved to higher energy, in agreement with the earlier results of section 5.2 taken at the single wavelength of 0.549μ (2.5 eV).

The changes due to the initial warming of $n^2 - k^2$, the real part of the dielectric constant, are shown in Fig.58. The shape of the curve is in general agreement with accepted values for bulk

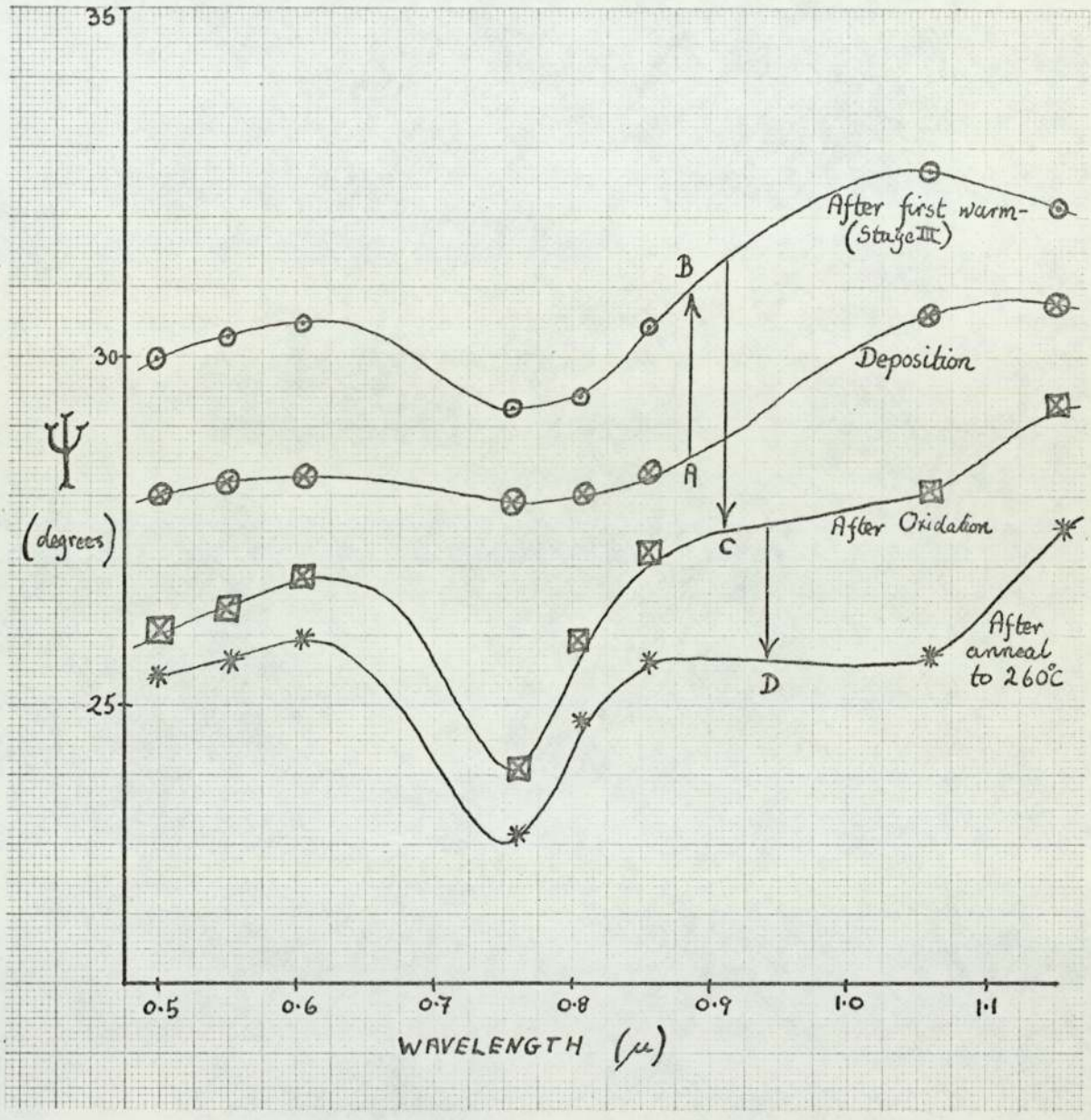

FIG. 55.

VARIATION OF Ψ THROUGHOUT EXPERIMENT (Film 19)

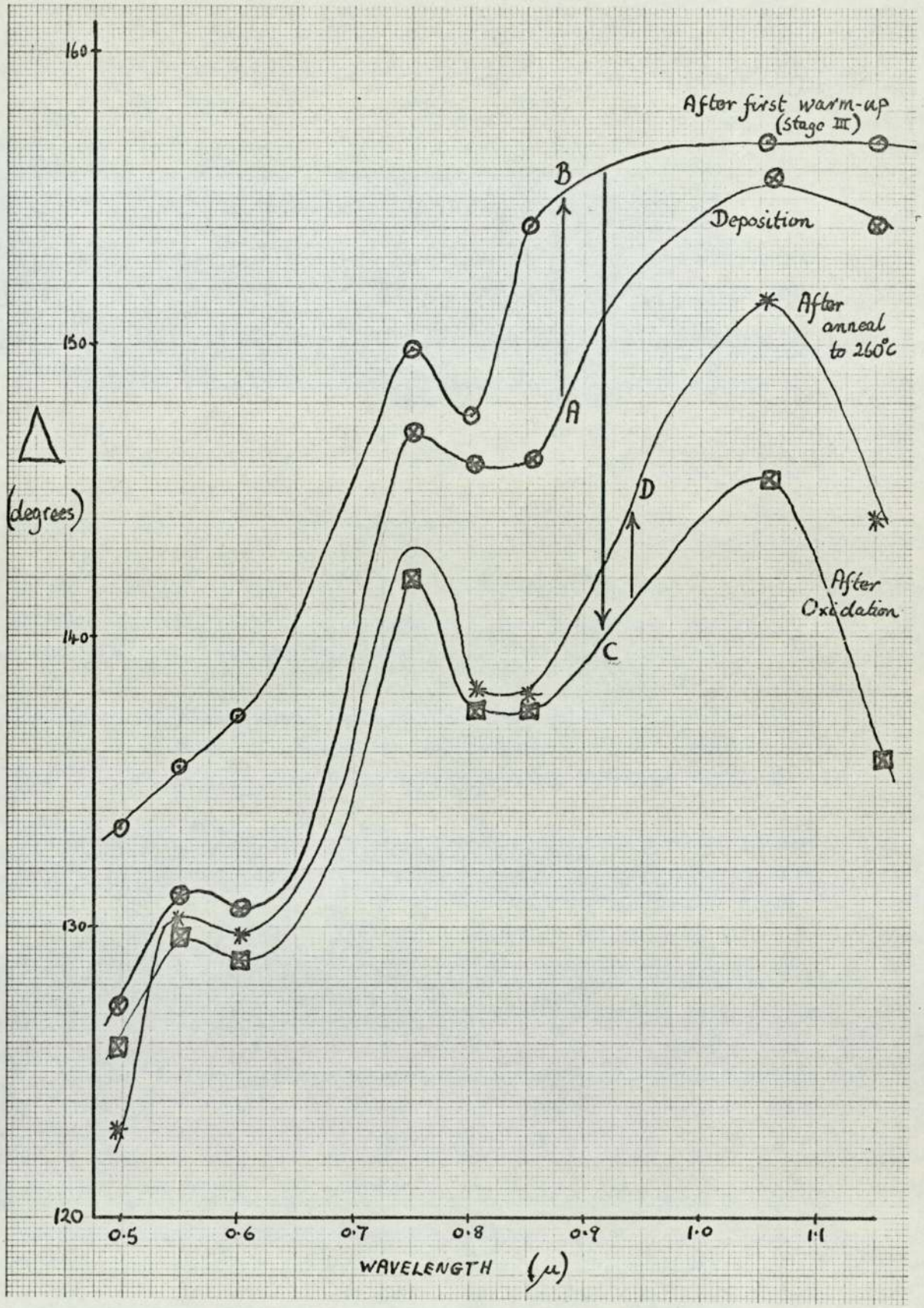

FIG. 56

VARIATION OF Δ THROUGHOUT EXPERIMENT (Film 19)

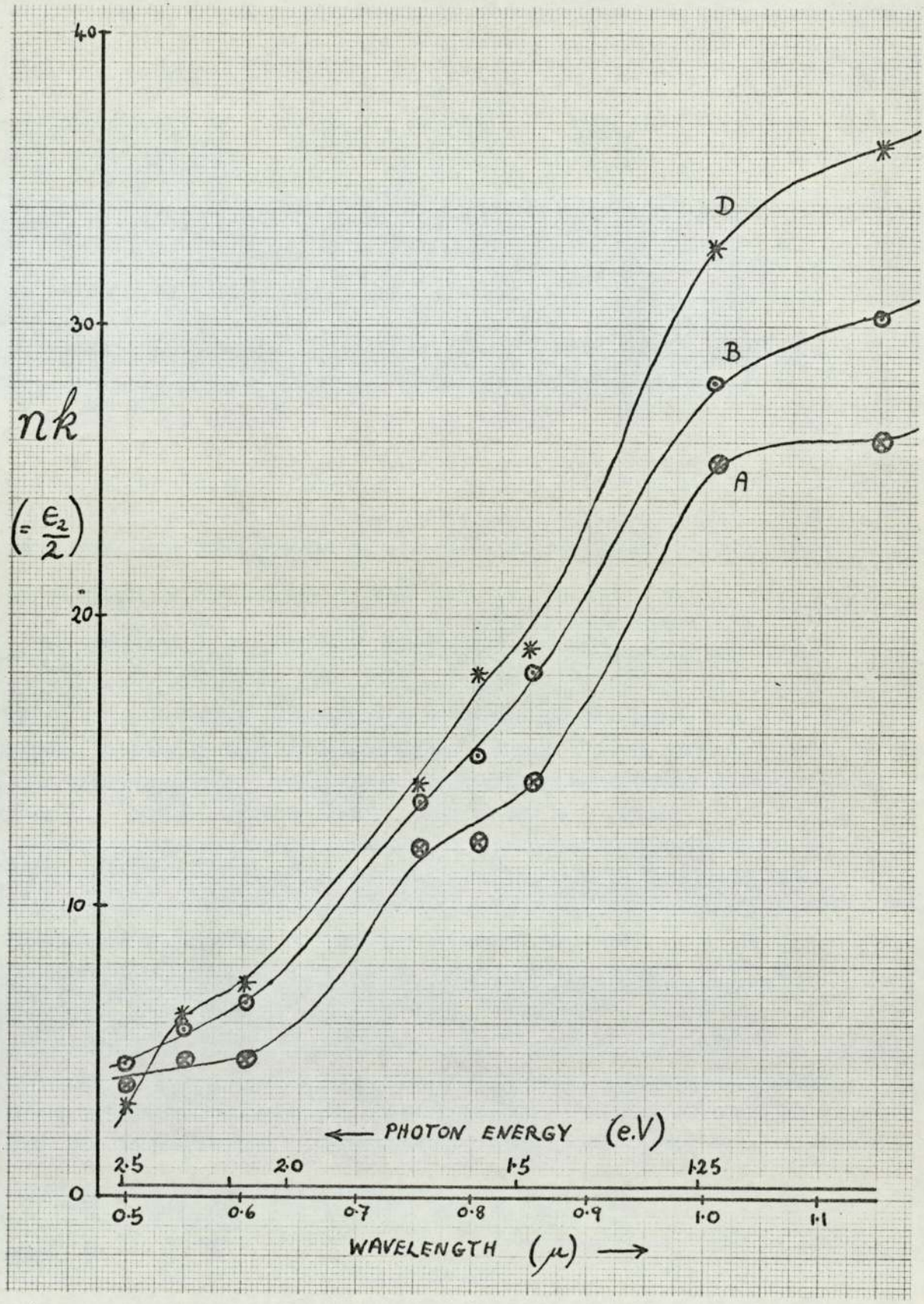

FIG. 57

VARIATION OF nk (Film 19)

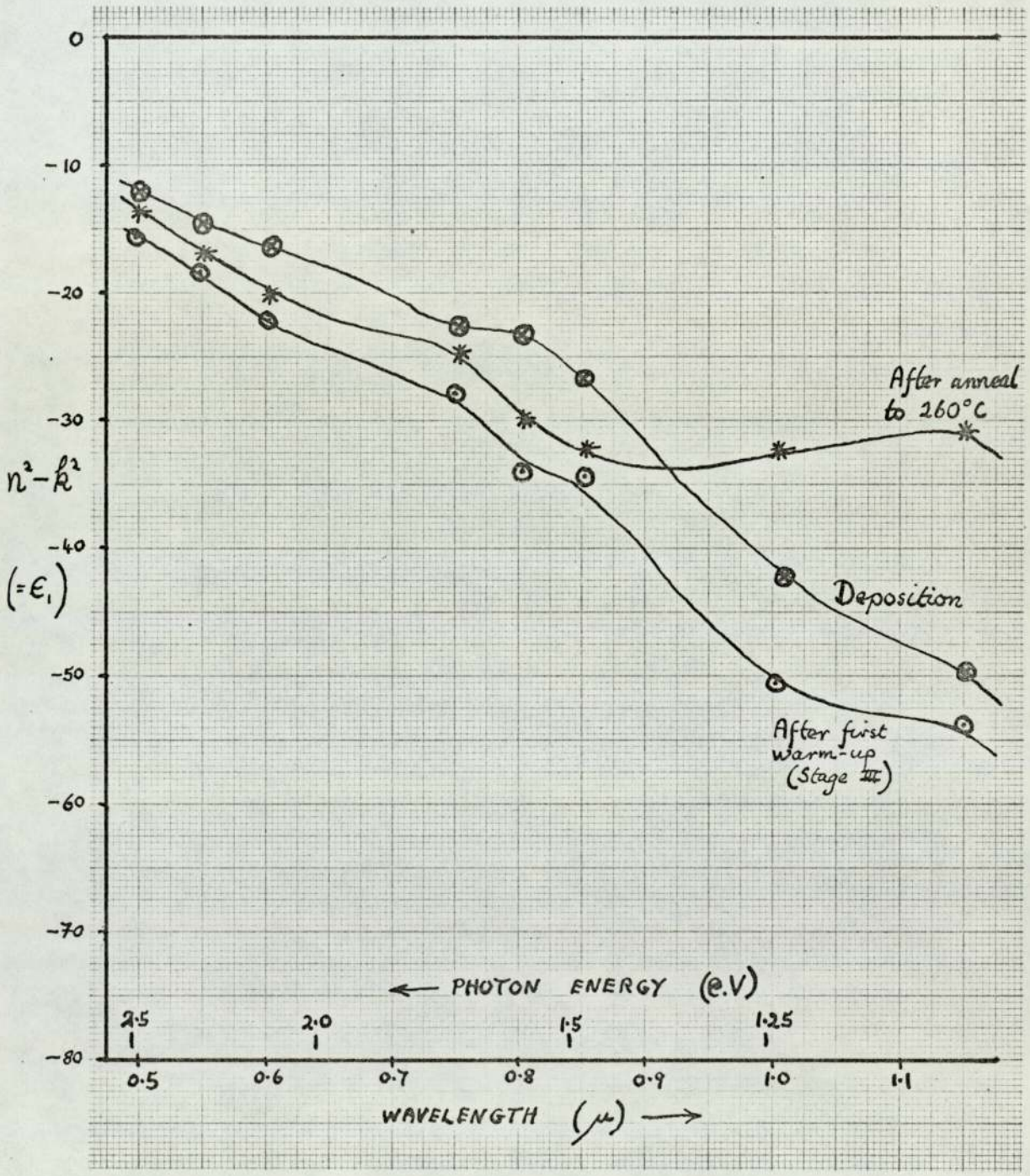

FIG. 58

VARIATION OF n^2-k^2 (Film 19)

TABLE 7 Stage III anneal for 11 nm film (film 19)

Wavelength (μ)		Values for Deposition at 77°K	Values at Room Temperature
1.150	n	3.35	3,70
	k	7.80	8.20
1.056	n	3.45	3.53
	k	7.35	7.95
0.851	n	2.51	2.80
	k	5.75	6.50
0.804	n	2.28	2.42
	k	5.35	6.31
0.753	n	2.30	2.38
	k	5.25	5.76
0.604	n	1.12	1.38
	k	4.20	4.90
0.549	n	1.20	1.30
	k	4.00	4.47
0.499	n	1.05	1.11
	k	3.65	4.10

aluminium (Fig.1) except that the inter-band peak at deposition is again moved towards lower energy (1.2 eV) compared to bulk aluminium. The effect of the Stage III anneal is to move the peak towards higher energy (as above) and this makes the value of $n^2 - k^2$ become more negative at the shorter wavelengths. Throughout the wavelength range investigated, the proportional reduction in $n^2 - k^2$ is approximately constant, amounting to about 8%. This is in accord with the previous measurements made at 549 nm in section 5.2 and can be interpreted (from equation 4) as a rise of $\frac{N^*}{m}$ of approximately 8%.

During the stage III anneal, the resistance of the same film (film 19), shown in Fig.59, is seen to fall by some 26% of the initial value. A determination of activation energy was made by the technique of section 5.1, and the result of 0.12 eV was obtained between temperatures of 208°K and 215°K.

6.1.2 Oxidation of Specimens

When exposed to the normal atmosphere for 48 hours, the

effects of oxidation produce the changes in Ψ and Δ, from curve B to curve C, shown in Figs. 55 and 56 respectively. Throughout the spectrum there is a fall in the values of both Ψ and Δ which, from calculations using program 3 is shown to be consistent with the formation of 35°A of aluminium oxide on the film surface.

6.1.3 High Temperature Anneals

After annealing film 19 to 260°C in high vacuum for approximately three hours, a decrease of Ψ and an increase of Δ were observed for all wavelengths. The changes produced by the anneal may be seen by comparing curves C and D on Figs. 55 and 56. The directions of change of both Ψ and Δ are the same as those observed in section 5.5 for the single wavelength of 549 nm and indicate further annealing of the specimens. The corresponding changes of n and k, assuming that the oxide thickness does not change and that any annealing in the oxide layer itself produces negligible effect, are shown in Table 8.

The corresponding changes of nk and $n^2 - k^2$ are shown in the graphs of Figs. 57 and 58. respectively. The annealing to 260°C produced a rise of nk in the short wavelength region consistent with the results of section 5.5, and a fall of nk in the long wavelength region. The effect can again be explained as a shift of the inter-band peak towards shorter wavelengths as a result of the anneal. Throughout the entire range investigated, the anneal produced an increase of $n^2 - k^2$. This suggests that further annealing was taking place. The inter-band peak is again seen to develop and to be shifted towards shorter wavelengths as a result of the anneal. However, Fig.59 shows that the resistance of the film increased as a result of the anneal. This phenomenon was expected, since a number of previous observations had shown the same effect. As before, the greater resistance was attributed to an increase of dislocations produced by differential thermal expansion between the film and the glass substrates.

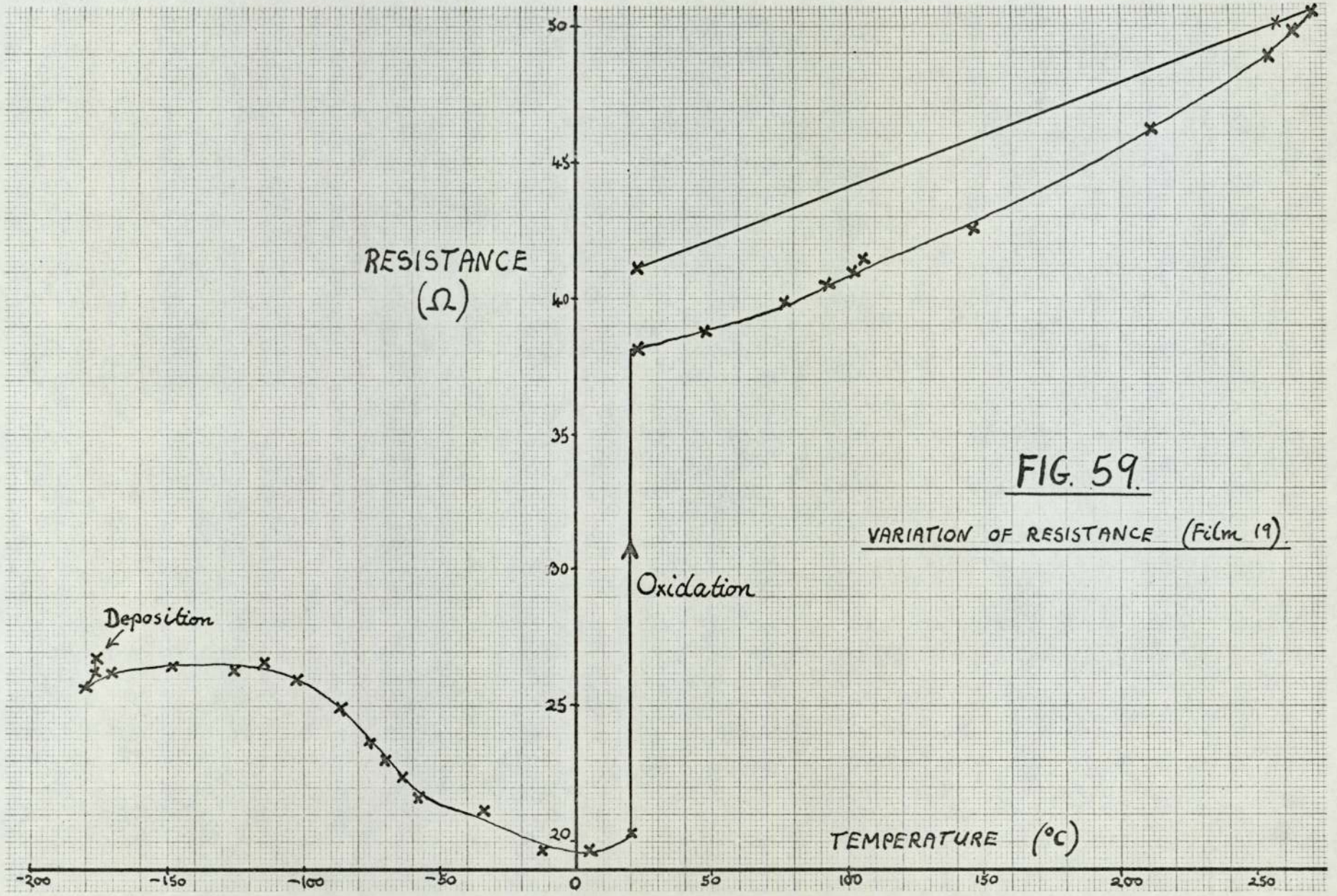

FIG. 59.

VARIATION OF RESISTANCE (Film 19).

TABLE 8 High Temperature Anneal for film 19

Wavelength (μ)		Values at Room Temperature (before anneal)	Room Temperature (After 260°C anneal)
1.15	n	3.70	4.9
	k	8.20	7.4
1.056	n	3.53	4.53
	k	7.95	7.25
.851	n	2.87	2.97
	k	6.39	6.26
.804	n	2.26	2.76
	k	5.70	5.61
.753	n	2.60	2.75
	k	5.66	5.46
.604	n	1.38	1.54
	k	4.90	4.81
.549	n	1.30	1.45
	k	4.47	4.41
.499	n	1.11	1.03
	k	4.10	3.85

Films deposited at room temperature show similar variations when fully oxidised and annealed to 260°C. Figs. 60 and 61 show the changes of Ψ and Δ respectively for the annealing of film 21, which had a thickness of 2 75 nm. As can be seen, the effect of the anneal increased Ψ and reduced Δ above 0.8μ wavelength, and produced the opposite changes below 0.8μ . The equivalent changes of n and k are set out in Table 9, and the corresponding variations in nk and $n^2 - k^2$ are shown in Figs. 62 and 63. The inter-band absorption peak for film 21 (27.5 nm) is seen to occur at approximately 0.8μ as expected for bulk aluminium. Once again, the effect of the anneal is consistent with a shift of the inter-band peak towards shorter wavelengths in both the nk and $n^2 - k^2$ curves.

6.2 Specimens on substrates of single crystal potassium bromide

With the ultimate aim of producing epitaxially grown single crystal aluminium films, having any desired crystallographic axis

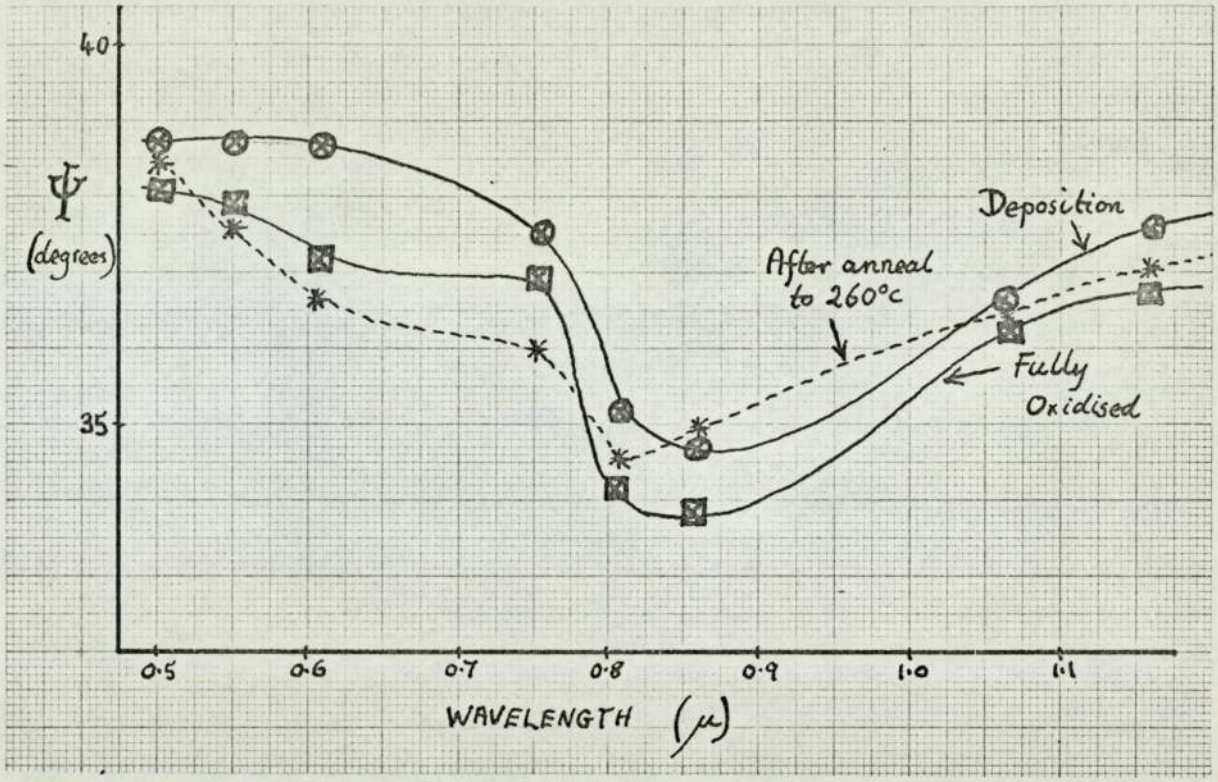

FIG. 60.

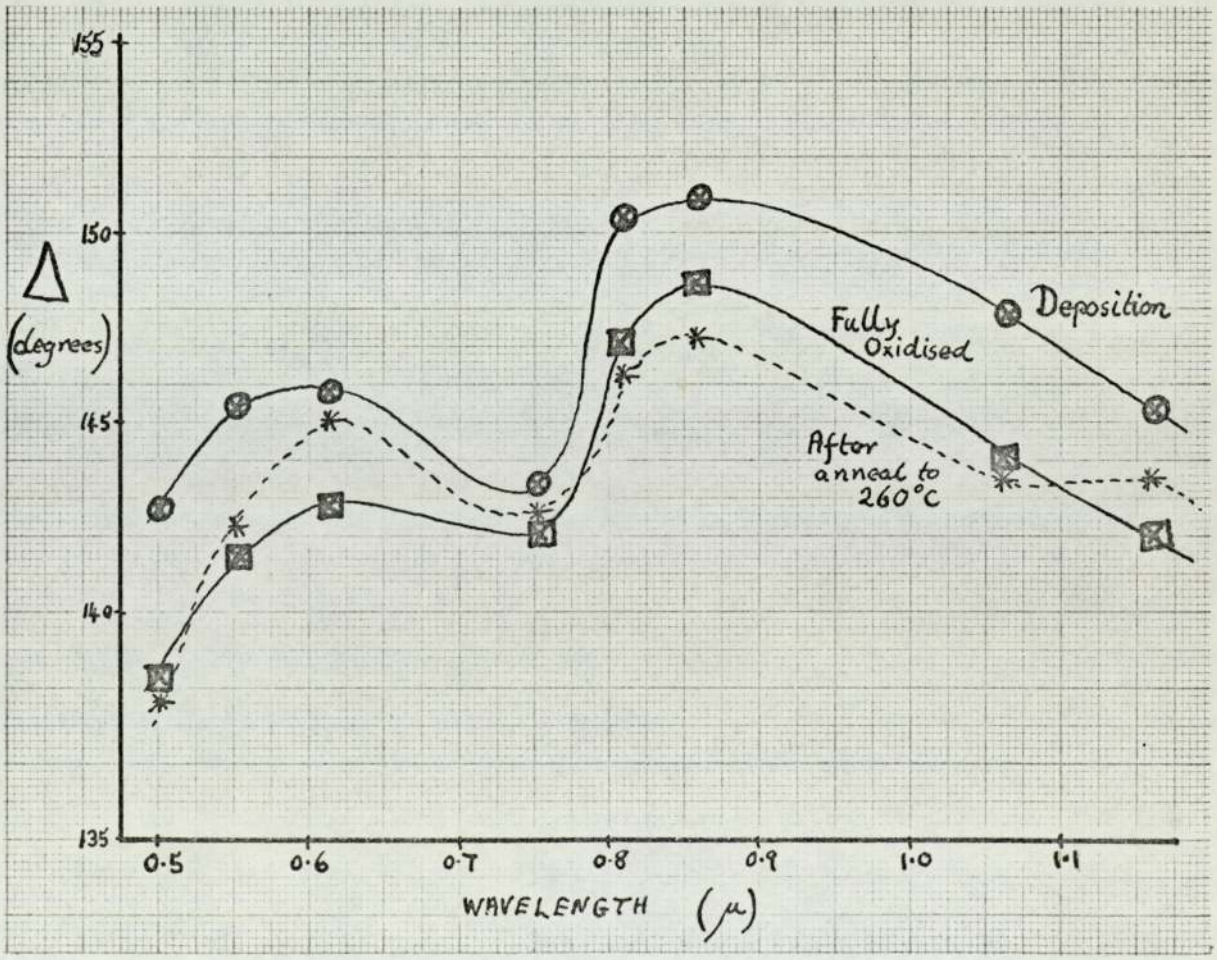

FIG. 61.

VARIATION OF Ψ AND Δ DURING EXPERIMENT (Film 21)

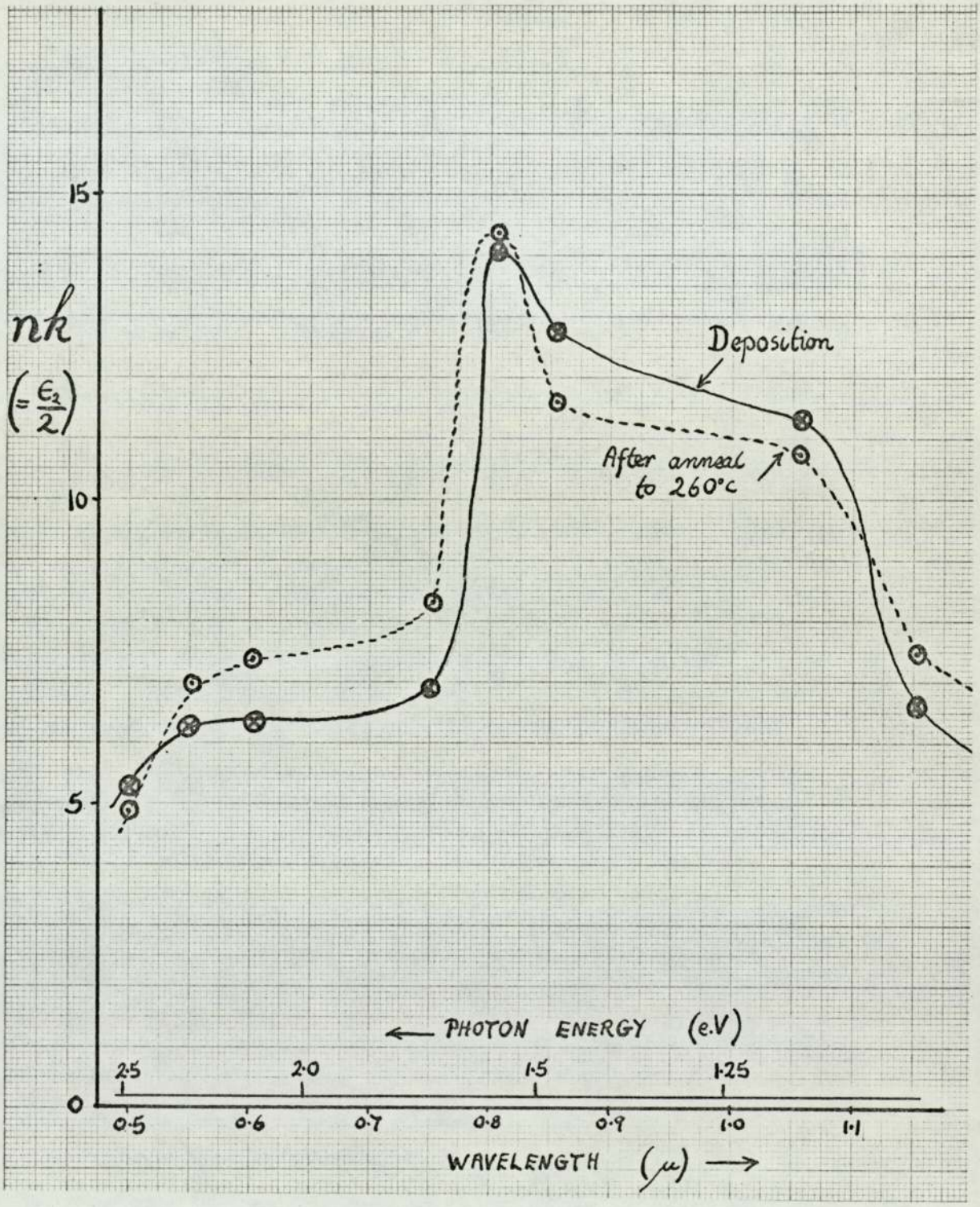

FIG. 62

EFFECT OF ANNEALING ON A ROOM-TEMP.-DEPOSITED FILM
(Film 21)

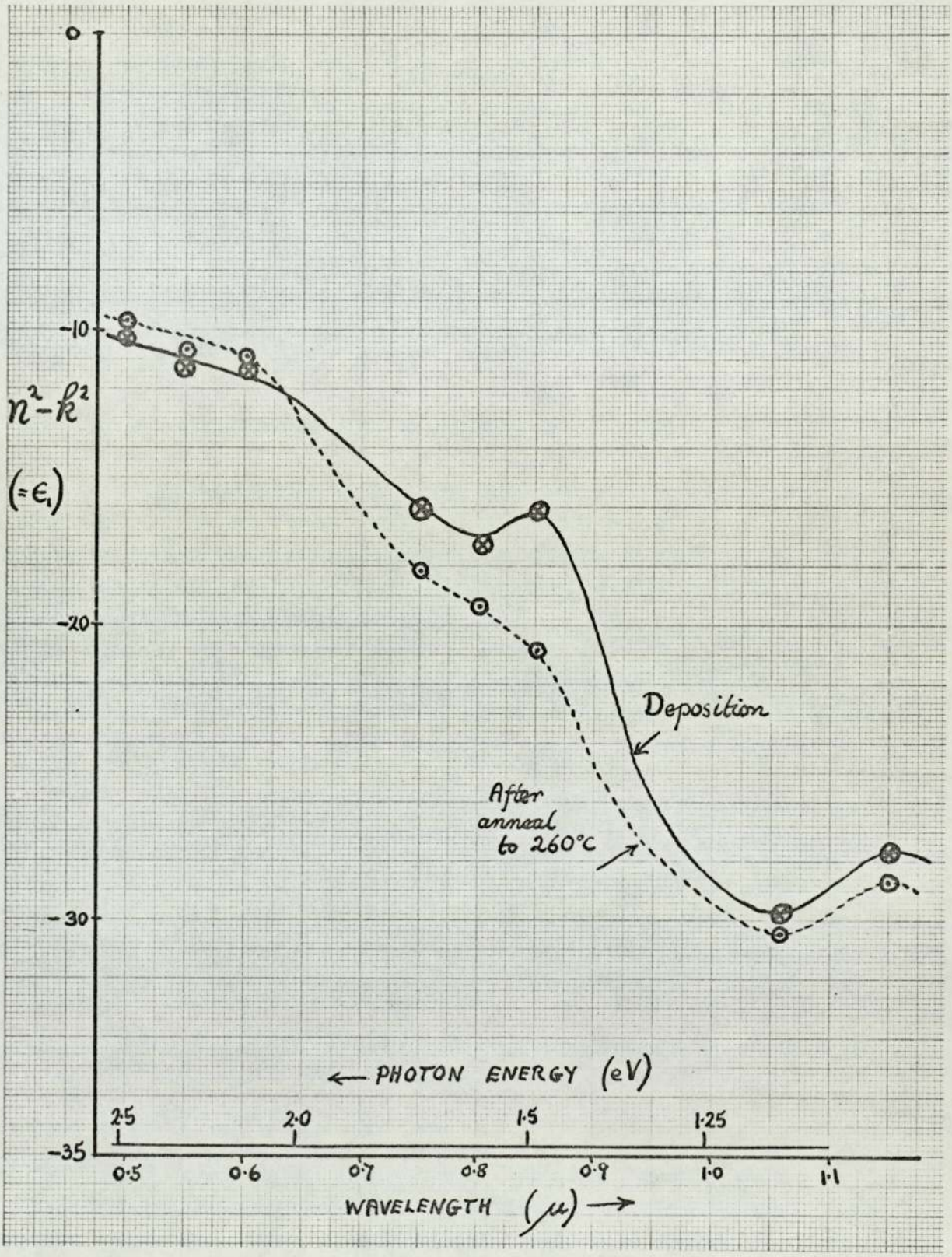

FIG. 63.

EFFECT OF ANNEAL ON n^2-k^2. (Film 21).

TABLE 9 Film 21 275°A Room Temperature Deposition

Wavelength (μ)		Deposition at Room Temperature	Room Temperature After 260°C Anneal
1.15	n	1.25	1.35
	k	5.28	5.53
1.056	n	1.93	1.88
	k	5.85	5.83
0.851	n	2.65	2.27
	k	4.80	5.10
0.804	n	2.88	2.76
	k	5.02	5.20
0.753	n	1.58	1.74
	k	4.32	4.60
0.604	n	1.66	2.01
	k	3.79	3.88
0.549	n	1.65	1.83
	k	3.77	3.78
0.499	n	1.48	1.36
	k	3.54	3.54

parallel to the plane of the films, specimens were deposited on to single crystal slabs of potassium bromide, as proposed by Landry and Mitchell.[133] Initially, films of various thicknesses were deposited at normal incidence on to the polished (100) face of the potassium bromide substrate, which was held at 77°K. From a consideration of the optimum conditions of substrate temperature and evaporation rate needed for the production of single crystal specimens, as established by Landry and Mitchell, it was expected that the specimens would be polycrystalline, and would therefore show similar behaviour to the films described in section 5. However, the advantage would be in the fact that the specimen films could be removed from the substrate and examined by transmission electron microscopy.

6.2.1 Annealing from 77°K (Stage III)

The variations of Ψ , Δ and electrical resistance during the stage III anneal to room temperature were all found to be

similar to those relating to films deposited on glass substrates. For example, Figs. 64 and 65 show the variations of Ψ and Δ for film 26, which, having a thickness of 12 nm, is comparable to film 19, of thickness 11 nm, which was deposited on glass. The values of n and k calculated for film 26 are shown in Table 10. The stage III anneal produced an increase of n and a reduction of k, as before, but the actual individual values of n were lower for films deposited on the crystal. This is explained in a consistent way by considering the greater roughness of the polished crystal surface compared with the glass.

Table 10 also shows the influence of temperature alone on the optical constants. The third column shows the values of n and k with the specimen returned to 77°K after the stage III anneal. The corresponding values of nk are shown in Fig.66 and it may be observed that the effect of temperature on nk is negligible at 0.549 nm wavelength as was previously observed in section 6.1.

TABLE 10 Optical Constants of film 26 (12 nm on KBr)

Wavelength		Deposition at 77°K	Room Temperature After Stage III	Return to 77°K After Stage III
1.94	n	1.30	1.75	1.68
	k	8.01	13.60	12.40
1.15	n	0.36	0.45	0.41
	k	4.50	8.26	7.76
1.056	n	0.41	0.62	0.55
	k	5.50	6.90	6.30
0.851	n	0.39	0.56	0.37
	k	5.60	8.06	7.60
0.804	n	0.35	0.65	0.39
	k	5.40	7.90	7.75
0.549	n	0.10	0.45	0.43
	k	5.20	6.70	6.80

However, the effect at other wavelengths indicates a smaller value of n and k, and hence of nk, for the lower temperature. This observation is consistent with direct measurements of optical absorption, which is proportional to nk, made for aluminium

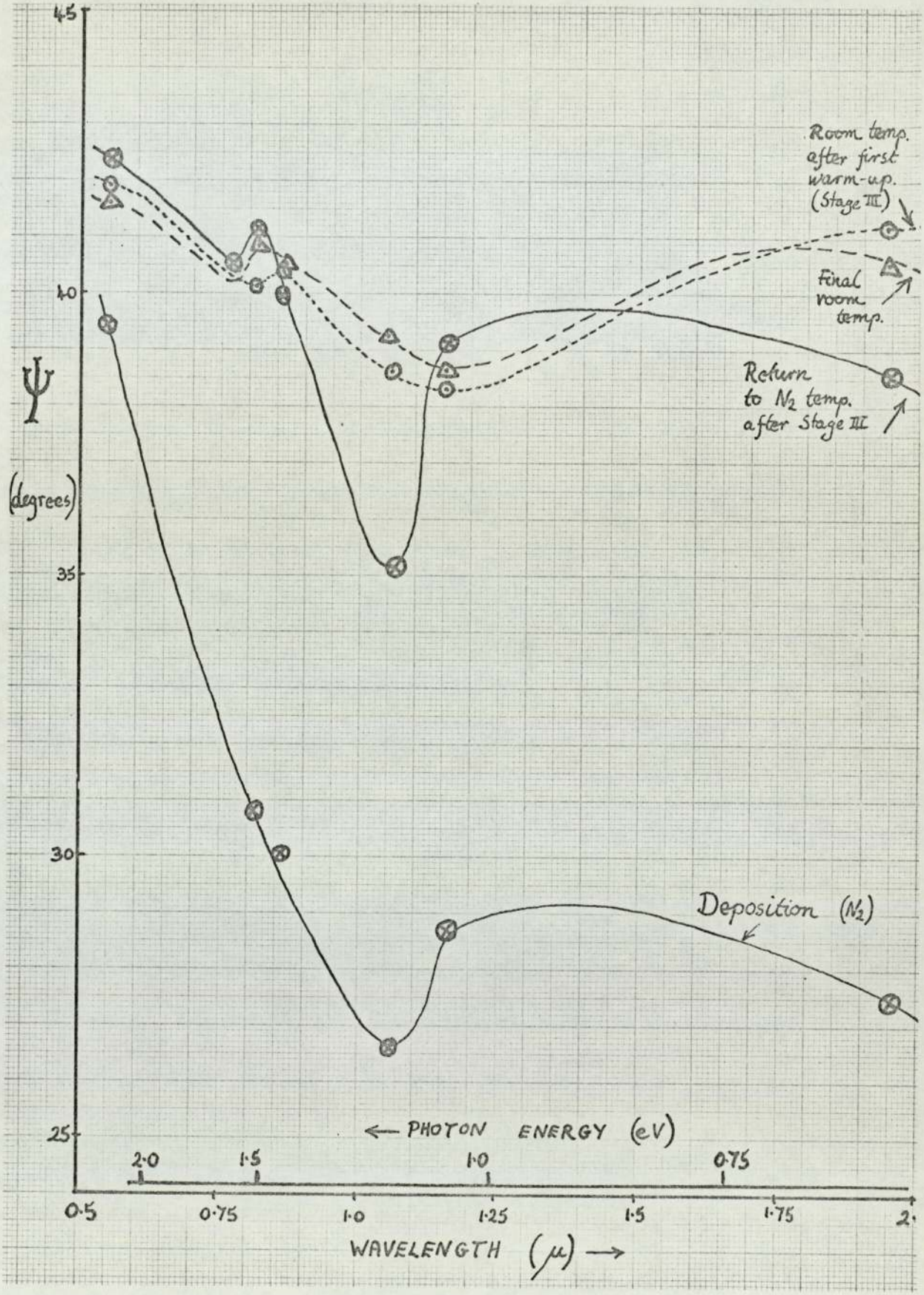

FIG. 64.

VARIATION OF Ψ ON KBr SUBSTRATE (Film 26)

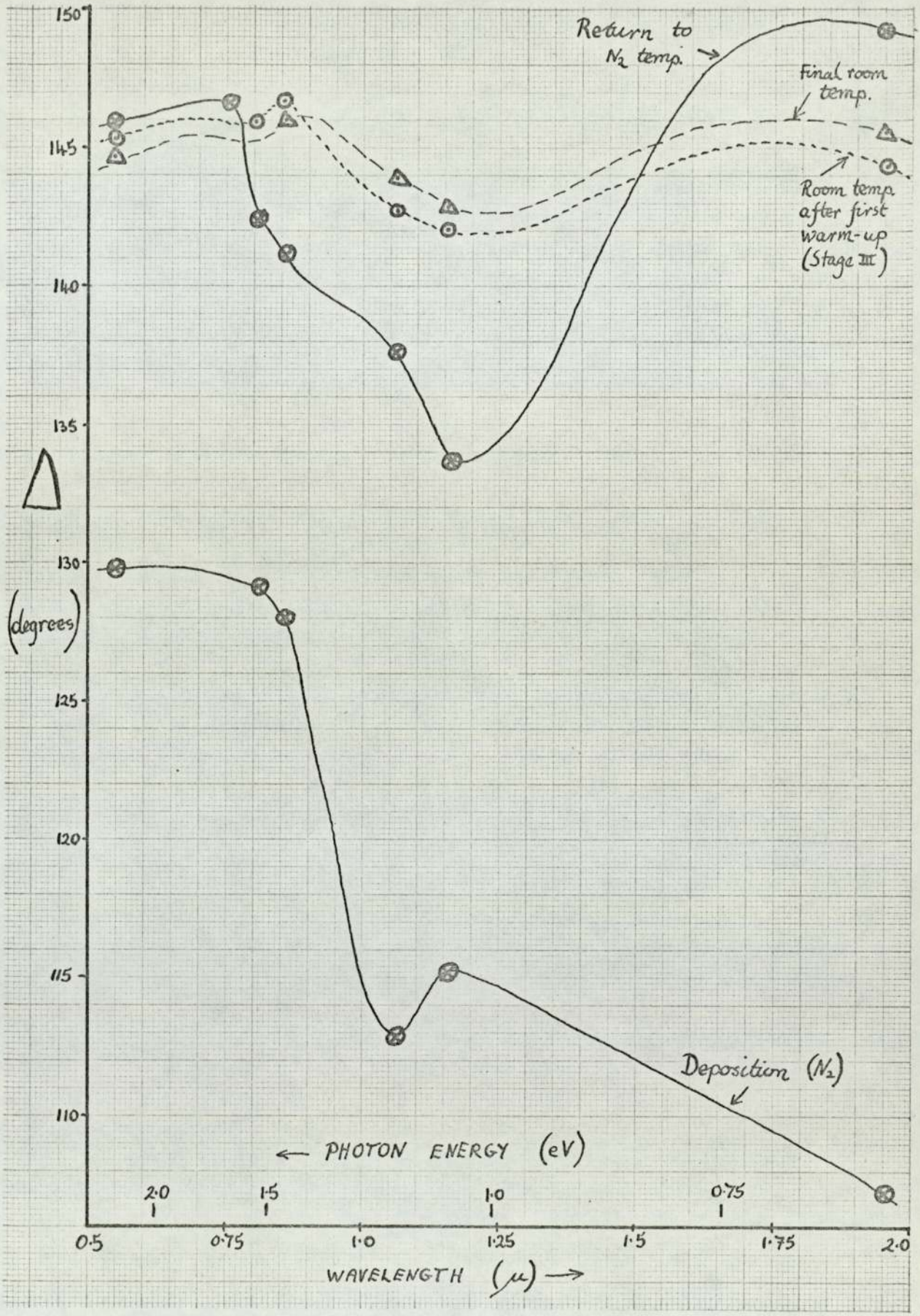

FIG. 65

VARIATION OF Δ ON KBr SUBSTRATE (Film 26)

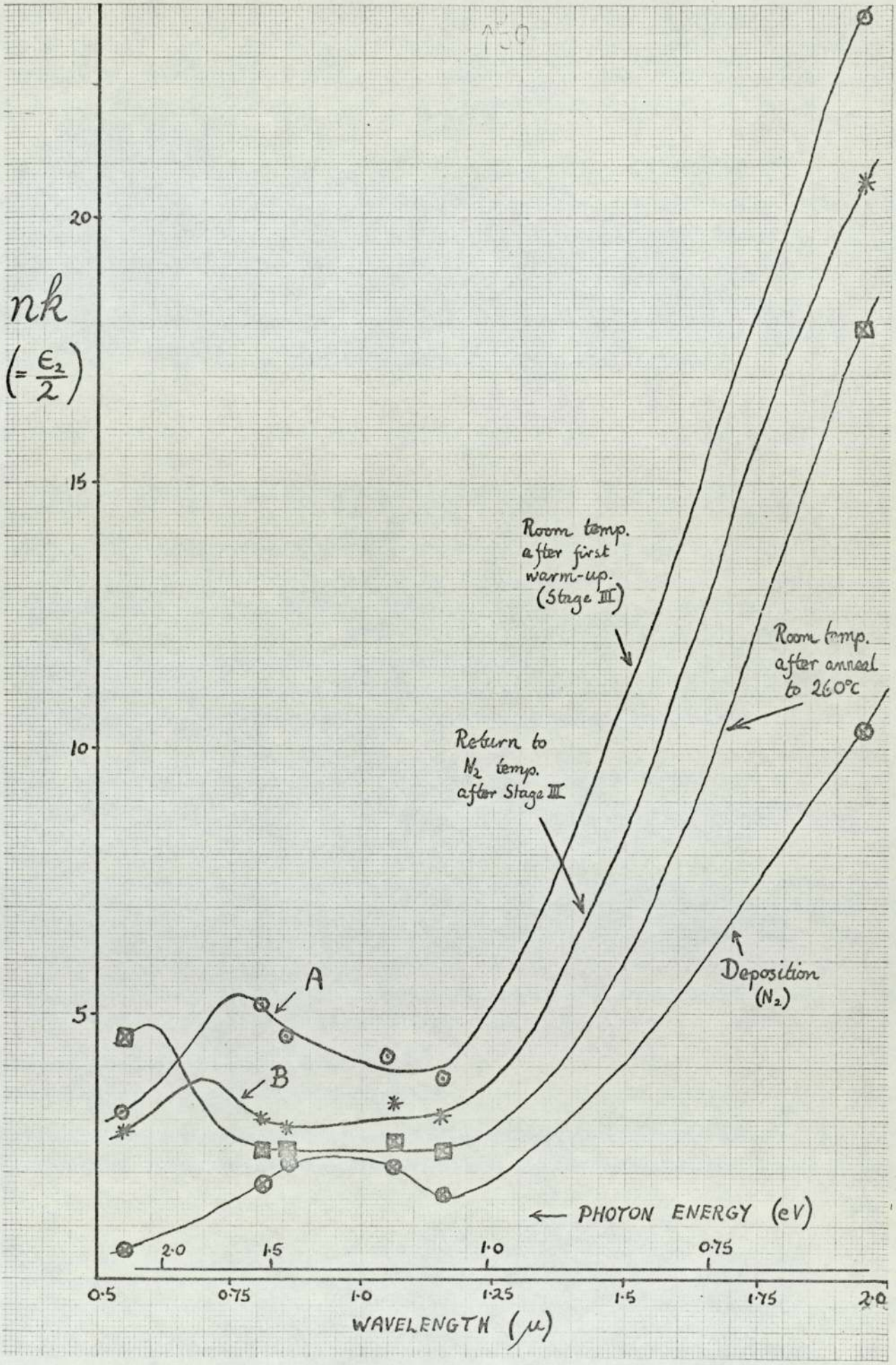

FIG. 66. VARIATIONS OF nk (Film 26)

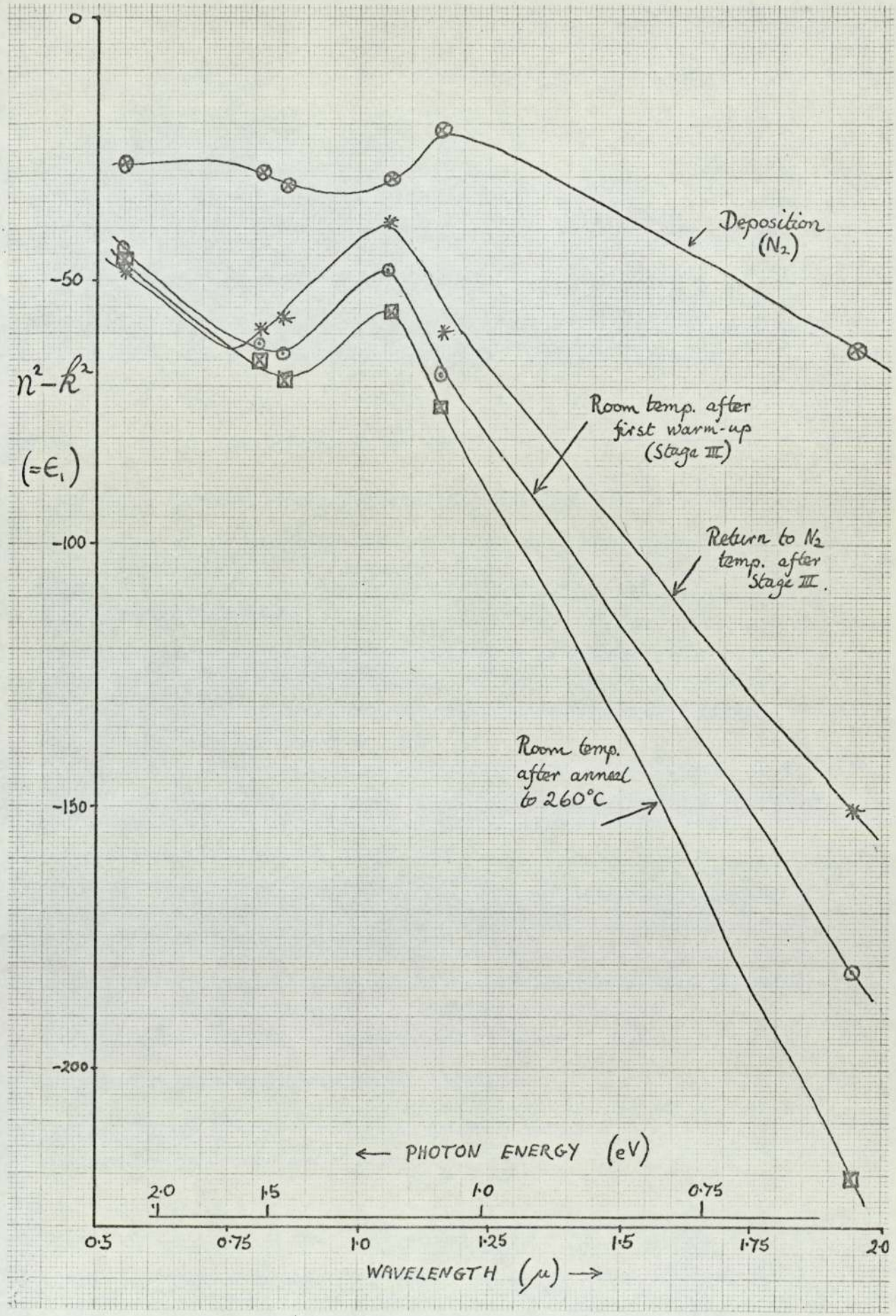

FIG. 67. VARIATIONS OF n^2-k^2 (Film 26)

by Hodgson[147] and more recently by Liljenval.[125A] (See Fig. 12A) Even if the changes of nk and of $n^2 - k^2$ due to temperature are taken into account, Figs. 66 and 67 show more clearly than the results of film 19 that the effect of the stage III anneal is to increase the magnitude of the inter-band absorption and also to shift the peak towards shorter wavelengths. They also indicate that the inter-band peak occurs at a wavelength of 0.95μ on deposition, a value comparable to that observed for film 19, which was of similar thickness, but considerably longer than the 0.8μ expected for bulk aluminium. These observations will be discussed later.

TABLE 11 Effect of annealing to 260°C (film 26)

Wavelength (μ)		Room Temperature Before anneal to 260°C	Room Temperature After anneal to 260°C
1.94	n	1.75	1.20
	k	13.60	14.95
1.15	n	0.45	0.27
	k	8.26	8.64
1.056	n	0.62	0.35
	k	6.90	7.45
0.851	n	0.56	0.27
	k	8.06	8.27
0.804	n	0.65	0.30
	k	7.90	8.01
0.549	n	0.45	0.43
	k	6.70	6.80

6.2.2 High Temperature Annealing

The variation of Ψ and Δ as a result of annealing to 260°C on the totally oxidised film 26 is shown in Figs. 68 and 69 respectively. The corresponding changes of n and k are found to be opposite in form to those of film 19 and all the other films deposited on glass, namely a reduction in the value of n and an increase in the value of k. These changes are shown in Table 11, while the corresponding variations in nk and $n^2 - k^2$ may be seen

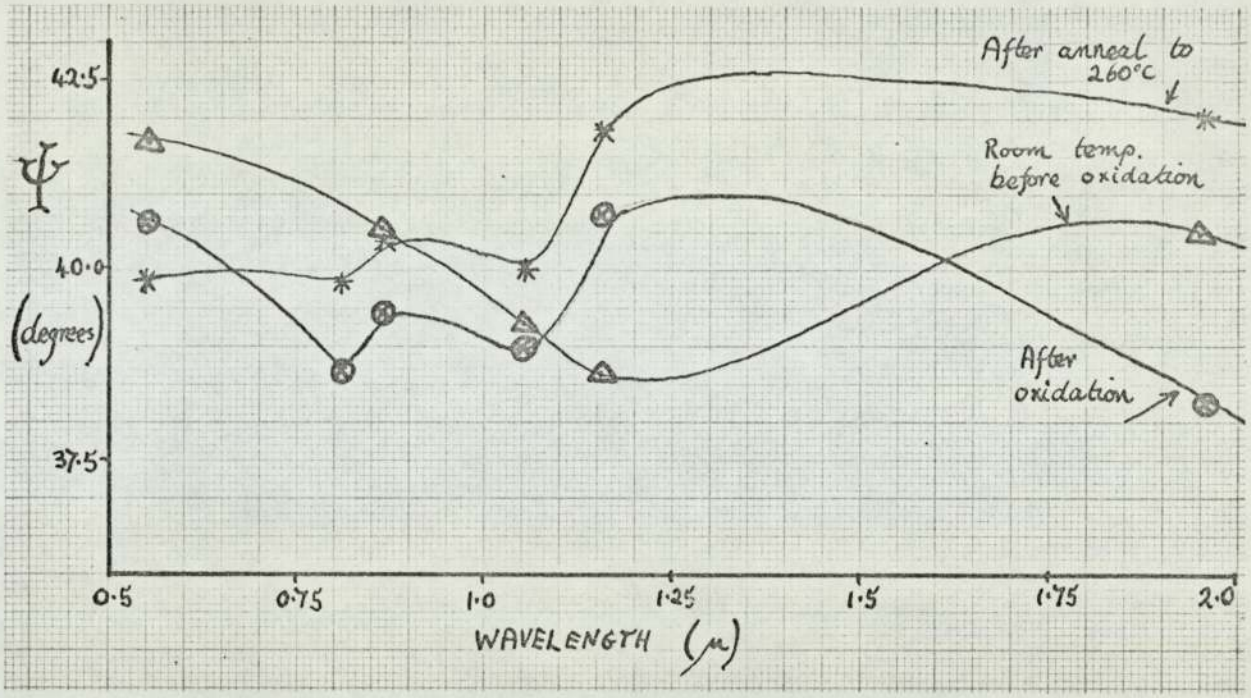

FIG. 68

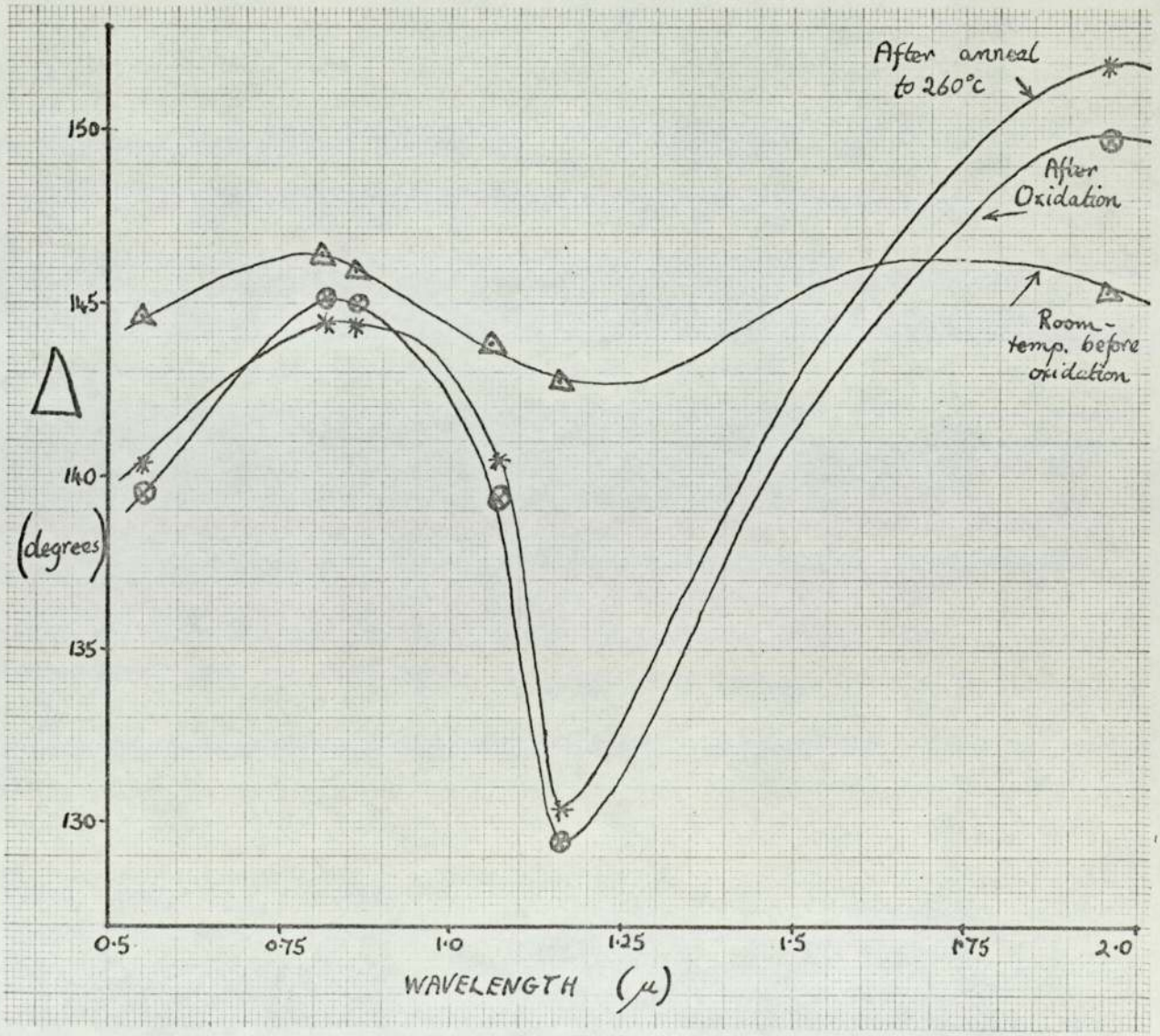

FIG. 69 OXIDATION AND 260°C ANNEAL OF FILM 26.

in Figs.66 and 67. It is observed that in common with films deposited on glass, the 260°C anneal produces a shift of the inter-band contribution to nk and $n^2 - k^2$ towards shorter wavelengths, but the essential difference lies in the fact that the free electron contribution to both nk and $n^2 - k^2$ becomes less. Exactly the opposite effect is observed for all films deposited on glass substrates.

The most probable explanation lies in the different coefficients of thermal expansion for the different substrates, which has been referred to previously in section 5.5. The mean strain induced by a rise in temperature ∂T is given by Wilcock et al.[133] as

$$\epsilon = (\alpha_f - \alpha_s)\,\partial T \qquad (7)$$

where α_f and α_s are the linear thermal coefficients of expansion for the film and substrate respectively. The mean coefficient of expansion for aluminium over the temperature range 20 to 300°C is 27×10^{-6} per °C (Handbook of Chemistry and Physics: Chemical Rubber Publishing Co.) and the corresponding value for Corning 0211 glass is 7.2×10^{-6} per °C (Manufacturers' data). With these values, a mean compressive strain of 0.8% is obtained for film deposited at -196°C. The known elastic limit for bulk aluminium is 0.15%, but studies of the mechanical properties of thin films of gold and silver by Menter and Pashley[154] have shown that the elastic limit for a thin film is several times larger than the bulk value. It seems reasonable, therefore, to conclude that the elastic limit is just exceeded during the high temperature anneal for films deposited on glass, and that this leads to some multiplication of dislocations and a permanent set in the film.

On the other hand, the mean coefficient of thermal expansion of potassium bromide crystal over the same temperature range is 40×10^{-6} per °C (American Institute of Physics Handbook). This

value is larger than that for aluminium so that the effect of the substrate would be expected to differ from the previous case. The results of Table 11 show that the value of n decreases while the value of k becomes greater, indicating further annealing of the film, and a removal of defects.

The electrical resistance of film 26 throughout the experiment is shown in Fig.70. The initial warm-up from 77°K (the stage III anneal) produced, as before, a fall of resistance of approximately 45% of the initial value. The activation energy, estimated at a mean temperature of 188°K was found to be 0.12 eV. This activation energy is shown compared to that of other films in Fig.48.

As with all previous films, deposited at 77°K, the high temperature anneal to 260°C produced an increase of resistance. The explanation of this rise is not certain. One possibility is suggested by the transmission electron micrograph of film 26 which is shown in Fig.80. The micrograph shows a number of cracks in the film which may have been caused by the comparatively greater expansion of the substrate producing fracture of the film. Calculations using equation (7) indicate that the expansive strain is 0.6% so that the elastic limit is exceeded.

6.2.3 Effect of Film Thickness

Table 12 shows the values of n and k for three films of thickness 35.0, 12.0 and 6.0 nm immediately after deposition at 77°K on the (100) face of a potassium bromide slab. The corresponding values of nk, related to the optical absorption, are plotted in Fig.71, and indicate that with increasing film thickness the total value of nk decreases, and the inter-band component develops. Even so, at a film thickness of 35 nm (almost equivalent optically to bulk aluminium) the inter-band peak is very broad compared to that of normal bulk metal and is centred at a longer wavelength of approximately 1.0μ .

This effect is also demonstrated in Fig.72 which shows the values of n for the same three films throughout the spectral range investigated.

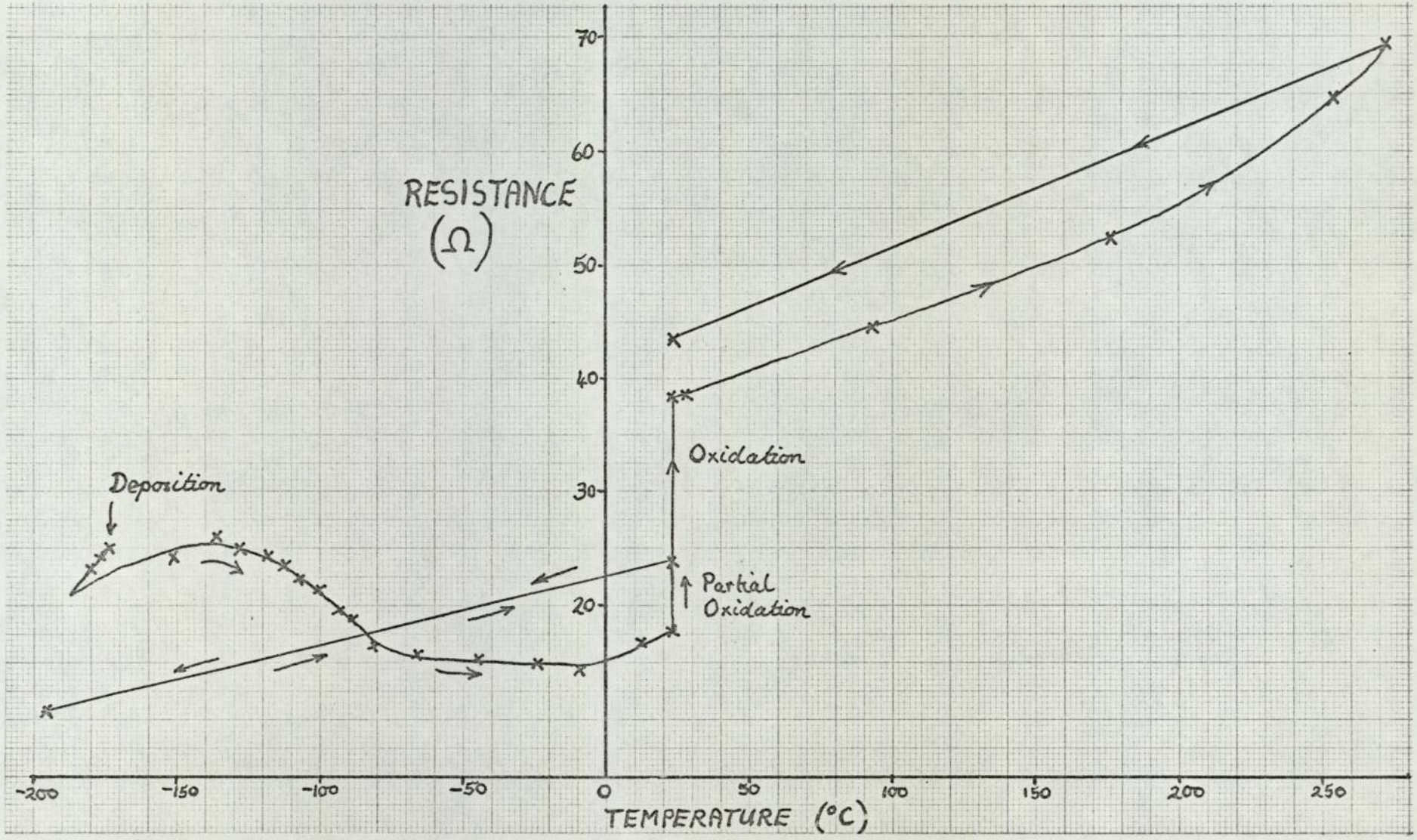

FIG. 70. VARIATION OF RESISTANCE OF FILM 26.

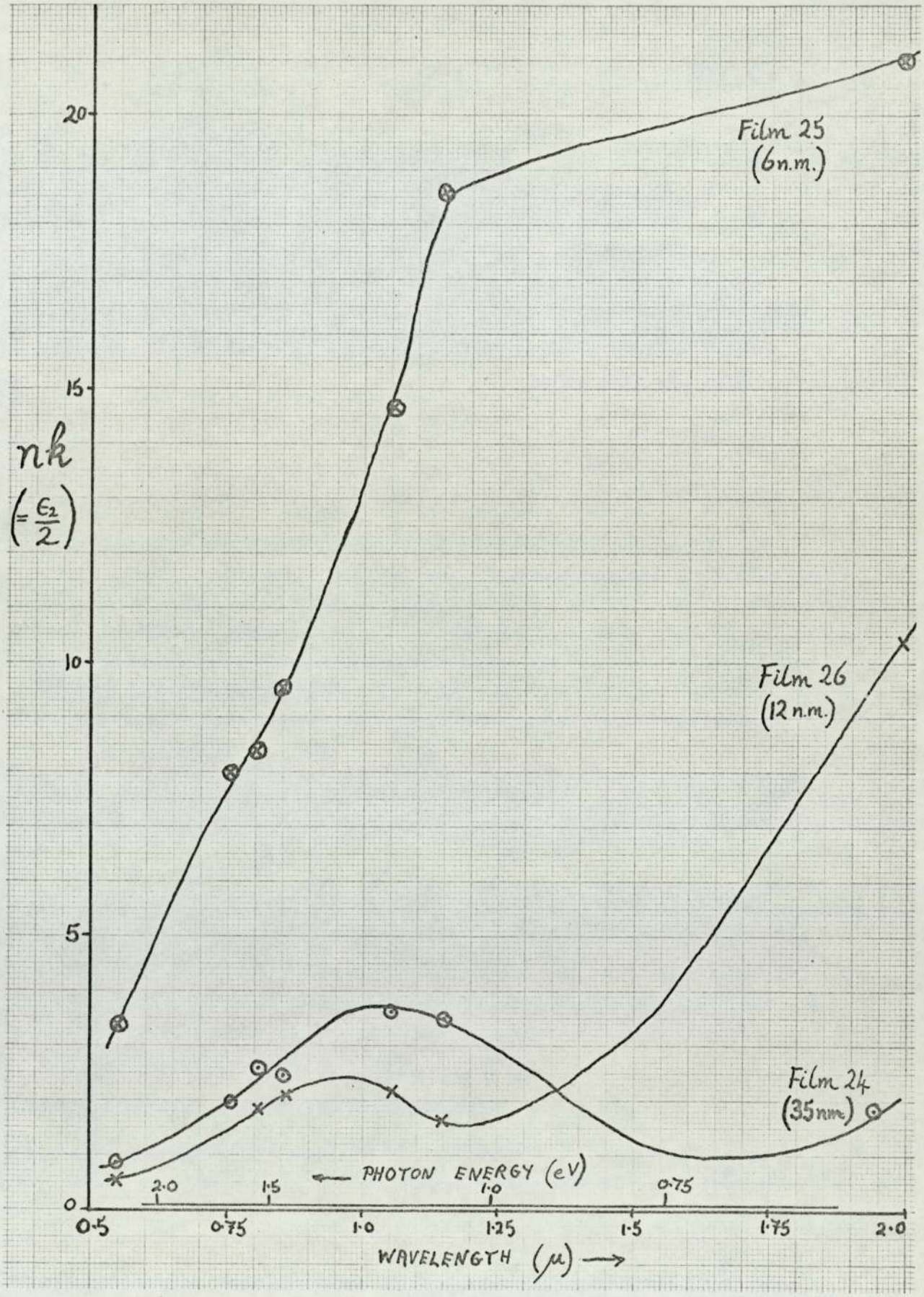

FIG. 71

EFFECT OF FILM THICKNESS ON DEPOSITION VALUES OF nk.

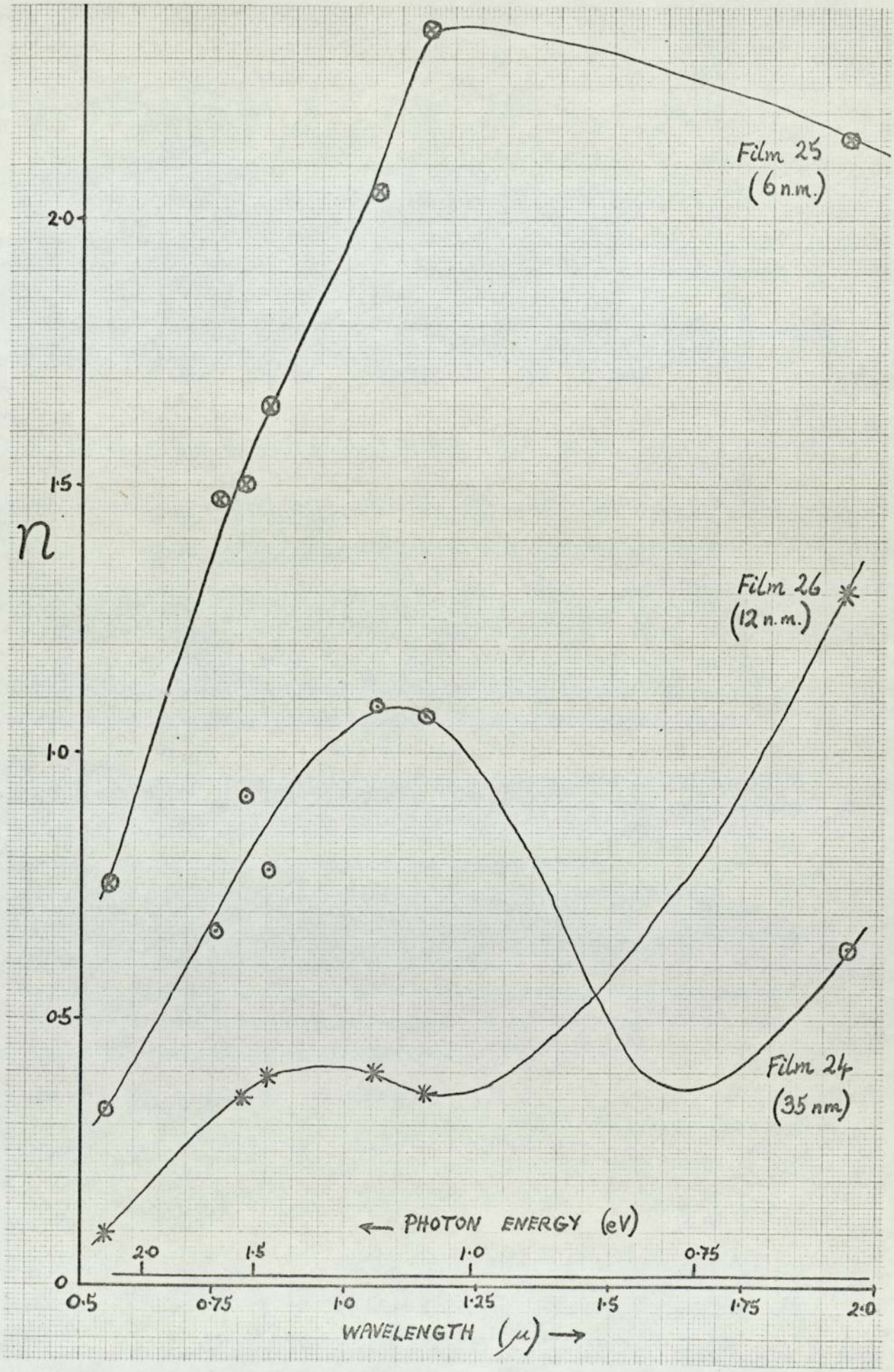

FIG. 72

EFFECT OF FILM THICKNESS ON DEPOSITION VALUES OF n

TABLE 12 Effect of film thickness on values of n and k on deposition at 77°K

Wavelength (μ)		Film 24 (35.0 nm)	Film 26 (12.0 nm)	Film 25 (6.0 nm)
1.94	n	0.63	1.30	2.15
	k	2.87	8.01	9.8
1.15	n	1.07	0.36	2.35
	k	3.28	4.50	7.9
1.056	n	1.09	0.41	2.05
	k	3.32	5.50	7.00
0.851	n	0.77	0.39	1.65
	k	2.96	5.60	5.80
0.804	n	0.93	0.35	1.50
	k	2.84	5.40	5.60
0.549	n	0.33	0.10	0.75
	k	2.62	5.20	4.55

6.2.4 Discussion

In the interpretation of the above results, the effects of film thickness and also of annealing have to be considered. Both are seen to affect the observations in similar ways and are therefore likely to be associated with the transition from a disordered to a more highly ordered state.

The effect of film thickness on the optical absorption $\epsilon_2 = 2nk$ can be understood in relation to Fig.50, which shows a sketch of the free electron absorption on which is superimposed the inter-band absorption peak. Comparing Figs. 71 and 50, it can be seen that the effect of increasing the film thickness from 6 nm to 35 nm is to decrease the free electron contribution to nk while the inter-band contribution becomes increasingly more significant.

Some insight into the changes that occur with film thickness may be reached by considering the published results of Miller[115] on liquid aluminium, shown in Fig.73. Curve A represents the measured optical absorption for liquid aluminium while curve B shows the accepted absorption for bulk solid aluminium. The liquid metal shows no trace of the absorption peak at 1.5 eV and it may be concluded that structure in the density of states curve near the

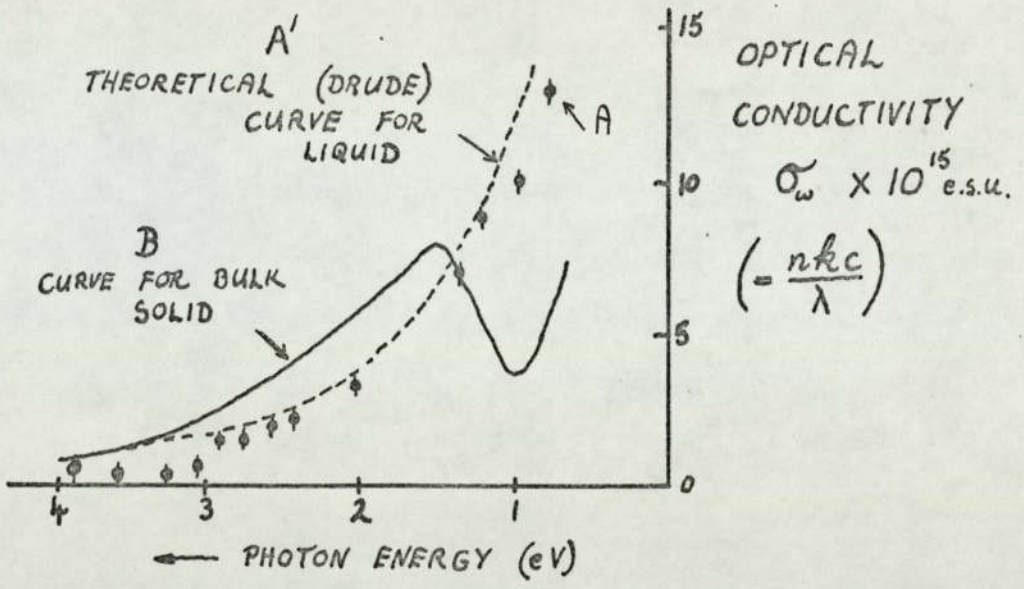

FIG. 73 A COMPARISON OF nk FOR SOLID AND LIQUID

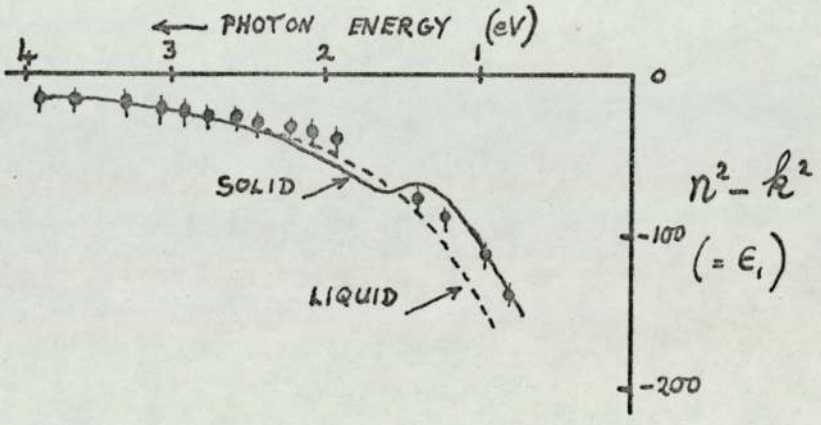

FIG. 73B COMPARISON OF n^2-k^2 FOR SOLID AND LIQUID (after MILLER)

Fermi energy is almost entirely absent. The band structure develops as the metal becomes solid, leading to an overall reduction in the absorption due to the free electrons, but a considerable increase of absorption in the inter-band region.

This is precisely the effect observed with increasing film thickness in section 6.2.3. The indication is, therefore, that very thin films deposited at 77°K are very disordered, almost liquid-like and possess little band structure. As the thickness increases and the films become more ordered, possibly an auto-epitaxy effect, the band structure takes shape and the inter-band absorption peak develops.

The results of section 5, shown in Table 1, are consistent with the above explanation. The measurements taken at a wavelength of 549 nm (i.e. an energy of 2.5 eV) occur on the tail of the inter-band peak where an increased film thickness would be expected to lead to a higher measured value of nk. This is seen to be the case. The results of Neal et al.[114] for films deposited at 77°K also indicate, as a general trend, that increased film thickness leads to larger values of nk.

Band structure is a consequence of short-range order and the preservation of the band structure for a certain degree of disorder has been shown theoretically by Gubanov.[155] Such preservation is inherent in the tight-binding approximation where the interactions of only a few neighbours are used to calculate an approximate band structure. However, certain results of measurements of the optical absorption of germanium and silicon made by Davis and Shaw[156] indicate that the concept of E, k curves and energy surfaces may break down in certain directions in a disordered material, while remaining valid in others. It is possible, therefore, that the specimen films deposited at 77°K retained sufficient structure in the [111] direction to provide recognisable electron diffraction patterns (as discussed in section 1.3) but that the band structure was suppressed in the region of the symmetry point W and along the

[110] direction so that the optical absorption peak at 1.55 eV, which originates from these regions, is absent. As the order in the crystal lattice is improved, either as a result of increased film thickness or as a result of annealing, the true band structure of aluminium develops and the inter-band absorption peak appears.

The changes may be considered with reference to Fig.74A which shows the face-centred-cubic lattice of aluminium and Fig.74B which shows a detailed portion of the Brillouin zone. It is known from the X-ray diffraction studies of Black and Cundall[157] that the nearest neighbour order is preserved in liquid aluminium. It is the next-nearest neighbour order which is affected. In particular, the order in the (111) planes is preserved while the order in the (200) planes is destroyed. It should be noticed (Fig.74A) that the (200) planes constitute the next-nearest neighbour positions so that if this periodicity is lost, then the (200) Bragg reflection plane, which forms the (100) face of the Brillouin zone (Fig.74B), ceases to have meaning. The point W, which contributes to the optical absorption, lies on this (200) Bragg reflection plane. It might be expected, therefore, that loss of next-nearest neighbour order would lead to loss of band structure around W and a large reduction in the optical inter-band absorption. As the periodicity of the (200) planes of the lattice improved, the optical inter-band absorption peak would develop.

Furthermore, it might be expected that the V_{200} component of the pseudopotential, which depends on the periodicity of the (200) lattice planes, would be reduced if these planes were disordered. As the structure improved, the values of $|V_{200}|$ would be expected to increase and the energy of maximum optical absorption, shown to be $2 \times |V_{200}|$, would also increase so that the absorption peak would move to higher energy (i.e. shorter wavelength).

The changes in the inter-band contribution to optical absorption brought about by annealing are shown most clearly in Fig.66 for a film deposited at 77°K and in Fig.62 for a film

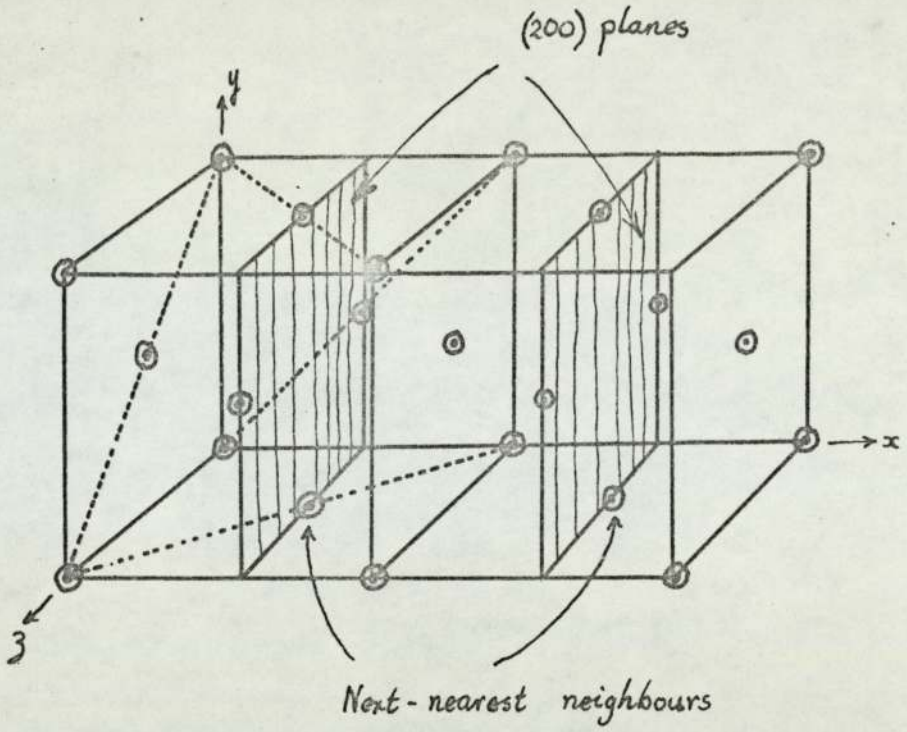

FIG. 74A FACE-CENTRED CUBIC LATTICE.

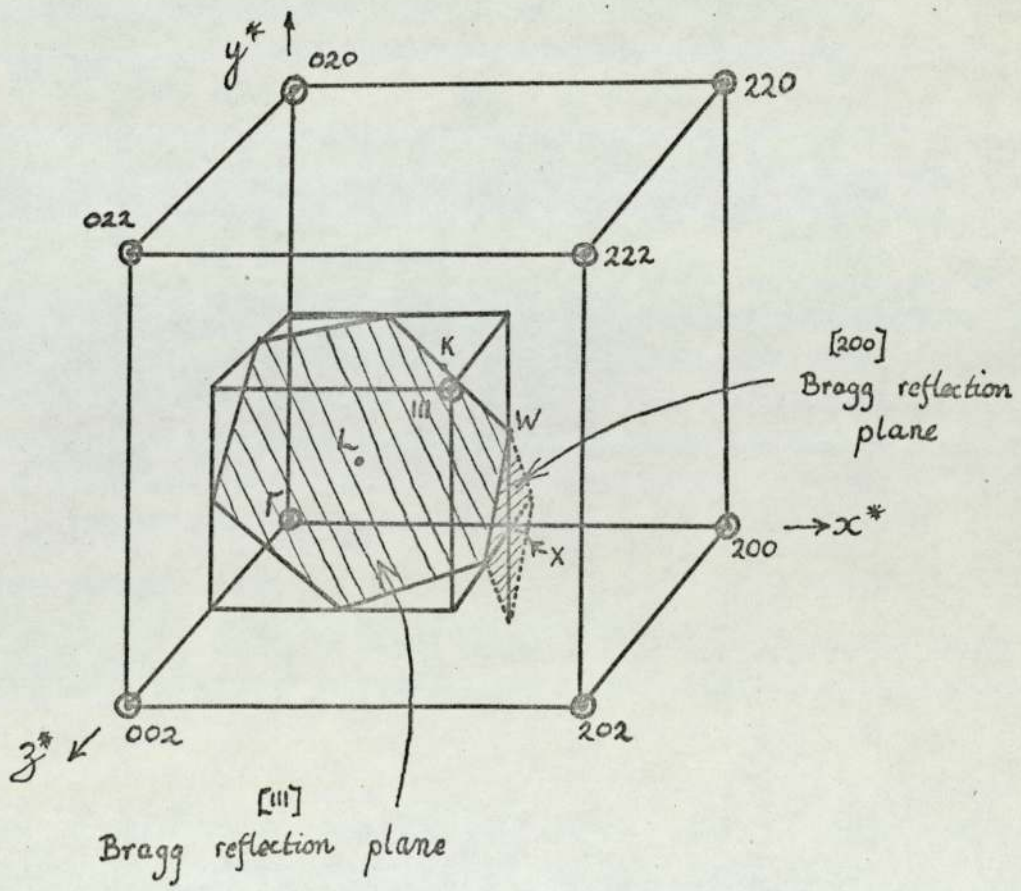

FIG. 74B PART OF BRILLOUIN ZONE FOR ALUMINIUM.

deposited at room temperature. In all cases the effect of annealing is the same; whether the stage III anneal from 77°K to room temperature, or the high temperature anneal to 260°C. The inter-band peak in the nk curve for a just-deposited film occurs at lower energy than the value of 1.55 eV expected for bulk aluminium, and the peak is shifted towards higher energy as a result of the anneal.

It is interesting to compare the above observations with the results of Stuke[158] on the variation of the complex part of the dielectric constant, ϵ_2 between amorphous and crystalline germanium, which are reproduced in Fig.74c. It can be seen that in the amorphous phase the absorption peak persists, although some structural detail is lost, and that the peak is shifted to a lower photon energy. Direct measurements of the optical density of states from photoemission experiments made by Donovan and Spicer[159] show consistent differences between the two phases of germanium.

An explanation of these differences has been proposed by Herman and Van Dyke[160] who suggested that the amorphous phase could be considered, to a first approximation, as a dilated germanium crystal. The measured density of amorphous germanium is 3.9 ± 0.4 g.cm^{-3} which is almost 30% less than for crystalline germanium, and corresponds to a dilated lattice constant of $1.11\,a_o$. Using the results of band structure calculations as a function of lattice constant, they calculated the value of ϵ_2 for both the amorphous and crystalline phases of germanium and obtained results in good agreement with the experimental curves of Stuke (Fig.74).

There are several criticisms made of the dilated crystal approximation. Davis and Shaw[156] suggest that the 10% dilation of the lattice constant is excessive, and quote evidence from X-ray diffraction experiments which indicates that the increase of lattice constant is probably less than 3%. However, the work of Donovan and Spicer and of Herman and Van Dyke shows that small changes in the lattice constant can significantly affect the band

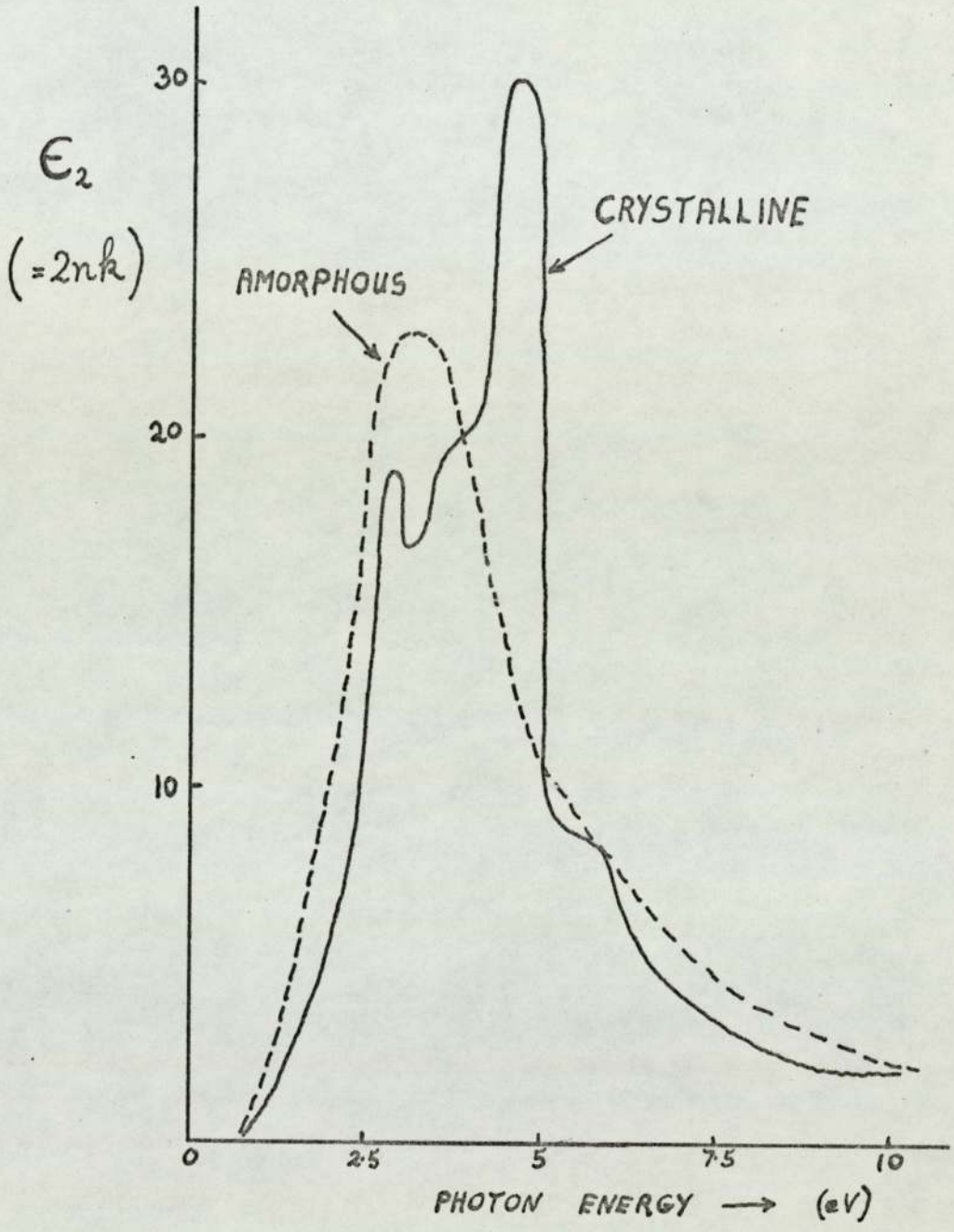

FIG. 74C COMPARISON OF AMORPHOUS AND CRYSTALLINE GERMANIUM. (after STUKE)

structure. This is relevant to the results of this work in view of the fact that thin aluminium films are known to have a lower density than bulk aluminium as shown previously in Fig.47.

It seems more probable that the shift of the inter-band absorption peak towards higher energy as a result of annealing is connected with the ordering of the (200) planes of the crystalline lattice and the development of the energy surfaces in directions in which the band structure was initially almost absent, particularly the (200) Bragg reflection plane as shown in Fig.74B, mentioned previously in this section.

This explanation shows greatest consistency for the case of the stage III anneal which has been attributed to the migration of (100) 'Dumbell' interstitials and their annihilation at vacancies (see section 5.1). The (100) interstitial in the face-centred-cubic structure is shown in Fig.9B and it can be observed that the resulting distortion does effectively act directly on the (200) lattice planes.

The effect of increased temperature on a stable, post-annealed film is known to produce both a decrease in the strength and a broadening of the inter-band absorption peak, as well as a shift of the maximum towards lower energy. (See Fig.12A) The effect is explained by the influence of the Debye-Waller factor on the pseudo-potential components, as discussed in section 2.1. In the present work, the variation in optical absorption due to temperature alone is shown in Fig.66. Curve A applies to a vapour-quenched film that has been annealed to room temperature, while curve B shows this same film returned to $77^{o}K$. The peak is seen to be broader and to occur at lower energy at the higher temperature in agreement with the recent results of Liljenvall et al.[125A] (Fig.12A)

CHAPTER 7

ASSOCIATED TECHNIQUES

7.1 Infra-red Spectrophotometer Results

Direct measurement of optical absorption over an extended wavelength range was made on several films on glass substrates using a PYE SP700 spectrophotometer. A diagram of the optical system of this instrument is shown in Fig.75. One of two lamps constitutes the source, a tungsten filament lamp for use in the visible and near infra-red and a deuterium arc lamp for use in the ultra violet. The change-over point is 0.33μ wavelength. Radiation from the lamp is directed on to the entrance slit of the monochromater by the mirrors M1 and M2. It is then dispersed by a prism (or by a diffraction grating in the 3μ wavelength region) and a narrow band of wavelengths is selected by the exit slit. The photometer works on the principle that the radiation passes alternately through the sample cell S' and the reference cell R', before falling on to a single detector. The output of the detector is amplified and switched between two channels S and R by an electronic switch which is synchronous with the alternation of the beams. Thus each output channel shows the intensity of radiation passing through only one of the cells. The recorder can be arranged to show either the ratio $\frac{S}{R}$, which is the transmittance of the sample cell with respect to the reference cell or the function 2 Log $\frac{S}{R}$, which is the absorbance of the sample cell with respect to the reference cell. The results for selected films, deposited at 77^{o}K on glass substrates, are shown in Fig.76. These may be directly compared with the ellipsometrically determined absorption (nk) shown, for example, in Fig.57, bearing in mind that the spectrophotometer results apply to films which are totally oxidised and have been previously annealed to 260^{o}C. Fig.76 shows that for a thick film the maximum of the interband absorption peak occurs at an energy of 1.55 eV as for bulk aluminium. In the thinner films, when fully oxidised and annealed, the maximum occurs

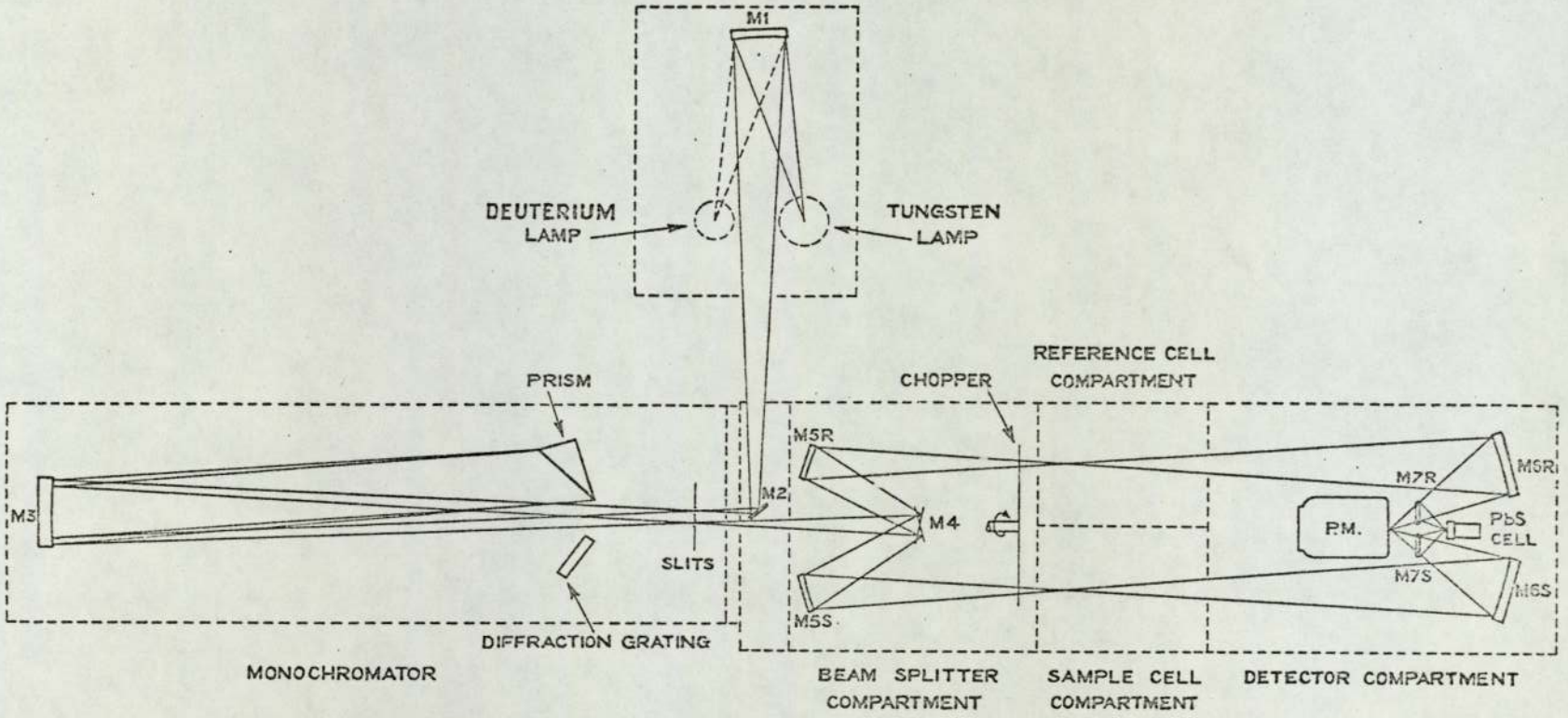

FIG. 75 OPTICAL SYSTEM FOR SP 700 SPECTROPHOTOMETER

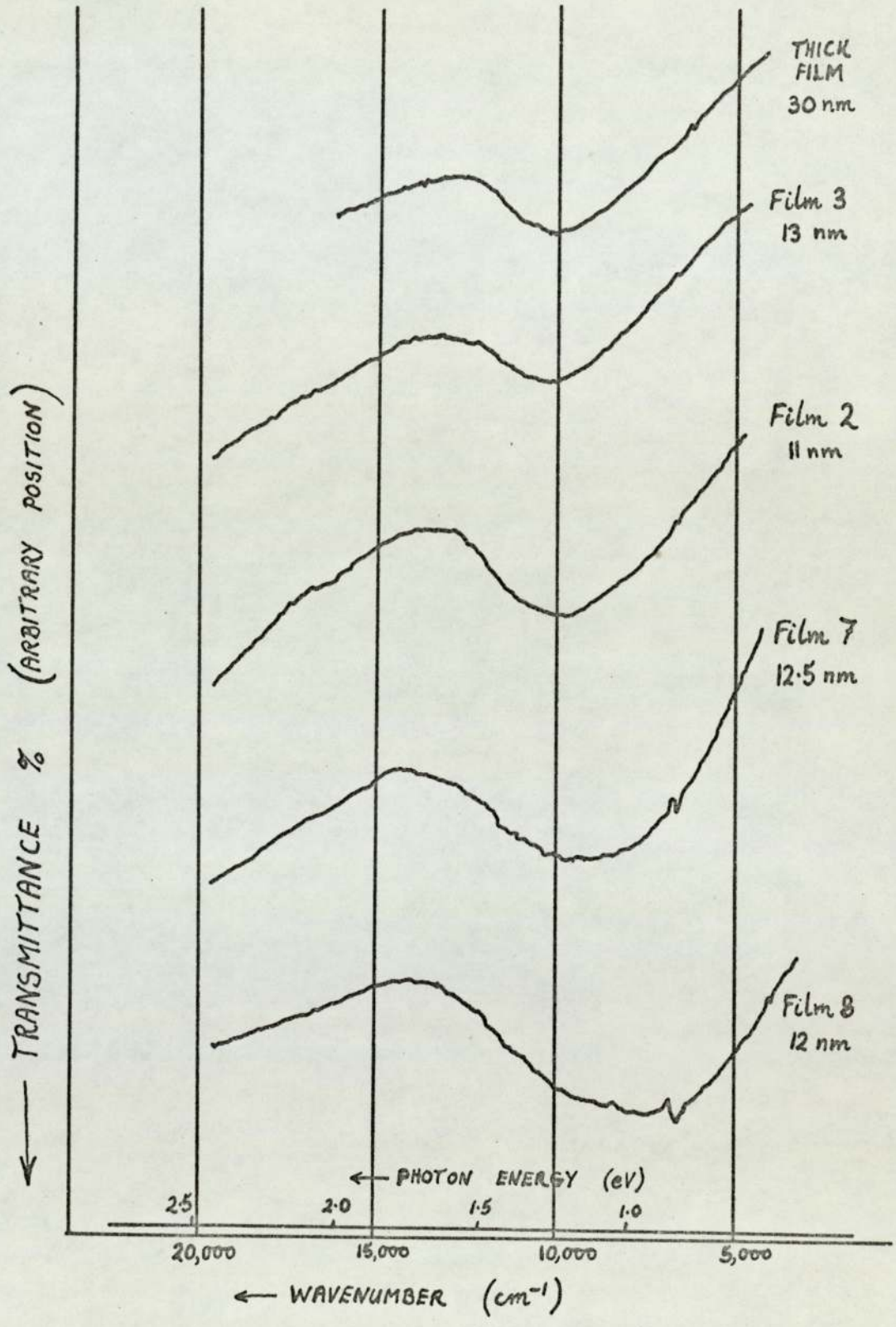

FIG. 76 SPECTROPHOTOMETER RESULTS

at higher energy. The direct effect of annealing to 260°C is indicated on Fig.77. It can be seen that the effect of the anneal is similar for both films. The maximum of the absorption peak is shifted towards higher energy (from 1.65 eV to around 1.75 eV in both cases). This shifting of the peak due to annealing is consistent with the ellipsometric results of section 6.

7.2 Electron Microscopy

As mentioned in section 1.2, it is desirable that an estimate of grain size be made where possible. Therefore, the films deposited at 77°K on the potassium bromide crystal substrates were 'floated' from the crystal by dissolving it in a suitable solvent. Water was found to produce great damage in such tenuous metal films, but methyl alcohol was found to be suitable. As an example, Fig.78 shows a transmission electron micrograph of film 24 taken on an E.M.6 microscope. The film, after all annealing experiments have been completed, is seen to have a mean grain size of approximately 40.0 nm.

An electron diffraction pattern, taken from the same area as that shown in Fig.78, is shown in Fig.79. An analysis of the ring pattern is set out in Table 13 below.

TABLE 13 Analysis of Diffraction Rings (film 24)

Ring Number	Diam. (cm)	Radius (cm)	d (Å)	A.S.T.M. for d	Planes
			–		(111)
			–		(200)
1	2.02	1.01	1.44	1.43	(220)
2	2.40	1.20	1.20	1.22	(311)
			–		(222)
			–		(400)
3	3.28	1.64	0.88	0.93	(331)
			–		(420)
			–		(422)
4	3.92	1.96	0.735	0.78	(511)

The fourth column shows the inter-planar spacing, d calculated from the radii of the diffraction rings, r, from the

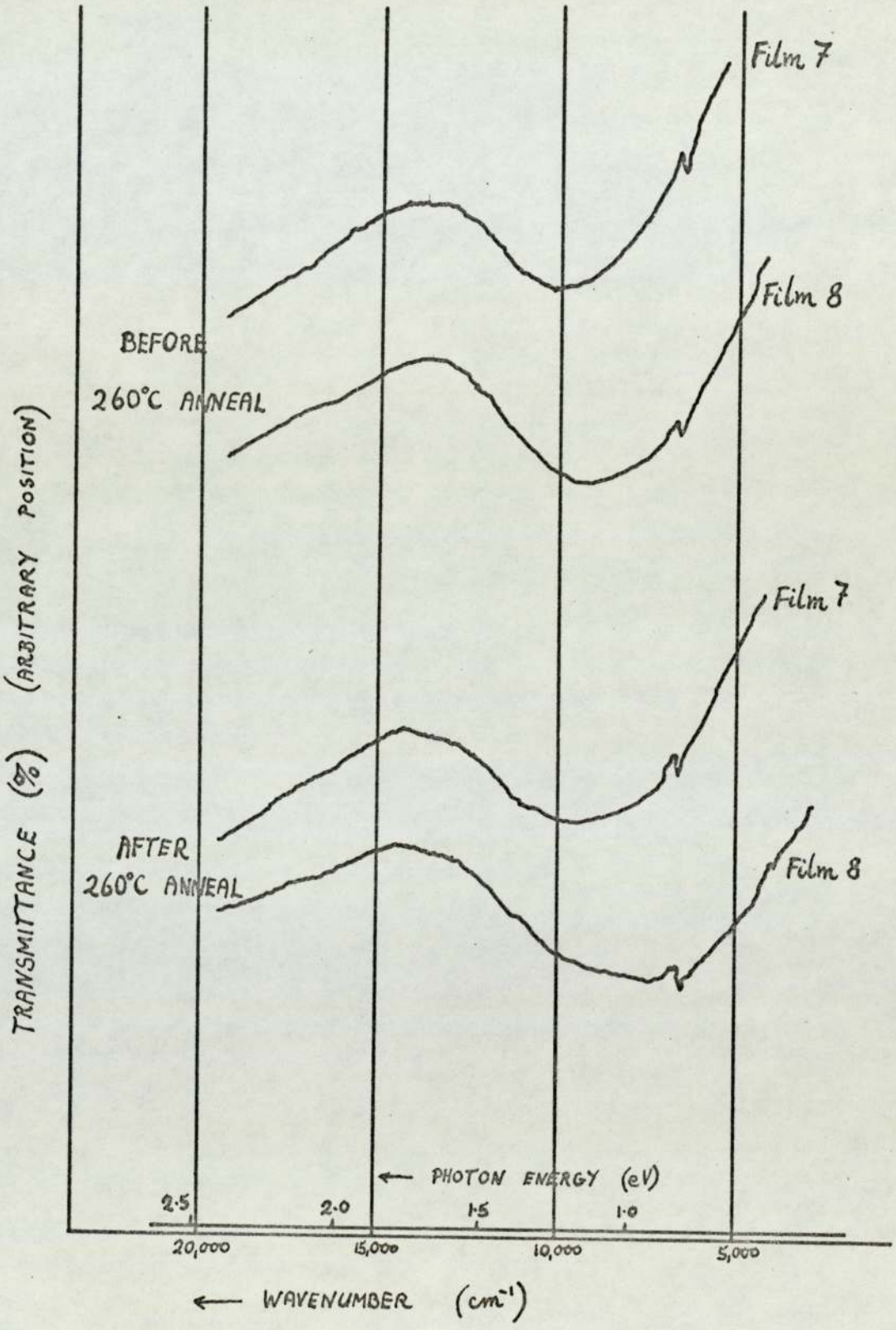

FIG. 77 EFFECT OF ANNEALING OF FILMS 7 AND 8.

FIG. 78 Electron micrograph of film 24.
55,000 X

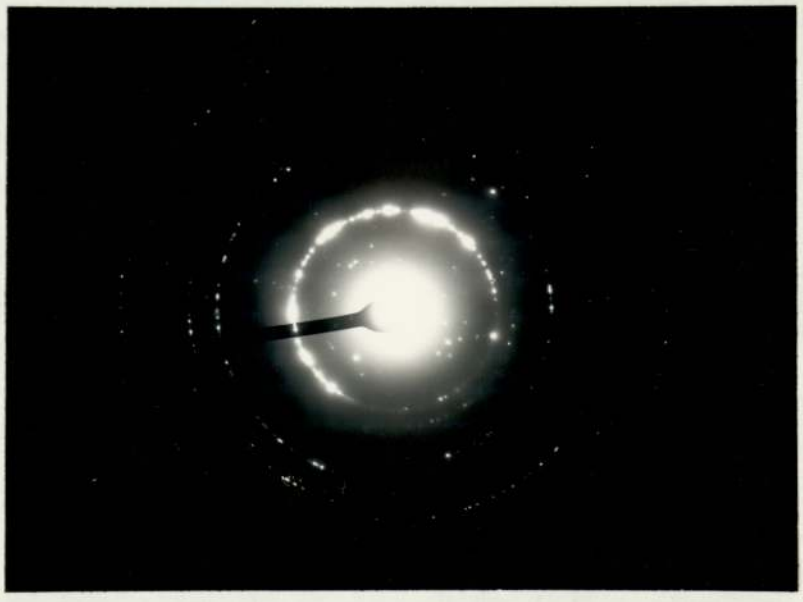

FIG. 79 Diffraction pattern of the same area
of film 24

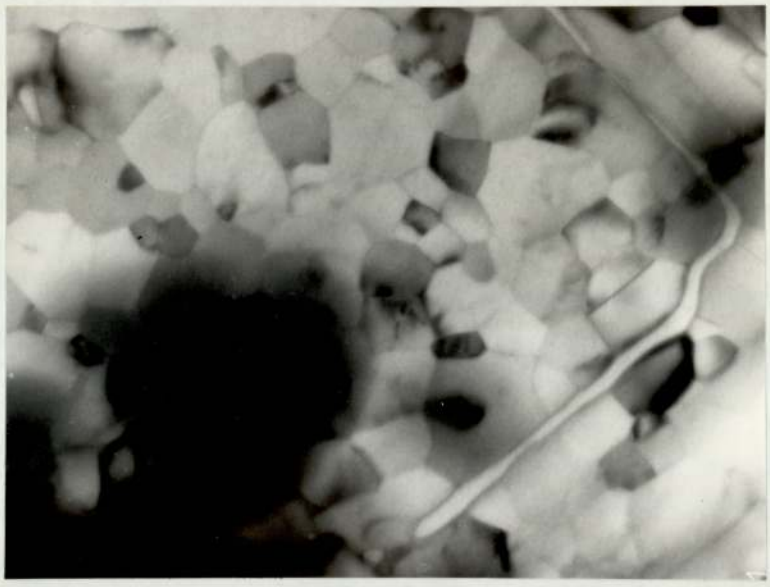

FIG. 80 Electron micrograph of film 26
55,000 X

formula

$$\lambda L = rd$$

where $\lambda.L$ is known as the 'camera constant'. For the E.M.6 microscope used, at an anode voltage of 80 KV and a magnificiation of 55,000. this was measured to be 1.44 Å.cm. The final column shows the accepted d spacings for aluminium (A.S.T.M. index) and indicates correct identification of the rings.

The absence of the expected (111) and (200) rings, together with the other missing diffraction rings indicated in Table 13, produce a standard diffraction pattern which indicates that the (111) planes lie parallel to the specimen surface.

CHAPTER 8

CONCLUSIONS

The aim of the experiments described in this work was to perform simultaneous measurements of the changes of optical and electrical properties of aluminium films brought about by annealing, and to correlate the observed variations.

By vapour quenching aluminium on to substrates held at 77°K, polycrystalline films of very small grain size were produced. ($\sim$ 2 nm). The grain boundaries in particular were the source of large numbers of crystal defects, especially vacancies. When the temperature of the specimens was raised to around room temperature, the resulting irreversible changes of electrical and optical properties were easily detectable with the comparatively simple apparatus employed. In all cases, the electrical resistance of the films became less as the temperature was increased, often by as much as 40%. The proportional reduction was less for thicker films. Application of standard techniques for the analysis of the recovery of resistivity after radiation damage in metals enabled the mechanism of annealing to be identified as predominantly the migration of (100) 'dumbell' interstitials to vacancies, which were annihilated in the process. The process was shown to obey approximately second order kinetics and was identified as stage III.

As a result of the removal of grain boundary vacancies, the grain boundary area was reduced and the large non-reversible fall of resistivity took place. The measured activation energy of $\sim$ 0.2 eV was found to be lower than the accepted value for interstitials in bulk aluminium, namely 0.4 eV and was found to increase at higher temperatures. It was concluded that the measured activation energy of migration of the interstitials was lowered by the attraction from near-by vacancies; an effect which became less significant at increased temperature as the annealing proceeded.

Some specimens were examined by transmission electron

microscopy. Electron diffraction patterns showed that the films were oriented with the (111) planes parallel to the substrate surface and that the final mean grain size was of the order of the film thickness ($\sim$ 30.0 nm).

Oxidation of a freshly deposited aluminium surface was found to be significant even at a total pressure of 1.5×10^{-9} torr. Measurements of resistance and of optical parameters Ψ and Δ on several films indicated an initial rate of 0.05 nm per hour, which over periods of several days was a logarithmic function of time. These measurements enabled an oxidation correction to be applied to all films.

The stage III anneal produced changes of the optical constants n and k, which together form the complex refractive index $\mathcal{N} = n - ik$, which were found to be similar for all samples observed at a wavelength of 0.549 nm. This occurred on substrates of both Corning 0211 glass and single crystal potassium bromide. In all cases the value of both n and k increased so that the product nk, which is proportional to optical absorption, also increased. At the same time the value of $n^2 - k^2$ became more negative, typically $\sim$ 8%, which was attributed to a rise in the effective number of free electrons, N*. This increase in N* was insufficient to explain the large increase in electrical conductivity so that a simultaneous increase of approximately 30% in the relaxation time, τ , was deduced.

From the Drude-Zener equations for free electrons, the combined increases of N* and τ would have led to a lower value of nk. However, as stated previously, the measured value of nk showed an increase during the stage III anneal. This larger value of nk was therefore interpreted as an increase in the inter-band absorption peak, centred at 0.8μ in aluminium, but still significant at 0.549μ .

Optical measurements on a number of films, made over an extended wavelength range (0.499μ to 1.94μ) using the ellipsometric

technique of Beattie, showed that the anneal from 77°K to room temperature resulted in an overall increase of optical absorption, but also showed that the inter-band peak which was almost absent immediately after deposition, developed during the anneal and was also shifted towards higher energy (shorter wavelength) as a result of the anneal. This was observed on substrates of both glass and single crystal potassium bromide.

A similar effect was observed with increasing film thickness. Thinner films ($\sim$ 6 nm) showed little evidence of the inter-band peak immediately after deposition, but as the film thickness was increased, the peak became larger and its position was moved towards higher energy.

The conclusion was similar in both cases. The films deposited at 77°K, particularly the thinner ones, possessed a disordered structure similar to that of liquid aluminium in which the nearest-neighbour order is preserved but the second-nearest neighbour is greatly disturbed. The specimens therefore retained sufficient structure in the (111) planes to give the electron diffraction patterns described by several observers, and yet showed little trace of the inter-band optical absorption peak which occurs in bulk aluminium due to the energy band structure in the region of the symmetry point W in the Brillouin zone. This observation is attributed to the loss of next-nearest neighbour order and hence a loss of periodicity in the (200) planes in the vapour-quenched specimens. The loss of the (200) periodicity leads to a breakdown in the concept of E - k curves in the (200) direction so that the (200) Bragg reflection plane (which contains the symmetry point W) is not defined. Hence, inter-band absorption is not possible.

During the stage III anneal, from 77°K to room temperature, the periodicity of the (200) planes improved, as a result of the migration of (100) 'dumbell' interstitials to vacancies. The band structure around W therefore developed and the absorption peak

appeared.

The movement of the peak towards higher energy during the stage III anneal is explained by a consideration of the V_{200} component of the pseudopotential, which is small in the disordered films and is increased as a result of the improved periodicity in the annealed film. Consequently, the energy of maximum absorption, which is given by

$$E = 2 \left| V_{200} \right|$$

is moved to higher energy.

The interband peak is known to become broader and to be shifted to lower energy as a result of increased temperature, an effect brought about by the influence of the Debye-Waller factor on the components of the pseudopotential. The annealing changes here described occur over and above these changes.

Annealing the aluminium specimens to approximately 550°K in vacuo produced an enhanced oxidation rate and the annealing experiments were therefore performed after total oxidation. There is experimental evidence to support the assumption made here, that the oxide layer does not increase in thickness or change appreciably in its optical constants as a result of the increased temperature. It was found that on glass substrates the free electron contribution to nk increased as a result of the anneal, while on the crystal substrates, the value decreased.

It was concluded that the explanation lay in the different thermal expansion coefficients of the film and substrates. The coefficient of expansion of the aluminium falls between the values of 0211 glass and KBr crystal. Thus, on the glass substrate the film is compressed beyond the elastic limit during the anneal, while on the crystal the film is extended. Both optical and electrical measurements are consistent with an increase of defects (i.e. dislocations) in the films on glass but a reduction of the defect concentration for the films on the crystal. On both substrates,

however, the interband contribution to the absorption increased as a result of the anneal and was shifted to higher energy. This occurred also for films deposited at room temperature. It is concluded that the explanation lies in further ordering of the (200) crystal planes as previously described.

There are a number of aspects of the present work which would merit further investigation. For example, the V_{111} component of the pseudopotential also produces a small optical absorption peak in the region of 0.5 eV. Since this is connected with the periodicity of the (111) planes, it would be interesting to observe whether this peak remained unaffected during annealing. The experimental difficulties would be great, however, since the wavelength involved ($\sim 3\mu$) is beyond the reach of the present ellipsometer components.

It would also be of interest to carry out actual radiation damage experiments on thin films and to compare the recovery characteristics with those of bulk material and also with those of vapour-quenched samples. Ideally, further experiments should be carried out at pressures below 10^{-10} torr so that oxidation is virtually eliminated. The oxidation corrections used in the present work could then be verified.

Finally, the ellipsometer on which the present measurements were performed was intended to be of simple, inexpensive construction. There is considerable scope for improvement of the optical components in order to make it comparable in accuracy to the modern instruments described in section 1.4.

APPENDIX 1

A. Defect Annealing Theory

From thermodynamic considerations it may be shown that a perfect crystal cannot exist above the absolute zero of temperature. For any crystal defect of formation energy U^f there exists at an absolute temperature T an equilibrium concentration C which is given by

$$C \propto e^{\left(-\frac{U^f}{kT}\right)}$$

where k is Boltzmann's constant.

If the defect concentration in a given sample is greater than the equilibrium value, as it may be for example after radiation damage or cold working or as a result of vapour quenching of the sample, the approach to equilibrium occurs at a rate which depends on several factors, namely, the temperature, the energy of migration of the defect, and the manner in which the defect is removed.

When a defect moves from one lattice site to another, the free energy of the crystal rises to a maximum at some intermediate configuration and then returns to its original value. Let the excess energy at the maximum be F_m, the free energy of activation for migration. If this energy is supplied by random fluctuations of vibrational energy, assumed to follow a Maxwell-Boltzmann law, then the probability of an energy F_m being available during one period of oscillation is given by $\exp\left\{-\frac{F_m}{kT}\right\}$. If the oscillation frequency of the defect is ν, then the number of jumps in a time dt is given by

$$dn = \nu \exp\left\{-\frac{F_m}{kT}\right\} dt \qquad (1)$$

hence

$$\frac{dn}{dt} = \nu \exp\left\{-\frac{F_m}{kT}\right\}$$

The free energy F_m may be written

$$F_m = U_m - T\Delta S_m$$

where U_m is the excess potential energy and ΔS_m the difference in entropy. We may then write

$$\frac{dn}{dt} = \nu \exp.\left\{\frac{\Delta S_m}{k}\right\} \exp.\left\{-\frac{U_m}{kT}\right\}$$

$$\therefore \quad \frac{dn}{dt} = A \exp.\left\{-\frac{U_m}{kT}\right\}$$

where **A** is an empirical constant, largely independent of temperature, often referred to as the 'frequency factor.'(161)

The rate at which the specimen crystal approaches equilibrium depends on the rate of jumping and on the number of jumps j, required for the defects to reach a sink. Let C represent the excess concentration of a single type of defect; then in the interval dt, during which C changes by -dC, each defect makes a number of jumps given by (1) and its chance of reaching a sink is therefore given by $\frac{1}{j} \cdot \nu \exp.\left\{-\frac{F_m}{kT}\right\}$.

Hence,

$$dC = -\frac{C\nu}{j} \exp.\left\{-\frac{F_m}{kT}\right\} dt \qquad (2)$$

which gives

$$C = C_0 \exp.\left\{-\frac{t}{\tau}\right\} \qquad (3)$$

where

$$\frac{1}{\tau} = \frac{\nu \exp.\left\{-\frac{F_m}{kT}\right\}}{j}$$

The above equation (3) is similar to that of a first-order chemical reaction. If the defects under consideration were of two types which annihilated each other on meeting, then j would be proportional to C^{-1} so that dC (from equation (2)) would be proportional to C^2. This would be an example of a 'second-order' reaction. In general, the reactions are too complex for the rate to be proportional to a simple power of the concentration C. A more general form of equation (2) is then more useful, namely

$$\frac{dC}{dt} = -f(C) \exp.\left\{-\frac{U_m}{kT}\right\} \qquad (4)$$

where $f(C)$ is some undetermined function of C which includes the frequency factor.

In metals, an important property of a lattice defect is the contribution it makes to electrical resistivity, as a result of

scattering of conduction electrons. The contributions made by individual defects are additive, as expressed by Matthiesson's law. Hence, the electrical resistivity over and above the value for an annealed specimen at the same temperature, may be taken as a measure of the concentration of defects. If $\Delta\rho$ is the excess resistivity, then the approach to equilibrium at a fixed temperature T_1 may be expressed, from equation (4) as

$$\frac{d}{dt}(\Delta\rho) = f(\Delta\rho)\exp\left\{-\frac{U_m}{kT_1}\right\}$$

In the isothermal annealing experiments of section 5.1, the fall of $\Delta\rho$ with time is observed at two close temperatures, T_1 and T_2. At the intersection of the two isothermals, where T_1 changes to T_2 the values of $\Delta\rho$ are the same and therefore the values of $f(\Delta\rho)$ are the same. The ratio of the two gradients then becomes

$$\frac{\left[\frac{d}{dt}(\Delta\rho)\right]_{At\ T_1}}{\left[\frac{d}{dt}(\Delta\rho)\right]_{At\ T_2}} = \exp.\left\{\frac{U_m}{k}\left(\frac{1}{T_2}-\frac{1}{T_1}\right)\right\} \qquad (5)$$

from which U_m may be determined.

Since the temperatures are fixed and the lattice vibration component of resistivity therefore constant at each temperature T_1 and T_2, the actual values of resistance of the specimen may be plotted against time, as indicated on Fig.45.

B. Determination of the order of reaction

In general it is possible to determine the recovery kinetics by an analysis of the isothermal curve.[75] Assuming the validity of the general reaction rate equation,

$$\frac{dC}{dt} = AC^{\gamma}\exp.\left\{-\frac{U_m}{kT}\right\}$$

where A is a constant and γ is the order of reaction,

we obtain $$\frac{dC}{C^{\gamma}} = -K\,dt$$

for a fixed value of temperature. Since $\Delta\rho$ is a measure of the defect concentration C, we may write $$\frac{d(\Delta\rho)}{(\Delta\rho)^{\gamma}} = -K\,dt$$

which, provided $\gamma \neq 1$, may be integrated to give

$$(\Delta\rho)^{1-\gamma} = K(\gamma-1)[t+M]$$

where

$$M = \frac{(\Delta\rho_o)^{1-\gamma}}{K(\gamma-1)}$$

Hence, taking logarithms of both sides

$$(1-\gamma)\,\mathrm{Log}(\Delta\rho) = \mathrm{Log}\,K(\gamma-1) + \mathrm{Log}\{t+M\}$$

$$\therefore \quad \mathrm{Log}(\Delta\rho) = \left(\frac{1}{1-\gamma}\right)\mathrm{Log}(t+M) + \frac{\mathrm{Log}\,K(\gamma-1)}{1-\gamma} \qquad (6)$$

If the reaction rate equation is valid, therefore, it is always possible to choose a positive value of M such that the plot of Log($\Delta\rho$) against Log($t+M$) yields a straight line. The order of reaction, γ, may then be determined from the slope of this line. See equation (6). The constant M represents the time required for the defect concentration to be reduced, as a result of annealing at temperature T, from an infinite value to that value corresponding to $\Delta\rho_o$. Thus M must always be positive.

If it is suspected that the order of reaction may be exactly 2, a simple test first used by Sosin and Rachal[85] may be applied. If $\gamma = 2$, then the general reaction rate equation becomes

$$\frac{dC}{dt} = -AC^2 \exp\left\{-\frac{U_m}{kT}\right\}$$

or

$$\frac{dC}{C^2} = -Q\,dt$$

at constant temperature. Integration gives

$$\frac{1}{C} = Qt + Z$$

and since $\Delta\rho$ is proportional to C

$$\frac{1}{\Delta\rho} = Q_1 t + Z_1$$

Hence, only if $\gamma = 2$, a plot of $\frac{1}{\Delta\rho}$ against t will produce a straight line.

APPENDIX 2

DESCRIPTION OF ALGOL COMPUTER PROGRAMS

a) Ellipsometry Program 2

The program is derived for the system shown in Fig. 14, which represents a parallel beam of monochromatic light incident at an angle ϕ_1, from vacuum (medium 1) on to the aluminium specimen (medium 2). The substrate (medium 3) has a roughened back so that reflections from the reverse side can be neglected. Since the metal film is absorbing, the refractive index is a complex quantity and the calculated angles of refraction are also complex. The physical interpretation of this is that the planes of equal phase are not parallel to the planes of equal amplitude. See Heavens[90], page 47, and Ditchburn[127], page 553.

The program sets out to calculate the values of ellipsometer parameters Ψ and Δ for a set of assumed values of n, k and thickness for the film. These assumed values are then varied until consistency with experimental observation is achieved. The calculations involve the manipulation of a large number of complex quantities by the process of rationalisation. The detailed algebra becomes extremely tedious so that only the mathematical outline is given.

The test of program 2 is attached and is shown divided into sections. After the normal preliminaries of declaration and reading-in of the values of n and k for the various media and the angle of incidence, section 1 commences the calculation of Cos ϕ_2.

Section 1

In general, $\mathcal{N}_2 \sin\phi_2 = \mathcal{N}_1 \sin\phi_1 = \mathcal{N}_x \sin\phi_x$ (i)

For medium 1, the vacuum, $\mathcal{N}_1 = 1$

Hence $$\cos\phi_2 = \sqrt{1 - \sin^2\phi_2} = \sqrt{1 - \left(\frac{\sin\phi_1}{\mathcal{N}_2}\right)^2} \qquad \text{(ii)}$$

$$\cos\phi_2 = \frac{1}{\mathcal{N}_2}\sqrt{(\mathcal{N}_2)^2 - \sin^2\phi_1}$$

Substituting for $\mathcal{N}_2$ from $\mathcal{N}_2 = n_2 - ik_2$

$$\cos\phi_2 = \frac{1}{\mathcal{N}_2}\left(n_2^2 - k_2^2 - 2in_2k_2 - \sin^2\phi_1\right)^{\frac{1}{2}}$$

```
22/17/43        01/10/71        COMPILED BY XALE MK.  5C
STATEMENT
    0   'SENDTO'(ED,ASTD-DEFAULT(0),.PROGRAM)
    0   'WORK' (ED,WORK FILE    (0))
    0   'BEGIN' 'COMMENT' FILM THICKNESS;                                                    7
    1   'INTEGER' I,I1;                                                                      8
    1   'REAL' C,C1,C2,C3,D,D1,D2,D3,D4,D5,D6,D7,D8,D9,D10,D11,D12,D13,E,E1,E2,              9
    2       E3,                                                                             10
    2       F,F1,F2,F3,F4,G,G1,G2,G3,G4,G5,G6,G7,G8,G9,G10,G11,G12,H,H1,H2,H3,              11
    2       H4,H5,H6,H7,H8,H9,L,L1,L2,L3,L4,L5,L6,L7,M1,M2,M3,M4,M5,M6,M7,M8,              12
    2       M9,M10,M11,M12,P,M,P1,P2,P3,P4,P5,P6,P7,P8,P9,Q,Q1,Q2,Q3,Q4,Q5,Q6,             13
    2       Q7,Q8,Q9,S,S1,S2,S3,S4,S5,S6,S7,S8,S9,S10,S11,T,T1,T2,T3,T4,T5,T6,             14
    2       T7,T8,U,U1,U2,U3,U4,U5,U6,U7,V,V1,V2,V3,V4,V5,V6,V7,W,W1,W2,W3,W4,            15
    2       Z,Z1,Z2,Z3,Z4,Z5,Z6;                                                            16
    2   'REAL' 'ARRAY' A[0:14],B[0:14],K[0:3],N[0:13],R[0:5],X[0:5],Y[0:5];                 17
    3       LL2:N[2]:=READ;    First Number on data card must be +                        18
    5       'IF' N[2]<0'THEN''GOTO'LL8:
    6       LL5:D4:=READ;      Step in film thickness.                                   19
    7    D9:=READ;  N[2]:=D9-0.2;  D10:=READ;  K[2]:=D10-0.4;        Film.
   11              N[3]:=READ;  }
   12              K[3]:=READ;  } SUBSTRATE                                               22
   13              T:=READ;   Angle of incidence (radians)                                23
   14              L:=READ;   Wavelength (A.U.)                                           24
   15             D:=READ;    Starting film thickness                                    25
   16              Z6:=READ;  Final film thickness                                        26
   17     LL6: NEWLINE(2);                                                                27
   18     WRITETEXT('('WAVELENGTH%=%')');  PRINT(L,5,0);  NEWLINE(1);
   21              WRITE TEXT ('('N2=')');                                                30
   22              PRINT (N[2],1,3);                                                      31
   23              WRITE TEXT ('('K2=')');                                                32
   24              PRINT (K[2],1,3);                                                      33
   25              WRITE TEXT ('('N3=')');                                                34
   26              PRINT (N[3],1,3);                                                      35
   27              WRITE TEXT ('('K3=')');                                                36
   28               PRINT (K[3],1,3);                                                     37
   29              NEWLINE(1);                                                            38
   30              WRITE TEXT ('('THICKNESS'('3S')'DELTA'('10S')'PSI')');                 39
   31              NEWLINE(1);                                                            40
```

```
LL4:I:=0;
LL1:X[I]:=K[2+I]*K[2+I];
                T4:=T;
    X[4]:=SIN(T4);
    X[4]:=X[4]*X[4];
    N[4+I]:=N[2+I]*N[2+I];
    X[2+I]:=N[4+I]-X[I]-X[4];
    Y[2+I]:=2*N[2+I]*K[2+I];
    X[4+I]:=X[2+I]*X[2+I];
    Y[4+I]:=Y[2+I]*Y[2+I];
    R[I]:=SQRT(X[4+I]+Y[4+I]);
    A[I]:=SQRT((R[I]+X[2+I])/2);
    A[4+I]:=N[2+I]*A[I];
    A[7+I]:=SQRT((R[I]-X[2+I])/2);
    A[9+I]:=A[7+I]*K[2+I]+A[4+I];
    A[4+I]:=X[I]+N[4+I];
    A[2+I]:=A[9+I]/A[4+I];
    B[I]:=K[2+I]*A[I];
    B[4+I]:=N[2+I]*A[7+I];
    B[2+I]:=(B[I]-B[4+I])/A[4+I];
    'IF' A[2+I]>0 'THEN' 'GOTO' LL3;
```

Section 1

Calculation of complex angles of refraction.

$\cos\phi_2 = A[2] + iB[2]$

$\cos\phi_3 = A[3] + iB[3]$

```
    A[2+I]:=-A[2+I];
    B[2+I]:=-B[2+I];
LL3:I:=I+1;
    'IF' I=1 'THEN' 'GOTO' LL1;
    C:=COS(T4);
    C1:=N[2]*C;
C2:=A[2]-C1;
    E2:=C1+A[2];
    D1:=K[2]*C;
    D2:=D1+B[2];
F2:=B[2]-D1;
    E:=C2*E2;
    E1:=D2*F2;
    G2:=E+E1;
    G:=E2*E2;
    G1:=F2*F2;
    G:=G+G1;
    G2:=G2/G;
    F:=C2*F2;
    F1:=D2*E2;
H2:=(F1-F)/G;
```

Section 2

Calculation of Fresnel coefficient $r_{12(p)}$

$r_{12(p)} = g_2 + ih_2$

```
74                H:=N[3]*A[2];
75                H1:=K[3]*B[2];
76                H4:=N[2]*A[3];
77                H5:=K[2]*B[3];
78          C3:=H4+H5-H-H1;
79                H8:=N[3]*B[2];
80                H9:=K[3]*A[2];
81                H6:=K[2]*A[3];
82                H7:=N[2]*B[3];
83                D3:=H9-H8+H7-H6;
84                E3:=H+H1+H4+H5;
85          F3:=H8+H7-H9-H6;
86                G4:=C3*E3;
87                G5:=D3*F3;
88                G6:=E3*E3;
89                G7:=F3*F3+G6;
90                G3:=(G4+G5)/G7;
91                F4:=C3*F3;
92          H3:=(D3*E3-F4)/G7;
```

Section 3.

$r_{23}(p) = g_3 + i h_3$

```
93                 P:=N[2]*A[2];
94                 P1:=K[2]*B[2];
95                P2:=C-P-P1;
96                P4:=N[2]*B[2];
97                P5:=K[2]*A[2];
98                S2:=C+P+P1;
99                Q2:=P4-P5;
100               T2:=P5-P4;
101               U:=P2*S2;
102               U1:=Q2*T2;
103               U4:=S2*S2;
104               U5:=U4+T2*T2;
105               U2:=(U+U1)/U5;
106               U7:=Q2*S2;
107               U6:=P2*T2-U7;
108               V2:=U6/U5;
```

Section 4.

$r_{12}(s) = u_2 + i v_2$

```
109               Q:=N[3]*A[3];
110               Q1:=K[3]*B[3];
111               P3:=P+P1-Q-Q1;
112               Q4:=B[3]*N[3];
```

Section 5.

```
113               Q5:=K[3]*A[3];
114               Q3:=P5-P4+Q4-Q5;
115               S3:=P+P1+Q+Q1;
116               T3:=P5-P4-Q4+Q5;
117               V:=P3*S3;
118               V1:=Q3*T3;
119               V4:=S3*S3;
120               V5:=V4+T3*T3;
121               U3:=(V+V1)/V5;
122               V6:=P3*T3;
123               V7:=Q3*S3;
124               V3:=(V6-V7)/V5;
```

$r_{23}(s) = u_3 + i v_3$

Section 6.

Calculation of $e^{-2i\delta_2}$

$e^{-2i\delta_2} = m_2 - iL_2$

```
M1:=P*P1;
M:=6.28318530*D/L:
M1:=M1*M;
L1:=(P4-P5)*M;
M3:=Exp(2*L1);
M:=2*M1;
M2:=M3*COS(M);
L2:=M3*SIN(M);
```

Section 7.

$r_{12}^{(p)} + r_{23}^{(p)} e^{-2i\delta_2} = A[11] + iB[11]$

```
L4:=G3*M2;
L5:=H3*L2;
A[11]:=G2+L4+L5;
L6:=H3*M2;
L7:=G3*L2;
B[11]:=H2+L6-L7;
```

Section 8.

$1 + r_{12}^{(s)} r_{23}^{(s)} e^{-2i\delta_2} = A[12] + iB[12]$

```
S4:=U2*U3*M2;
S5:=V2*V3*M2;
S6:=L2*V3*U2;
S7:=L2*V2*U3;
A[12]:=1+S4-S5+S6+S7;
S8:=V2*U3*M2;
S9:=U2*M2*V3;
S10:=U2*U3*L2;
S11:=V2*V3*L2;
B[12]:=S8+S9-S10+S11;
```

Section 9.

$1 + r_{12}^{(p)} r_{23}^{(p)} e^{-2i\delta_2} = A[13] + iB[13]$

```
Q6:=G2*G3*M2;
Q7:=H2*H3*M2;
Q8:=H2*L2*G3;
Q9:=H3*L2*G2;
A[13]:=1+Q6-Q7+Q8+Q9;
P6:=H2*G3*M2;
P7:=H3*G2*M2;
P8:=L2*G2*G3;
P9:=H2*H3*L2;
B[13]:=P6+P7-P8+P9;
```

Section 10

$r_{12}^{(s)} + r_{23}^{(s)} e^{-2i\delta_2} = A[14] + iB[14]$

```
T5:=U3*M2;
T6:=V3*L2;
A[14]:=U2+T5+T6;
T7:=M2*V3;
T8:=U3*L2;
B[14]:=V2+T7-T8;
```

Section 11

$$\frac{r_{13}^{(p)}}{r_{13}^{(s)}} = \frac{g_{11} + i m_{11}}{g_{12} + i m_{12}}$$

```
R[2]:=A[11]*A[12];
G11:=R[2]-B[11]*B[12];
R[3]:=B[11]*A[12];
M11:=A[11]*B[12]+R[3];
R[4]:=A[13]*A[14];
G12:=R[4]-B[13]*B[14];
R[5]:=B[13]*A[14];
M12:=A[13]*B[14]+R[5];
```

```
173                 W1:=G11*G12;
174                 W2:=M11*M12;                                                    182
175                 W3:=G12*G12;                    Section 12                      183
176                 W4:=W3+M12*M12;                                                 184
177                 W:=(W1+W2)/W4;      r13(P)/r13(s) = W + iZ = Tan Ψ e^(iΔ)       185
178                 Z1:=G12*M11;                                                    186
179                 Z2:=G11*M12;                                                    187
180                 Z:=(Z1-Z2)/W4;                                                  188
181                                                                                 189
182                       Z3:=180*ARCTAN(Z/W)/(4*ARCTAN(1));                        190
183           'IF'Z3>0'THEN''GOTO'LL7;
183           Z3:=180+Z3;                                   Section 13.
184               LL7:Z4:=W*W;
185                                                                                 191
186                       Z5:=180*ARCTAN(SQRT(Z4+Z*Z))/(4*ARCTAN(1));               192
186                 I1:=ENTIER(D+.6);                                               194
187                 PRINT (I1,4,0);                                                 195
188                 PRINT (Z3,5,3);                                                 196
189                 PRINT (Z5,6,3);                   Section 14.                   197
190                 NEWLINE(1);                                                     198
191                 D:=I1+D4;                                                       199
192                 'IF' D<Z6 'THEN' 'GOTO' LL4;                                    200
193           D:=60;   N[2]:=N[2]+0.2;  D11:=D9+0.2;
196           'IF'N[2]'LE'D11'THEN''GOTO'LL6;
197           N[2]:=D9-0.2;  K[2]:=K[2]+0.4;  D12:=D10+0.4;
200           'IF'K[2]'LE'D12'THEN''GOTO'LL6;
201                 'GOTO' LL2;
202                 LL8:;                                                           202
203           'END';                                                                203
NO OF BUCKETS USED     29                                                         203
COMPILED   #AXXX          EC
```

In general, the square root of a complex number may be determined by writing

$$\sqrt{a - ib} = c - id$$

and by then squaring, and equating real and imaginary parts, the values of c and d may be found.

Hence $$\cos\phi_2 = \frac{1}{N_2}(c - id) \qquad \text{(iii)}$$

where $$c = \sqrt{\frac{\sqrt{(n_2^2 - k_2^2 - \sin^2\phi_1)^2 + 4n_2^2k_2^2} + (n_2^2 - k_2^2 - \sin^2\phi_1)}{2}}$$

and is calculated as C = A(I) in statement 43.

Also $$d = \sqrt{\frac{\sqrt{(n_2^2 - k_2^2 - \sin^2\phi_1)^2 + 4n_2^2k_2^2} - (n_2^2 - k_2^2 - \sin^2\phi_1)}{2}}$$

and is calculated as d = A(7) in statement 45.

Division of equation (iii) by N_2 and rationalisation gives

$$\cos\phi_2 = A[2] + iB[2] \qquad \text{statements 48 and 51.}$$

Statements 55 and 56 arrange to calculate the value of $\cos\phi_3$ as A[3] + i B[3] by changing the optical constants of n_3 and k_3. The angle of incidence used is still ϕ_1, and this is valid because of the invariance of $N_x \sin\phi_x$. Thus,

$$\begin{aligned}\cos\phi_3 &= \sqrt{1 - \sin^2\phi_3} \\ &= \sqrt{1 - \left(\frac{N_2}{N_3}\sin\phi_2\right)^2} \\ &= \sqrt{1 - \left(\frac{N_2}{N_3}\cdot\frac{N_1}{N_2}\sin\phi_1\right)^2} \\ &= \sqrt{1 - \left(\frac{\sin\phi_1}{N_3}\right)^2}\end{aligned}$$

the form of which is identical to equation (ii).

Section 2

This part of the program calculates the Fresnell coefficient $r_{12(p)}$ as a function of N_2, N_1 and ϕ_1. It is based on the formula

$$r_{12(p)} = \frac{N_1\cos\phi_2 - N_2\cos\phi_1}{N_1\cos\phi_2 + N_2\cos\phi_1}$$

where $\cos\phi_2$ is complex as calculated in Section 1, and N_2 is also complex. The result is given in the form

$$r_{12(p)} = g_2 + ih_2$$

Section 3

This part calculates $r_{23(p)}$ from the relation

$$r_{23(p)} = \frac{N_2 \cos\phi_3 - N_3 \cos\phi_2}{N_2 \cos\phi_3 + N_3 \cos\phi_2}$$

All quantities on the right-hand side of the equation are complex. The values of $\cos\phi_2$ and $\cos\phi_3$ are those calculated in Section 1. The result is given as

$$r_{23(p)} = g_3 + ih_3$$

Section 4

This section calculates $r_{12(s)}$ from the relation

$$r_{12(s)} = \frac{N_1 \cos\phi_1 - N_2 \cos\phi_2}{N_1 \cos\phi_1 + N_2 \cos\phi_2}$$

$$r_{12(s)} = u_2 + iv_2$$

Section 5

This section calculates $r_{23(s)}$ from the relation

$$r_{23(s)} = \frac{N_2 \cos\phi_2 - N_3 \cos\phi_3}{N_2 \cos\phi_2 + N_3 \cos\phi_3}$$

$$r_{23(s)} = u_3 + iv_3$$

Having now calculated all the angles of refraction and all the possible Fresnel coefficients for the various interfaces, the program proceeds on the basis of calculating the Fresnel coefficient for two surfaces taken together and treated as a single effective boundary. Following the technique of Vasiček calculations commence at the surface and work towards the substrate. See Fig.14. In Chapter 2.1, it was shown that the two boundaries could be treated as a single interface having Fresnel coefficients r_{13} given by

$$r_{13} = \frac{r_{12} + r_{23} e^{-2i\beta_2}}{1 + r_{12} r_{23} e^{-2i\beta_2}} \qquad \text{(iv)}$$

two forms of which exist, one for the (p) and one for the (s) components.

β_2 is a factor that takes account of the phase difference and the amplitude reduction in traversing the film once. As shown

in Chapter 2.1,

$$\beta_2 = \frac{2\pi}{\lambda} N_2 d_2 \cos\phi_2$$

$$\beta_2 = \frac{2\pi}{\lambda}(n_2 - ik_2) d_2 \cos\phi_2$$

Hence the quantity $e^{-2i\beta_2}$ in equation (iv) becomes

$$e^{-2i\beta_2} = \exp\left\{-\frac{4\pi}{\lambda} k_2 d_2 \cos\phi_2\right\} \exp\left\{-\frac{4\pi i}{\lambda} n_2 d_2 \cos\phi_2\right\}$$

Hence $$e^{-2i\beta_2} = e^{-a_2}\cos\gamma_2' - i\, e^{-a_2}\sin\gamma_2'$$

where $$a_2 = \frac{4\pi}{\lambda} k_2 d_2 \cos\phi_2$$

and $$\gamma_2' = \frac{4\pi}{\lambda} n_2 d_2 \cos\phi_2$$

Section 6

This part calculates the value of $e^{-2i\beta_2}$ and expresses the result as

$$e^{-2i\beta_2} = p - iq$$

where p is called M(2) and q is called L(2) in statements 131 and 132 respectively.

Section 7

This calculates the numerator of equation (iv) for the (p) component

$$r_{12(p)} + r_{23(p)} e^{-2i\beta_2} = A[11] + i\,B[11]$$

Section 10

This part performs the same calculation as section 7 but for the (s) components.

$$r_{12(s)} + r_{23(s)} e^{-2i\beta_2} = A[14] + i\,B[14]$$

Section 9

This part calculates the denominator of equation (iv) for the (p) component.

$$1 + r_{12(p)} r_{23(p)} e^{-2i\beta_2} = A[13] + i\,B[13]$$

Section 8

This part performs the same calculation as section 9 but for the (s) component.

$$1 + r_{12(s)} r_{23(s)} e^{-2i\beta_2} = A[12] + i\,B[12]$$

Section 11

By combining sections 7 and 9, the value of $r_{13(p)}$ is

obtained

$$r_{13(p)} = \frac{A[11] + iB[11]}{A[13] + iB[13]} = \rho_{(p)} e^{i\Delta_p}$$

and also by combining sections 10 and 8, the value of $r_{13(s)}$ is obtained

$$r_{13(s)} = \frac{A[14] + iB[14]}{A[12] + iB[12]} = \rho_{(s)} e^{i\Delta_s}$$

The ratio of these reflection coefficients for the (p) and (s) components can then be written

$$\frac{r_{13(p)}}{r_{13(s)}} = \frac{\rho_{(p)} e^{i\Delta_p}}{\rho_{(s)} e^{i\Delta_s}} = \rho e^{i\Delta} = \mathrm{Tan}\Psi\, e^{i\Delta}$$

where, from section 2.1

$$\Delta = \Delta_p - \Delta_s$$

and

$$\mathrm{Tan}\Psi = \left|\frac{\rho_{(p)}}{\rho_{(s)}}\right|$$

Hence

$$\mathrm{Tan}\Psi\, e^{i\Delta} = \frac{A[11] + iB[11]}{A[13] + iB[13]} \times \frac{A[12] + iB[12]}{A[14] + iB[14]} \qquad (v)$$

Section 11 of the program calculates first the numerator and then the denominator of the above equation (v) and expresses the result in the form

$$\mathrm{Tan}\Psi\, e^{i\Delta} = \frac{G[11] + iM[11]}{G[12] + iM[12]}$$

Section 12

This part continues the calculation and expresses the result as a single complex quantity

$$\mathrm{Tan}\Psi\, e^{i\Delta} = W + iZ$$

See statements 177 and 180.

Section 13

Since any complex number may be expressed in two forms

$$W + iZ = \sqrt{W^2 + Z^2}\, e^{i\,\mathrm{Tan}\left(\frac{Z}{W}\right)}$$

this part of the program makes a calculation of

$$\Delta = \mathrm{Tan}^{-1}\left(\frac{Z}{W}\right) \qquad \text{(radians)}$$

$$\Delta = \frac{180}{\pi}\,\mathrm{Tan}^{-1}\left(\frac{Z}{W}\right) \qquad \text{(degrees)}$$

Since the value of Δ is calculated from a $\tan^{-1}$ function, values of Δ between 0 and 90 degrees will be interpreted as a

positive angle and values of Δ between 90 and 180 degrees, for which the tangent is negative, will be interpreted as a negative angle. In this case 180 degrees must be added to the negative angle to obtain the correct Δ . This is arranged by statements 182 and 183.

Section 14

This section calculates the value of Ψ from

$$Tan\,\Psi = \sqrt{W^2+Z^2}$$

$$\therefore \quad \Psi = \frac{180}{\pi} Tan^{-1}\sqrt{W^2+Z^2} \qquad \text{(degrees)}$$

In this way, the final values of Ψ and Δ are determined from the known optical constants of the media. The data cards for program 2 must contain the following information, in this order.

+ 1.0 Any positive number will serve to make the computer accept the data card. A negative number will cause the computer to stop. This facility is added so that a number of different calculations may be made consecutively.

The step increase in metal film thickness in Angstrom units.

n_2 for the metal film

k_2 for the metal film

n_3 for the substrate

k_3 for the substrate

The angle of incidence in radians

The wavelength of light used in Angstrom units

The starting film thickness (A.U.)

The final film thickness (A.U.)

b) Ellipsometry Program 3

In order to interpret the experimental observations on oxidised aluminium films, the author developed a program for the calculation of Ψ and Δ from the assumed optical constants for a system of three layers (i.e. oxide, metal, substrate). A copy of the program is enclosed and it can be seen that it represents an

```
28/09/71          COMPILED BY XALE MK.  5C

'SENDTO'(ED,ASTD-DEFAULT(0),,PROGRAM)
'WORK' (ED,WORK FILE   (0))
'BEGIN' 'COMMENT' THREE LAYER SYSTEM;
'INTEGER' I,I1;
'REAL' C,C1,C2,C3,D,D1,D2,D3,D4,D5,D6,D7,D8,D9,D10,D11,D12,D13,E,E1,E2,
    E3,
    F,F1,F2,F3,F4,G,G1,G2,G3,G4,G5,G6,G7,G8,G9,G10,G11,G12,H,H1,H2,H3,
    H4,H5,H6,H7,H8,H9,L,L1,L2,L3,L4,L5,L6,L7,M1,M2,M3,M4,M5,M6,M7,M8,
    M9,M10,M11,M12,P,M,P1,P2,P3,P4,P5,P6,P7,P8,P9,Q,Q1,Q2,Q3,Q4,Q5,Q6,
    Q7,Q8,Q9,S,S1,S2,S3,S4,S5,S6,S7,S8,S9,S10,S11,T,T1,T2,T3,T4,T5,T6,
  T7,T8,U,U1,U2,U3,U4,U5,U6,U7,V,V1,V2,V3,V4,V5,V6,V7,W,W1,W2,W3,W4,
    Z,Z1,Z2,Z3,Z4,Z5,Z6;

  'REAL' 'ARRAY' A[0:14],B[0:14],K[0:8],N[0:13],R[0:5],X[0:5],Y[0:5];
      LL2:N[2]:=READ;
      'IF' N[2]<0'THEN''GOTO'LL8;
      LL5:D4:=READ;     Step in thickness of oxide layer.
          N[2]:=READ;  }
          K[2]:=READ;  } Oxide
          N[3]:=READ;  }
          K[3]:=READ;  } Metal
  N[4]:=READ;          }
  K[4]:=READ;          } Substrate.
          T:=READ;       Angle of incidence (radians)
          L:=READ;       Wavelength (A.U.)
          D:=READ;         Starting thickness of oxide A.U.
          Z6:=READ;        Final thickness of oxide A.U.
  D12:=READ;           Starting thickness of metal A.U.
  LL6:NEWLINE(2);
          WRITE TEXT ('('N2=')');
          PRINT (N[2],1,3);
          WRITE TEXT ('('K2=')');
          PRINT (K[2],1,3);
          WRITE TEXT ('('N3=')');
          PRINT (N[3],1,3);
          WRITE TEXT ('('K3=')');
           PRINT (K[3],1,3);
  WRITE TEXT('('N4=')');
  PRINT(N[4],1,3);
  WRITE TEXT('('K4=')');
  PRINT(K[4],1,3);
          NEWLINE(2);
  LL9:NEWLINE(2);
  WRITE TEXT('('THICKNESS%OF%METAL%FILM=')');
  PRINT(D12,5,1);
  WRITE TEXT('('AU')');
  NEWLINE(1);
  WRITE TEXT('('OXIDE')');
  NEWLINE (1);
          WRITE TEXT ('('THICKNESS'('3S')'DELTA'('10S')'PSI')');
          NEWLINE(1);
```

```
41                  LL4:I:=0;
42                  LL1:X[I]:=K[2+I]*K[2+I];
43                                  T4:=T;
44                          X[4]:=SIN(T4);
45                          X[4]:=X[4]*X[4];
46                          N[5+I]:=N[2+I]*N[2+I];
47                          X[2+I]:=N[5+I]-X[1]-X[4];
```

Section 1

Calculation of complex angles of refraction.

$\cos\phi_2 = A[2] + iB[2]$

$\cos\phi_3 = A[3] + iB[3]$

$\cos\phi_4 = A[4] + iB[4]$

```
48                          Y[2+I]:=2*N[2+I]*K[2+I];
49                          X[4+I]:=X[2+I]*X[2+I];
50                          Y[4+I]:=Y[2+I]*Y[2+I];
51                          R[I]:=SQRT(X[4+I]+Y[4+I]);
52                          A[I]:=SQRT((R[I]+X[2+I])/2);
53                          A[4+I]:=N[2+I]*A[I];
54                          A[7+I]:=SQRT((R[I]-X[2+I])/2);
55                          A[9+I]:=A[7+I]*K[2+I]+A[4+I];
56                          A[4+I]:=X[I]+N[5+I];
57                          A[2+I]:=A[9+I]/A[4+I];
58                          B[I]:=K[2+I]*A[I];
59                          B[4+I]:=N[2+I]*A[7+I];
60                          B[2+I]:=(B[I]-B[4+I])/A[4+I];
61                  'IF' A[2+I]>0 'THEN' 'GOTO' LL3;
62                          A[2+I]:=-A[2+I];
63                          B[2+I]:=-B[2+I];
64                  LL3:I:=I+1;
65                          'IF' I=1 'THEN' 'GOTO' LL1;
66              'IF'I=2'THEN''GOTO'LL1;
```

Section 2

$r_{12}^{(p)} = g_2 + ih_2$

```
67                          C:=COS(T4);
68                          C1:=N[2]*C;
69                  C2:=A[2]-C1;
70                          E2:=C1+A[2];
71                          D1:=K[2]*C;
72                          D2:=D1+B[2];
73                  F2:=B[2]-D1;
74                          E:=C2*E2;
75                          E1:=D2*F2;
76                          G2:=E+E1;
77                          G:=E2*E2;
78                          G1:=F2*F2;
79                          G:=G+G1;
80                          G2:=G2/G;
81                          F:=C2*F2;
82                          F1:=D2*E2;
83                  H2:=(F1-F)/G;
```

Section 3

$r_{23}^{(p)} = g_3 + ih_3$

```
84                          H:=N[3]*A[2];
85                          H1:=K[3]*B[2];
86                          H4:=N[2]*A[3];
87                          H5:=K[2]*B[3];
88                  C3:=H4+H5-H-H1;
89                          H8:=N[3]*B[2];
90                          H9:=K[3]*A[2];
91                          H6:=K[2]*A[3];
92                          H7:=N[2]*B[3];
93                          D3:=H9-H8+H7-H6;
94                          E3:=H+H1+H4+H5;
95                  F3:=H8+H7-H9-H6;
96                          G4:=C3*E3;
97                          G5:=D3*F3;
98                          G6:=E3*E3;
99                          G7:=F3*F3+G6;
100                         G3:=(G4+G5)/G7;
101                         F4:=C3*F3;
102                 H3:=(D3*E3-F4)/G7;
```

```
103                          P:=N[2]*A[2];
104                          P1:=K[2]*B[2];
105                         P2:=C-P-P1;
106                         P4:=N[2]*B[2];
107   Section 4.            P5:=K[2]*A[2];

108                         S2:=C+P+P1;
109                         Q2:=P4-P5;
110                         T2:=P5-P4;
111                         U:=P2*S2;
112   r12 = u2 + i V2       U1:=Q2*T2;
113   (5)                   U4:=S2*S2;
114                         U5:=U4+T2*T2;
115                         U2:=(U+U1)/U5;
116                         U7:=Q2*S2;
117                         U6:=P2*T2-U7;
118                         V2:=U6/U5;
-------------------------------------------
119                         Q:=N[3]*A[3];
120                         Q1:=K[3]*B[3];
121                         P3:=P+P1-Q-Q1;
122                         Q4:=B[3]*N[3];
123     Section 5           Q5:=K[3]*A[3];
124                         Q3:=P5-P4+Q4-Q5;
125                         S3:=P+P1+Q+Q1;
126   r23 = u3 + i V3       T3:=P5-P4-Q4+Q5;
127   (5)                   V:=P3*S3;
128                         V1:=Q3*T3;
129                         V4:=S3*S3;
130                         V5:=V4+T3*T3;
131                         U3:=(V+V1)/V5;
132                         V6:=P3*T3;
133                         V7:=Q3*S3;
134                         V3:=(V6-V7)/V5;
-------------------------------------------
135                         M1:=P+P1;
136     Section 6           M:=6,28318530*D/L;
137                         M1:=M1*M;
138                         L1:=(P4-P5)*M;
139   e^-2iδ2 = M2 - i L2   M3:=EXP(2*L1);
140                               M:=2*M1;
141                         M2:=M3*COS(M);
142                         L2:=M3*SIN(M);
-------------------------------------------
143                  H:=N[4]*A[3];
144                  H1:=K[4]*B[3];
145                  H4:=N[3]*A[4];
146                  H5:=K[3]*B[4];
147                  C3:=H4+H5-H-H1;
148   Section 7.     H8:=N[4]*B[3];
149                  H9:=K[4]*A[3];
150                  H6:=K[3]*A[4];
151 r34 = g4 + i h4  H7:=N[3]*B[4];
152 (p)              D3:=H9-H8+H7-H6;
153                  E3:=H+H1+H4+H5;
154                  F3:=H8+H7-H9-H6;
155                  G4:=C3*E3;
156                  G5:=D3*F3;
157                  G6:=E3*E3;
158                  G7:=F3*F3+G6;
159                  G4:=(G4+G5)/G7;
160                  F4:=C3*F3;
161                  H4:=(D3*E3-F4)/G7;
```

```
162                     Q:=N[41*A[4];
163                     Q1:=K[4]*B[4];
164                     P:=N[31*A[3];
165                     P1:=K[3]*B[3];
166  Section 8          P3:=P+P1-Q-Q1;
167                     Q4:=B[4]*N[4];

168                     Q5:=K[4]*A[4];
169                     P4:=N[3]*B[3];
170                     P5:=K[3]*A[3];
171  r(34)(s) = u4+iV4  Q3:=P5-P4+Q4-Q5;
172                     S3:=P+P1+Q+Q1;
173                     T3:=P5-P4-Q4+Q5;
174                     V:=P3*S3;
175                     V1:=Q3*T3;
176                     V4:=S3*S3;
177                     V5:=V4+T3*T3;
178                     U4:=(V+V1)/V5;
179                     V6:=P3*T3;
180                     V7:=Q3*S3;
181                     V4:=(V6-V7)/V5;
182                     M1:=P+P1;
183  Section 9.         M:=6.2831853*D12/L;
184                     M1:=M1*M;
185                     L1:=(P4-P5)*M;
186  e^(-2iδ3) = M3-iL3 M6:=EXP(2*L1);
187                     M:=2*M1;
188                     M3:=M6*COS(M);
189                     L3:=M6*SIN(M);
190                                   L4:=G3*M2;
191      Section 10.                  L5:=H3*L2;
192                                   A[11]:=G2+L4+L5;
193  r(12)(p) + r(23)(p) e^(-2iδ2) = A[11]+iB[11]  L6:=H3*M2;
194                                   L7:=G3*L2;
195                                   B[11]:=H2+L6-L7;
196                                   S4:=U2*U3*M2;
197      Section 11.                  S5:=V2*V3*M2;
198                                   S6:=L2*V3*U2;
199                                   S7:=L2*V2*U3;
200  1+r(12)(s) r(23)(s) e^(-2iδ2) = A[12]+iB[12]  A[12]:=1+S4-S5+S6+S7;
201                                   S8:=V2*U3*M2;
202                                   S9:=U2*M2*V3;
203                                   S10:=U2*U3*L2;
204                                   S11:=V2*V3*L2;
205                                   B[12]:=S8+S9-S10+S11;
206                                   Q6:=G2*G3*M2;
207                                   Q7:=H2*H3*M2;
208      Section 12.                  Q8:=H2*L2*G3;
209                                   Q9:=H3*L2*G2;
210                                   A[13]:=1+Q6-Q7+Q8+Q9;
211                                   P6:=H2*G3*M2;
212  1+r(12)(p) r(23)(p) e^(-2iδ2) = A[13]+iB[13]  P7:=H3*G2*M2;
213                                   P8:=L2*G2*G3;
214                                   P9:=H2*H3*L2;
215                                   B[13]:=P6+P7-P8+P9;
```

```
216                          T5:=U3*M2;
217      Section 13.         T6:=V3*L2;
218                          A[14]:=U2+T5+T6;
219 r(s)12 + r(s)23 e^-2iδ2 = A[14] + iB[14]  T7:=M2*V3;
220                          T8:=U3*L2;
221                          B[14]:=V2+T7-T8;
```

```
222              R[2]:=A[11]*A[13];
223                G11:=R[2]+B[11]*B[13];
224              R[3]:=B[11]*A[13];
225                M11:=R[3]-A[11]*B[13];
226              R[4]:=A[13]*A[13];
227              R[5]:=R[4]+B[13]*B[13];
```

Section 14

$$r_{13}^{(p)} = \frac{r_{12}^{(p)} + r_{23}^{(p)} e^{-2i\delta_2}}{1 + r_{12}^{(p)} r_{23}^{(p)} e^{-2i\delta_2}}$$

$$r_{13}^{(p)} = g_{11} + i M11$$

```
228                G11:=G11/R[5];
229                M11:=M11/R[5];
```

```
230              R[2]:=A[14]*A[12];
231                G12:=R[2]+B[14]*B[12];
232              R[3]:=B[12]*A[14];
233                M12:=B[14]*A[12]-R[3];
234              R[4]:=A[12]*A[12];
235              R[5]:=B[12]*B[12]+R[4];
236                G12:=G12/R[5];
237              M12:=M12/R[5];
```

Section 15

$$r_{13}^{(s)} = g_{12} + i M12$$

```
238              L4:=G4*M3;
239              L5:=H4*L3;
240              A[11]:=G11+L4+L5;
241              L6:=H4*M3;
242              L7:=G4*L3;
243              B[11]:=M11+L6-L7;
```

Section 16.

$$r_{13}^{(p)} + r_{34}^{(p)} e^{-2i\delta_3} = A[11] + iB[11]$$

```
244              S4:=G12*U4*M3;
245              S5:=M12*V4*M3;
246              S6:=L3*V4*G12;
247              S7:=L3*M12*U4;
248              A[12]:=1+S4-S5+S6+S7;
249              S8:=M12*U4*M3;
250              S9:=G12*M3*V4;
251              S10:=G12*U4*L3;
252              S11:=M12*V4*L3;
253              B[12]:=S8+S9-S10+S11;
```

Section 17

$$1 + r_{13}^{(s)} r_{34}^{(s)} e^{-2i\delta_3} = A[12] + iB[12]$$

```
254              Q6:=G11*G4*M3;
255              Q7:=M11*H4*M3;
256              Q8:=M11*L3*G4;
257              Q9:=H4*L3*G11;
258              A[13]:=1+Q6-Q7+Q8+Q9;
259              P6:=M11*G4*M3;
260              P7:=H4*G11*M3;
261              P8:=L3*G11*G4;
262              P9:=M11*H4*L3;
263              B[13]:=P6+P7-P8+P9;
```

Section 18

$$1 + r_{13}^{(p)} r_{34}^{(p)} e^{-2i\delta_3} = A[13] + iB[13]$$

```
264              T5:=U4*M3;
265              T6:=V4*L3;
266              A[14]:=G12+T5+T6;
267              T7:=M3*V4;
268              T8:=U4*L3;
269              B[14]:=M12+T7-T8;
```

Section 19.

$$r_{13}^{(s)} + r_{34}^{(s)} e^{-2i\delta_3} = A[14] + iB[14]$$

```
270                 R[2]:=A[11]*A[12];
271                 G11:=R[2]-B[11]*B[12];
272                 R[3]:=B[11]*A[12];
273                 M11:=A[11]*B[12]+R[3];
274                 R[4]:=A[13]*A[14];
275                 G12:=R[4]-B[13]*B[14];
276                 R[5]:=B[13]*A[14];
277                 M12:=A[13]*B[14]+R[5];
278                 W1:=G11*G12;
279                 W2:=M11*M12;
280                 W3:=G12*G12;
281                 W4:=W3+M12*M12;
282                 W:=(W1+W2)/W4;
283                 Z1:=G12*M11;
284                 Z2:=G11*M12;
285                 Z:=(Z1-Z2)/W4;
286                       Z3:=180*ARCTAN(Z/W)/(4*ARCTAN(1));
287       'IF'Z3>0'THEN''GOTO'LL7;
288       Z3:=180+Z3;
289           LL7:Z4:=W*W;
290                       Z5:=180*ARCTAN(SQRT(Z4+Z*Z))/(4*ARCTAN(1));
291                 I1:=ENTIER(D+.6);
292                 PRINT (I1,4,0);
293                 PRINT (Z3,5,3);
294                 PRINT (Z5,6,3);
295                 NEWLINE(1);
296                 D:=I1+D4;
297       D12:=D12-0.783*D4;
298                 'IF' D<Z6 'THEN' 'GOTO' LL9;
299                 D:=0;
300       'GOTO'LL2;
301                 LL8:;
302       'END';
```

Section 20

$$\frac{r_{14}(p)}{r_{14}(s)} = \frac{\left(\frac{A[11]+iB[11]}{A[13]+iB[13]}\right)}{\left(\frac{A[14]+iB[14]}{A[12]+iB[12]}\right)} = \frac{G11+iM11}{G12+iM12}$$

Section 21

$$\frac{r_{14}(p)}{r_{14}(s)} = W+iZ = \tan\Psi e^{i\Delta}$$

Section 22

$$\Delta = \tan^{-1}\frac{Z}{W}$$

Section 23

$$\Psi = \tan^{-1}\sqrt{W^2+Z^2}$$

Section 24

Correction for oxidation reducing metal thickness.

extension of program 2, further sections having been added for the calculation of $\cos\phi_4$, $r_{34(p)}$ and $r_{34(s)}$.

The program calculates an effective r_{13} for both (p) and (s) components by combining the first two boundaries into an effective single interface, as before. It then repeats the method using an equation similar to (iv) to combine this interface with the remaining boundary and arrive at effective values of r_{14} for the entire system. See sections 16 to 20.

For an oxide layer of zero thickness, the values of Ψ and Δ computed are, of course, identical to those from program 2.

For the very thin aluminium films, which are the subject of most of the experiments reported here, a correction must be applied to allow for the fact that as the oxide layer grows, the metal layer is reduced. This is done in statement 297 for which it was calculated, from the known densities of bulk aluminium and aluminium oxide that the formation of a layer of oxide of thickness D4, requires the annihilation of a layer of aluminium of thickness 0.78 (D4). This correction is not likely to be exact, but ensures that some consideration is given to the effect. The data cards for program 3 must contain the following data in this order:

+ 1.0 Any positive number to ensure data acceptance. Step in oxide layer thickness (A.U.)

n_2, k_2 } oxide layer constants

n_3, k_3 } metal film constants

n_4, k_4 } substrate constants

Angle of incidence in radians

Wavelength of light used (A.U.)

Starting thickness of oxide layer (A.U.)

Final thickness of oxide layer (A.U.)

Starting thickness of aluminium film.

APPENDIX 3

SPECIMEN RESULTS USING COMPENSATOR METHOD OF ELLIPSOMETRY

With the ellipsometer aligned and set up as described in section 4.1.3, the procedure for determination of the reference azimuths, described fully in section 4.2.4, leads to results for which the table below is typical. For easier pattern development, the figures are given to the nearest degree.

REFERENCE AZIMUTHS. CORRESPONDING "CROSSED" POSITIONS

π_p	172	α_s	42
π_p'	352	α_s'	222
π_s	82	α_p	312
π_s'	262	α_p'	132

Compensator Reference Azimuth

With the polariser and analyser set at π_s' and α_p' respectively, the minimum light intensity occurs for 342° and 252° on the compensator scale. It was shown that 342° represents the fast axis parallel to the plane of incidence and therefore the compensator reference azimuths are as follows:

Fast axis at $+\frac{\pi}{4}$ $\quad 342 - 45 = 297^{\circ}$

Fast axis at $-\frac{\pi}{4}$ $\quad 342 + 45 = 27^{\circ}$

A set of results, taken for an aluminium film, is shown below. The numbering of the polariser and analyser pairs is explained in section 2.3

Compensator $+\frac{\pi}{4}$, 297°

P_1	P_2	P_3	P_4
205	139	25	319

A_1	A_2	A_3	A_4
153	63	333	243

Compensator $-\frac{\pi}{4}$, 27^{o}

P_1	P_2	P_3	P_4
139	205	319	25

A_1	A_2	A_3	A_4
291	201	111	21

The values of Ψ are calculated from the polariser readings and the values of $\varkappa$ are calculated from the analyser readings by performing the operation shown in the table below:

Compensator $+\frac{\pi}{4}$, 297^{o}	P_1	P_2	P_3	P_4
	$P_1 - 172$	$172 - P_2$	$P_3 - 352$	$352 - P_4$
	A_1	A_2	A_3	A_4
	$A_1 - 42$	$A_2 - 312$	$A_3 - 222$	$A_4 - 132$
Compensator $-\frac{\pi}{4}$, 27^{o}	P_1	P_2	P_3	P_4
	$172 - P_1$	$P_2 - 172$	$352 - P_3$	$P_4 - 352$
	A_1	A_2	A_3	A_4
	$42 - A_1$	$312 - A_2$	$222 - A_3$	$132 - A_4$

The procedure leads to an indicated value of

$\Psi = 33^{o}$ and $\varkappa = 111^{o}$, from which

$\Delta = 132^{o}$

APPENDIX 4

SPECIMEN RESULTS USING BEATTIES METHOD OF ELLIPSOMETRY

The reference azimuths for the HR polaroids are given in the following table. The pairs of related 'crossed' positions are indicated.

π_s	$339^\circ 21'$	α_p	$245^\circ 7'$
π_p	$69^\circ 21'$	α_s	$155^\circ 7'$

The eight pairs of polariser - analyser scale settings required to give the azimuths ψ_p and ψ_A as described in section 2.4 for the required intensity measurements are as follows:

	Polariser		Analyser	
I_1	$\pi_p - 45$	$24^\circ 21'$	α_s	$155^\circ 7'$
I_2		$24^\circ 21'$	α_p	$245^\circ 7'$
I_3		$24^\circ 21'$	$\alpha_p + 45$	$290^\circ 7'$
I_4		$24^\circ 21'$	$\alpha_p - 45$	$200^\circ 7'$
I_1	$\pi_p + 45$	$114^\circ 21'$	α_s'	$335^\circ 7'$
I_2		$114^\circ 21'$	α_p'	$65^\circ 7'$
I_3		$114^\circ 21'$	$\alpha_p + 45$	$290^\circ 7'$
I_4		$114^\circ 21'$	$\alpha_p - 45$	$200^\circ 7'$

Some typical results taken on an opaque gold film covered with barium stearate for a wavelength of 549 nm are given below:

I_1	I_2	I_3	I_4	I_1'	I_2'	I_3'	I_4'
9.80	9.21	12.42	7.33	10.68	7.59	7.01	12.22

Mean values :

$\bar{I}_1$	$\bar{I}_2$	$\bar{I}_3$	$\bar{I}_4$
10.24	8.40	12.32	7.17

From which

$$\rho = \sqrt{\frac{I_3}{I_1}} = 0.9055 = \tan \Psi$$

$$\therefore \Psi = 42^\circ 8'$$

and

$$\cos \Delta = \tfrac{1}{2}\left(\frac{1}{\rho} + \rho\right)\left\{\frac{I_3 - I_4}{I_3 + I_4}\right\}$$

$$\cos \Delta = 0.2695$$

from which $\Delta = 105^\circ 38'$

APPENDIX 5

J. Phys. F: Metal Phys., 1971, Vol. 1. Printed in Great Britain

Variation of optical and electrical properties due to annealing of thin, vapour quenched aluminium films

K. R. O'SHEA and R. W. FANE
Department of Physics, The University of Aston in Birmingham
Gosta Green, Birmingham 4, UK
MS received 20*th April* 1971

Abstract. Aluminium films of 11 to 13 nm thickness have been prepared in UHV on glass substrates held at 77°K. The changes of resistance and complex refractive index on subsequent heat treatment were related to a change in the effective electron density and relaxation time consistent with the Drude–Zener theory. The optical and electrical measurements were corrected for the effects of oxide growth, which was observed to take place at all pressures. This correction was deduced from a study of the oxidation of films of similar thickness.

1. Introduction

The work described here forms part of a continuing program of investigation of thin metal films and the correlation between electrical and optical properties during annealing.

Previous measurements of n and k, the real and imaginary parts of the complex refractive index, and their variation on annealing have been reported for aluminium films ranging in thickness from 40 to 120 nm (Neal *et al.* 1970). These were coupled with measurements of structural defects made by variance analysis of x-ray line profiles. (Grimes *et al.* 1970).

Recent interest in the annealing of defects in metals has been confined mostly to gold, silver, copper and tungsten. Seeger *et al.* (1960), Chechetenko *et al.* (1969), Dobson and Hopkins (1968).

The study of aluminium raises additional experimental problems because of its chemical affinity for oxygen. It is for this reason that the technique of ellipsometry is particularly useful. The ellipsometer measures two parameters ψ and Δ, which, provided that the film thickness is known, can be used to compute the optical constants n and k for a surface. In the visible region of the spectrum the measured values of n and k are extremely sensitive to any formation of an oxide layer: even 0·5 nm average coverage is readily detectable. However, additional difficulties of interpretation can arise for films below 15 nm thickness, when the changes of ψ and Δ are in the same direction and even of similar magnitude for both oxidation and annealing.

2. Present Work

In the present series of experiments, the aim was to measure changes of optical constants and defect structure continuously and simultaneously, using electrical resistance as a measure of the concentration of defects. The various changes could then be followed throughout the annealing process and the nature of the changes deduced. Measurements have been made on thin films, 10 to 20 nm, for several reasons:

(i) The disordering influence of the substrate leads to a greater concentration of defects in thinner films, and tends to be less important for thicker ones.

(ii) The formation of aluminium oxide causes a reduction in thickness of the metal and leads to a higher resistance; an effect which is proportionately greater for a thinner film.

(iii) Due to the penetration depth of electro-magnetic waves in a highly absorbing metal, (approx 10 nm in Al) the optical measurements give information on the entire thickness of the film.

As expected, the amount of disorder introduced into the metal film is greater if it is deposited on to a substrate held at 77°K. On warming to room temperature, the resulting decrease of electrical resistance may be as much as 40%. (Buckel and Hilsch 1954).

This process has been examined in detail and tentatively attributed to the migration of vacancies from grain boundaries. The thermal activation energy for the process has been estimated.

Since the film thickness is an important parameter in the calculation of optical constants, and for most methods such thin films are almost at the limit of measurement for reasonable accuracy, each film thickness was estimated by several methods, namely:

(i) Fringes of equal chromatic order. (Scott 1950).

(ii) Quartz crystal thickness monitor.

(iii) Photographic densitometer to measure the percentage of light transmitted by the films.

(iv) Electrical resistivity.

(v) The changes of electrical resistance and of the parameters ψ and Δ on total oxidation of the films.

(vi) Mechanical measurements using a 'talystep' instrument.

Where appropriate, a correction was applied for any oxide layer present. Only when all these methods gave consistent results was the film thickness finalized, and computations of n and k performed on an ICL 1905 computer.

3. Experimental Details

The UHV system was of conventional type as previously described by Fane and Neal (1968). It incorporated a diffusion pump charged with DC 705 oil and two vapour traps between the pump and the stainless steel chamber. The upper trap was baked with the experimental chamber to 400°C enabling an ultimate pressure of 2×10^{-10} Torr to be consistently obtained. The substrate of Corning 0211 glass was supported on a stainless steel block welded to a stainless steel tube. Inside this tube was a second thinner tube with a heater block attached to its end, which when bolted in position, made good contact with the substrate block. By filling the inside tube with liquid nitrogen and activating the heater, the substrate could be held at any temperature from −196°C to 500°C. See figure 1.

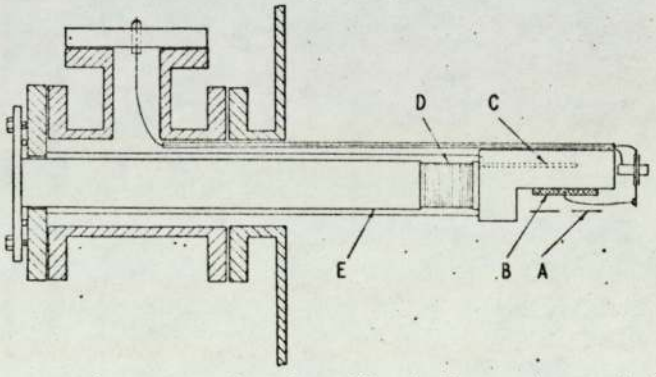

Figure 1. Arrangement for support of specimen film. A, Evaporation mask; B, glass substrate; C, block thermocouple hole; D, heater wound over block; E, liquid nitrogen container. In use, the central tube is vertical.

Electrical connections were made to the films by gold wires (0·005 inch diam) thermally bonded on to previously prepared nichrome/aluminium contact areas.

The specimen of aluminium (99·999 %) was evaporated from a tungsten filament at a rate of approximately 10 nm per minute: the maximum pressure during evaporation being $\sim 10^{-8}$ Torr. The experimental chamber also incorporated a 'Mini-mass' residual gas analyser and a quartz crystal thickness monitor.

Resistance measurements were made manually with a potentiometer, using the four point probe method, normal precautions being taken in reversing the film current (100μA) to eliminate thermal effects.

The arrangement of the optical components was similar to that previously described by Fane and Neal (1970). A parallel beam of plane-polarized, monochromatic light of wavelength 549 nm fell on the specimen at an angle of incidence of 64° and was reflected through the compensator which was chosen to be exactly quarter wave for the light used. At the end of each experiment, measurements were performed with the Kodial windows removed and a correction applied to all previous measurements.

To enable more rapid ellipsometer readings to be taken only two of the possible four quadrants were used. Consequently the reproducibility of the parameters ψ and Δ is somewhat lower than normal ($\pm 10'$ instead of $\pm 5'$). Although the ellipsometer described is of comparatively simple construction the *changes* of n and k with which we are chiefly concerned, are of fairly high accuracy (1 or 2 per cent).

4. Results and Discussion

The variation of the resistance of a typical film with temperature is shown in figure 2. During the initial warm-up from the deposition temperature of 77 K to room temperature (stage III anneal) there is a fall of resistance, amounting to about 40% of the initial value for the case illustrated.

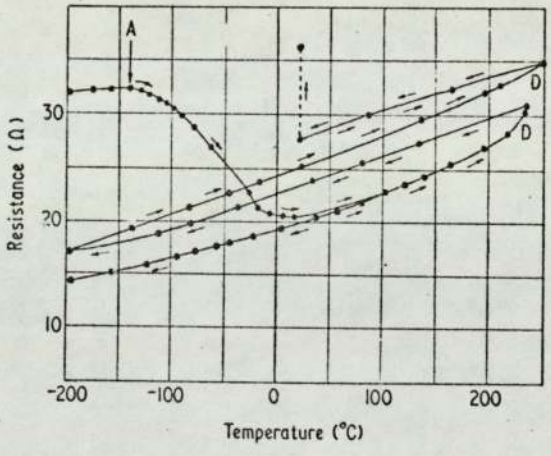

Figure 2. Variation of resistance with heat treatment (Film 2).

Thicker films show the same effect but the proportional change is less. Around room temperature there is a resistance minimum, followed by an approximately linear rise with temperature as in normal metallic behaviour. Returning the specimen to 77 K shows that irreversible changes have taken place.

At this stage the temperature coefficient of resistance of the film illustrated was 0·0015 per °C and the resistivity at 0 C was 12·1 μΩ cm. The corresponding values for bulk aluminium are 0·0045 per C and 2·45 μΩ cm respectively.

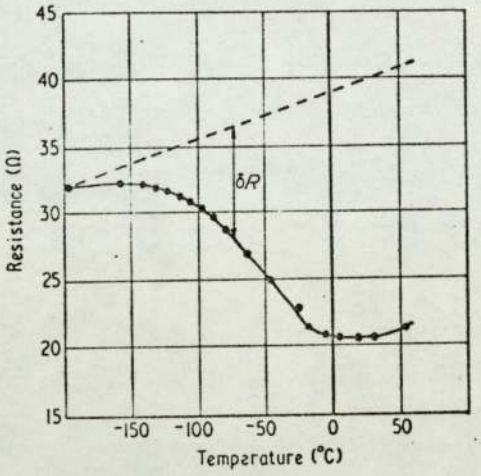

Figure 3. Resistance fall during stage III anneal (Film 2).

4.1. *Anneal to room temperature (stage III): Electrical measurements*

A detailed examination of the stage III anneal has been made for a number of films. The determination of δR, the resistance attributable to the annealing of defects, is illustrated in figure 3. Semi-logarithmic plots of δR against $1/T$ are shown in figure 4 and are compared with the results of Buckel and Hilsch (1950).

The straight lines obtained indicate an annealing process with a single activation energy. Lidiard (1968).

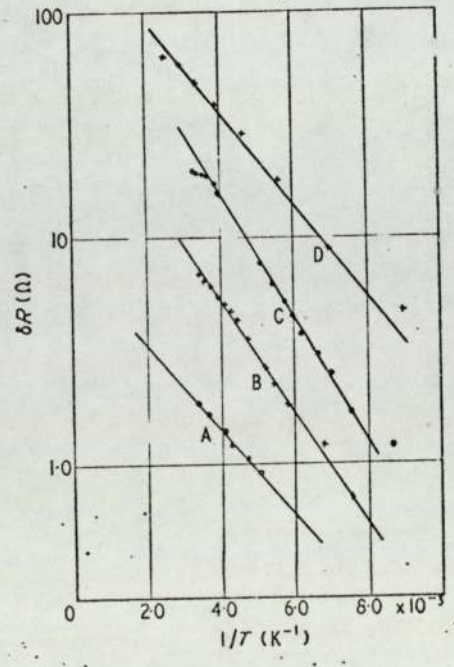

Figure 4. Stage III anneal. Plot of δR against $1/T$ for various films A. 85 nm thickness. B. film 3. C. film 2. D. 20 nm thickness (after Buckel and Hilsch).

Further experiments were performed to carry out a 'ratio of slopes' analysis to determine this activation energy. As explained by Thompson (1969), it is required to measure the rate of fall of resistance with time at two fixed temperatures T_1 and T_2 which should be close together. The ratio of these slopes just before and just after the change lead to the activation energy U, defined by the equation:

$$\frac{\{d(\Delta R)/dt\}_{\text{At } T_1}}{\{d(\Delta R)/dt\}_{\text{At } T_2}} = \exp \frac{u}{k}\left(\frac{1}{T_1} - \frac{1}{T_2}\right)$$

Figure 5 is typical of several films investigated, the mean activation energy of which was found to be $0{\cdot}20 \pm 0{\cdot}05$ eV.

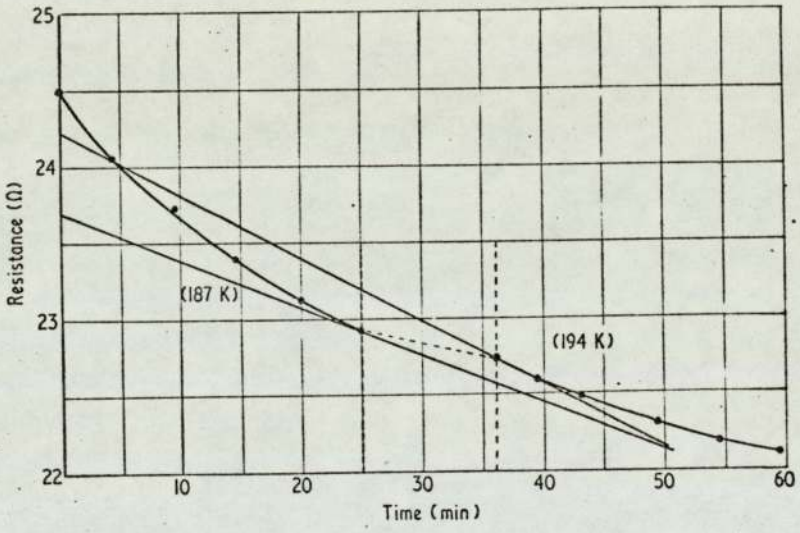

Figure 5. Activation energy calculation (Film 12).

Apart from the smaller activation energy, the results obtained above show marked similarity with those of Ceresawa (1969) in which cold working of bulk aluminium at 77 K produced defects which annealed out between -100°C and 0°C with an activation energy of 0·05 eV. These defects were proposed to be single vacancies. On the other hand Neugebauer (1964) suggests that the fall of resistance in quenched metal films on warming is caused by grain growth, a fact supported by electron microscopy. Andrews has estimated the specific grain boundary resistivity in pure aluminium as $2{\cdot}45 \times 10^{-12}$ Ω cm^2. On this basis, the magnitude of resistance fall observed is quite consistent with the reduction of grain boundary area as crystal grains grow from a deposition value of ~ 0·4 nm to a size of the order of the film thickness, 11 nm.

If the major part of the recovery can be ascribed to the disappearance of grain boundary area as a result of the migration of trapped multiple vacancies, as envisaged by Gleiter (1969) it is possible that the high defect concentration may partly explain the low value obtained for the activation energy. See, for example, Dawson *et al.* (1968).

It does appear likely that the defect concentration in films vapour quenched at 77 K would be extremely high. Indeed, if we take the resistivity of vacancies in aluminium as that given by Cotterill (1963) as $1{\cdot}4 \times 10^{-6}$ Ω cm per at% vacancy, then the measured defect contribution to resistivity would indicate about 6·5 at% vacancy. It is interesting to note that Mader and Nowick (1967) deduce a similar figure of 7 at % vacancy in quenched copper and silver films.

On commencement of the stage III anneal the resistance was always found to increase slightly at first. (See figure 2.) This is caused by the rise in temperature of the substrate during film deposition. A thin-film copper–nickel thermocouple was deposited on the substrate where an aluminium film could be deposited directly over the junction. The thermocouple was annealed and calibrated both before and after formation of the specimen film. A temperature rise of 60°C was recorded as a result of thermal radiation from the filament and a further rise of 5°C occurred as the specimen film was formed from the vapour.

Since halting the warm-up at any temperature θ and cooling again to 77 K results in linear metallic behaviour between θ and 77 K, a further fall of resistance occurring only when the temperature θ is exceeded, it may be concluded that the true deposition temperature was some 65°C above liquid nitrogen temperature. This is then seen to correspond to the peak value of resistance during the warm up. (See point A on figure 2.) The magnitude of the above effect is consistent with other direct measurements of temperature rise during film deposition made by Namba (1968).

4.2. *Anneal to room temperature (stage III): Optical measurements*

The variation of optical parameters ψ and Δ for the same film, corrected for strain in the windows, is shown in figure 6. As for all other films, the value of both ψ and Δ were

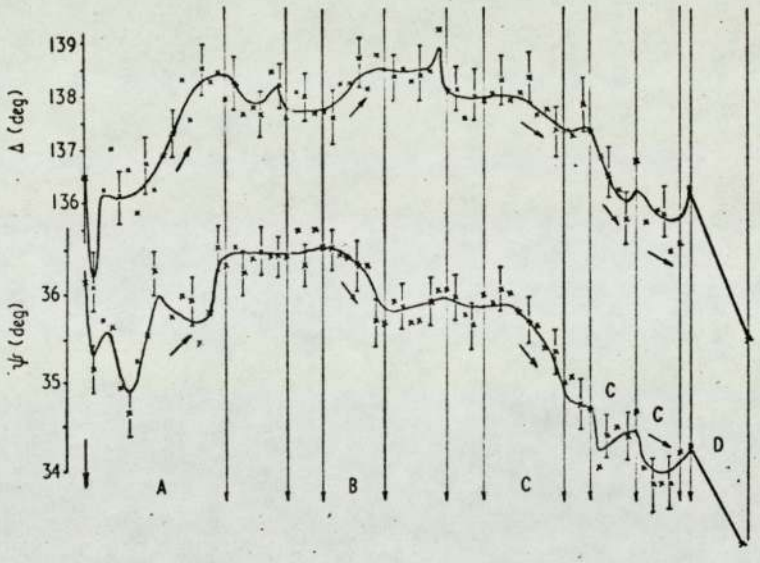

Figure 6. Variation of Optical Parameters ψ and Δ throughout life of film 2. A, Initial warm-up (stage III). B, anneal to 100°C. C, anneal to 260° (Several). D, final oxidation.

Table 1. Optical constants of aluminium films immediately after deposition at 77 K

Film Number	Metal thickness (nm)	ψ	Δ	n	k	$n^2 - k^2$	nk
2	11·0	36·13	136·58	0·70	5·45	−29·21	3·82
3	13·0	35·55	139·22	1·08	5·15	−25·35	5·55
7	12·5	33·88	134·77	0·92	4·73	−21·52	4·35
12	12·5	33·38	133·87	0·92	4·61	−20·40	4·24
8	12·0	32·53	133·57	0·98	4·55	−19·74	4·48

observed to rise during the first warm-up (during which time the resistance is falling). In terms of the complex refractive index $N = n - ik$, these changes can be interpreted as an increase in the value of k and an increase in the value of n, the product nk thus becoming greater. (See table 2.)

Table 2. Optical and electrical changes produced by the stage III anneal

Film number	Metal thickness (nm)	Increase of $\psi°$	Increase of $\Delta°$	% fall of $n^2 - k^2$	% Rise of nk	% rise in Conductivity	Atomic % Vacancy Removed
2	11·0	0·54	2·30	7·95	43	37	6·5
3	13·0	0·50	1·33	5·90	7	10	2·9
7	12·5	0·32	1·70	5·00	23	26	4·5
12	12·5	0·14	1·97	4·30	18	28	4·4
8	12·0	0·20	0·90	1·80	16	23	4·1

On the whole, the measured values of n are in reasonable agreement with theoretical values given by Ehrenreich *et al.* (1963), namely $n = 0{\cdot}99$ and $k = 6{\cdot}5$. To assess the results of table 2 in the light of the optical theory of metals, the standard Drude–Zener approximations for conduction electrons may be recalled;

$$\epsilon_1 = n^2 - k^2 = 1 - \frac{4\pi N^* e^2}{m\omega^2} \tag{1}$$

$$\epsilon_2 = 2nk = \frac{4\pi N^* e^2}{m\omega^2 \tau} \tag{2}$$

$$\sigma_0 = \frac{N^* e^2 \tau}{m} \tag{3}$$

where the complex dielectric constant $\epsilon = \epsilon_1 - i\epsilon_2$; N^* is the effective electron density and τ the relaxation time; σ_0 is the dc-conductivity.

These equations were derived for conduction electrons only and do not apply in the region where interband absorption occurs. Figure 7 is a sketch of the general shape of the absorption spectrum of aluminium and shows that the present measurements, made at 2·5 eV, fall in a region of the aluminium absorption spectrum where interband transitions

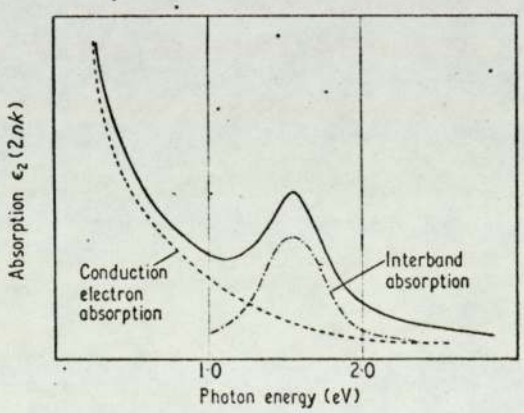

Figure 7. Absorption spectrum of aluminium.

are significant. However, equation (1) is still valid in this region although equation (2) is not, as shown by Sokolov (1967).

Table 2 shows that the stage III anneal produces a drop in the value of $n^2 - k^2$, indicating from equation (1) that the value of N^*/m has increased. In a qualitative way it would be expected that the disappearance of vacancies would lead to an increase of N^*, the effective electron density. In fact, table 2 indicates a possible correlation between the fall of $n^2 - k^2$ and the estimated vacancy concentration that has annealed out.

Taking film 2 as an example, table 2 also shows that the increase of N^*/m, $\sim 8\%$ is insufficient to account for the observed increase of conductivity, $\sim 37\%$. Equation (3) shows that to account for the observed increase of conductivity it is therefore necessary that the relaxation time, τ, should increase at the same time, by about 30%.

The combined effect of an increase of N^*/m and an increase of τ would be expected to produce, from equation (2), a reduction of the conduction electron contribution to nk of approximately 23%. However, the effect of the annealing is to increase the interband contribution to the absorption, so that the observed value of nk increases by approximately 40%. Abeles and Theye (1969), working with gold films, have also observed larger values of nk for films of increased perfection in the region of interband transitions. The proposed increase of N^*/m and the increase in τ as the vacancies are annealed out of the film are also in agreement with the results of Abeles and Theye (1969).

4.3. *Anneal to 100°C (Stage IV)*

The changes of ψ and Δ when films are heated to 100°C are shown in figure 6. The value of ψ falls while the value of Δ rises. Table 3 shows that this corresponds to a rise of n accompanied by a small reduction in the value of k.

Table 3. Optical and electrical changes produced by the anneal to 100°C (stage IV)

Film Number		ψ	Δ	n	k	$n^2 - k^2$	nk	Resistance (Ω)
2	Before 100°C Anneal	36·67	138·88	0·79	5·67	−31·53	4·48	20·6
2	After 100°C	35·82	139·82	0·98	5·60	−30·40	5·48	20·0

The anneal produced only a small decrease in resistance (figure 2). The observed changes are due to two opposing effects; firstly annealing, which makes Δ and ψ increase and the resistance fall, and secondly oxidation, which makes Δ and ψ fall and the resistance rise.

4.4 *Anneal to 250°C*

During the heating of film 2 to 250°C it was observed that the resistance increased at higher temperatures at a greater rate than would result from lattice vibrations alone. Similar results were also observed for subsequent heating cycles (see points D on figure 2). At the same time (figure 6) the values of ψ and Δ both show a decrease. The direction of change of these three variables are the same as during final oxidation of the film (figures 2 and 6). The extent of changes on final oxidation also indicate that some oxidation had already taken place during the life of the film. In fact, figure 2 and figure 6 show that, after the first few hours, there is a steady upward drift in resistance and a downward drift of ψ and Δ, all indicating oxidation.

4.5. *Oxidation experiments*

Further experiments were undertaken in which films were deposited under identical conditions and maintained in UHV for varying lifetimes before finally exposing them to

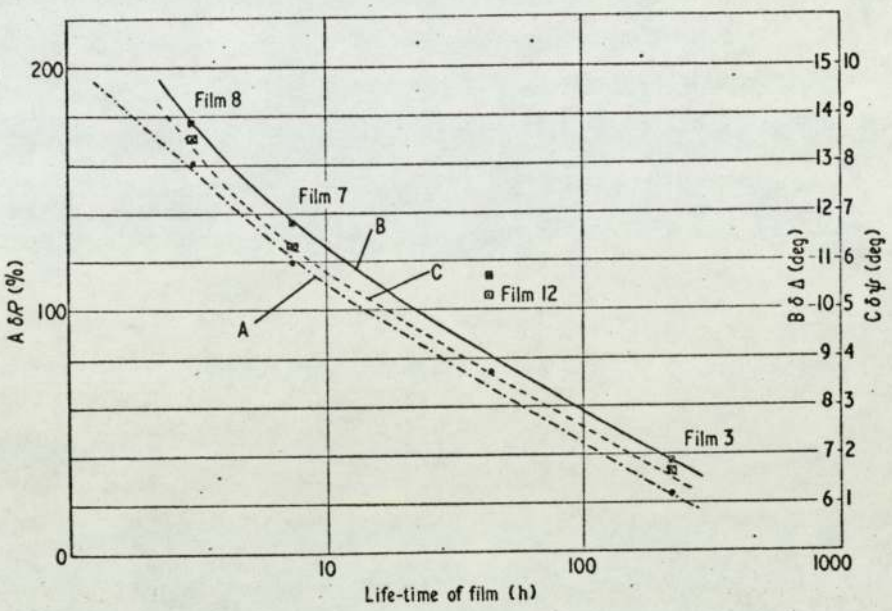

Figure 8. Changes of resistance, ψ and Δ on final oxidation A, Percentage rise of resistance. B, reduction of Δ. C, reduction of ψ.

the atmosphere. Table 4, together with figure 8 shows a clear dependence of the extent of these final changes on the lifetimes of the films. We may conclude that oxidation was occurring throughout the life of the films.

Calculations indicate a rate of oxide formation of 0·05 nm per hour on a completely fresh surface. For the measured partial pressure of oxygen of 2×10^{-11}Torr during the experiment, this oxidation rate is consistent with times of monolayer formation. Table 4 may also be used to extrapolate to a hypothetical 'zero' lifetime and thus make a correction for oxidation effects.

Further experiments were undertaken to observe the properties of a film maintained at a constant temperature (46°C) in UHV. Figure 9 shows the corresponding variation of ψ, Δ and resistance which all proceed in the direction of oxidation, even at the total pressure of $1{\cdot}5 \times 10^{-9}$Torr, again equivalent to a rate of 0·05 nm per hour on a clean surface. The rate is seen to increase to 0·4 nm per hour at a higher pressure of $1{\cdot}5 \times 10^{-8}$Torr, and to return to the original rate when the pressure is reduced again. The linear dependence of oxide layer thickness on lg (time) agrees with the previous findings of Fane and Neal (1970).

The above results are important in view of the large number of optical measurements on aluminium published, in which base pressures are quoted of the order of 10^{-6}Torr or

Table 4. Optical and electrical changes produced by exposure of the films to the atmosphere

Film Number	Thickness (nm)	Total lifetime (hrs)	Fall of ψ°	Fall of Δ°	Reduction of Conductivity %
8	12·0	3	8·56	13·85	162
7	12·5	7½	6·36	11·80	120
12	12·5	43	5·73	10·40	88
3	13·0	219	1·65	6·80	24

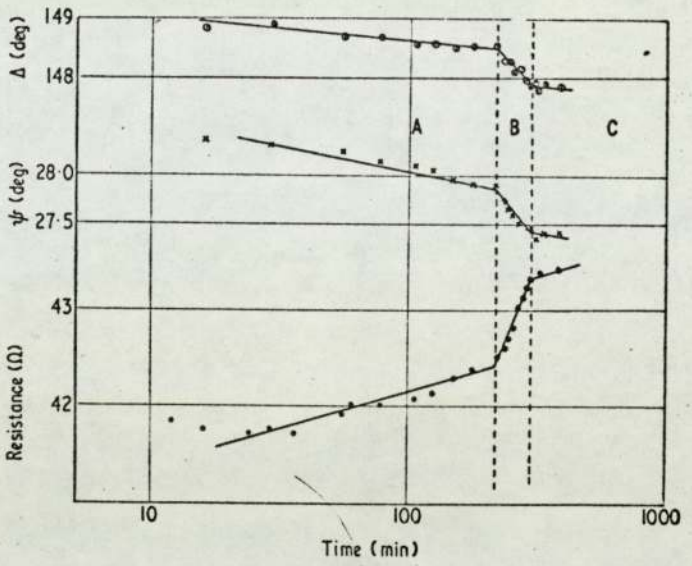

Figure 9. Simultaneous variation of resistance, ψ and Δ due to oxidation. Region **A**, $1{\cdot}5 \times 10^{-9}$Torr. Region B, $1{\cdot}5 \times 10^{-8}$Torr. Region C, $1{\cdot}5 \times 10^{-9}$Torr. Temperature throughout 46°C.

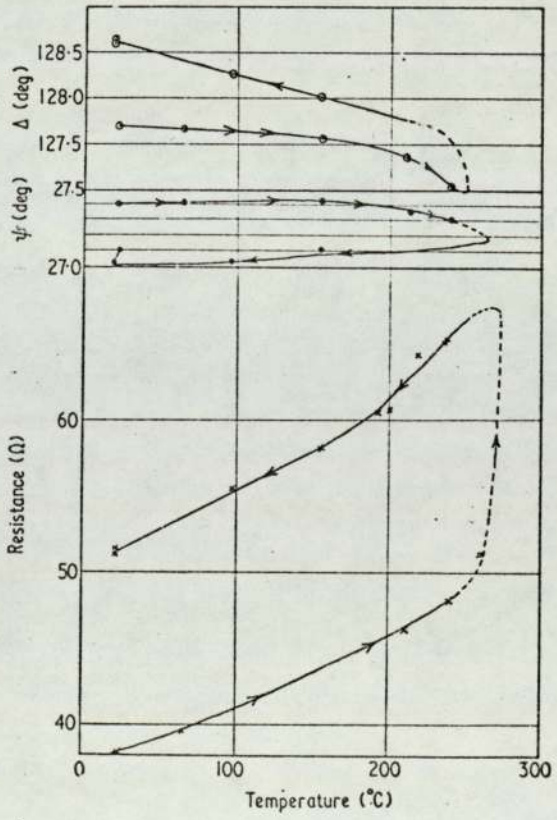

Figure 10. Variation of resistance, ψ and Δ during anneal of fully oxidized film 12.

higher. Measurements made at these pressures are almost certainly performed on oxidized surfaces. It is of interest to note that if an oxidized surface were interpreted as a clean surface, the calculated values of n and k would both be smaller than the true values. This reaffirms the conclusions of Fane and Neal (1970) for thicker films. It does mean, however, that the changes of n and k produced during annealing of thinner films (Neal *et al.* 1970) must be partly explained by oxide formation.

One possible way of avoiding the problem would be to completely oxidize a film, by exposing it to the atmosphere for several days and when the equilibrium layer of 35Å was achieved to then anneal the films in vacuo.

4.6. *Annealing of totally oxidized films to 250°C*

The results of such experiments are shown in figures 10 and 11 for films deposited at 77 K and at 296 K respectively. The changes produced are similar for both films, namely a rise of resistance, a fall of ψ and a rise of Δ. For the thickness of films involved this indicates a rise in the value of n, with k remaining almost constant. See table 5. The experiments of Klei (1969) confirm that the oxide layer only grows significantly above 35 Å for temperatures above 350°C, and so may be assumed stable in these experiments.

This being the case, the increase of resistance and also the larger value of n are attributed to a higher defect concentration, possibly brought about by the differential thermal expansion between the glass substrate and the film producing an increase of dislocation density, as suggested by Grimes *et al.* (1970).

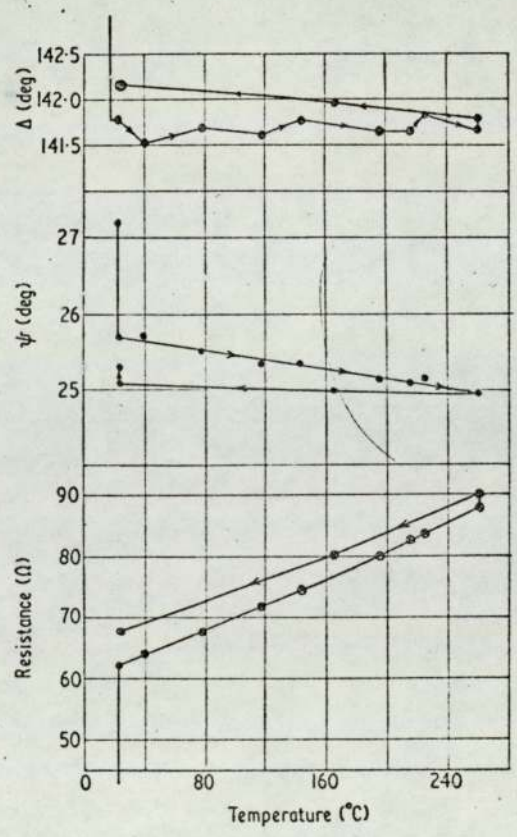

Figure 11. Variation of resistance, ψ and Δ during anneal of fully oxidized, room-temperature deposited, film 4.

Table 5. Effect of annealing on a totally oxidized film

Film number		ψ	Δ	n	k	$n^2 - k^2$	nk	Resistance Ω
12	Before 250°C Anneal	33·52	135·84	1·05	4·73	−21·27	4·97	38·2
12	After 250°C	33·12	136·84	1·16	4·72	−20·93	5·48	51·3

5. Conclusions

Aluminium films of the order 11·0 to 13·0 nm thickness deposited at 77 K are in a high state of disorder, having a grain size of approximately 0·4 nm and a vacancy concentration of 6–7 at %.

On warming to room temperature the crystal grains grow; largely due to the migration of single and multiple vacancies to the surface. The resistance falls by as much 40% as a result of the consequent rise in the effective number of free electrons and a large increase in relaxation time.

Even at a total pressure of 10^{-9}Torr oxidation of a fresh aluminium surface proceeds at a rate of 0·05 nm per hour. Over extended periods, the oxide layer thickness is a logarithmic function of time.

Annealing clean aluminium films in UHV to high temperature leads to uncertainty as a result of enhanced rate of oxide formation. Annealing films which have first been completely oxidized indicates that n rises as a result of a multiplication of defects.

Further studies over a wide spectral range are in progress and will be the subject of a later communication.

Acknowledgments

One of us (KRO) gratefully acknowledges the financial support of the Science Research Council. Thanks are due to P. Chapman of the National Physical Laboratory for assistance with the 'talystep' measurements.

References

Abeles, F., and Theye, M. L., 1969, *European Research Office US Army Contract* DAJA3F-67-C-o945.

Andrews, P. V., West, M. B., and Robeson, C. R., 1969. *Phil. Mag.* 19, 887–98.

Buckel, W., and Hilsch, R., 1954. *Z. Phys.*, 138, 112–25.

Ceresawa, S., 1969, *Phil. Mag.*, 19, 99–104.

Chechetenko, V. V., *et al.*, 1969. *Sov. Phys. Solid St.* 11, 1122–3.

Cotterill, R. M. J., 1963. *Phil. Mag.*, 8, 1937–44.

Dawson, H. *et al.*, 1968. *Lattice defects and their interactions*, Ed. Hasiguti (New York and London: Gordon and Breach) p681.

Dobson, P. J., and Hopkins, B. J., 1968, *J. Phys. D: Appl. Phys.* 1, 1241.

Ehrenreich, H., Philipp, H. R., and Segall, B., 1963. *Phys. Rev.* 132, 1918–28.

Fane, R. W., and Neal, W. E. J., 1968. *Proc. 4th Int. Vacuum Congress* (The Institute of Physics and the Physical Society: London) p 510.

Fane, R. W., and Neal, W. E. J., 1970, *J. Opt. Soc. Amer.*, 60, 790–3.

Gleiter, H., 1969, *Acta. Metal.*, 17, 565–73.

Grimes, N. W., Pearson, J. M., Fane, R. W., and Neal, W. E. J., 1970. *Phil. Mag.*, 21, 177–87.

Klei, 1969, *Material Sci. Engng.* (Neth), 3, 71.

Lidiard, A. B., 1968, *Sci. Prog.*, 56, 103–129.

Mader, S., and Nowick, A. S., 1967, *Acta. Metal.*, 15, 203–14.

Namba, Y., 1968, *Japan. Appl. Phys.*, 7, 783–4.

Neal, W. E. J., Fane, R. W., and Grimes, N. W., 1970. *Phil. Mag.* 21. 167–75.

Neugebauer, C. A., 1964, *Physics of Thin Films*. Vol. 2, (New York: Academic Press) p 37.

Scott, G., McLaughlan, T. A., and Sennet, R. S., 1950, *J. appl. Phys.*, 21, 843.

Seeger, A., Schiller, P., and Kronmuller, H., 1960. *Phil. Mag.*, 5. 853.

Sokolov, A. V., 1967, *Optical Properties of Metals* (Blackie), p. 111.

Thompson, M. W., 1969, *Defects and radiation damage in metals*, (London: Cambridge University Press) p. 32.

Table 5. Effect of annealing on a totally oxidized film

Film number		ψ	Δ	n	k	$n^2 - k^2$	nk	Resistance Ω
12	Before 250°C Anneal	33·52	135·84	1·05	4·73	−21·27	4·97	38·2
12	After 250°C	33·12	136·84	1·16	4·72	−20·93	5·48	51·3

5. Conclusions

Aluminium films of the order 11·0 to 13·0 nm thickness deposited at 77 K are in a high state of disorder, having a grain size of approximately 0·4 nm and a vacancy concentration of 6–7 at %.

On warming to room temperature the crystal grains grow; largely due to the migration of single and multiple vacancies to the surface. The resistance falls by as much 40% as a result of the consequent rise in the effective number of free electrons and a large increase in relaxation time.

Even at a total pressure of 10^{-9} Torr oxidation of a fresh aluminium surface proceeds at a rate of 0·05 nm per hour. Over extended periods, the oxide layer thickness is a logarithmic function of time.

Annealing clean aluminium films in UHV to high temperature leads to uncertainty as a result of enhanced rate of oxide formation. Annealing films which have first been completely oxidized indicates that n rises as a result of a multiplication of defects.

Further studies over a wide spectral range are in progress and will be the subject of a later communication.

Acknowledgments,

One of us (KRO) gratefully acknowledges the financial support of the Science Research Council. Thanks are due to P. Chapman of the National Physical Laboratory for assistance with the 'talystep' measurements.

References

Abeles, F., and Theye, M. L., 1969, *European Research Office US Army Contract* DAJA3F-67-C-o945.

Andrews, P. V., West, M. B., and Robeson, C. R., 1969. *Phil. Mag.* 19, 887–98.

Buckel, W., and Hilsch, R., 1954. *Z. Phys.*, 138, 112–25.

Ceresawa, S., 1969. *Phil. Mag.*, 19, 99–104.

Chechetenko, V. V., *et al.*, 1969. *Sov. Phys. Solid St.* 11, 1122–3.

Cotterill, R. M. J., 1963. *Phil. Mag.*, 8, 1937–44.

Dawson, H. *et al.*, 1968. *Lattice defects and their interactions*, Ed. Hasiguti (New York and London: Gordon and Breach) p681.

Dobson, P. J., and Hopkins, B. J., 1968. *J. Phys. D: Appl. Phys.* 1, 1241.

Ehrenreich, H., Philipp, H. R., and Segall, B., 1963. *Phys. Rev.* 132, 1918–28.

Fane, R. W., and Neal, W. E. J., 1968. *Proc. 4th Int. Vacuum Congress* (The Institute of Physics and the Physical Society: London) p 510.

Fane, R. W., and Neal, W. E. J., 1970, *J. Opt. Soc. Amer.*, 60, 790–3.

Gleiter, H., 1969, *Acta. Metal.*, 17, 565–73.

Grimes, N. W., Pearson, J. M., Fane, R. W., and Neal, W. E. J., 1970. *Phil. Mag.*, 21, 177–87.

Klei, 1969, *Material Sci. Engng.* (Neth), 3, 71.

Lidiard, A. B., 1968, *Sci. Prog.*, 56, 103–129.

Mader, S., and Nowick, A. S., 1967, *Acta. Metal.*, 15, 203–14.

Namba, Y., 1968, *Japan. Appl. Phys.*, 7, 783–4.

Neal, W. E. J., Fane, R. W., and Grimes, N. W., 1970. *Phil. Mag.* 21, 167–75.

Neugebauer, C. A., 1964, *Physics of Thin Films*, Vol. 2, (New York: Academic Press) p 37.

Scott, G., McLaughlan, T. A., and Sennet, R. S., 1950, *J. appl. Phys.*, 21, 843.

Seeger, A., Schiller, P., and Kronmuller, H., 1960. *Phil. Mag.*, 5, 853.

Sokolov, A. V., 1967, *Optical Properties of Metals* (Blackie), p. 111.

Thompson, M. W., 1969, *Defects and radiation damage in metals*, (London: Cambridge University Press) p. 32.

REFERENCES

1	Drude, P.	'Theory of Optics' Trans. by C.R. Mann and R.A. Millikan (London) 1902
2	Cauchy, A.L.	Compt. Rend. 8 560 1839; also Compt. Rend. 26 p.88 1848
3	Hagen, E. and Rubens, H.	Ann. Physik 11 873 1903
4	Zener, C.	Nature 132 p.968 1953
5	Hagen, E. and Rubens, H.	Ann. Physik. 1 352 1900 Ann. Physik. 11 873 1903 Phil. Mag. 7 157 1904
6	Fosterling, K. and Freedericksz, V.	Ann. Physik. 40 201 1913
7	Wood, R.W.	Phys. Rev. 44 353 1933 Nature 131 582 1933
8	Mott, N.F. and Jones, H.	'Theory of the properties of metals and alloys' (Clarendon Press, Oxford) 1936 2nd edn. (Dover, New York) 1958
9	Sommerfeld, A. and Frank, N.H.	Rev. Mod. Phys. 3 1 1931
10	Bloch, F.	Z. Physik 52 555 1928
11	Kronig, R.L.	Proc. Roy. Soc. 124 409 1929 Proc. Roy. Soc. 133 255 1931
12	Frolich, H.	Z. Physik 81 297 1933
13	Wilson, A.H.	'Theory of Metals' (Cambridge) 1936 Proc. Roy. Soc. 151 274 1935
14	Blakemore, J.S.	'Solid State Physics' (Saunders, London) 1969 p.154
15	Dingle, R.B.	Physica 19 312, 348, 729 1953
16	Ginzburg, V.L.	Dokl. Akad. Nauk. SSSR 97 999 1954
17	Pippard, A.B.	Proc. Roy. Soc. A191 385 1947
18	Sokalov, A.V.	'Optical Properties of Metals' (Blackie, London) 1967 p.168
19	Schulz, L.G.	Adv. Phys. 6 102 1957
20	Lenham, A.P. and Treherne, D.M.	J. Opt. Soc. Ann. 56 1076 1966
21	Gurzhi, R.N.	Sov. Phys. JETP 8 673 1959

22	Abeles, F. and Theye, M.L.	Report of European Research Office. U.S. Army. Contract No. DAJA37-67-C-0945 1969
23	Roberts, S.	Phys. Rev. 114 104 1959
24	Motulevich, G.P.	'Optical Properties of non-transition Metals' Review. Sov. Phys. Uspekhi 12 N1 80 1969
25	Mendelowitz, H.	Proc. Phys. Soc. 75 664 1960
26	Hass, G. and Tousey, R.	Opt. Soc. Ann. 49 N6 593 1959
27	Schulz, L.G. and Tangherlini, F.R.	J. Opt. Soc. Amer. 44 362 1954
28	Beattie, J.R. and Conn, G.K.T.	Phil. Mag. 46 222 1955
29	Bennet, H.E., Silver, M. and Ashley, E.J.	J. Opt. Soc. An. 53 1089 1963
30	Madden, R.P., Canfield, L.R. and Hass, G.	J. Opt. Soc. Amer. 53 620 1963
31	Fane, R.W. and Neal, W.E.J.	J. Opt. Soc. Amer. 60 N6 790 1970
32	O'Shea, K.R. and Fane, R.W.	Journal Phys. F (Metals) (to be published 1971)
33	Ehrenreich, H., Philipp, H.R., and Segall, B.	Phys. Rev. 132 N5 1918 1963
34	Jahode, F.C.	Phys. Rev. 107 1261 1957
35	Philipp, H.R. and Taft, E.A.	Phys. Rev. 113 1002 1959
36	Ehrenreich, H. and Philipp, H.R.	Phys. Rev. 128 1622 1962
37	Segall, B.	Phys. Rev. 131 121 1963
38	Powell, C.J.	J. Opt. Soc. Am. 60 N1 78 1970
39	Hughes, A.J., Jones, D. and Lettington, A.H.	J. Phys. C (Solid State) 2 Ser 2 102 1969
40	Harrison, W.A.	Phys. Rev. 118 1182 1962 Phys. Rev. 129 2503 1963
40A	Harrison, W.A.	Pseudopotentials in the study of metals. (Benjamin, New York) 1966
41	Heine, V.	'Low Temperature Physics' LT9 Part B (Plenum Press, New York) 1964 p.698

42	Heine, V.	'Optical Properties of Metals and Alloys' Proc. 1st Internat. Coll. Paris 1965 ed. by F. Abeles (North Holland, Amsterdam) p.16 1966
43	Ziman, J.M.	Advances in Physics 13 89 1964
44	Blakemore, J.S.	Solid State Physics (Saunders, London) 1969
45	Ashcroft, N.W.	Phil. Mag. 8 2055 1963
46	Ashcroff, N.W. and Sturm, K.	Phys. Rev. 3 N6 1898 1971
47	Mayer, H.	'Structure and Properties of thin films' p.225 Ed. by Neugebauer et al. (John Wiley, New York) 1958
48	Drumheller, C.E.	Journal de Physique 25 198 1964
49	Thomson, J.J.	Proc. Cam. Phil. Soc. 11 120 1901
50	Fuchs, K.	Proc. Cam. Phil. Soc. 34 100 1938
51	Sondheimer, E.H.	Phys. Rev. 80 401 1950
52	Cotterill, R.M.J.	Phil. Mag. 8 1937 1963
53	Yoshida, S. et al.	J. Phys. Soc. Japan 18 Supp.11 98 1963
54	Clarebrough, L.M.	Phil. Mag. 6 807 1961 Phil. Mag. 7 115 1962
55	Silcox, J. and Whelan, M.J.	Phil. Mag. 5 1 1960
56	Panseri, C. and Federighi, T.	Phil. Mag. 3 1223 1958
57	Simmons, R.O. and Balluffi, R.W.	Phys. Rev. 117 62 1960
58	Rider, J.G. and Foxton, C.T.B.	Phil. Mag. 23 289 1966
59	Yoshida, S.	J. Phys. Soc. Japan 20 N9 1662 1965
60	Komnik, Y.F., and Palatnik, L.S.	Sov. Phys. Solid State 7 N2 429 1965
61	Neuman, M.R. and Wen, H.K.	J. Appl. Phys. (Communications) 37 3327 1966
62	Ivanov, G.A. and Papov, A.M.	Sov. Phys. Solid State 5 1040 1962
63	Mayadas, A.F., Feder, R., and Rosenberg, R.	J. Vac. Sci. and Technol. 6 N4 690 1969
64	For example: Campbell, D.S.	'Use of Thin Films in Physical Investigations' (Acad. Press, New York) 1966 p.315

65	Kooy, C. and Nieuwenhuizen, J.M.	Proc. Int. Symp. on Thin Films Gottingen, 1966
66	Drumheller, C.E.	'Transactions of Fourth National Symposium on Vacuum Technology' American Vacuum Soc. p.27 1957
67	Mayadas, A.F., Shatzkes, M., and Janak, J.	Appl. Phys. (Letters) 14 N11 345 1969
68	Buckel, W. and Hilsch R.	Z. fur Physik. 138 112 1954
69	Buckel, W.	Z. fur Physik 138 136 1954
70	Bosnell, J.	Thin Sol. Films 3 233 1969
71	Bosnell, J. and Voisey, A.	Thin Sol. Films 6 N2 107 1971
72	Mader, S. and Nowick, A.S.	Acta. Met. 15 215 1967 Acta. Met. 15 203 1967
73	Chopra, K.L.	Phys. Stat. Sol. 32 489 1969
74	Baule, J.E. and Koehler, J.S.	Phys. Rev. 107 1493 1957
75	Meechan, C.J. and Brinkman, J.A.	Phys. Rev. 103 33 1193 1956
76	Thompson, M.W.	'Defects and Radiation damage in metals' (Cam. Univ. Press) 1969 p.264
77	Keefer, D. and Sosin, A.	Appl. Phys. Letters 3 185 1964
78	De Sorbo, W. and Turnbull, D.	Acta Met. 7 83 1959 Phys. Rev. 115 560 1959
79	Neugebauer, C.A.	'Physics on Thin Films' Vol.2, ed. by Hass (Acad. Press, London) 1964 p.39
80	Seeger, A.	2nd Geneva Conf. on Peaceful uses of Atomic Energy 6 250 1958
81	Meechan, C.J., Sosin, A., and Brinkman, J.	Phys. Rev. 120 411 1960
82	Bauer, W., Seeger, A., and Sosin, A.	Phys. Letters 24A 195 1967
83	Lidiard, A.B.	Sci. Prog. (Oxf.) 56 103 1968
84	Johnson, R.A. and Brown, E.	Phys. Rev. 127 446 1962
85	Sosin, A. and Rachal, L.H.	Phys. Rev. 130 2238 1963
86	Tolanski, S.	'Multiple Beam Interferometry' (Oxford Univ. Press) 1948

87	Murmann, H.	Z. Physik 80 161 1933 Z. Physik. 101 643 1936
88	Male, D.	Acad. Sci., Paris 230 1349 1950
89	Schopper, H.	Z. Physik 131 215 1952
90	Heavens, O.	'Optical Properties of Thin Solid Films' (Dover, New York) 1965
91	Rayleigh, Lord.	Phil. Mag. 33 1 1892
92	Drude, P.	Weid. Ann. (Leipzig) 39 481 1890 Weid. Ann. (Leipzig) 43 126 1891
93	Winterbottom, A.B.	Norske Videnskabers Selskab (Trondheim) 1955
94	Tool, A.Q.	Phys. Rev. 31 1 1910
95	Hauschild, H.	Wied. Ann. 63 816 1920
96	Fry, T.C.	J. Opt. Soc. Am. 15 137 1927 J. Opt. Soc. Am. 22 307 1932
97	Ives, H.E.	J. Opt. Soc. Am. 15 374 1927
98	Summers, R.D.	J. Opt. Soc. Am. 24 251 1934
99	Tronstad, L. and Borgman, C.W.	J. Opt. Soc. Am. 30 349 1934
100	Tronstad, L. and Feachem, C.G.P.	Proc. Roy. Soc. 145A 115 1934
101	Tronstad, L. and Hoverstad, T.	Trans. Farad. Soc. 30 1114 1934
102	Lowery, H. and Moore, R.L.	Phil. Mag. 13 938 1932
103	Lowery, H. and Wilkinson, H.	Phil. Mag. 22 769 1936
104	Lowery, H. and Bor, J.	Phil, Mag. 20 390 1935
105	Lowery, H. and Smare, D.L.	Proc. Phys. Soc. 49 345 1937
106	Lebernight, C.E. and Lustman, B.	J. Opt. Soc. Am. 29 59 1939
107	Tronstadt, L.,	T. Farad. Soc., 31 1151 1935
108	McPherson, L.	Proc. Phys. Soc. 52 210 1940
109	Rothen, A.	Rev. Sci. Instr. 16 26 1945
110	Rothen, A. and Hanson, M.	Rev. Sci. Instr. 19 839 1948 Rev. Sci. Instr. 20 66 1949 Rev. Sci. Instr. 28 283 1957
111	Elliott, A. Ambrose, E.J. and Temple, R.	J. Opt. Soc. Am. 38 212 1948

112	Beattie, J.R.	Phil. Mag. 46 235 1955
113	Hayfield, P.C.S. and White, G.W.T.	'Ellipsometry in the measurement of surfaces and thin films.' Washington Symposium, 1963.
114	Neal, W.E.J. Fane, R.W., and Grimes, N.W.	Phil. Mag. 21 N169 167 1970
115	Miller, Jane C.	Phil. Mag. 20 1115 1969
116	McCrackin, F.L., Passacaglia, E. Stromberg, R. and Steinberg, H.L.	J. Research Nat. Bur. of Standards 67A 363 1963
117	Archer, R.J.	J. Opt. Soc. Am. 52 970 1962
118	Archard, J.F., Clegg, P.L. and Taylor, A.M.	Proc. Phys. Soc. 65B 758 1952
119	Bòr J. and Pryzbylski J.	J. Sci. Instr. (G.B.) 40 108 1963
120	Gilham, E.J.	Nature (G.B.) 178 1412 1956
121	Gilham, E.J. and King, R.I.	J. Sci. Instr. (G.B.) 38 21 1961
122	Williamson, S.J., Weingart, J.M. and Andrews, R.D.	J. Opt. Soc. Am. 54 337 1964
123	King, R.J.	J. Sci. Instr. 43 924 1966
124	Seward, R.J.	Ph.D. Thesis, Univ. of Southampton 1967
125	Archard, J.F., Taylor, A.M.	J. Sci. Instr. (G.B.) 25 407 1948
125A	Liljenvall, H.G., Mathewson, A.G. and Myers, H.P.	Solid State Comm. 9 169 1971
126	Abeles, F.	Ann. de Physique 3 504 1948
127	Ditchburn, R.W.	'Light' (Blackie, London) 1952 p.480 (reprinted 1963)
128	Rouard, P.	Ann. de Physique 7 291 1937
129	Vasicek, A.	J. de Physique 11 342 1950
130	Born, M., Wolf, E.	'Principles of Optics' (Pergamon, London) 1970 p.31
131	Conn, G.K.T. and Eaton, G.K.	J. Opt. Soc. Am. 44 N7 546 1954
132	Jarrard, H.G.	J. Opt. Soc. Am. 42 N3 159 1952
133	Landry, J.D. Mitchell, E.N.	Phys. Rev. Communications, p.3400 1969
134	Scott, G.	J. Appl. Phys. 21 843 1950

134A	Koehler, W.F.	J. Opt. Soc. Am. 43 738 1953
134B	Shultz, L.G.	J. Opt. Soc. Am. 41 261 1951
135	Murr, L.E.	Mat. Res. Bull. 2 787 1967
136	Ceresawa, S.	Phil. Mag. 19 99 1969
137	Neugebauer, C.A.	Physics of Thin Films, Vol.2 (Acad. Press) 1964 p.37
138	Andrews, P.V.	Phil. Mag. 19 887 1969
139	Gleiter, H.	Acta. Met. 17 N5 565 1969
140	de Sorbo and Turnbull, D.	Physics Rev. 115 560 1959
141	Frederighi, T.	Lattice defects in quenched metals p.217 (Acad. press, London) 1965
142	Meechan, C.J. and Brinkman, J.A.	Phys. Rev. 103 N5 1193 1956
143	Sosin, A. and Rachal, L.H.	Phys. Rev. 130 N6 2238 1963
144	Dawson, H.	Lattice defects and their interactions ed. Hasiguti (Gordon and Breach Sci. Pub.) p.681 1968
145	Monch, N. and Sander, W.	Z. Physik 170 93 1962
145A	Hartman, T.E.	Measurement Techniques for Thin Films ed. by B. Schwartz. J. Electrochemical Soc. 1967 p.169
146	Namba, Y.	Jap. J. Appl. Phys. 7 783 1968
147	Hodgson, J.N.	Optical absorption and dispersion in solids. (Chapman and Hall, London) 1970 p.53
148	Sokolov, A.V.	Optical properties of metals (Blackie,) 1967, p.111
149	Abeles, F. and Theye, M.L.	European Research Office, U.S. Army Contract JAJA3F-67-C-0945 1969
150	Vasicek	Ellipsometry in the measurement of thin films (Nat. Bur. Stds. U.S. Misc. Pub. 256) (U.S. Goot Printing Office, Washington) 1961 p.25
151	Klei	Material, Sci. Engng (Neth.) 3 N2 71 1969
152	Grimes, N.W., Neal, W.E.J. and Fane, R.W.	Phil. Mag. 21 N169 177 1970
153	Wilcock, J.D., Campbell, D.S., and Anderson, J.C.	Thin Solid Films 3 13 1969

154	Menter, J.W. and Pashley, D.W.	'Structure and properties of thin films' ed. by C. Neugebauer (John Wiley, New York) 1959 p.111
155	Gubanov, A.I.	'Quantum Electron Theory of Amorphous Conductors' (Consultants Bureau N.Y.) 1965
156	Davies, E.A. and Shaw R.F.	Journal of Non-crystalline solids 2 406 1970
157	Black, P.J. and Cundall, J.A.	Acta. Cryst. 19 807 1965
158	Stuke, F.	'Festkorperprobleme' 9 46 1969
159	Donovan, T.M. and Spicer, W.E.	Phys. Rev. (letters) 21 1572 1968
160	Herman, F. and Van Dyke, J.P.	Phys. Rev. (letters) 21 1575 1968
161	Thompson, M.W.	'Defects and Radiation Damage in metals' (Cam. Univer. Press) 1969 p.10
162	Chopra, K.L.	'Thin Film Phenomena' (McGraw Hill, N.Y.) 1969 p.389

ACKNOWLEDGEMENTS
****

This work was carried out with the financial support of the Science Research Council at the University of Aston in Birmingham. Thanks are due to Professor S. E. Hunt, the head of the Physics Department, and many members of the academic staff, who gave advice and encouragement, particularly Mr. N. W. Grimes and Dr. W.E.J. Neal. The co-operation of Mr. F. Lane and the staff of the Physics Department workshop is gratefully acknowledged and also the assistance of Mr. W. Cooper with some of the drawings. Mr. P. Chapman of the National Physical Laboratories, Teddington, kindly contributed with some 'talystep' thickness measurements. The author must finally thank Dr. R. W. Fane for acting as supervisor of this work and for reading the manuscript.